

https://dspace.org/

Insights into sources and ore-forming processes of Cu-sulphide mineralization of the Phalaborwa Igneous Complex, from coupled Cu and Fe isotope and trace element systematics

Le Bras, Loïc Yves

2020
https://hdl.handle.net/10539/31084

Downloaded from a DSpace repository. https://dspace.org/



Insights into sources and ore-forming processes of Cu-sulphide mineralization of the Phalaborwa Igneous Complex, from coupled Cu and Fe isotope and trace element systematics

Loïc Yves Le Bras

A thesis submitted to the Faculty of Science, University of the Witwatersrand in fulfilment of the requirements for the degree of Doctor of Philosophy

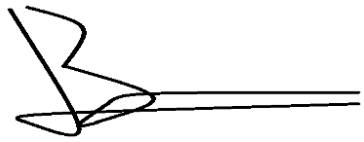
School of Geosciences

University of the Witwatersrand

Johannesburg, July 2020

Declaration

I declare that this thesis is my own, unaided work. It is being submitted for the Degree of Doctor of Philosophy at the University of the Witwatersrand, Johannesburg. It has not been submitted before for any degree or examination in any other University.



_____

Loïc Y. Le Bras Loic

30th day of July 2020 in Paris, France

Abstract

The Loolekop Pipe of the Phalaborwa Igneous Complex, Limpopo, South Africa, is the only known occurrence of a carbonatite – phoscorite sequence-hosted Cu-sulphide deposit of economic relevance. Despite significant research effort, some aspects of carbonatite- and phoscorite-hosted Cu-sulphide metallogenesis have remained elusive. In an attempt to address some outstanding research questions, this study focused on several specific points: (i) To characterize and classify sulphide textures and types, (ii) to constrain relative timing of ore-forming process(es), and (iii) to identify the metal source(s) involved in Cu mineralization. To this end, microfocus X-ray tomography and Mineral Liberation Analysis, combined with trace elements, Platinum-Group Elements (PGE) and Cu – Fe isotope systematics have been used to establish a comprehensive model of the metallogenesis in the Loolekop Pipe.

The Loolekop Pipe is the result of the successive emplacement of carbonatized melt pulses. The first unit to be emplaced was composed of a phoscorite – carbonatite sequence, where phoscorite is concentrated at the margins of the intrusion and carbonatite towards its centre. Due to the presence of mineral layering, this rock type is described as banded carbonatite. A structural event caused renewal of igneous activity and the intrusion of a second carbonatite pulse within a stockwork, known as transgressive carbonatite.

Several Cu-sulphide generations were identified across the Loolekop Pipe. The first major form of Cu mineralization is characterized by chalcopyrite veins, which, considering the sharp contact with the host-rock, precipitated along fractures within the Loolekop Pipe. The second form is composed of sub-vertical sulphide layers hosted in both the banded carbonatite and the phoscorite. These layers are parallel to banding in the phoscorite and banded carbonatite. The magmatic assemblages are composed of bornite and chalcopyrite in various proportions. Three main textures can be observed among Cu-sulphide layers. The first texture consists of small (<1 mm) bornite and chalcopyrite grains. These grains are dispersed within the layer and are not associated with each other. Bornite can be found as isolated grains dispersed in the gangue without the presence of structural features, combined with chalcopyrite replacement or exsolution patches or laths. Bornite grains may locally host chalcocite veinlets and combined chalcocite and covellite replacement along its external boundaries. Isolated chalcopyrite can also be found, as well as trace amounts of cubanite. The second texture is characterized by stretched mm-sized bornite-chalcopyrite assemblages, which, considering the irregular surface, most likely derived from the merging of bornite and chalcopyrite grains. These assemblages are stretched in the same direction, suggesting the intervention of a magmatic flow process. The third and last texture shows mm(s)-wide chalcopyrite planar cumulates. Therefore, the

mineralogical makeup cannot be considered as representative. The last major form of Cu-sulphide is constituted by valleriite [$(Fe^{2+},Cu)_4(Mg,Al)_3S_4(OH,O)_6$], which resulted from both *in-situ* replacement of magmatic and hydrothermal sulphides, as well as dissolution and re-precipitation of Cu along small fractures in close proximity to magmatic and hydrothermal sulphides.

Similar PGE contents in the Primitive Mantle (5 ppb for Ru; 3.6 ppb for Pd; 6.6 ppb for Pt, respectively) and the Loolekop Pipe (1 to 4 ppb Ru; 2 to 8 ppb Pd; 1 to 9 ppb Pt) suggest a mantle origin of the sulphide material. Furthermore, low PGE contents coupled with heavy Fe isotope signatures (δ^{56}Fe of 0.07 to 0.29‰) of banded carbonatite and phoscorite indicate a limited degree of partial melting and sulphide liquid extraction (~10%). Considering the preferential fractionation of Co and Zn into sulphide phases, the enrichment of both Co and Zn contents in whole-rocks (5 to 100 ppm and 15 to 100 ppm, respectively) relative to sulphides (0.1 to 40 ppm and 1 to 10 ppm, respectively) suggest some assimilation of external material and early interruption of chemical exchange between sulphide liquid(s) and melt(s).

Platinum-Group Element concentrations in the Cu-sulphide assemblages reveal an enrichment of Pd-group PGE (PPGE; Pt and Pd) over Ir-group PGE (IPGE; Ir, Os and Ru). Palladium concentrations in sulphides range from 35 to 310 ppb, while Os and Ir range from <4 to 49 ppb and <1 to 4 ppb, respectively. Platinum contents range from <2 to 31 ppb, which can be explained by the extraction of Pt from sulphide phases through crystallization at depth of sperrylite ($PtAs_2$) and its sequestration elsewhere. The PPGE enrichment over IPGE indicates the involvement of a monosulphide solid solution (mss) – intermediate solid solution (iss) system, where a sulphide liquid formed an IPGE-rich mss remaining at depth, and a Cu- and PPGE-rich sulphide liquid, which, by further ascent in the pipe and cooling down of the system, evolved into magmatic bornite and chalcopyrite. Iron and Cu isotope compositions of Cu-sulphides confirm a hypogene origin of these phases. Employing *in-situ* micro-drilling, values of δ^{65}Cu range between -1.3 and 0.8‰ and δ^{56}Fe values between -0.6 and 0.3‰. Likewise, sulphide separates show similar variations in δ^{65}Cu values between -0.7 and 0.4‰ and δ^{56}Fe values between -0.7 and 0.4‰. The alternation of sub-vertical banded carbonatite and phoscorite bandings, and a progressive decrease of phoscorite abundance towards the core of the pipe suggest the involvement of several magma pulses with a decreasing Fe-oxide and apatite component, from which phoscorite and banded carbonatite formed by immiscibility due to pressure drop. Relative proportions of bornite and chalcopyrite change from one sulphide layer to another, suggesting the presence of sulphide liquids of different compositions in the

melt pulses. Despite this aspect, the similar Fe and Cu isotopic signatures indicate both a common material source and similar ore-forming processes.

The similar distribution patterns, but lower concentrations of PGE in hydrothermal chalcopyrite relative to magmatic assemblages suggest that hydrothermal chalcopyrite along fractures within the core of the Loolekop Pipe may have resulted from the dissolution of magmatic sulphides and an iss phase by high-temperature hydrothermal fluids at depth, and subsequent re-precipitation of the dissolved material into a stockwork. However, light Fe isotope compositions (δ^{56}Fe values between -0.7 and -0.2‰) of hydrothermal chalcopyrite indicate leaching and breakdown of magnetite at depth, which is the most likely assumption.

Late-stage valleriite is consistently associated with both magmatic and hydrothermal sulphides. It shows that valleriite resulted from the alteration of these sulphide assemblages. The presence of valleriite along fractures within primary sulphides and around the boundaries of the grains indicate *in-situ* alteration of magmatic and hydrothermal sulphide assemblages and their replacement by valleriite. The presence of valleriite along fractures in proximity to primary sulphide phases indicates limited dissolution – precipitation. The preservation of primary sulphide assemblages in fracture-free samples illustrates the importance of late-stage fluid circulation for valleriite formation. The presence of gangue-filled veins in close spatial association to valleriite and other primary sulphide assemblages confirms the limited influence of dissolution – precipitation. Therefore, the presence of large valleriite veins in previous studies can be explained by the alteration and replacement of primary and hydrothermal assemblages. The higher concentrations of As and Pb in valleriite relative to magmatic sulphides (1 ppm vs 0.1 ppm for As; 100 to 840 ppm vs 13 to 380 ppm Pb, respectively) suggest a crustal origin of late-stage fluids. However, dissolution of magmatic and hydrothermal sulphides and precipitation of valleriite may also have contributed to this anomaly.

The involvement of several magma pulses seems to be a classical feature for the formation of a banded carbonatite – phoscorite sequence, as observed for instance, in the Kovdor complex, Russia. Likewise, formation of phoscorite and carbonatite either by immiscibility or cumulate formation appears to be similar to other phoscorite – carbonatite sequences, such as in Kovdor or Salitre in Brazil. The main difference between the Loolekop Pipe and other phoscorite – carbonatite occurrences is the presence of significant amounts of Cu-sulphides. The occurrence of a significant amount of hydrothermal chalcopyrite can be partly explained by massive leaching of phoscorite-hosted magnetite by high-temperature fluids, although the presence in the Loolekop Pipe of sub-vertical magmatic Cu-sulphide layers remains unexplained, and the metal source unconstrained. Another phoscorite – carbonatite sequence hosted by the

Salmagorskii Igneous Complex also contains Cu-sulphides, which appears to be post-magmatic, and which cannot be the case for the Loolekop-hosted sulphide layers. A possible explanation may be contribution from a Cu- and S-rich, and compositionally heterogeneous mantle underlying the Phalaborwa Igneous Complex at the time of magmatism.

Acknowledgments

The Centre of Excellence for Integrated Mineral and Energy Resource Analysis (CIMERA) is thanked for funding this project.

I would like to thank Robert Bolhar for giving me the opportunity to work on this topic. His help, suggestions, ideas and constant support have been essential to the success of this project. Lab work could not have been possible without my co-supervisor, Grant Bybee, who gave helpful advice on setting up the ion exchange method. His unconditional support for analytical work and interest in method development made this project possible. Paul Nex provided useful advice and constructive opinions on the metallogenic model and his help is greatly acknowledged.

Staff of the Palabora Mining Company, in particular Thabitha Moyana and Paulien Lourens, are thanked for providing the samples necessary for this study.

Tomographic analysis could not have been done without the help of Lunga Bam, Jakobus Hoffman and Frikkie De Beer at NECSA. The setup of the ion exchange chromatography procedure could not have been done without the advice of Vincent Balter. Emmanuelle Albalat has my specific gratitude for her help for Fe isotopic measurements.

A special mention has to be given to Henriette Ueckermann at the University of Johannesburg for her patience during the method setup and the measurements on the MC-ICPMS, and to Bradley Guy for his help during MLA analysis.

I would like to thank Lechelle Goslin and Cameron Penn-Clarke for their support, their useful advice and for always being there.

The courage and patience of Abigail Ayikwei to bear a grumpy Frenchman for three years is hereby acknowledged with a special mention of her ability to tolerate the persistent smell of strong coffee in the office. Thank you very much to my friends Emma, Marc, Ross, Alex Le Lion, Thomas, Julien, Louise and Paul for keeping me more or less sane.

My parents Florence and Olivier Le Bras, as well as my brother Ronan, have my eternal gratitude for their unconditional support. I could not have achieved this degree without them.

Table of contents

Declaration ii
Abstract iii
Acknowledgments vii
Table of contents viii
List of figures xii
List of Tables xvi
1. Introduction 1
1.1 The Loolekop Cu-sulphide deposit 2
1.2 Aims 3
1.3 Approach 3
1.4 Thesis structure 4
1.5 Contributions to publications 5
2. Chapter 2: Geological setting 7
2.1 Regional Geology 7
2.2 The Phalaborwa Igneous Complex 9
2.3 The Loolekop Pipe 9
3. Chapter 3: Platinum-Group and Trace Elements in Cu-sulphides from the Loolekop Pipe, Phalaborwa: Implications for Ore-Forming Processes 12
3.1 Introduction 12
3.2 Materials and methods 12
3.2.1 Mineral Liberation Analyzer 13
3.2.2 LA-ICP-MS 13
3.2.3 Whole-rock analysis 14
3.3 Results 15
3.3.1 Silicate and oxide mineralogy 15
3.3.2 Ore mineralogy 15
3.3.3 Whole-rock geochemistry 20
3.3.4 Mineral chemistry 24
3.4 Discussion 25
3.4.1 Textural and paragenetic sequence analysis 27
3.4.1.1 Magmatic sulphide assemblages 27
3.4.1.2 Secondary alteration sulphide phases 30
3.4.2 A possible mantle source and sulphide liquid evolution 31
3.4.3 PGM content 34

3.4.4 Incorporation of surface-derived lithospheric material? 36
3.5 Conclusions 37
4. Chapter 4: Three-Dimensional Textural Model of Sulphide Mineralization from the Loolekop Intrusion, Phalaborwa: An Indicator for Ore-Forming Processes and Carbonatite-Phoscorite Emplacement 39
4.1 Introduction 39
4.2 Copper sulphides in the Loolekop pipe 40
4.3 Sample and methods 41
4.3.1 Samples 41
4.3.2 Tomography 41
4.3.3 Mineral Liberation Analysis 42
4.4 Results 43
4.4.1 Spatial resolution 43
4.4.2 Mineral associations 45
4.4.3 Planar sulphide layers 50
4.5 Discussion 51
4.5.1 Textures and origin of magmatic sulphide mineralization 51
4.5.2 Sulphide layer formation processe(s) 52
4.5.3 Formation of hydrothermal sulphides 53
4.5.4 Late-stage alteration characteristics 55
4.5.5 Gas bubbles as potential carriers of sulphide liquid 55
4.6 Conclusions 56
5. Chapter 5: Copper and Iron Isotopic Analysis and Spatially Resolved Sampling: A New Method for Ore Characterization 58
5.1 Introduction 58
5.2 Background 58
5.2.1 Isotope fractionation processes 58
5.2.2 Ion Exchange Chromatography 64
5.3 Sampling 65
5.3.1 Laser microtomy 65
5.3.2 Drilling 68
5.4 Chromatography mechanisms and method choice 70
5.5 Chemistry 72
5.5.1 Material 72
5.5.2 Dissolution 73
5.5.3 Ion exchange chromatography 73

5.6 Measurements 76
5.6.1 Copper 76
5.6.2 Iron 77
5.6.3 Optimization 79
5.7 Conclusions 79
6. Chapter 6: Copper and Iron Isotope Variations in Cu-sulphides from the Phalaborwa Carbonatite: A Fingerprint for Ore-Forming Processes 81
6.1 Introduction 81
6.2 Methods 85
6.2.1 Sampling 85
6.2.2 Chemical separation 85
6.2.3 MC-ICP-MS measurements 86
6.3 Results 88
6.3.1 Mineral association 88
6.3.2 Magmatic and hydrothermal assemblages 88
6.3.3 Alteration phases 91
6.3.4 Copper isotopes 91
6.3.4.1 Sulphide separates 91
6.3.4.2 *In-situ* drilling 93
6.3.5 Iron isotopes 96
6.3.5.1 Whole-rock analysis 96
6.3.5.2 Sulphide separates 96
6.3.5.3 *In-situ* drilling 98
6.3.5.4 Magnetite separates 98
6.4 Discussion 99
6.4.1 Partial melting and mantle origin 99
6.4.2 Hypogene origin and isotopic fractionation between primary sulphides 100
6.4.3 Hydrothermal assemblage source and formation processes. 101
6.4.4 Fluid circulation and valleriite formation 103
6.4.5 Origin of magnetite 103
6.4.6 Model for Cu mineralization 104
6.5 Conclusions 107
7. Chapter 7: Discussion and Conclusions 109
7.1 Methods and tools 109
7.2 Copper-sulphide classification 110

7.2.1 Magmatic assemblages 110
7.2.2 Hydrothermal mineralization 111
7.2.3 Late-stage alteration phases 111
7.3 A revised model 112
7.3.1 Mantle source, partial melting and intrusive processes 112
7.3.2 Early sulphide formation mechanisms 115
7.3.3 A complex hydrothermal ore-forming process 116
7.3.4 Late stage alteration 117
7.4 Perspectives 117
8. References 120
Appendix A: List of samples used for PGE and trace element investigations (Chapter 3) ... 147
Appendix B: Mineral Liberation Analysis data (Chapter 3) 148
Appendix C: Whole-rock major element compositions (Chapter 3) 175
Appendix D: Whole-rock trace element compositions (Chapter 3) 177
Appendix E: Whole-rock PGE compositions (Chapter 3) 181
Appendix F: Trace element compositions of sulphide assemblages and location of the spots in the polished mounts (Chapter 3) 182
Appendix G: Summary of PGE and trace element mss/sulphide liquid and iss/sulphide liquid fractionation coefficients (Chapter 3) 211
Appendix H: List of samples used for microCT investigations (Chapter 4) 212
Appendix I: MicroCT results (Chapter 4) 213
Appendix J: Iron and Cu isotope analyses (Chapter 6) 214

List of figures

Figure 2.1: Regional map of southern Africa showing the main structure and geological units (modified after Vielreicher et al., 2000 and Wu et al., 2011). 8

Figure 2.2: Geological map of the Phalaborwa Igneous Complex (a), with an enlarged view of the Loolekop Pipe carbonatite-phoscorite complex (b) and a cross section of the intrusion (section c). Modified after Palabora Mining Company Ltd Staff (1976). 11

Figure 3.1: Photomicrographs of representative sulphide phases. Cbn=cubanite, Cct=chalcocite, Ccp=chalcopyrite, Cv=covellite, Bn=bornite, Mag=magnetite, Py=pyrite, V=valleriite. (a) Banded carbonatite. Bornite with chalcopyrite lamellae, isolated in a carbonate gangue matrix. (b) Banded carbonatite. Assemblage of bornite with magnetite surrounded by carbonates. Strong alteration of bornite and replacement by covellite at the rims. (c) Phoscorite. Bornite with chalcopyrite lamellae, post-emplacement fracturing and alteration to valleriite, (d) (e) and (f) transgressive carbonatite. Massive chalcopyrite with cubanite exsolution lamellae and fractures filled with Fe-oxide phases and valleriite. Also visible inclusions of bornite and pyrite. 17

Figure 3.2: MLA mineral maps obtained from polished blocks of banded carbonatite: (a) sample SL94 B22 and (b) SL140 B08(2). 18

Figure 3.3: MLA mineral maps obtained from polished blocks of (a) transgressive carbonatite (sample SL139 B62(2)c) and (b) phoscorite (sample SL139 B62(2)a). 19

Figure 3.4: Primitive Mantle-normalized lithophile element variation graph for lithophile elements. Normalization values from Lyubetskaya and Korenaga (2007). Order of elements from Sun and McDonough (1989). 21

Figure 3.5: Primitive Mantle-normalized variation graph for REE. Normalization values from Lyubetskaya and Korenaga (2007). 23

Figure 3.6: Diagrams showing trace element concentrations in sulphides from the different rock types within the Loolekop Pipe (a) bornite in banded carbonatite (BC); (b) chalcocite in BC; (c) chalcopyrite in BC; (d) valleriite in BC; (e) bornite in phoscorite (PC); (f) chalcopyrite in PC; (g) valleriite in PC; (h) bornite in transgressive carbonatite (TC); (i) chalcopyrite in TC and (j) valleriite in TC. 26

Figure 3.7: Sulphide PGE contents in the different rock types of the Loolekop Pipe with (a) concentrations in banded carbonatite (BC), (b) in phoscorite (PC) and (c) in transgressive carbonatite (TC). 28

Figure 3.8: Primitive Mantle-normalized PGE and Au concentrations for different deposits. Copper porphyry deposits are Baula Nuasahi in India, Galore Creek and Island Copper in Canada; Elatsite in Bulgaria and Skouries in Greece. Data from Augé et al. (2005). O'okiep PGE concentrations by Maier et al. (2012). Bulk continental crust values from Rudnick and Gao (2003). Normalization values from Lyubetskaya and Korenaga (2007). 33

Figure 3.9: Crystallization and precipitation model of the different sulphide phases in the Loolekop Pipe. Melts were generated by low-degree partial melting of a metasomatized sub-continental lithospheric mantle. (i) During its ascent, the sulphide melt forms an IPGE-rich mss cumulate and a Cu- and PPGE-rich sulphide liquid, which crystallizes upward and exsolves a PPGE-rich sulphide liquid forming sulphide blebs that precipitated in bornite. (ii) The iss was remobilized through high-temperature hydrothermal fluids and formed massive chalcopyrite-cubanite mineralization in a stockwork. (iii) Late-stage fluids leached the previously emplaced sulphides and formed a massive valleriite mineralization..... 35

Figure 3.10: Primitive mantle-normalized diagrams showing trace element patterns of averaged sulphide type compositions. In (a) banded carbonatite; (b) phoscorite; (c) transgressive carbonatite and (d) continental crust. Normalization values from Lyubetskaya and Korenaga (2007)..... 37

Figure 4.1: Description of the method applied for data processing, from data acquisition to the 3D model creation. 42

Figure 4.2: (a) Raw microCT 2D projection of sulphide phases (medium grey) in a carbonatite matrix from the sample HD027 – 17 (Appendix H). (b)Electron microscopic picture of the same slice, showing higher spatial resolution. (c) High-resolution mineral map corresponding to a part of the picture (b)..... 45

Figure 4.3: Photomicrographs of different sulphide assemblages observed in the Loolekop Pipe. Bn = bornite, Cbn = cubanite, Ccp = chalcopyrite, Mag = magnetite, V = valleriite. (a) Typical bornite grain associated with chalcopyrite dispersed in the gangue. (b) Similar features to (a), with a valleriite-filled fracture network, and association of magnetite with bornite. (c) and (d) disseminated grains of chalcopyrite within gangue, with small chalcopyrite interstitial veinlets between gangue minerals..... 46

Figure 4.4: Photomicrographs of different sulphide assemblages observed in the Loolekop Pipe. Bn = bornite, Cbn = cubanite, Ccp = chalcopyrite, Cc = chalcocite, Mag = magnetite. (a) Interstitial chalcopyrite and magnetite between gangue grains. (b) Parallel magnetite-filled veinlets, also hosting chalcopyrite in their axial zones. (c) Bornite grains with chalcocite alteration within the gangue close to magnetite. (d) and (e) Dispersed grains of magnetite and bornite with interstitial chalcopyrite veinlets with locally interstitial bornite veinlets across the gangue (top of picture d). Presence of small chalcopyrite interstitial veinlets between gangue minerals. (f) Assemblage of cubanite and magnetite within carbonate gangue..... 48

Figure 4.5: Photomicrographs of several sulphide assemblages within the Loolekop Pipe. Bn = bornite, Cbn = cubanite, Ccp = chalcopyrite, Cc = chalcocite, Mag = magnetite, V = valleriite. (a) Complex assemblage of cubanite and chalcopyrite hosting both pyrite and magnetite. (b) Hydrothermal sulphide assemblages with both chalcopyrite and cubanite cut by late-stage veins filled by magnetite and valleriite. (c) Bornite, together with magnetite disseminated within the gangue. Bornite may host significant amounts of chalcocite. Gangue-hosted, parallel magnetite veinlets are observed. (f) Interstitial magnetite between gangue grains with late-stage valleriite. 49

Figure 4.6: Synthesis of the different types of primary sulphides. Picture (a) shows large patches of bornite (purple) and chalcopyrite (orange). Sulphide textures in (b) display alternating layers of sulphides with different textures. The sulphides in picture (c) show strong alteration leading to the formation of valleriite (green). Picture (d) displays a massive chalcopyrite vein at the top and underlying parallel sulphide layers. 50

Figure 4.7: Model of the sulphide mineralization formation within the Loolekop Pipe. The first step shows the successive intrusion of melt pulses, each forming phoscorite along their external boundaries and carbonatite towards the core of the intrusion as well as sub-vertical sulphide layers. The second step is characterized by a structural event and the precipitation of chalcopyrite from high-temperature hydrothermal fluids along the fractures. The third step shows the appearance of valleriite associated to late-stage fractures in chalcopyrite and bornite layers. 54

Figure 4.8: Phlogopite (dark grey) surrounded by sulphide aureoles (light grey) in a calcite matrix. 56

Figure 5.1: Elution curve for the ion exchange chromatography procedure described in Table. 5.4 for Cu and Fe separation. 75

Figure 5.2: Three Fe isotopes correlation graph for measurement quality control. 78

Figure 5.3: Summary of the procedure, from sampling to measurement, for sulphide Cu and Fe isotopic ratio determination. 80

Figure 6.1: Summary of δ^{65}Cu variations for different sulphide ore deposit types and locations worldwide as well as values for chondrites and Bulk Silicate Earth. Porphyry δ^{65}Cu values were published by Maréchal et al. (1999), Larson et al. (2003), Graham et al. (2004), Mathur et al. (2009, 2012) and Mirnejad et al. (2010). Skarn-type deposit δ^{65}Cu values were measured by Wang et al. (2017). Values of δ^{65}Cu values for Alexandrinka and Besshi Volcanic Hosted Massive Sulphide (VHMS) deposits were summarized from Mason et al. (2005) and Ikehata et al. (2011), respectively. Magmatic deposit δ^{65}Cu values were taken from Larson et al. (2003) and Zhao et al. (2019). Submarine hydrothermal δ^{65}Cu values were published by Zhu et al. (2000) and Rouxel et al. (2004). δ^{65}Cu variation for supergene minerals was published by Maréchal et al. (1999), Zhu et al. (2000), Larson et al. (2003), Mathur et al. (2009), Mirnejad et al. (2010) and Ikehata et al. (2011). Granite δ^{65}Cu values were published by Li et al. (2009). Enstatite Chondrite Bulk Earth (ECBE), Chondrite Bulk Earth (CBE) and Bulk Silicate Earth (BSE) δ^{65}Cu values were published by Savage et al. (2015). 83

Figure 6.2: Summary of δ^{56}Fe variations for different sulphide ore deposit types and locations worldwide as well as values for chondrites and mantle peridotites. Porphyry δ^{56}Fe values were published by Graham et al. (2004), Wawryk and Foden (2017) and J.-X. Li et al. (2018). Skarn-type deposit δ^{56}Fe values were measured by Wang et al. (2011, 2015). Values of δ^{56}Fe values for hydrothermal deposits were published by Markl et al. (2006b). Magmatic deposit δ^{56}Fe values were taken from Wawryk and Foden (2015) and Zhao et al. (2019). Chondrite δ^{56}Fe values were published by Poitrasson et al. (2004), Mullane et al. (2005), Needham et al. (2009), Craddock and Dauphas (2011) and Hezel et al. (2018). Peridotite mantle δ^{56}Fe values were summarized from Zhu et al. (2002), Beard and Johnson (2004), Williams et al. (2004, 2005),

Weyer et al. (2005), Schoenberg and von Blanckenburg (2006), Weyer and Ionov (2007), Zhao et al. (2010, 2012), Huang et al. (2011) and Poitrasson et al. (2013). 84

Figure 6.3: Iron three-isotope plot of □-values for sulphides. The slope is close to the theoric value (1.475). Uncertainties are ±2 SD. 87

Figure 6.4: Photomicrographs of the different sulphide phases present in the Loolekop Pipe. Bn=bornite, Py=pyrite, V=valleriite, Cbn=cubanite, Cc=chalcocite, Cv=covellite, Mag=magnetite. (a) and (b) Primary magmatic chalcopyrite and chalcopyrite-bornite assemblages, disseminated into carbonate gangue and associated with Fe-oxides in both the phoscorite and the banded carbonatite. (c) and (d) Hydrothermal vein-hosted sulphide assemblages composed of chalcopyrite and cubanite (c). These veins may locally host pyrite (d). (e) Alteration of bornite as thin veinlets of chalcocite and covellite replacement at the outer edges of the mineral. (f) Alteration of primary bornite-chalcopyrite assemblage and replacement by late-stage valleriite. 90

Figure 6.5: Cu isotopic compositions. (a) Histogram showing Cu isotopic compositions of sulphide separates. (b) Copper isotopic composition of magmatic, hydrothermal and late-stage alteration sulphides sampled by drilling into polished mounts. 95

Figure 6.6: Fe isotope ratio analyses. (a) Histogram showing Fe isotopic compositions of sulphide separates as well as whole-rocks. (b) Iron isotopic compositions of magmatic, hydrothermal and late-stage alteration sulphides sampled by drilling into polished mounts. . 97

Figure 6.7: Evolution of sulphide phases in the Cu-Fe-S system during cooling of a sulphide liquid, with a focus on the central portion of the Cu-Fe-S system. The sulphide liquid at the origin of the monosulphide solid solution (mss) and intermediary solid solution (iss) also crystallized directly as bornite (bn), chalcopyrite (ccp), pyrrhotite (po), pyrite (py), troilite (tr) and cubanite (cbn), mostly as complex assemblages. Modified after Ebel and Naldrett (1997) (a), Cabri (1973) (b) and Sugaki et al. (1975) (c). 106

Figure 7.1: Simplified model illustrating the various ore-forming processes for Cu-sulphides in the Loolekop Pipe. 114

List of Tables

Table 3.1: Summary of sulphide assemblages and textures in the different rock types of the Loolekop Pipe. 20

Table 3.2: Mineral association statistics for the different sulphides. 22

Table 3.3: Whole-rock PGE and Au concentrations. 24

Table 4.1: Summary of sulphide types and their respective textures within the Loolekop Pipe. 47

Table 5.1: Trace element composition of the resin Crystalbond 509. 67

Table 5.2: Trace element composition of drilled natural quartz against the composition of undrilled sample. 69

Table 5.3: Distribution coefficients D for Cu and Fe for several ion exchange resins depending on the molarity of eluting acid (modified after van der Walt et al., 1985). 71

Table 5.4: Ion exchange chromatography procedure implemented for Cu and Fe separation from sulphides. Procedure modified from Maréchal et al. (1999) and Sossi et al. (2015). 75

Table 5.5: Cup configuration of Nu Plasma II MC-ICP-MS for Cu measurements. 76

Table 5.6: Characteristics of Nu Plasma II and Thermo Scientific Neptune Plus MC-ICP-MS for measurements of Cu and Fe, respectively. 76

Table 6.1: Ion exchange chromatography procedure for separation of Cu, Fe and Zn for 1 ml of AG1-X8 (200-400 mesh) resin used with 0.8 X 7 cm columns. 86

Table 6.2: Measured Fe and Cu isotopic composition of geologic standards and comparison with the recommended values (Fe values from Craddock and Dauphas; 2011; Cu values from Sossi et al., 2015). 88

Table 6.3: Cu and Fe isotopic compositions of different sulphide separates from the Loolekop Pipe sampled from whole-rocks. Sulphides are abbreviated as bn = bornite, ccp = chalcopyrite, v = valleriite. 92

Table 6.4: Cu and Fe isotopic compositions of sulphides in the Loolekop Pipe drilled into polished mounts from different assemblages. Sulphides are abbreviated as bn = bornite, ccp = chalcopyrite, v = valleriite. 94

Table 6.5: Fe isotopic compositions of the different rock types of the Loolekop Pipe. 96

Table 6.6: Fe isotopic composition of magnetites (Mag) sampled in the different rock types of the Loolekop Pipe. Rock types are abbreviated as banded carbonatite = BC, phoscorite = PC and transgressive carbonatite = TC. 98

Introduction

Copper has been used for more than 10,000 years for a wide range of applications. This element was initially used for the crafting of tools and weapons during the Copper Age, before its strength was discovered when alloyed with Sn (bronze) and various metals and metalloids (such as Ni, Zn for brass) (O'Brien, 2015). Such alloys are widely used for industrial purposes due to their favourable physical and chemical properties, in particular low friction coefficients. The high conductivity leads to extensive use as conductors in electric cables and electronic devices. The resistance of Cu to corrosion makes it very useful in plumbing. Copper has also been used in arts and architecture (roofing, cladding and flashing) for thousands of years. Furthermore, this element played a significant role in the economy due to its use in coinage. Due to its properties and applications, global Cu consumption (and consequently price) is directly dependant on industrial development. The development of the Chinese industrial sector since the 1970s makes this metal, together with Fe and Al, a key to China's continued economic growth and it is, therefore, considered a critical metal in the mining industry (Pitron, 2018).

Nowadays, Cu is mainly mined in giant porphyry deposits located in the Andes in Chile and Peru, as well as in western Papua New Guinea, exemplified by the Grasberg Igneous Complex. Sediment-hosted stratabound Cu deposits, which can also contain vein-hosted Cu-sulphides, are the second most important Cu deposit type of economic interest (Saintilan et al., 2018). A genetic model for this type of deposit has been suggested by Brown (2014). However, the applicability of this model to some deposits within the Central African Copperbelt (El Desouky et al., 2010; Hitzman and Broughton, 2017; Sillitoe et al., 2017), the Kupferschiefer (Jowett, 1992; Oszczepalski, 1999; Blundell et al., 2003), and the White Pine Cu deposit (Mauk et al., 1992) may be questionable. The most profitable deposits of this type are located in the Central African Copperbelt in the Katangan Basin in Democratic Republic of Congo and Zambia. The Kodaro-Udokan Basin in Russia, as well as the Zechstein Basin in central Europe, are also of economic significance (Saintilan et al., 2018). Copper ores are also mined together with Ni ores in magmatic sulphide deposits, such as in Noril'sk-Talnakh in Siberia and Sudbury in Canada (Naldrett, 2004).

The Loolekop Cu-sulphide deposit, Limpopo Province, South Africa, is one of the biggest Cu deposits in southern Africa, and is hosted by a carbonatite-phoscorite assemblage in the Phalaborwa Igneous Complex. Occurrences of the carbonatite-phoscorite series are particularly rare (Krasnova et al., 2004a and 2004b) and Cu mineralized examples are even rarer. The Loolekop Cu-sulphide deposit is the only known case hosting Cu-sulphides at modal

concentrations of current economic interest. The Loolekop Cu deposit is particularly complex and hosts several magmatic, hydrothermal and secondary generations of sulphide assemblages (Heinrich, 1970; Vielreicher et al., 2000). After being studied for more than sixty years (Forster, 1958; Van Rensburg, 1965; Palabora Mining Company Ltd Staff, 1976), sulphide classification, metal source and ore-forming processes of the Cu mineralization remain unclear, making the investigation of ore-forming processes within the Loolekop Pipe of significant interest for the understanding of this unusual major Cu deposit.

1.1 The Loolekop Cu-sulphide deposit

Copper-sulphides in the Loolekop intrusion have been studied since the 1950s. Divergent sulphide classifications and models have been proposed to explain the sulphide paragenesis (Lombaard et al., 1964; Heinrich, 1970; Palabora Mining Company Ltd Staff, 1976, Vielreicher et al., 2000; Giebel et al., 2019). However, consensus has been reached regarding several features of the Cu mineralization. It is acknowledged that chalcopyrite is the dominant Cu-sulphide in the Loolekop Pipe, mainly due to the presence of large chalcopyrite veins in the core of the intrusion (Palabora Mining Company Ltd Staff, 1976; Vielreicher et al., 2000). Bornite, often associated with chalcopyrite, is reported to be the second most abundant sulphide in the intrusion, dispersed within both banded carbonatite and phoscorite (Lombaard et al., 1964; Palabora Mining Company Ltd Staff, 1976; Eriksson, 1989; Vielreicher et al., 2000). Chalcocite is present as intergrowths in bornite, along µm-wide fractures (Rudashevsky et al., 2004). However, coarse chalcocite isolated in the gangue has also been observed by Lombaard et al. (1964). Myrmekitic intergrowths of chalcocite with bornite have been observed locally (Rudashevsky et al., 2004). Late-stage valleriite has been observed in association with all sulphide assemblages mentioned above as result of fluid alteration (Palabora Mining Company Ltd Staff, 1976; Milani et al., 2017a; Giebel et al., 2019).

Several hypotheses for the sulphide paragenesis have been proposed. Copper-sulphides may have been derived from a single hydrothermal event (Forster, 1958). In contrast, according to Lombaard et al. (1964), significant amounts of vein-hosted chalcopyrite within the core of the pipe, and dispersed bornite, as well as sulphide layers towards the edge of the Loolekop Pipe, point to a two-stage sulphide-forming process. This model includes (i) the crystallization of bornite-dominated sulphide assemblages in banded carbonatite and phoscorite and (ii) a Cu-rich fluid circulation episode forming massive chalcopyrite veins within the core of the pipe. Heinrich (1970) suggested that the presence of several Cu-sulphide phases resulted from mineralogical zoning, with high-temperature chalcopyrite-cubanite assemblages in the centre

and low-temperature bornite in phoscorite and banded carbonatite. It has also been suggested that fluids circulating within a fracture network were responsible for the precipitation of massive chalcopyrite veins in the centre of the Loolekop Pipe (Palabora Mining Company Ltd Staff, 1976). More recent studies suggest a three-step ore-forming process with (i) an early magmatic stage characterized by the formation of dispersed bornite in both banded carbonatite and phoscorite, followed by (ii) fluid circulation within the core of the pipe, causing the precipitation of transgressive carbonatite-hosted chalcopyrite and, finally (iii) a late-stage fluid circulation episode leading to valleriite deposition as a film on pre-existing magmatic and hydrothermal sulphides (Vielreicher et al., 2000). Basson et al. (2017) characterized the core-hosted Cu mineralization as wide and long sulphide lenses. The most recent model proposed by Giebel et al. (2017) suggests the formation of primary Cu-sulphides in one single stage, postdating the emplacement of phoscorite and carbonatite, followed by a late valleriite alteration.

1.2 Aims

As shown in Section 1.1, many aspects relating to the formation of Cu-sulphides within the Loolekop Pipe have remained unclear and contentious. Despite an overall consensus regarding the main mineral phases present within the Loolekop Pipe, the origin, nature and formation of some minor textural features remain elusive. Specific textures as indicators for specific sulphide-forming processes have not been systematically documented and examined, and are therefore still controversial. This thesis aims to provide a better understanding of the Cu-sulphide mineralization within the Loolekop Pipe by focusing on four specific objectives:

- Refine the inventory of Cu-sulphide assemblages, textures and associations.
- Determine the relative timing of the Cu-sulphide phases.
- Identify the ore-forming process(es).
- Identify the source of the sulphides.

1.3 Approach

Previous relevant studies were mostly restricted to the use of optical and electron microscope, as well as electron microprobe. Consequently, an innovative approach using new analytical methods is required to develop truly new insights into ore-forming processes and sulphide assemblage classification. In order to address the aims listed above, a multi-

disciplinary approach was adopted using different analytical methods, each focused on addressing specific aspects of the metallogenesis of the Loolekop Pipe:

- For the identification of the source(s) of sulphides as well as the different steps of the sulphide liquid evolution, Platinum-Group Element (PGE) and trace element analysis was conducted with both laser-ablation (LA-ICP-MS) and solution-based inductively-coupled-mass spectrometry (ICP-MS).
- Microfocus X-ray tomography (microCT) was selected for its three-dimension imaging capacity. Together with Mineral Liberation Analysis (MLA) and optical microscopy, these techniques enabled detailed documentation and characterization of Cu-sulphide assemblages, producing a comprehensive and representative classification.
- Sulphide crystallization and postdating event(s) affecting the Cu-ore phases are challenging to identify on the exclusive basis of mineral associations and trace element compositions. Copper and Fe isotope analysis by multi collector (MC)-ICP-MS is a powerful tool for the determination of ore-forming processes since isotope fractionation is sensitive to changes in physical and chemical conditions prevalent in a specific environment. This method has therefore been chosen for the characterization of conditions of sulphide crystallization and alteration, as well as the identification of the sulphide source(s).

Evidence acquired by combining these three methods leads to the development of a new model concerning the formation of Cu-sulphides in the Loolekop Pipe.

1.4 Thesis structure

This thesis is divided into seven chapters, with Chapters 3, 4 and 6 forming parts of scientific articles in various stages of the publication process. The article corresponding to Chapter 3 has been published in *Mineralium Deposita* (doi: 10.1007/s00126-020-01005-4). The manuscript for Chapter 4 is in preparation and will be submitted for publication in *Minerals*. Chapter 6 has been submitted for publication in *Mineralium Deposita* with the manuscript reference MIDE-D-20-00114 and is under review at the time of thesis submission. Chapter 1 outlines the scope of this study, provides a detailed background, and outlines the approaches taken to solve the difficulties that have been identified. Chapter 2 summarizes the geology of the Phalaborwa Igneous Complex and the Loolekop Pipe. Chapter 3 presents a PGE and trace element geochemistry-based study of the Cu-sulphides to understand ore-forming processes, including MLA-based texture analysis. Chapter 4 is dedicated to the study of sulphide textures and assemblages by tomography. Chapter 5 provides an overview on the development and

implementation of the ion exchange chromatography for Cu and Fe separation applied to sulphides and oxides. Chapter 6 is then an application of Cu and Fe isotope systematics to Cu-sulphides from the Loolekop Pipe to fingerprint ore-forming processes. Chapter 7 provides a synthesis of the results and interpretations of Chapters 3, 4 and 6, and presents a revised and integrated metallogenetic model for Cu-sulphides within the Loolekop Cu deposit. Detailed methodologies are presented in each specific chapter and repetitive parts of articles have been merged and inserted into the introductory chapters. Appendices at the end of the thesis contain all analytical data produced in this study.

1.5 Contributions to publications

Chapter 3:

Loic Y. Le Bras, Robert Bolhar, Grant M. Bybee, Paul A. M. Nex, Bradley M. Guy, Thabitha Moyana and Paulien Lourens published in *Mineralium Deposita*. doi: 10.1007/s00126-020-01005-4.

Le Bras, L. Y. – 70% (Produced the written work, obtained analytical data.)

Bolhar, R. – 15% (Provided project design and funding, edited and corrected the successive manuscript drafts.)

Bybee, G. M. – 5% (Edited and corrected the successive manuscript drafts.)

Nex, P. A. M. – 5% (Assisted with sulphide formation model, edited and corrected the successive manuscript drafts.)

Guy, B. M. – 3% (Assisted with Automated Mineralogical Analysis using MLA.)

Moyana, T. – 1% (Technical support during sampling.)

Lourens, P. – 1% (Technical support during sampling.)

Chapter 4:

Loic Y. Le Bras, Robert Bolhar, Lunga Bam, Bradley M. Guy, Grant M. Bybee and Paul A. M. Nex, in preparation.

Le Bras, L. Y. – 70% (Produced the written work, obtained analytical data, processed the microCT results.)

Bolhar, R. – 15% (Provided project design and funding, edited and corrected the successive manuscript drafts.)

Bam, L. – 5% (Assisted with microCT data acquisition and data processing.)

Guy, B. M. – 5% (Assisted with Automated Mineralogical Analysis using MLA.)

Bybee, G. M. – 2% (Edited and corrected the successive manuscript drafts.)

Nex, P. A. M. – 3% (Edited and corrected the successive manuscript drafts.)

Chapter 6:

Loic Y. Le Bras, Robert Bolhar, Henriette Ueckermann, Paul A. M. Nex, Emmanuelle Albalat, Vincent Balter and Grant M. Bybee submitted to *Mineralium Deposita*. Manuscript reference: MIDE-D20-00114.

Le Bras, L. Y. – 70% (Produced the written work, set up the analytical procedure, obtained analytical data.)

Bolhar, R. – 10% (Provided project design and funding, edited and corrected the successive manuscript drafts.)

Ueckermann, H. – 5% (Assisted with Cu isotope measurements.)

Nex, P. A. M. – 3% (Assisted with sulphide mineralogy, edited and corrected the successive manuscript drafts.)

Albalat, E. – 2% (Assisted with Fe isotope measurements.)

Balter, V. – 2% (Assisted with implementation of the analytical procedure.)

Bybee, G. M. – 8% (Assisted with implementation of Fe and Cu chemical separation techniques, edited and corrected the successive manuscript drafts.)

Chapter 2
Geological setting

2.1 Regional Geology

The 3.6 to 2.7 Ga Kaapvaal Craton in Southern Africa is the outcome of large-scale Archaean igneous activity forming a gneissic complex and the postdating emplacement of igneous, sedimentary and volcanic sequences (Poujol et al., 2003; Eglington and Armstrong, 2004). This Craton is delimited by the Namaqua-Natal belt at its southern and western borders and by the Limpopo belt at its northern limit (Fig. 2.1; Clendenin et al., 1988; Roering et al., 1992; Eriksson and Altermann, 1998). The Kaapvaal Craton is marked by the presence along lineaments of greenstone belts (>3.1 Ga, Robb and Meyer, 1995), such as the Barberton Greenstone Belt, comprised of metamorphosed sedimentary as well as ultramafic volcanic rocks (komatiites) (Armstrong et al., 1990; de Ronde and de Wit, 1994; Heubeck and Lowe, 1994; Parman et al., 1997; Lowe and Byerly, 1999, 2007). The Barberton Greenstone Belt is regarded as a remnant of an Archaean fold and thrust belt located at the eastern margins of the Kaapvaal Craton (de Wit, 1982; de Ronde and de Wit, 1994; Lowe, 1994).

The Dominion Group and the Witwatersrand and Ventersdorp Supergroups form volcano-sedimentary sequences, combined into the Witwatersrand Triad, overlying the Archaean gneisses and granitoids of the Kaapvaal Craton (Bowen et al., 1986; Marsh et al., 1989; Coward et al., 1995). The Dominion Group (3.086 – 3.074 Ga; Robb and Meyer, 1995) is composed of a sedimentary unit, hosting Au and U placers, successively overlain by mafic lavas and felsic volcanic rocks that show an alternation of pyroclastic flows and volcanoclastic sediments (Crow and Condie, 1987; Jackson, 1992; Agangi et al., 2020). The Witwatersrand Supergroup can be divided into the West Rand Group (2.970 – 2.914 Ga; Robb and Meyer, 1995) consisting of sands, greywackes and shales and the Central Rand Group (2.894 – 2.714 Ga; Robb and Meyer, 1995) made up of fluvial sands, conglomerates and shales (Pretorius, 1976; Coward et al., 1995; Jahn and Condie, 1995). The Ventersdorp Supergroup is a slightly metamorphosed sequence comprising three distinct groups (Winter, 1976; Crow and Condie, 1988; Wronkiewicz and Condie, 1990; Van der Westhuizen et al., 1991). The Klipriviersberg Group, composed of mafic volcanic rocks is overlain by bimodal volcanic rocks capped with sediments and tuffs from the Platberg Group (Bowen et al., 1986; Myers et al., 1990; Van der Westhuizen et al., 1991). The Pniel Group at the top of the sequence, is constituted by an arenaceous unit capped by mafic to intermediate volcanic rocks.

The Neoarchaean to Palaeoproterozoic Transvaal Supergroup was deposited in a foreland basin after the Witwatersrand Triad and is made up of a basal quartzite (Black Reef Quartzite) overlain by the Chuniespoort Group dominated by carbonates, which is in turn overlain by the Pretoria Group, which contains alternating quartzites, shales, and volcanic rocks (Walraven et al., 1990; Hartzer, 1995; Schweitzer et al., 1995; Eriksson and Altermann, 1998; Catuneanu and Eriksson, 1999). The Transvaal Supergroup rocks are preserved in both the Griqualand West Basin and the Transvaal Basin.

The Bushveld Layered Complex intruded the sedimentary and volcanic rocks of the Transvaal Supergroup in the north-eastern part of the Kaapvaal Craton, forming five distinct lobes (Eastern, Western, Far Western, Southern and Northern lobes) and formed successively the PGE- and Cr-rich mafic Rustenburg Layered Suite, the Rashoop granophyres and Lebowa Granite Suite (Hartzer, 1995; Zeh et al., 2015). The Rustenburg Layered Suite is divided in five main units, which are the Marginal Zone, the Lower Zone, the Critical Zone, the Main Zone and the magnetite-rich Upper Zone (Von Gruenewaldt et al., 1985; Cawthorn and Walraven, 1998; Cawthorn, 2015). The complex is the outcome of successive intrusions into the Kaapvaal Craton (Kruger, 1994; Eales and Cawthorn, 1996; Wilson, 2015). The Rustenburg Layered Suite was emplaced at 2.055.91 ± 0.26 Ma in less than 1.02 Ma (± 0.63), approximately synchronously with the Phalaborwa Igneous Complex (PIC) (Zeh et al., 2015).

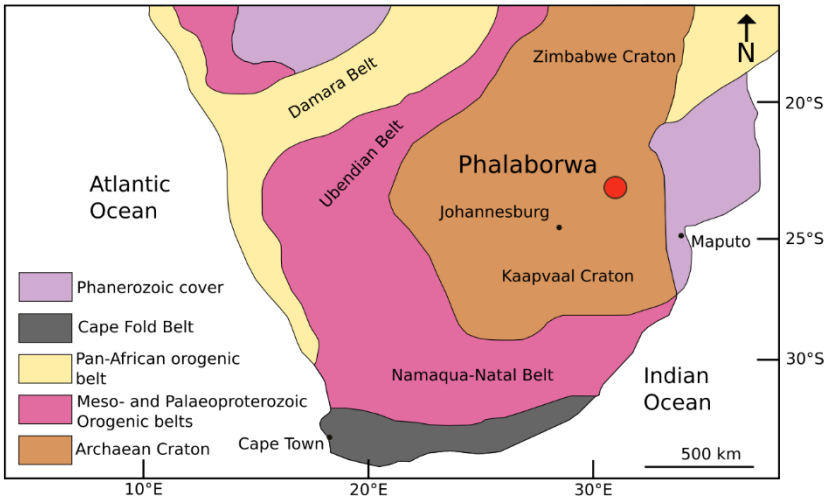


Figure 2.1: *Regional map of southern Africa showing the main structure and geological units (modified after Vielreicher et al., 2000 and Wu et al., 2011).*

2.2 The Phalaborwa Igneous Complex

The ellipsoid-shaped PIC occupies a surface area of about ~18 km² and is elongated in a north-south direction (Fig. 2.2a). It was originally emplaced as a concentric intrusion into >2900 Ma granitoids and gneisses in the northeast of the Kaapvaal Craton, South Africa (Wu et al., 2011). The PIC is composed of three adjacent circular and zoned lobes along the north-south axis of the complex, corresponding to three distinct intrusive pipes (Fig. 2.2a). The PIC rock types range from ultramafic/mafic at the rim, to carbonatitic in the centre (Heinrich, 1970; Eriksson, 1982, 1989). The first rock type to be emplaced into the gneissic-granitic rocks of the Kaapvaal Craton was a mica-bearing clinopyroxenite with phlogopite and high abundances of apatite (Lombaard et al., 1964; Hanekom et al., 1965; Heinrich, 1970; Eriksson, 1982). The phlogopite was altered locally into vermiculite by supergene weathering (Palabora Mining Company Ltd Staff, 1976). The main clinopyroxenite unit shows variable mineral alignment caused by flow differentiation of the melt during emplacement (Eriksson, 1982). The latter rock type is surrounded by feldspathic clinopyroxenite at the contact with the Kaapvaal granite-gneiss. Some fenitization occurred on a local scale (Eriksson, 1982), particularly along the contact between the granite-gneiss country rocks and the clinopyroxenite. Postdating the main clinopyroxenite unit, clinopyroxene-bearing pegmatites were emplaced into the three circular lobes (Fig. 2.2a). The mineralogical and chemical composition of the pegmatites varies between the different pipes: the northern pegmatite consists of a phlogopite-diopside-apatite ring surrounding a diopside-serpentine-phlogopite rock. The southern pegmatite on the other hand is a single unit composed of phlogopite and diopside, as well as fluorapatite and minor serpentine. The pegmatite in the central pipe is composed of a phlogopite-diopside-fluorapatite rock (Lombaard et al., 1964; Eriksson, 1982). Phoscorite (an apatite-, magnetite-, forsterite- and minor calcite-bearing igneous rock) intruded both the northern and central pipes after the pegmatites. A series of syenite plugs with an age of 2068 ± 17 Ma (zircon U-Pb) were also emplaced into the Kaapvaal granite around the complex (Yuhara et al., 2003; Wu et al., 2011). Later mafic dykes (U-Pb in apatite: 2062 ± 53 Ma) crosscut all the above-mentioned rock types (Wu et al., 2011).

2.3 The Loolekop Pipe

The central intrusive pipe (Loolekop) is characterized by an association of phoscorite and banded carbonatite (Fig. 2.2b). Previous studies, aimed at determining the emplacement age of the Loolekop Pipe using U-Pb isotopic analysis of baddeleyite, found comparable ages of

2059.8 ± 0.8 Ma and 2060.6 ± 0.5 Ma (Heaman and LeCheminant, 1993; Reischmann, 1995). More recently, Wu et al. (2011) focused on both zircon and baddeleyite from different rock types within the Loolekop Pipe and obtained an emplacement age of 2060 ± 4 Ma, illustrating that all the intrusive phases of the complex were effectively emplaced simultaneously. The phoscorite contains coarse-grained (~5 mm to 6 cm) apatite and magnetite, as well as calcite and some forsterite and phlogopite. This unit is characterized by strong planar mineral alignment, formed by magnetite and apatite. The banded carbonatite is medium- to coarse-grained (1 mm to 2 cm) and consists of calcite with minor dolomite, magnetite, and apatite and small amounts of biotite, phlogopite and forsterite (Lombaard et al., 1964; Hanekom et al., 1965; Heinrich, 1970; Palabora Mining Company Ltd Staff, 1976). Banded carbonatite, like phoscorite, shows mineral alignment, which was ascribed to magmatic flow by Lombaard et al. (1964). The contact between the banded carbonatite and phoscorite varies from sharp to gradational. Both the banded carbonatite and phoscorite contain disseminated Cu-sulphide mineralization. The interlayering and sub-vertical nature of this intrusion can be explained by the rapid ascent of magma pulses related to the presence of five intersecting major faults rotated with respect to one another, which formed zones of weakness (Fig. 2.2c; Basson et al., 2017). The intersection of these zones of weakness at the centre of the Loolekop Pipe may have resulted in the rotation of the intrusive volume of ascending magma or, alternatively, in the post-emplacement torsion of the pipe. These processes may have contributed to deformation of the rock units within the Loolekop Pipe (Basson et al., 2017).

Subsequent igneous activity caused brecciation of the pipe (Lombaard et al., 1964; Heinrich, 1970), allowing the ascent and emplacement of a second carbonatite pulse, the transgressive carbonatite, which cross-cuts the above-mentioned units of the Loolekop Pipe along structural features (Fig. 2.2b). The transgressive carbonatite is composed of coarse-grained (5 mm to 5 cm) calcite and dolomite with trace amounts of magnetite. Circulation of mineralizing fluids in the transgressive carbonatite was structurally controlled and led to significant enrichment in Cu-sulphide along fractures, relative to the other parts of the Loolekop intrusion (Palabora Mining Company Ltd Staff, 1976). The sulphide content varies significantly within the transgressive carbonatite due to the structural controls (Palabora Mining Company Ltd Staff, 1976). Late gabbro dykes cut all the rock types described above on a northeast-southwest axis, but their orientation is locally affected by fault and shear zones.

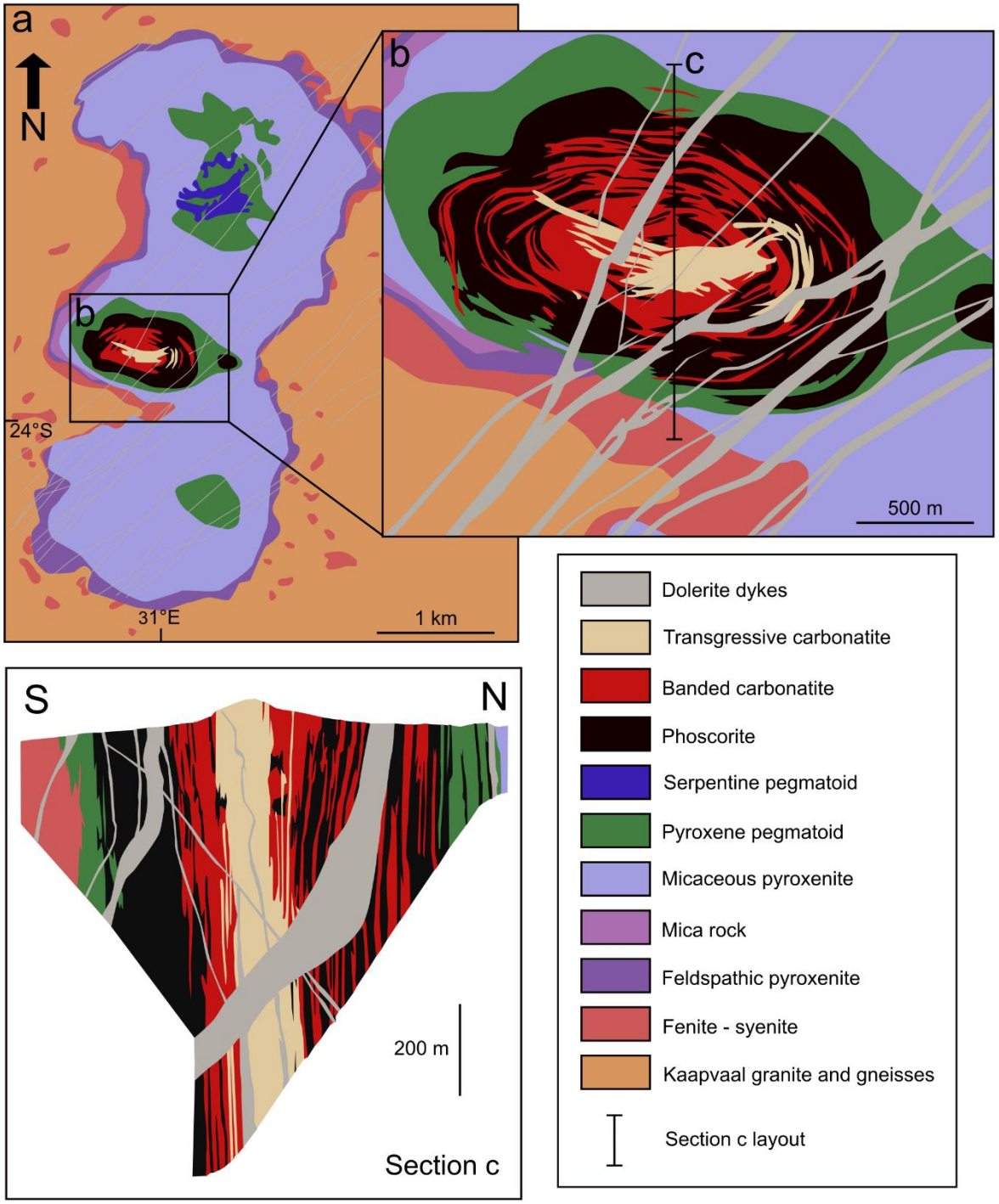


Figure 2.2: *Geological map of the Phalaborwa Igneous Complex (a), with an enlarged view of the Loolekop Pipe carbonatite-phoscorite complex (b) and a cross section of the intrusion (section c). Modified after Palabora Mining Company Ltd Staff (1976).*

Chapter 3

Platinum-Group and Trace Elements in Cu-sulphides from the Loolekop Pipe, Phalaborwa: Implications for Ore-Forming Processes.

This chapter was submitted to and has been published in *Mineralium Deposita* as a manuscript entitled "Platinum-Group and Trace Elements in Cu-sulphides from the Loolekop Pipe, Phalaborwa: Implications for Ore-Forming Processes" by Loic Y. Le Bras, Robert Bolhar, Grant M. Bybee, Paul A. M. Nex, Bradley M. Guy, Thabitha Moyana and Paulien Lourens. doi: 10.1007/s00126-020-01005-4.

3.1 Introduction

Textural studies, coupled with trace element and PGE analysis, have proved particularly effective in testing metallogenic models of Cu sulphide mineralization (Bezmen et al., 1994; Mungall et al., 2005; Barnes et al., 2006; Klemd et al., 2016; Piña et al., 2012). Partition coefficients of PGE and other trace elements (e.g., As, Bi, Co, Se, Sn, Te, Zn) between the sulphide and gangue phases have been used to constrain the petrogenetic origin of magmatic and hydrothermal sulphides (Barnes et al., 1997; S.-J. Barnes, et al., 2008; Dare et al., 2010 2011). Due to the various partition coefficients of trace elements between the sulphide phases, the abundances of these elements may provide clues to the origin of the Loolekop sulphides at different mineralization stages, and by extension, the sources of Cu and other base metals and subsequent differentiation processes (Bockrath et al., 2004; Barnes and Ripley, 2016). Here, we use a combination of optical petrography, quantitative mineral mapping and *in-situ* trace element analysis (LA-ICP-MS), as well as whole-rock geochemistry to assess the metallogenesis of Cu-sulphide mineralization within the principal rock types of the Loolekop Pipe, namely phoscorite, banded carbonatite and transgressive carbonatite.

3.2 Materials and methods

Sixteen Cu-sulphide-rich samples were selected from the banded carbonatite, phoscorite, transgressive carbonatite, as well as micaceous clinopyroxenite, from the drill core yard of the Palabora Mining Company (Appendix A). A single polished epoxy mount (30 mm diameter) was prepared for every sulphide-rich specimen. For each sample, representative rock powders for whole-rock trace element and PGE analysis were prepared.

3.2.1 Mineral Liberation Analyzer

Automated mineralogical analyses were performed on polished epoxy mounts from each of the 16 samples using a Mineral Liberation Analyzer (MLA) to determine the distribution and association of minerals (Appendices A and B). The mineral paragenesis was established through the determination of mineral association statistics considering their surrounding mineral phases. This approach also allows the characterization of sulphide assemblages using mineral associations.

Automated mineralogical analyses were carried out at the University of Johannesburg using a FEI Quanta 600 Mineral Liberation Analyzer (MLA) equipped with a field-emission gun and two Bruker Xflash X-ray detectors. The back-scatter electron (BSE) grey level was calibrated using three standards (Cu, quartz and Au). The X-ray detectors were automatically calibrated using the Cu standard. The X-ray collection time was set to 10 ms for sulphide phases and 30 ms for gangue phases. The electron accelerating voltage was adjusted to 25 keV, the working distance was 13 mm and the current on the specimen was 10 nA.

Two modes, namely XBSE and GXMAP, were employed for the MLA analyses. The XBSE mode is considered as a fast mapping mode since a single X-ray analysis point is collected per each BSE grey-scale phase. This mode is not suitable for complex ore types, where multiple phases can exhibit similar BSE intensities, which results in the erroneous discrimination of phases (e.g., magnetite and pyrite). To overcome this shortcoming, the GXMAP mode was selected for samples characterized by complex mineral assemblages and textural relationships. The GXMAP mode represents a slower, but more accurate mapping mode, since X-ray spot analyses are collected on a pre-defined XY grid of points with a spacing of 23 µm.

3.2.2 LA-ICP-MS

Laser Ablation-ICP-MS analysis was performed on sulphides within the polished mounts for determining trace element and PGE concentrations subsequent to the determination of ideal targets by MLA mapping. Laser Ablation-ICP-MS analyses were performed at the Geozentrum Nordbayern at the University of Erlangen-Nürnberg, Germany, using an Agilent 7500c ICP-MS combined with an Excimer 193 nm Teledyne laser. The external calibration for Ru, Rh, Pd, Os, Ir, Pt and Au utilized the Po724 B2 SRM standard and calibration for Re used the $(Fe,Ni)_{1-x}S$ Sulphide standard from the University of Münster (Wohlgemuth-Ueberwasser et al., 2007). The MASS-1 polymetal sulphide from the USGS was utilized for the external calibration of

Co, Ni, Cu, Zn, As, Se, Cd, Pb and Bi. Sulphur concentrations obtained by microprobe analysis served as an internal standard.

The beam diameter was set to 20, 25 or 35 µm depending on the size of target sulphide grains. Repetition rate and fluence were set at 17 Hz and 3 J cm^{-2}, respectively. The duration of an analysis was 43 s, with 20 s of background measurement (He, Ar and instrument) and 23 s of ablation. ^{29}Silicon, ^{33}S, ^{34}S and ^{63}Cu were measured with an integration time of 10 ms per isotope, ^{59}Co, ^{60}Ni, ^{67}Zn, ^{75}As, ^{77}Se, ^{82}Se, ^{106}Cd, ^{111}Cd, ^{208}Pb and ^{209}Bi with 25 ms per isotope, and ^{99}Ru, ^{101}Ru, ^{103}Rh, ^{105}Pd, ^{108}Pd, ^{185}Re, ^{189}Os, ^{193}Ir, ^{195}Pt and ^{197}Au with 30 ms. Results for several isotopes could not be used, like ^{99}Ru, ^{101}Ru, ^{103}Rh,^{105}Pd and ^{108}Pd due to Co, Cu, Ni and Zn argide interferences. The data processing was performed using the software GLITTER (van Achterbergh et al., 2000).

3.2.3 Whole-rock analysis

Composite samples were used for whole-rock geochemical analysis. Multiple pieces of drill core were selected at regular intervals along the drill core and were combined to form representative samples of each specific lithology. The pieces were crushed, milled in a swing-mill pot, and homogenized to avoid sampling bias due to inherent heterogeneities, such as magmatic/tectonic foliations and Cu-sulphide micro-veins. Whole-rock powder aliquots (75 g) were sent to Intertek Genalysis in Perth, where sulphide pre-concentration was achieved by fire assay Ni sulphide collection. The resulting samples were then dissolved and analyzed by ICP-MS, along with the standard AMIS0499. The difference between measured and recommended values of the AMIS0499 data is 4% for Ru, 5.51% for Rh, 0.83% for Pd, 1.49% for Ir, 5.6% for Pt and 16.5% for Au. For whole-rock trace element analysis, 50 mg of powder was digested in a MARS microwave digester with a high-purity acid mixture of 3HF:2HNO_3 and converted into nitric form. Analysis was performed using a Thermo Fisher iCAP at the Earth Lab of the University of the Witwatersrand using the certified reference materials BHVO-2 and BCR-2 for quality control. The analytical uncertainty for elements with a concentration of >200 ppm was <4%, while concentrations <200 ppm produced an analytical uncertainty >5%. Cobalt is an exception since its concentration in the standard is 45 ppm, and the difference between the measured and certified values is about 1%.

3.3 Results

3.3.1 Silicate and oxide mineralogy

The four different sulphide-bearing rock types in the Loolekop Pipe show characteristic differences in modal mineral abundances and types of minerals. In the banded carbonatite, petrographic observations reveal the dominance of calcite and dolomite. Apatite, phlogopite and magnetite are present in variable proportions, reaching maximum modal abundances of 30, 60 and 40%, respectively. Some 50 to 500 µm-sized Cu-sulphides are observed. Copper-sulphides are present as disseminated aggregates within the rock. Minor amounts of diopside are also present. The phoscorite shows large crystals of anhedral magnetite, as well as phlogopite and apatite crystals associated with calcite grains, with modal abundances of 10 - 60%, 0 - 30%, 10 - 60% and 15 - 45%, respectively. The mineralogical make-up of phoscorite is highly variable between samples. Some forsterite was also observed, but its modal abundance rarely exceededs 10%. In some areas, calcite, apatite and magnetite have fractures filled with Cu-sulphides. The transgressive carbonatite is composed of large crystals of calcite and dolomite hosting minor apatite, with sizes varying between 50 and 500 µm. Locally, some magnetite with a maximum diameter of 500 µm was also observed. The micaceous clinopyroxenite is composed of apatite, ilmenite, phlogopite and diopside, the abundances of which are highly variable and dependent on the sampling location. Nevertheless, phlogopite modal abundance can reach up to 60% in the studied samples and forms a dominant assemblage with apatite. The rock type is generally devoid of sulphides.

3.3.2 Ore mineralogy

The Cu mineralization in both the banded carbonatite and phoscorite consists of assemblages of bornite and chalcopyrite in variable proportions disseminated within the gangue (Figs. 3.1a, 3.1b, 3.1c, Appendix B). A summary of the different textures and ore assemblages is given in Table 3.1 combined with Figs. 3.1a-f. Bornite represents the major phase of the mineralization in these two rock types, with chalcopyrite occurring in the form of lamellae or aggregates (Figs. 3.1a, 3.1c and 3.3). The MLA results show a clear distinction in the mineral association characteristics of Cu sulphides between the banded carbonatite and phoscorite (Figs. 3.2 and 3.3, Table 3.2). In fact, the bornite-chalcopyrite assemblages show an affinity with magnetite and the assemblages are rarely exclusively associated with carbonates or other gangue phases. The mineral association statistics (Table 3.2) highlight that sulphide phases are mostly associated with each other and form aggregates (chalcopyrite, chalcocite and bornite). The absence of fractures associated with the bornite-chalcopyrite assemblages indicates a

magmatic origin of this primary phase. Chalcocite, as well as covellite, occur in very small amounts, and can be locally observed as an alteration product of bornite (Figs. 3.1a and 3.1b, Table 3.2).

Transgressive carbonatite-hosted massive chalcopyrite veins are present in an almost pure calcite-dolomite aggregate with very few other minerals (Figs. 3.1d, 3.1e and 3.1f, Tables 3.1 and 3.2). Veins observed in this study are usually up to several cm-wide. However, the Palabora Mining Company Ltd Staff (1976) reported the presence of veinlet networks with a width of several metres. In one sample, chalcopyrite coexists with bornite, forming an assemblage similar to those present in both banded carbonatite and phoscorite (Fig. 3.3). The vein-hosted chalcopyrite typically shows cubanite exsolution lamellae, which is an exclusive feature of transgressive carbonatite-hosted chalcopyrite (Figs. 3.1d and 3.1e). Locally, cubanite entirely replaces chalcopyrite. Chalcopyrite within the transgressive carbonatite shows µm-wide fracture infill of magnetite and late-stage alteration phases (Fig. 3.1f). Pyrite (10 to 30 µm) is locally observed in these veins (Fig. 3.1f). Pyrrhotite may also be present as small grains (10 to 30 µm) in chalcopyrite veins, but is particularly rare in the Loolekop Pipe.

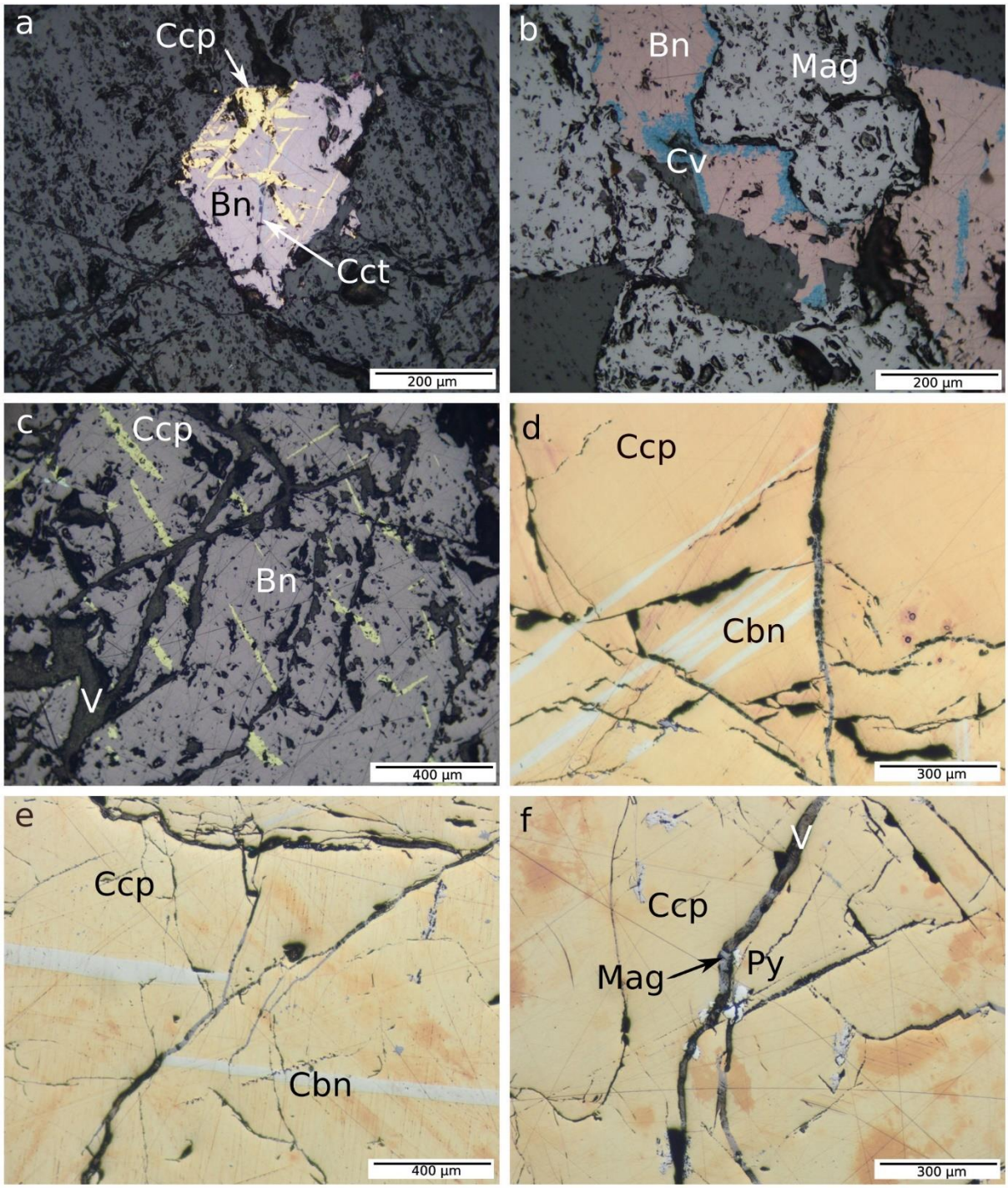


Figure 3.1: *Photomicrographs of representative sulphide phases. Cbn=cubanite, Cct=chalcocite, Ccp=chalcopyrite, Cv=covellite, Bn=bornite, Mag=magnetite, Py=pyrite, V=valleriite. (a) Banded carbonatite. Bornite with chalcopyrite lamellae, isolated in a carbonate gangue matrix. (b) Banded carbonatite. Assemblage of bornite with magnetite surrounded by carbonates. Strong alteration of bornite and replacement by covellite at the rims. (c) Phoscorite. Bornite with chalcopyrite lamellae, post-emplacement fracturing and alteration to valleriite, (d) (e) and (f) transgressive carbonatite. Massive chalcopyrite with cubanite exsolution lamellae and fractures filled with Fe-oxide phases and valleriite. Also visible inclusions of bornite and pyrite.*

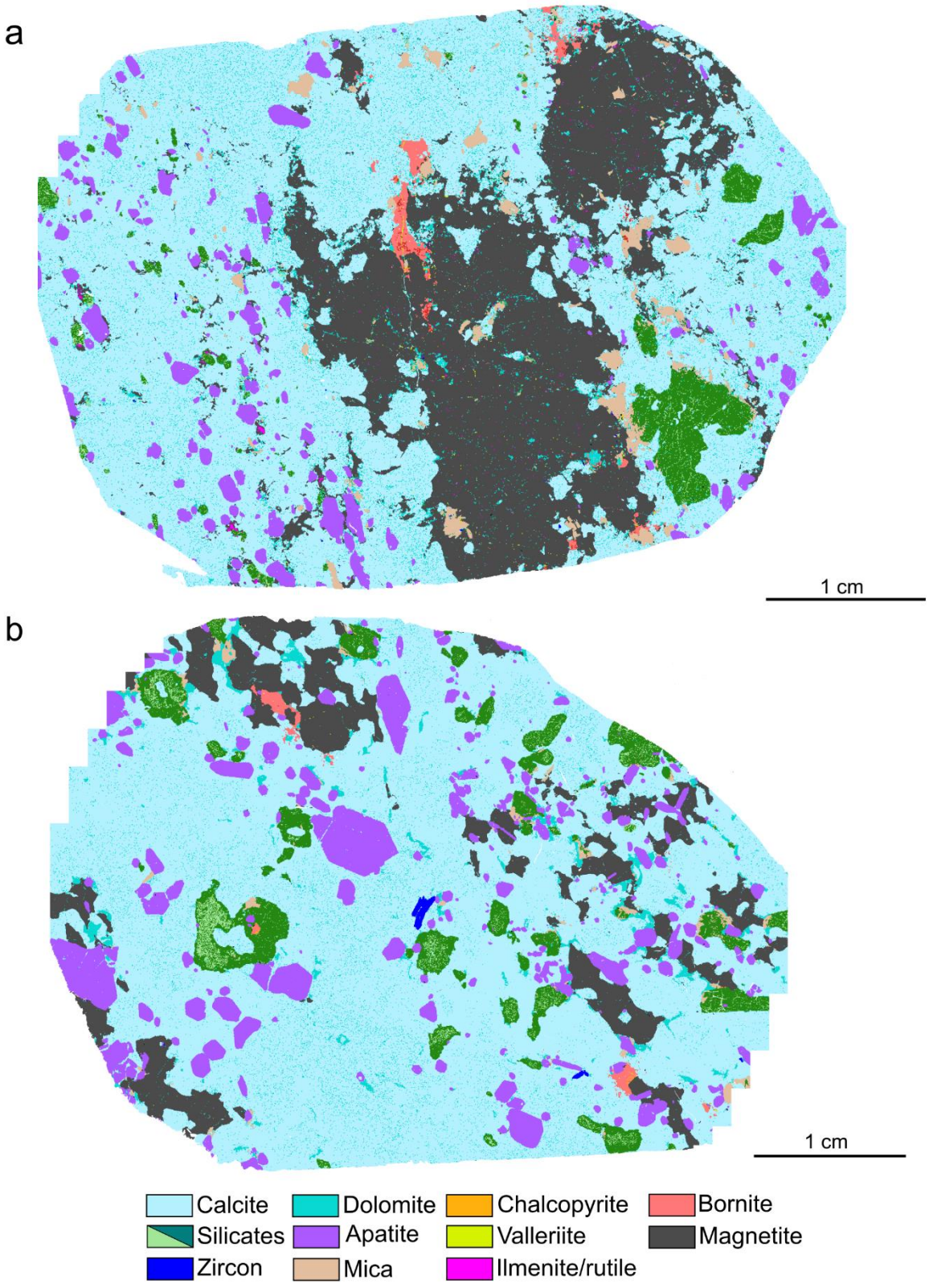


Figure 3.2: *MLA mineral maps obtained from polished blocks of banded carbonatite: (a) sample SL94 B22 and (b) SL140 B08(2).*

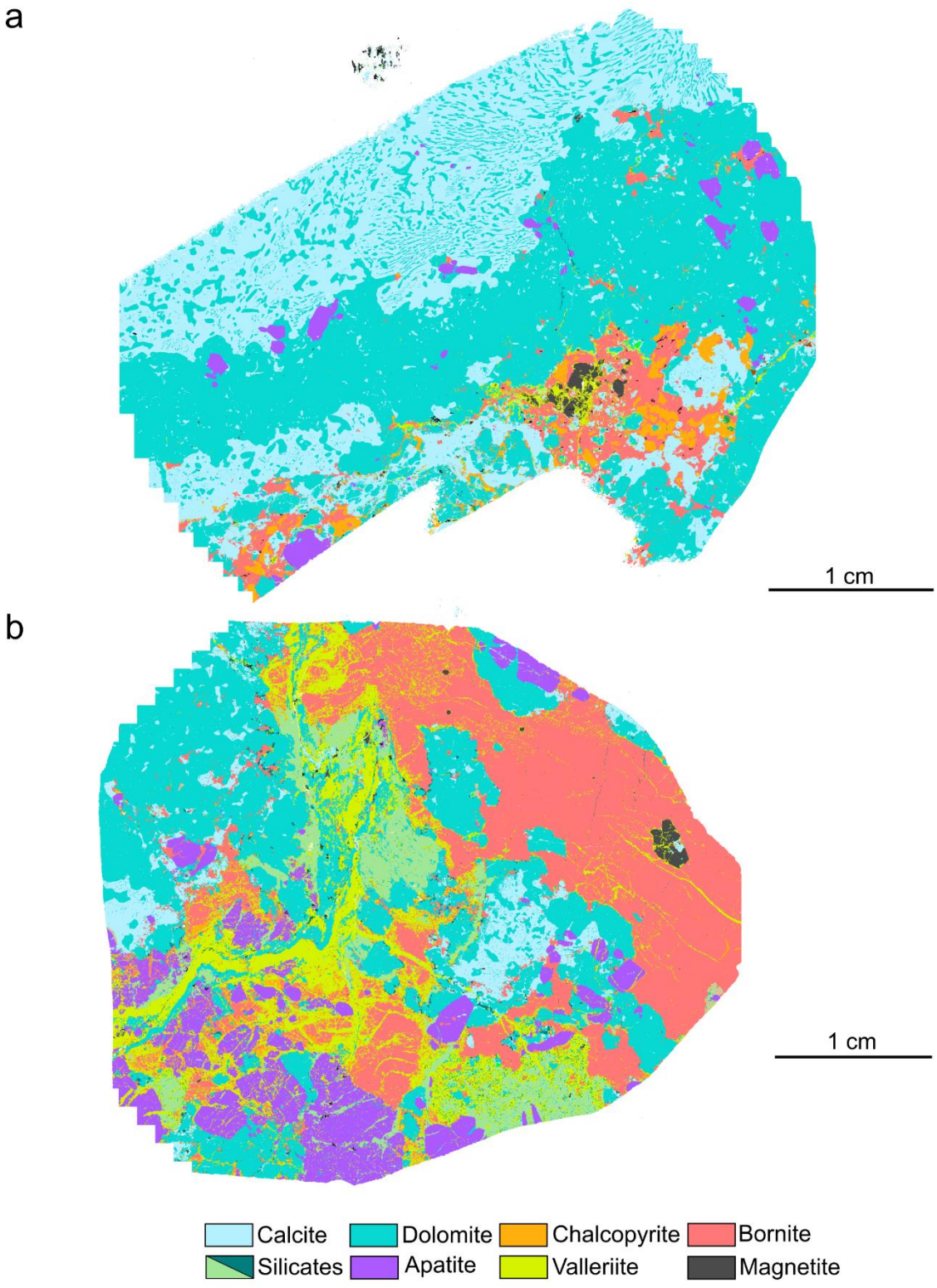


Figure 3.3: *MLA mineral maps obtained from polished blocks of (a) transgressive carbonatite (sample SL139 B62(2)c) and (b) phoscorite (sample SL139 B62(2)a).*

Table 3.1: *Summary of sulphide assemblages and textures in the different rock types of the Loolekop Pipe.*

	Banded Carbonatite/Phoscorite	Transgressive Carbonatite
Dominant sulphides phases	Bornite -Dispersed within the gangue with minor chalcopyrite (Fig. 3.1a) Valleriite -Along fractures and around chalcopyrite, bornite and magnetite (Fig. 3.1c)	Chalcopyrite -Veins (cm) across the gangue Valleriite -Along fractures and around chalcopyrite (Fig. 3.1f)
Minor sulphides phases	Chalcopyrite -Lamellae in bornite -Aggregates with bornite Chalcocite -Veinlets in bornite (Fig. 3.1a) -Replacement of bornite at the borders of the grains (Fig. 3.1b) Covellite -Replacement of bornite at the border of the grains (Fig. 3.1b)	Cubanite -Exsolutions in chalcopyrite (Fig. 3.1d and 3.1e) -Large grains (cm)

Valleriite is unusual in many aspects when compared to the other sulphide phases. While it is present in all of the rock types of the Loolekop Pipe, it tends to be concentrated within the ore-rich zones, regardless of the host-rock, and is commonly associated with primary magmatic sulphides (Fig. 3.3). Valleriite also precipitated along fractures within the gangue, as well as in small fractures in magnetite. Mineral association statistics demonstrate that valleriite and primary Cu-sulphides are not exclusively related (Table 3.2).

3.3.3 Whole-rock geochemistry

The Primitive Mantle (PRIMA)-normalized lithophile element distribution is similar for phoscorite, banded carbonatite and transgressive carbonatite (Fig. 3.4, Appendix C). The micaceous clinopyroxenite shows a normalized pattern that is overall similar to those of the carbonatitic rocks. However, Cs and Rb are more enriched in micaceous clinopyroxenite than in any other rock types within the Loolekop Pipe by an order of magnitude (Fig. 3.4). Positive anomalies can also be observed for Th and U in micaceous clinopyroxenite compared with phoscorite and transgressive carbonatite and, to a greater extent, with banded carbonatite. Lead is also slightly elevated in micaceous clinopyroxenite and phoscorite relative to transgressive carbonatite and banded carbonatite. Both phoscorite and micaceous clinopyroxenite have a slightly lower Sr enrichment over PRIMA compared to banded carbonatite and transgressive

carbonatite (100 x PRIMA against 200 x PRIMA, respectively), but remain in the same order of magnitude. Phoscorite and micaceous clinopyroxenite have similar positive P anomalies one order of magnitude higher than both banded carbonatite and transgressive carbonatite. Titanium is enriched over PRIMA values in both micaceous clinopyroxenite and phoscorite (factor of 3 and 2, respectively) compared to banded carbonatite and transgressive carbonatite, which show depletion (0.2 and 0.04 x PRIMA, respectively).

Primitive Mantle-normalized rare earth element patterns are similar between the different rock types. The $[La/Sm]_N$ ratio ranges between 1.8 and 3.0 and $[Gd/Yb]_N$ between 14.4 and 23.3. The $[Eu/Eu^*]_N$ ratios show a negative anomaly in all the rock types ($Eu/Eu^* = Eu/\sqrt{[(Sm)(Gd)]}$; from 0.7 to 0.8). All heavy-REE (HREE; Tb to Lu) have similar order of magnitude of PRIMA-normalized values in the different rock types (Fig. 3.5). Light-REE enrichment (La to Gd) in phoscorite is similar to micaceous clinopyroxenite.

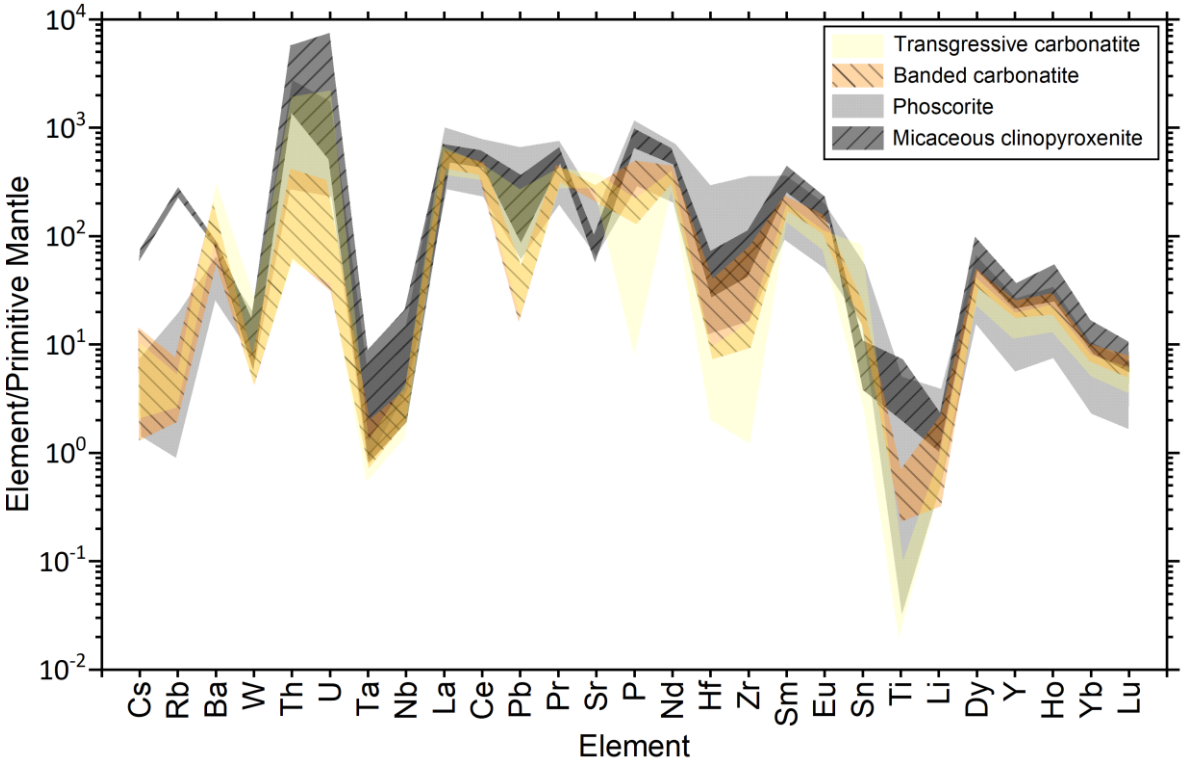


Figure 3.4: *Primitive Mantle-normalized lithophile element variation graph for lithophile elements. Normalization values from Lyubetskaya and Korenaga (2007). Order of elements from Sun and McDonough (1989).*

Table 3.2: *Mineral association statistics for the different sulphides.*

Rock type	Phases	Mineral association (%)			
		Chalcopyrite[e]	Bornite	Chalcocite[f]	Valleriite
BC[a]	Silicates	3	4.5	6	5
	Carbonates	45	61	49	35
	Apatite	1	1	1	5
	Magnetite	8	14	26	37
	Chalcopyrite	-	17	2	3.5
	Bornite	38	-	9	12
	Chalcocite	1	0.5	-	2
	Valleriite	3	2	7	-
	Total	99	100	100	99.5
PC[b]	Silicates	19	15	4	36.5
	Carbonates	17	37	34	19
	Apatite	7	6	14	9
	Magnetite	24	20	29	17.5
	Chalcopyrite	-	6	0.5	6
	Bornite	11	-	10.5	10
	Chalcocite	6	3	-	2
	Valleriite	16	12.5	7.5	-
	Total	100	99.5	99.5	100
TC[c]	Silicates	0.0	0.5	0.00	0.5
	Carbonates	74	66	44	55
	Apatite	0.0	1	0.0	1
	Magnetite	0.5	1	1	26.5
	Chalcopyrite	-	14	15.5	3
	Bornite	18	-	32	14
	Chalcocite	0.0	0.0	-	0.00
	Valleriite	7	18	8	-
	Total	99.5	100.5	100.5	100
MP[d]	Silicates	27.5	78.5	59	85
	Carbonates	1.5	0.5	0.0	0.0
	Apatite	40	12	3	9
	Magnetite	9	0.0	0.0	2
	Chalcopyrite	-	8	0.0	3
	Bornite	18	-	37	1
	Chalcocite	0.0	0.0	-	0.0
	Valleriite	4	0.5	0.0	-
	Total	100	99.5	99	100

[a]Banded carbonatite
[b]Phoscorite
[c]Transgressive carbonatite
[d]Micaceous clinopyroxenite
[e]Include cubanite
[f]Include covellite

The whole-rock Pd-group PGE (PPGE; Pd and Pt) contents change with Cu abundances (Appendices D and E). The PPGE are enriched compared to Ir-group PGE (IPGE; Ir, Os, Ru, and Rh), the latter being below the limit of detection (LOD), except for Ru (maximum of 4 ppb). Concentrations of PPGE range from 1 to 9 ppb (Table 3.3) in all rock types. Micaceous clinopyroxenite is the most enriched in PPGE (Pt = 9 ppb; Pd = 8 ppb) compared to the other rock types (Table 3.3). The concentrations of Pd differ from the concentrations of Pt (Table 3.3). Generally, PGE are enriched in phoscorite compared to banded carbonatite, and to a greater extent, to transgressive carbonatite. The Pd/Pt ratio in all the rock types is significantly different to the Pd/Pt ratio of PRIMA (Pd/Pt: banded carbonatite = 2.5, phoscorite = 3.3, micaceous clinopyroxenite = 0.9, PRIMA = 0.5; Lyubetskaya and Korenaga, 2007). However, due to the absence of Pt in the transgressive carbonatite, the Pd/Pt ratio cannot be calculated for this rock type. Ruthenium can reach concentrations up to 4 ppb, while other IPGE elements, such as Ir, Os and Rh, occur at concentrations below LOD (1 ppb).

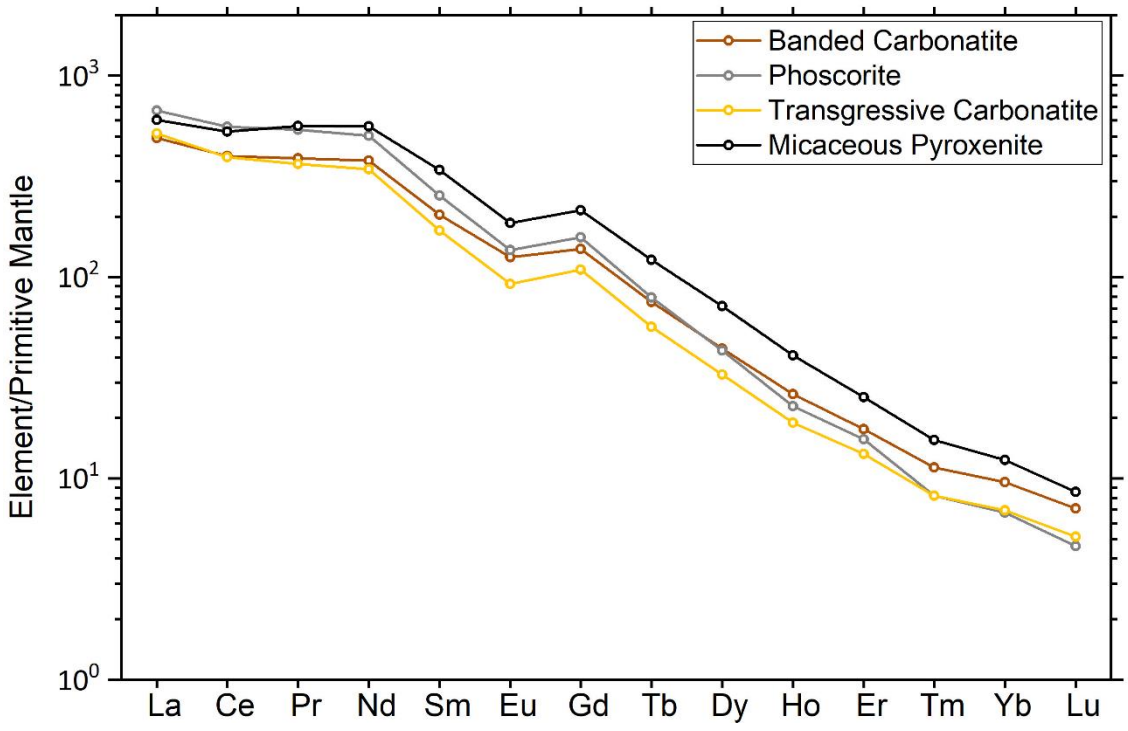


Figure 3.5: *Primitive Mantle-normalized variation graph for REE. Normalization values from Lyubetskaya and Korenaga (2007).*

Table 3.3: *Whole-rock PGE and Au concentrations.*

Element (ppb)	LOD (ppb)	SL140-B08(2)	SL94-B22	SL139-B61(2)b	SL139-B63(2)b	SL139-B62(2)a	SL139-B62(2)c	VS-12-B61(ol)
		BC[a]	BC	BC/PC[b]	PC	PC	TC[c]	MP[d]
Ru	1	<LOD	<LOD	1	2	4	<LOD	1
Pd	1	<LOD	5	2	2	8	2	8
Pt	1	<LOD	2	1	1	2	<LOD	9
Au	2	21	42	23	41	34	14	22

[a]Banded carbonatite
[b]Phoscorite
[c]Transgressive carbonatite
[d]Micaceous clinopyroxenite

3.3.4 Mineral chemistry

In-situ analysis of trace elements in disseminated Cu-sulphides reveals similar abundance distributions in various host rock types (Fig. 3.6 and Appendix F). Chalcopyrite in all rock types contains a significant amount of Ni (from 2100 ppm in transgressive carbonatite to 3800 ppm in banded carbonatite and between 1500 and 5000 ppm in phoscorite) (Fig. 3.6). Valleriite shows a wide range of Ni concentrations in banded carbonatite and phoscorite (12 - 2450 ppm). The Zn contents range from 0.7 to 10 ppm in all the sulphide minerals (Appendix F), showing higher concentrations in chalcopyrite (3.9 - 4.5 ppm) than in bornite (0.6 - 2.5 ppm) among banded carbonatite and phoscorite (Fig. 3.6). Zinc is enriched in valleriite compared to disseminated sulphides (Appendix F). Both valleriite and chalcopyrite generally contain more Co compared to bornite and chalcocite. However, in all the minerals the concentrations are highly variable. Valleriite contains significant, but highly variable concentrations of Co (Fig. 3.6). Valleriite has slightly higher concentrations of Cd in all the rock types (from 2 to 13 ppm) compared to other sulphide phases. Chalcopyrite is more depleted in Cd (0.5 - 1 ppm) than bornite (~ 3 ppm) (Fig. 3.6). As for many other trace elements, the concentrations are variable among these different minerals (Fig. 3.6). Lead is also highly variable across all the sulphides and enriched in chalcopyrite and chalcocite, when compared to bornite (Fig. 3.6). However, in valleriite, the concentrations are generally two to ten times higher (Appendix F). In the primary bornite-chalcopyrite assemblages, Se shows substantial variations among the different sulphide types (3 - 16 ppm). Selenium concentration variations are small within the samples, but can be significant from one sample to another. Arsenic is present at similar concentrations in all the sulphide phases (Fig. 3.6). Bismuth is present in transgressive carbonatite-hosted sulphide phases, mainly in bornite, chalcocite and chalcopyrite, but also locally within valleriite (Fig.

3.6). Some elements like Ni and Bi have an erratic behaviour. Concentrations in valleriite do not always correlate with chalcopyrite and bornite. Bismuth in valleriite is higher than in chalcopyrite in phoscorite, but lower in banded carbonatite. Likewise, Ni is lower in bornite from banded carbonatite and phoscorite, but higher in transgressive carbonatite. The presence of micro-inclusions in the minerals may explain these differences.

In-situ ICP-MS analysis results show that PGE contents are generally low in all the Cu-sulphide phases (Fig. 3.7 and Appendix F). Palladium is the most abundant element in sulphides at concentrations above the detection limit with an average of 98 ppb (in 61 out of 94 analyses; 33 below LOD). In contrast, Pt, Os and Ir occur in small amounts with averages of 13, 15 and 3 ppb, respectively (above LOD in 20, 19 and 14 out of 94 analysis, respectively; 74, 75 and 80 analyses below LOD, respectively). Concentrations of Pd (35 - 310 ppb) differ from Pt, Os and Ir (2 - 32 ppb, 4 - 49 ppb, 1 - 4 ppb, respectively) by one order of magnitude. Despite an overall low concentration, the PGE patterns for the bornite-chalcopyrite assemblages in the banded carbonatite-phoscorite, and the transgressive carbonatite-hosted chalcopyrite, are similar.

3.4 Discussion

Previous studies suggest that the Loolekop Pipe was emplaced in at least three pulses following partial melting of a metasomatized lithospheric mantle (Bolhar et al., 2020). The whole-rock REE distribution patterns of the micaceous clinopyroxenite, banded carbonatite, phoscorite, and transgressive carbonatite suggest a common source or origin (Fig. 3.5). Moreover, normalized trace element and REE data, as well as structural observations, suggest that (i) the sources of banded carbonatite and phoscorite are geochemically indistinguishable (Figs. 3.4 and 3.5; Milani et al., 2017b), and (ii) that the origin of the banded carbonatite and phoscorite banding is possibly related to rotational movement during the ascent of melt(s) or after the emplacement of the rocks (Basson et al. 2017). Combined melt immiscibility and rotation may have led to the preferential formation of phoscorite at the outer rims of the intrusion, while generating banded carbonatite towards the centre owing to density differences (Giebel et al., 2019).

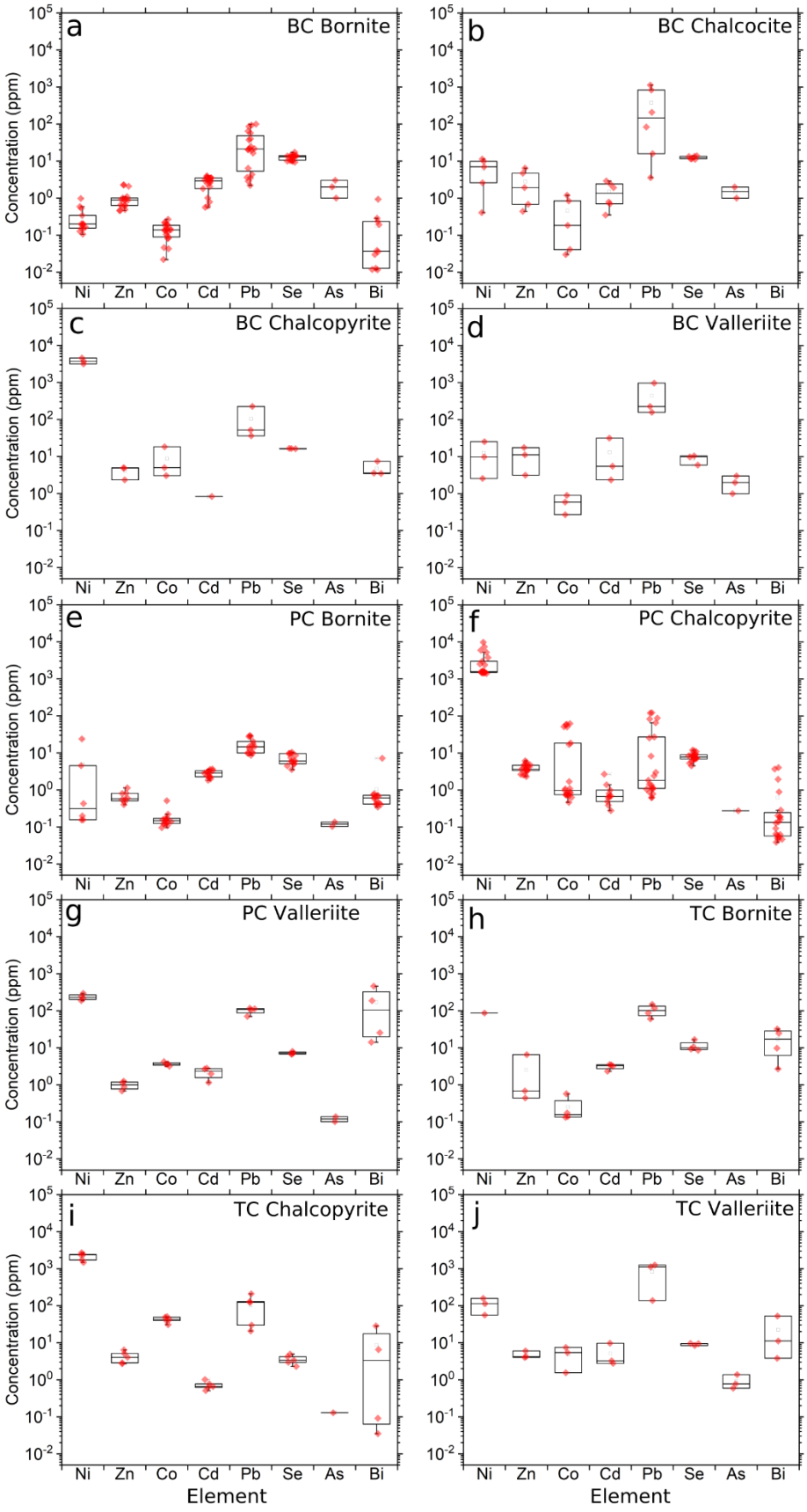


Figure 3.6: *Diagrams showing trace element concentrations in sulphides from the different rock types within the Loolekop Pipe (a) bornite in banded carbonatite (BC); (b) chalcocite in BC; (c) chalcopyrite in BC; (d) valleriite in BC; (e) bornite in phoscorite (PC); (f) chalcopyrite in PC; (g) valleriite in PC; (h) bornite in transgressive carbonatite (TC); (i) chalcopyrite in TC and (j) valleriite in TC.*

3.4.1 Textural and paragenetic sequence analysis

3.4.1.1 Magmatic sulphide assemblages

The primary magmatic Cu-sulphide mineralization is divided in two groups: bornite with chalcopyrite exsolution/replacement features and chalcopyrite with cubanite exsolutions, respectively. The first Cu-sulphide assemblage is considered as magmatic as the sulphide blebs are not associated with any structural features (Figs. 3.1a, 3.1b and 3.1c), neither at the micro- nor the macro-scale (Palabora Mining Company Ltd Staff, 1976). This assemblage is composed of bornite with chalcopyrite exsolution, both as lamellae and patches in highly variable amounts, and is present in the mineral alignments of banded carbonatite and phoscorite layers, rarely in micaceous clinopyroxenite, and occasionally in transgressive carbonatite as relics of banded carbonatite-phoscorite mineralization (Figs. 3.1, 3.2 and 3.3). Primary sulphides in both banded carbonatite and phoscorite appear to be interstitial with respect to apatite, magnetite and carbonates. In the absence of textural evidence for circulation of mineralizing fluids, it is suggested that primary sulphide phases crystallized together with magnetite, apatite, and carbonates. Textures clearly indicate that sulphide crystallization occurred after the formation of gangue minerals.

Bornite with laths of chalcopyrite similar to those observed in banded carbonatite- and phoscorite-hosted assemblages was produced in experimental studies by a recrystallization reaction through the heating of pre-existing bornite at 200-250°C (Durazzo and Taylor, 1982; K. Li et al., 2018). This suggests post-emplacement heating of banded carbonatite and phoscorite, both of which host the primary magmatic bornite-chalcopyrite assemblage in the Loolekop Pipe. The reheating may have occurred during the transgressive carbonatite emplacement or during a late stage hydrothermal stage (at 200-250°C) that was responsible for the precipitation of late chalcopyrite. Cobalt, Ni, and to a lesser extent Zn enrichment in the primary chalcopyrite lamellae over bornite within the banded carbonatite-phoscorite rock interlayering indicate partitioning of these trace elements in the lamellae (Fig. 3.6 and Appendix F). The siderophile nature of Co and Ni, as well as the chalcophile nature of Zn, explain their fractionation into chalcopyrite due to the higher proportion of Fe in chalcopyrite compared to bornite (Goldschmidt, 1937; Barnes, 2016).

The presence of primary bornite is unusual in magmatic Cu-sulphide deposits. In most cases, bornite is the result of a retrograde reaction of chalcopyrite during cooling. Various hypotheses regarding the origin of primary bornite exist. It has been suggested that bornite

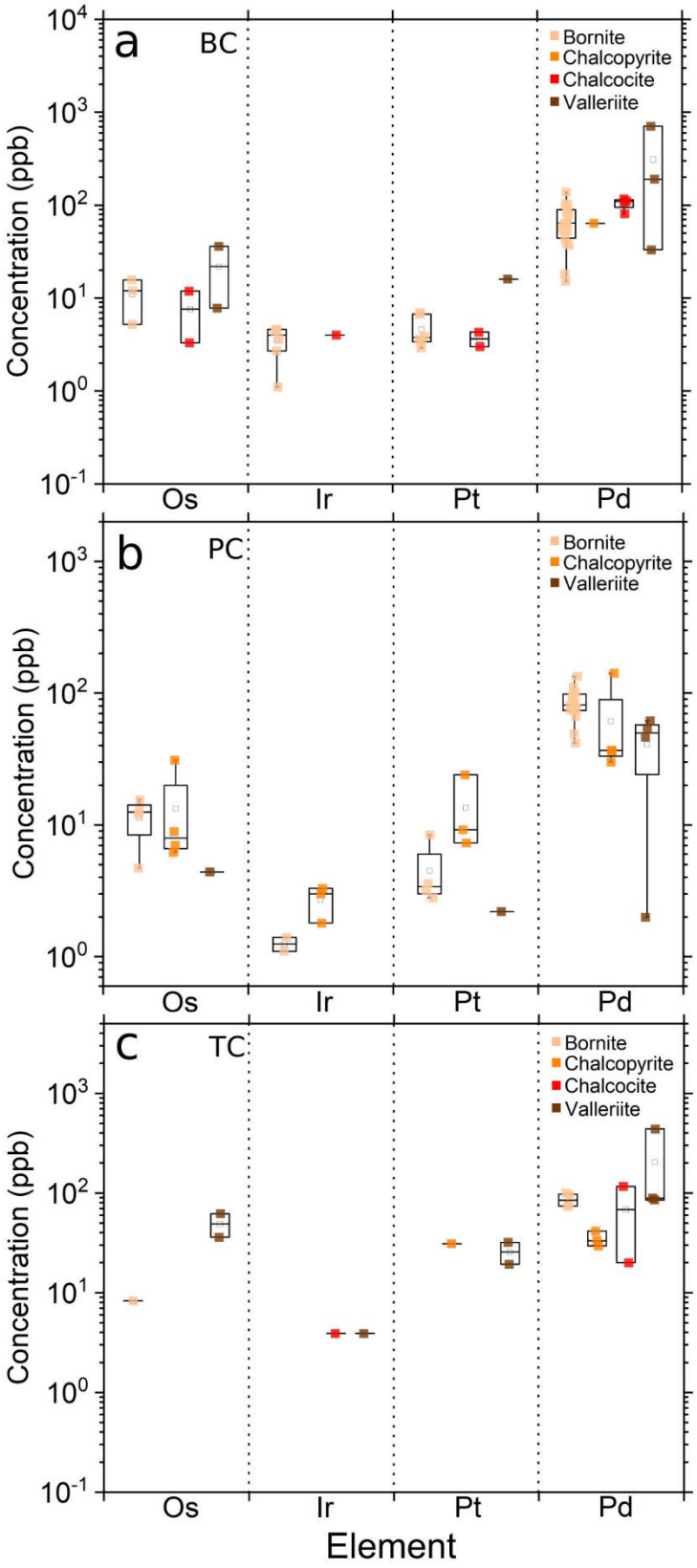


Figure 3.7: *Sulphide PGE contents in the different rock types of the Loolekop Pipe with (a) concentrations in banded carbonatite (BC), (b) in phoscorite (PC) and (c) in transgressive carbonatite (TC).*

resulted from desulphurization through oxidation of pyrrhotite and chalcopyrite (Cawthorn and Meyer, 1993), which also produced significant amounts of magnetite (Maier and Barnes, 1996). This mechanism may explain the presence of primary bornite in both phoscorite and banded carbonatite as well as the significant amounts of magnetite. However, this fails to explain the presence of both primary chalcopyrite and bornite. Thus, this feature may be due to a heterogeneous heating of the Loolekop Pipe during the emplacement of transgressive carbonatite and/or the circulation of high-temperature hydrothermal fluids, as it would have caused the local replacement of bornite by chalcopyrite, while in other places, only thin chalcopyrite laths would have been exsolved.

As stated earlier, the differentiation of the first melt pulse into phoscorite and banded carbonatite may have occurred by the torsion of the intrusion related to the intersection of oriented major fault zones combined with melt immiscibility (Basson et al., 2017; Giebel et al., 2019). This explains the preferential build-up of magnetite cumulates along the contact with the micaceous clinopyroxenite, and a decrease of magnetite content in the rock towards the centre of the pipe. Giebel et al. (2019) suggested that banded carbonatite and phoscorite were derived from a common melt, which separated in response to a drop of temperature and/or pressure during its ascent. The presence of phoscorite at the border of the intrusion may be related to a difference in density between the two melts. As the textural observations suggest a certain affinity of sulphides with magnetite instead of a pure sulphide-carbonate gangue association (Figs. 3.2 and 3.3), and the density of bornite as the main sulphide phase is similar to that of magnetite (5.09 and 5.2 $g.cm^{-3}$, respectively), it appears that its distribution was controlled by processes similar to those involved in the formation of magnetite cumulates, thus causing their association with primary sulphides (Table 3.2). Considering the similar PGE concentrations in both phoscorite- and banded carbonatite-hosted primary sulphides, and assuming indistinguishable sources for the phoscorite and banded carbonatite (Milani et al., 2017a), the primary sulphides in the two rock types may also share the same origin and paragenesis (Fig. 3.6 and Appendix F).

The second primary magmatic mineralization type is composed of chalcopyrite with cubanite lamellae occurring in large veins (Figs. 3.1d, 3.1e and 3.1f). In some cases, cubanite also occurs as large patches within the veins. Cubanite is an indicator of a high-temperature hydrothermal process (cooling from 400°C) responsible for the precipitation of this chalcopyrite-cubanite assemblage (Schwartz, 1927; Ramdohr, 1969; Dutrizac, 1976; Craig and Vaughan, 1994). Chalcopyrite precipitated from high-temperature hydrothermal fluids circulating through the stockwork in the core of the Loolekop Pipe. Chalcopyrite veins occur

along sharply-defined fractures in transgressive carbonatite, indicating that fluid circulated once the system was in solid state. Similar trace element compositions of primary and hydrothermal sulphides suggest that chalcopyrite-forming fluids had a magmatic origin (Fig. 3.6). Bornite trapped within carbonate gangue has been observed in the transgressive carbonatite, which suggests that this primary sulphide was mechanically removed from the banded carbonatite, or phoscorite, and transported with the melt during emplacement of the transgressive carbonatite.

3.4.1.2 Secondary alteration sulphide phases

The Loolekop Pipe has been affected by two alteration events, which differed in intensity. In both events, the alteration is characterized by the overprint of magmatic sulphides. The first alteration event exclusively affected the bornite-chalcopyrite assemblages within both the banded carbonatite and phoscorite, suggesting that it occurred prior to the emplacement of the transgressive carbonatite and the precipitation of the chalcopyrite veins. Alteration resulted in the crystallization of minor chalcocite and covellite around magmatic bornite-chalcopyrite aggregates, as well as in fractures and veinlets within the latter (Figs. 3.1a and 3.1b). Such veinlets are cut by re-heating-related laths of chalcopyrite, indicating that alteration occurred within both the banded carbonatite and phoscorite before the emplacement of the transgressive carbonatite and the subsequent precipitation of the hydrothermal chalcopyrite veins (Fig. 3.1a).

The second and most important stage of alteration is dominated by the crystallization of valleriite, which occurs within all of the rock types in the pipe. This mineral constitutes a significant part of the Cu ore in the Loolekop intrusion. The presence of valleriite along cracks across magmatic sulphides, as well as along grain boundaries, indicates formation that post-dates the crystallization of all the other Cu mineralization phases (Figs. 3.1c and 3.3). The hydrothermal chalcopyrite is cross-cut by µm-wide fractures infilled with magnetite and valleriite, suggesting the circulation of oxidizing fluid(s). Circulation of oxidizing fluids may have triggered desulphurization of magmatic sulphides causing their breakdown into valleriite and magnetite according to the following equations:

$$4CuFeS_2 + (0-3)Al + (0-3)Mg + 3Fe + 10O + (0-6)H = Fe_3O_4 + (Fe^{2+}, Cu)_4(Al, Mg)_3S_4(OH, O)_6 + 4S + (0-4)Cu + (0-4)Fe \quad (3.1)$$

$$4Cu_5FeS_4 + (0-3)Al + (0-3)Mg + 3Fe + 10O + (0-6)H = Fe_3O_4 + (Fe^{2+}, Cu)_4(Al, Mg)_3S_4(OH, O)_6 + 12S + (16-20)Cu + (0-4)Fe \quad (3.2)$$

The presence of Al and Mg in the fluids may be caused by a dissolution of gangue minerals during late-stage fluid alteration like phlogopite and diopside. The presence of Fe can be related to a leaching and breakdown of primary magnetite. Copper, Fe and S released during alteration may be at the origin of valleriite precipitation along fractures in the gangue.

The presence of valleriite along cracks and veins in gangue minerals, such as carbonates, silicates and phosphates in all the rock types, suggests dissolution of magmatic sulphides (Craig and Vaughan, 1994), involving Cu-bearing fluids circulating along cracks within the gangue, and subsequent precipitation of valleriite (Fig. 3.3).

Despite the presence of some discrepancies in trace element compositions between valleriite and primary sulphides which may be explained by the presence of some micro-inclusions in the minerals, the similar trace element concentration patterns in these two assemblages support a genetic link between them (Fig. 3.6). The concentrations of Pb, Bi and As in valleriite relative to magmatic assemblages suggest remobilization of primary sulfide material by late-stage fluids and heterogeneous concentration of trace element during precipitation in the secondary phases due to variable amounts of valleriite relative to bornite and chalcopyrite. Relative enrichment of Pb, Bi and As in valleriite compared to bornite and chalcopyrite may also be related to dissolution of sulphide phases by magmatic fluids. Similar fluid-incompatible Ni and Pt contents in both valleriite and magmatic sulphides are consistent with desulphurization of magmatic sulphides. Dissolution of Platinum Group Minerals (PGM) at depth may also explain the Pt enrichment.

3.4.2 A possible mantle source and sulphide liquid evolution

Previous studies suggest that both banded carbonatite and phoscorite were derived from a common mantle source (Milani et al., 2017a, 2017b; Bolhar et al., 2020). Considering the preferential fractionation of PGE into sulphide phases and the concentration of these elements in mantle, the low concentrations of PGE in sulphides suggest a low degree of partial melting, which may have led to the formation of several pulses of carbonated and oxidized magma into the Loolekop Pipe (Peach et al., 1990; Lyubetskaya and Korenaga, 2007). Enrichment of PPGE over IPGE as documented in other studies focusing on base-metal sulphide magmatic deposits, points towards the presence of a monosulphide solid solution (mss) - intermediate solid solution (iss) system characterized by fractionation of PPGE into an ascending Cu-enriched sulphide liquid, accompanied by IPGE partioning into a Fe-rich mss cumulate remaining at depth (Holwell and McDonald, 2010). The presence of the same PPGE over IPGE enrichment in the sulphide assemblages indicates that a similar process operated in the Loolekop Pipe with the

fractionation at depth of a Cu-rich sulphide liquid from a mss, its ascent and subsequent crystallization into a Cu-rich iss phase followed by the exsolution of PPGE- and Cu-enriched sulphide liquid blebs to produce the bornite-chalcopyrite sulphide assemblage.

Platinum-Group Element concentrations in the Loolekop Pipe are compared to concentrations in Cu porphyry deposits as well as in the O'okiep Cu-Ni deposit, Namaqualand, South Africa (Fig. 3.8). The PRIMA-normalized diagram shows significant differences in PGE concentrations between Cu porphyry deposits and rocks of the Loolekop Pipe suggesting different metallogenetic histories. Gold and PGE concentrations in the Loolekop Pipe are lower by 1 to 3 orders of magnitude. The lower Pt and Pd concentrations in transgressive carbonatite-hosted hydrothermal sulphides compared to banded carbonatite- and phoscorite-hosted primary bornite and chalcopyrite are inconsistent with pre-concentration of PGE into sulphide phases and their leaching by hydrothermal fluids as may occur in Cu porphyry deposits (Augé et al., 2005). Maier et al. (2012) proposed a model for the O'okiep Cu-Ni sulphide deposit, similar to the one proposed in our study of the Cu mineralization of the Loolekop Pipe. This model suggests low-degree partial melting of a fertile subcontinental lithospheric mantle (SCLM) producing a Large Ion Lithophile Elements-, High Field Strength Elements-, volatile- and Cu-enriched melt with low PGE contents, accompanied by mss-iss fractionation of sulphide phases. The fact that the Loolekop Pipe is sub-vertical indicates rapid emplacement of the magma. The significant differences between Loolekop and O'okiep PGE signatures are related to lower degrees of partial melting at Phalaborwa, eventually together with a PGE-depleted source.

Hydrothermal chalcopyrite veins contain lower concentrations of PGE compared to the bornite-chalcopyrite assemblage in banded carbonatite and phoscorite (Table 3.3). However, the PGE in such Cu-sulphides show a similar pattern when compared with patterns observed for banded carbonatite, phoscorite and micaceous clinopyroxenite. This strongly suggests (i) an identical source for the PGE and, consequently, for the PGE-bearing Cu-sulphide phases in transgressive carbonatite, banded carbonatite, phoscorite and micaceous clinopyroxenite and (ii) a continuous extraction of the PGE from the iss phase by exsolution of a Cu-rich sulphide liquid during ore formation (Table 3.3). This process explains the relative enrichment of PGE in micaceous clinopyroxenite over banded carbonatite, phoscorite and transgressive carbonatite. The high concentration of PPGE in micaceous clinopyroxenite, despite a low Cu-sulphide content, is a direct consequence of PPGE fractionation into the early sulphide liquid exsolving from the iss, and the continuous extraction of the sulphide liquid until the production of an almost PGE-free sulphide phase.

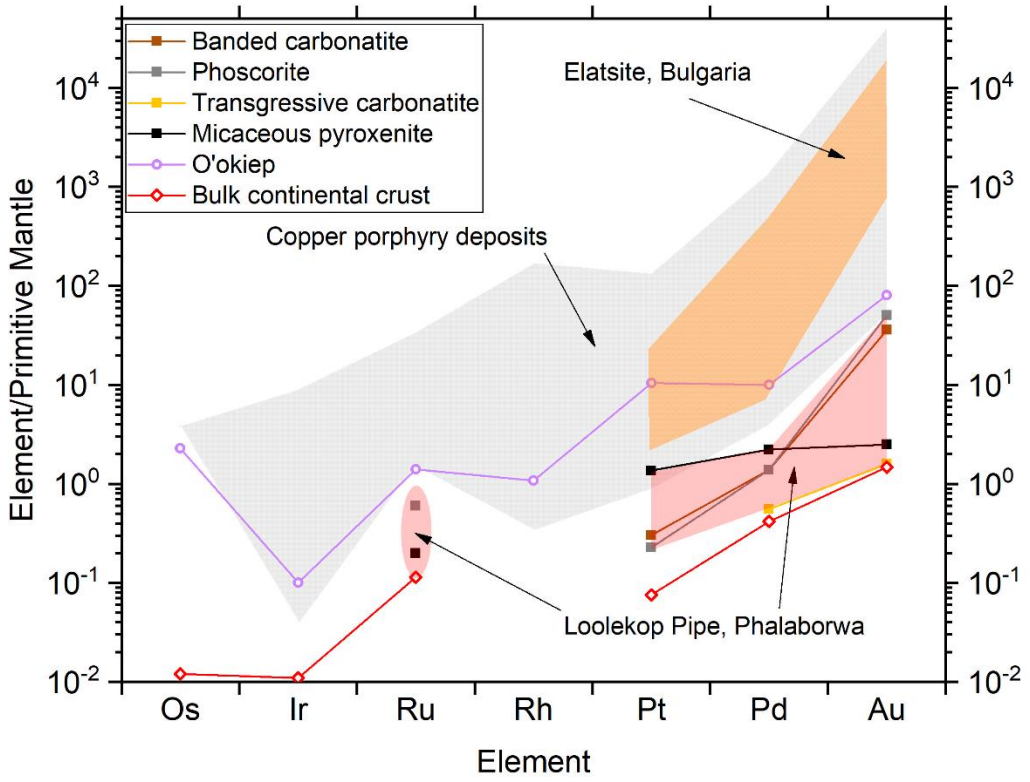


Figure 3.8: *Primitive Mantle-normalized PGE and Au concentrations for different deposits. Copper porphyry deposits are Baula Nuasahi in India, Galore Creek and Island Copper in Canada; Elatsite in Bulgaria and Skouries in Greece. Data from Augé et al. (2005). O'okiep PGE concentrations by Maier et al. (2012). Bulk continental crust values from Rudnick and Gao (2003). Normalization values from Lyubetskaya and Korenaga (2007).*

Monosulphide solid solution/sulphide liquid and iss/sulphide liquid partition coefficients for PGE (Appendix G; Barnes et al., 2001; Barnes and Ripley, 2016) demonstrate the preferential fractionation of PPGE into the abovementioned residual Cu-rich sulphide liquid over iss after its formation, suggesting that PGE-bearing phases in the Loolekop Pipe formed from this residual liquid and constitute the primary Cu-sulphide mineralization (Fig. 3.9). This is another indicator that the first phase of Cu-sulphide mineralization can be considered to be magmatic in origin.

Rare pyrite and pyrrhotite, both mss-derived phases within Cu-sulphides (Fig. 3.1f), formed through subsolidus transformation under 600°C (Ballhaus and Sylvester, 2000; Dare et al., 2011; Barnes and Ripley, 2016). The presence of mss-derived minerals can be related to the fast ascent of the melt(s), which may have caused the radical removal of small portions of the mss cumulate before its transformation into Fe-rich sulphides. The general paucity of pyrrhotite and pyrite in the Loolekop Pipe may reflect a lack of preservation of the mss phase. A possible explanation is the oxidation subsequent to fractionation of the mss to form Fe-oxides, and its ascent with the melt, although the whole-rock PGE contents do not support this hypothesis. It

is plausible that a Cu-rich sulphide liquid and Ti-rich Fe-oxides co-existed, explaining the low concentration of Ru in the Ti-rich Fe-oxides and, by extension, in the phoscorite. Alternatively, two distinct Fe-oxide phases (magnetite and ilmenite) may have resulted from both processes.

3.4.3 PGM content

Previous studies found PGM in highly mineralized samples, as well as in sulphide concentrate, and detected the predominant presence of sperrylite ($PtAs_2$) over other PGM in the Loolekop Pipe. Sperrylite from Cu-sulphide concentrate was observed to be closely associated with the chalcopyrite-bornite-chalcocite phase in carbonatite (Rudashevsky et al., 2004). Whole-rock compositions clearly document significant contents of both Pt and Pd in similar amounts compared to Ir, Os and Rh (Table 3.3). Within Cu-sulphide phases, Pd can be found in greater amounts relative to Pt (Appendix F).

As indicated by Helmy et al. (2010), formation of sperrylite ($PtAs_2$) may occur before the formation of the mss phase suggesting the initial predominance of Pt prior to mss – Cu-rich sulphide liquid fractionation, triggering the crystallization of sperrylite. The presence of small amounts of sperrylite is likely to be related to the sequestration of most of these PGM either at depth or out of the Loolekop intrusion, as suggested by the Pt content of the micaceous clinopyroxenite sample (Table 3.3).

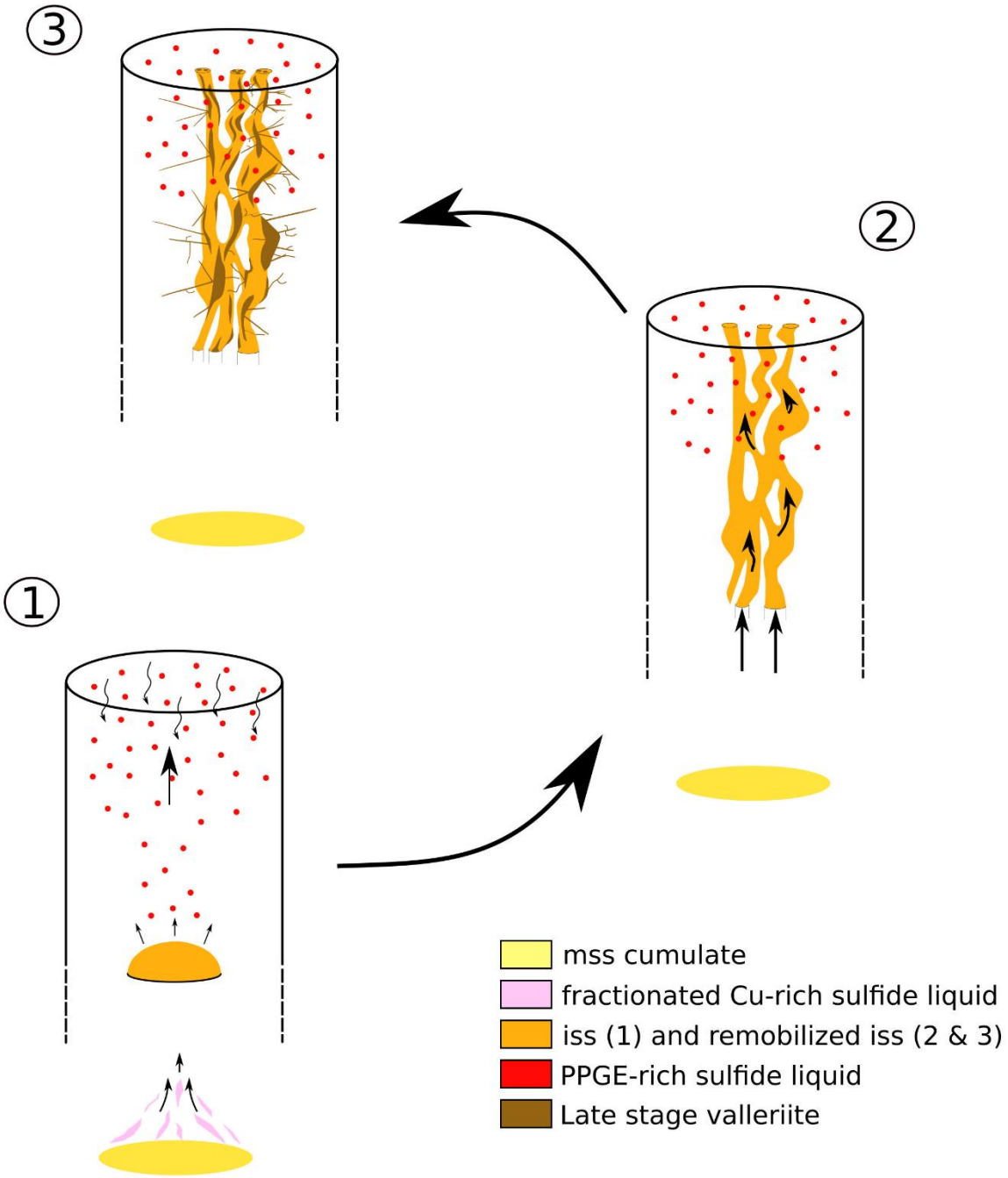


Figure 3.9: *Crystallization and precipitation model of the different sulphide phases in the Loolekop Pipe. Melts were generated by low-degree partial melting of a metasomatized sub-continental lithospheric mantle. (i) During its ascent, the sulphide melt forms an IPGE-rich mss cumulate and a Cu- and PPGE-rich sulphide liquid, which crystallizes upward and exsolves a PPGE-rich sulphide liquid forming sulphide blebs that precipitated in bornite. (ii) The iss was remobilized through high-temperature hydrothermal fluids and formed massive chalcopyrite-cubanite mineralization in a stockwork. (iii) Late-stage fluids leached the previously emplaced sulphides and formed a massive valleriite mineralization.*

3.4.4 Incorporation of surface-derived lithospheric material?

Mantle-normalized trace element patterns of average continental crust and sulphides from PIC show some resemblance (Fig. 3.10). This compositional similarity is consistent with Sr, Nd and multiple S isotope data: Metasomatized SCLM-sourced melt is suggested by the high $^{87}Sr/^{86}Sr$ ratios (from 0.7042 to 0.711 in calcite and apatite; Wu et al., 2011) and low ε_{Nd} in apatite ranging from -3.4 to -7.5 (Farmer et al., 1989; Maier and Barnes, 2004; Wu et al., 2011). In addition, *in-situ* S isotopic analysis of sulphides revealed the presence of mass-independent fractionation of sulphur, suggesting subduction-induced metasomatism and partial melting of a heterogenous mantle beneath the Kaapvaal craton (Bolhar et al., 2020).

In our study, slight differences in trace element contents between whole-rock and Cu-sulphide phases may be related to the distinct geochemical behaviour of elements during fractionation between sulphides and a melt/fluid phase. Specific trace element concentrations give clues to the evolution of the Cu-sulphide phases. Cobalt, as a moderately chalcophile element with a mss/sulphide liquid partition coefficient of greater than unity, tends to concentrate into the mss (Barnes and Ripley, 2016). The differences of Co content between whole-rock and Cu-sulphide phases indicate a lack of equilibration and an interruption of the chemical exchange between sulphide liquid and carbonate melt prior to the formation of the iss, but postdating Cu-sulphide liquid-mss fractionation.

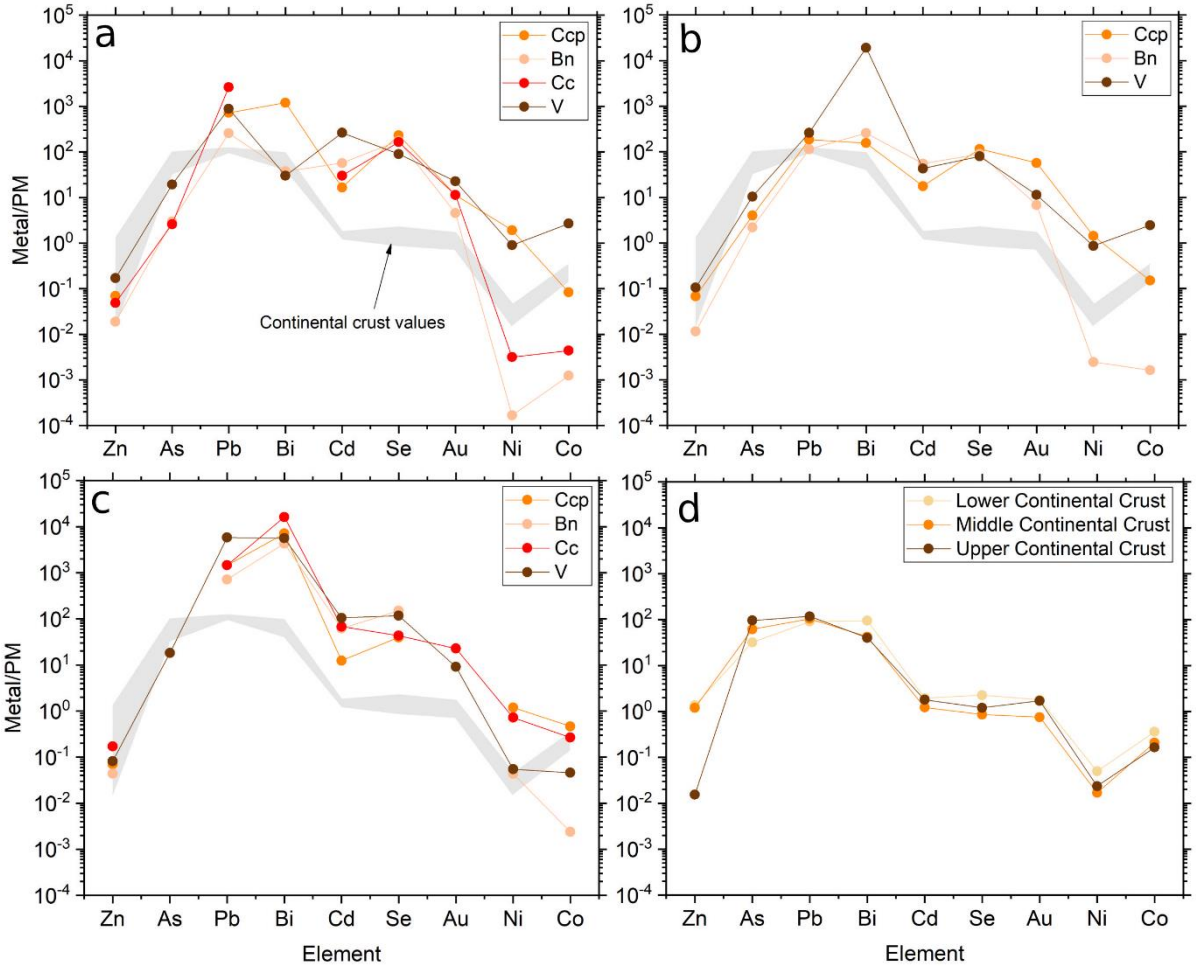


Figure 3.10: *Primitive mantle-normalized diagrams showing trace element patterns of averaged sulphide type compositions. In (a) banded carbonatite; (b) phoscorite; (c) transgressive carbonatite and (d) continental crust. Normalization values from Lyubetskaya and Korenaga (2007).*

3.5 Conclusions

Both *in-situ* and whole-rock PGE analyses document that Cu-sulphides are of mantle origin and formed by separation of a PPGE- and Cu-enriched sulphide liquid from an IPGE-enriched mss cumulate. Despite some minor variations, PGE abundances are similar between the different Cu-sulphides across the Loolekop Pipe, suggesting that a common source contributed to Cu-sulphide ores. The low PGE contents of the sulphides may have resulted from low-degree partial melting of the mantle. The similar PRIMA-normalized trace element distribution patterns among all sulphide phases of the Loolekop Pipe are consistent with multiple S and Sr isotopic data from previous studies, suggesting incorporation of surface-derived material, although the source remains unclear.

Copper-sulphide precipitation occurred during several successive stages (Fig. 3.9): (i) Initially, a PPGE- and Cu-enriched sulphide liquid exsolved from an iss, crystallizing a Cu- and

PPGE-rich sulphide phase within the banded carbonatite and phoscorite. (ii) Magmatic sulphides were locally affected by fluids, which formed chalcocite and covellite along their outer rims. (iii) High-temperature hydrothermal fluids remobilized the iss, and precipitated chalcopyrite with cubanite exsolutions in a stockwork within the pipe. (iv) Finally, magmatic and hydrothermal sulphides were leached and (partly) remobilized by crustal fluids resulting in the formation of valleriite around primary sulphide assemblages and in fractures across all rock types.

The bornite-dominated mineralization is common to both phoscorite and banded carbonatite, showing similar trace element compositions. Bornite exsolved chalcopyrite in response to reheating of the assemblage during emplacement of the transgressive carbonatite or hydrothermal fluid circulation. The association of magmatic bornite – chalcopyrite assemblage with magnetite within the carbonatite – phoscorite sequence confirms that (i) banded carbonatite and phoscorite were derived from a compositionally similar melt, and (ii) torsion of the Loolekop Pipe facilitated the formation of sulphide-rich magnetite cumulates through gravity separation.

Valleriite is ubiquitous as a late-stage secondary alteration mineral within all the rock types around and within magmatic and hydrothermal Cu-sulphides. Derivation of valleriite from primary magmatic and hydrothermal Cu-sulphides is supported by similarity of trace element compositions and textural associations. Valleriite is associated with alteration features of primary sulphides indicating a desulphurization by oxidizing fluids and the formation of valleriite and magnetite. Valleriite precipitation in veins is also observed within the carbonate gangue suggesting that Cu was remobilized from the Cu-sulphides.

Chapter 4

Three-Dimensional Textural Model of Sulphide Mineralization from the Loolekop Intrusion, Phalaborwa: An Indicator for Ore-Forming Processes and Carbonatite-Phoscorite Emplacement

This chapter is intended to be submitted for publication to *Minerals* as a manuscript entitled "Three-dimensional textural model of sulphide mineralization from the Loolekop intrusion, Phalaborwa: an indicator for ore-forming processes and carbonatite-phoscorite emplacement" by Loic Y. Le Bras, Robert Bolhar, Lunga Bam, Bradley M. Guy, Grant M. Bybee and Paul A. M. Nex.

4.1 Introduction

The Loolekop Pipe of the Phalaborwa Igneous Complex (PIC) is unique in hosting an economic Cu-sulphide deposit within a carbonatite-phoscorite sequence. This deposit has been mined since 1956 by the Palabora Mining Company Ltd., mainly for Cu but also for other by-products, such as Fe and U. Copper-sulphide mineralization within the Loolekop Pipe has been extensively studied since the middle of the 20th century (Lombaard et al., 1964; Hanekom et al., 1965; Eriksson, 1982; Groves and Vielreicher, 2001; Wu et al., 2011; Giebel et al., 2017). Despite extensive research aimed at defining and describing Cu-sulphides in the Loolekop Pipe, ore-forming and late-stage alteration processes are not yet adequately characterized (Heinrich et al., 1970; Palabora Mining Company Ltd Staff, 1976; Vielreicher et al., 2000; Milani et al., 2017a, b; Le Bras et al., 2020). Previous research was based on optical and electron microscope observations as well as on microprobe analysis of Cu-sulphides (Rudashevsky et al., 2004; Giebel et al., 2017). While such methods provided important constraints on textures and phase compositions, the information derived from them is not representative of the entire Cu-sulphide mineralization due to the small surface exposure of the epoxy mounts and thin sections, potentially causing biased interpretations concerning the metallogenesis. Accurately describing the heterogeneity of the Cu-sulphide deposit within the Loolekop Pipe is critical considering the spatial variability of mineral associations and textures. A sufficiently comprehensive study using above-mentioned analytical methods would require a significant number of samples and analyses. The use of three-dimensional analytical methods would provide a sufficiently comprehensive dataset to establish a more adequate classification of the Loolekop-hosted Cu-sulphides.

Due to its ability to examine internal features, structures and density variations, micro-focus X-ray tomography (microCT) has been successfully used to characterize various types of mineralization (S. J. Barnes et al., 2008; Godel et al., 2010; Cnudde and Boone, 2013; Barnes et al., 2016; Barnes et al., 2019). Such analysis is particularly useful in deciphering textural relationships between ore minerals, and consequently identifying ore-forming processes. This method is advantageous as it is non-destructive since it is based on the collection of two-dimensional (2D) X-ray projections of a rotating sample followed by an image reconstitution to produce a three-dimensional (3D) model by compiling the projections.

Copper-sulphide mineralization in the Loolekop Pipe is particularly complex. The high spatial variability and the diversity of sulphide phases make the identification of the paragenesis challenging. Three-dimensional microCT analysis of drill core pieces from different rock types of the Loolekop Pipe provides comprehensive and representative information regarding the distribution, shape and mineral association of the Cu-sulphide aggregates. Spatial relationships between the different Cu-bearing phases can also be identified. The use of this method for the characterization of Cu-sulphides of the Loolekop Pipe of the PIC constitutes a novel approach for contributing to the understanding of the metallogenesis of this unusual deposit.

4.2 Copper sulphides in the Loolekop pipe

Chalcopyrite is known to be the dominant sulphide within the Loolekop Pipe (Palabora Mining Company Ltd Staff, 1976). It occurs as two different types defined by mineral association and textures. The first type is characterized by the presence of sub-vertical veinlets occurring in wide zones (up to several m) along fractures within the transgressive carbonatite, constituting the largest part of the sulphide mineralization (Palabora Mining Company Ltd Staff, 1976; Vielreicher et al., 2000). In this type of mineralization, chalcopyrite tends to be associated with cubanite, the latter being present as exsolution lamellae or grains (Lombaard et al., 1964; Palabora Mining Company Ltd Staff, 1976; Le Bras et al., 2020). The second chalcopyrite type is characterized by the presence of dispersed grains (50 to 500 µm) within both banded carbonatite and phoscorite associated with intricate intergrowths of bornite (Palabora Mining Company Ltd Staff, 1976). Disseminated grains of chalcopyrite have also been observed within the host rock.

Bornite has been reported as the second most abundant sulphide in the Loolekop Pipe and the dominant phase within the banded carbonatite – phoscorite sequence. It is associated with dispersed chalcopyrite in banded carbonatite and phoscorite, but may also occur as isolated grains. Both bornite and chalcopyrite may be isolated within the carbonated gangue, although

they are also associated with magnetite and apatite cumulates. Chalcocite has been observed in association with bornite, either as small veinlets within the grains or at their edges, together with covellite as a replacement phase.

Late-stage valleriite occurs as an alteration product of primary sulphides along cracks and along the edges of these minerals. Various trace sulphides have been observed in the Loolekop rocks, such as pentlandite, millerite, bravoite, tetrahedrite, sphalerite, pyrite and galena. Several PGM have also been detected in sulphide concentrate samples (Bulakh et al., 1998; Rudashevsky et al., 2004).

4.3 Sample and methods

4.3.1 Samples

A total of 45 pieces of drill core of variable lengths from two boreholes were selected from the Palabora Mining Company drill core collection for this microCT-based study. The drill cores have an initial diameter of 3 cm and have been cut in quarters along the drilling axis. A quarter was collected for each sample for analysis. In some cases, half of the drill core was taken. The boreholes that were sampled were drilled sub-horizontally at the second lift level of the mine, approximately 1250 m below the surface. Twelve samples from different rock types were chosen for microCT analysis based on their high Cu-sulphide contents, to ensure an optimal characterization of the mineralization (Appendix H). After the tomography, a polished epoxy mount was prepared from one specific piece of drill core to be used for the identification of the different ore phases.

4.3.2 Tomography

Analyses were performed at the Micro-focus X-ray Radiography and Tomography (MIXRAD) facility at the South African Nuclear Energy Corporation (NESCA), Pelindaba, South Africa. The drill core samples were placed in a Plexiglas® cylinder and held in place by pieces of polystyrene to avoid any movement of the samples in the cylinder during the scanning. The system is a Nikon XTH 225 CT with a multi-metal (Mo, Cu, Ag, W) reflection target X-ray tube (source). To optimize the image contrast, the exposure time was set to 4 s and the source voltage to 100 kV. A 0.5 mm Cu filter was used to minimize the impact of beam hardening and to improve X-ray penetration. A 16-bit dynamic range Perkin Elmer flat-panel detector was employed to capture the projections. This detector has an effective size of 400 mm x 400 mm and a pixel size of 200 µm x 200 µm. The device was described in detail by Hoffman and De Beer (2012). The attenuation 2D projections or radiographs were reconstructed using

CT Pro 3D software, and the structure and mineralogical make-up of the samples were modelled using VGStudio Max 3.2 according to the procedure described in Fig. 4.1.

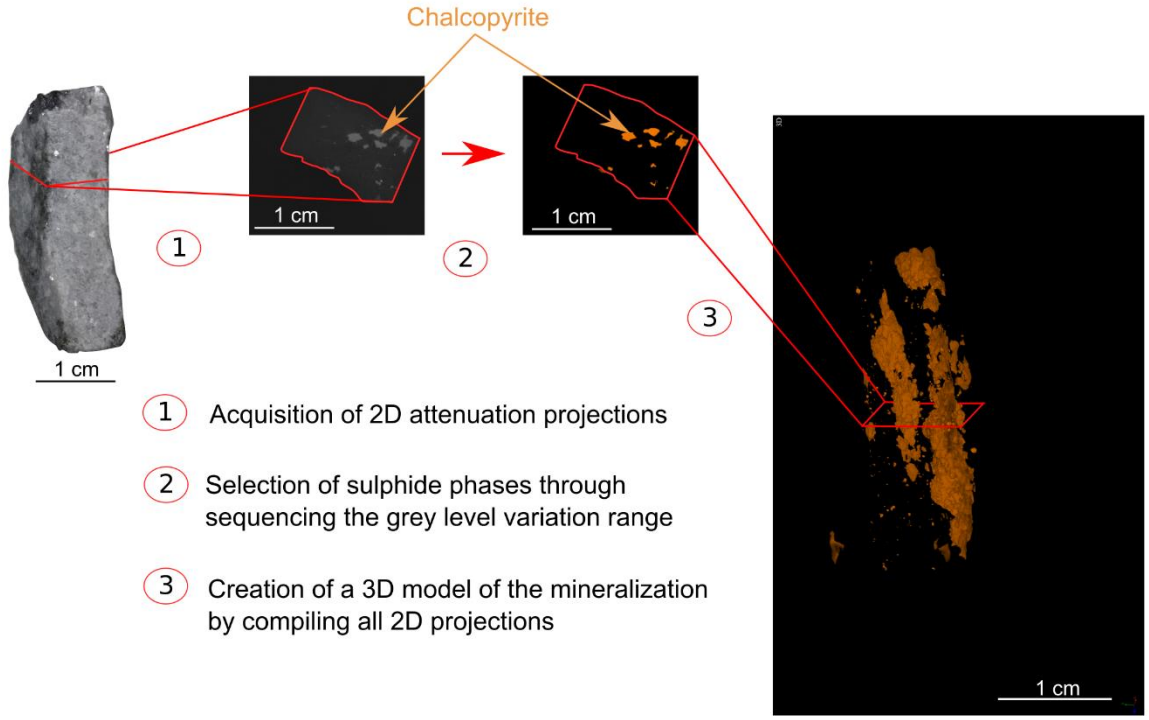


Figure 4.1: *Description of the method applied for data processing, from data acquisition to the 3D model creation.*

4.3.3 Mineral Liberation Analysis

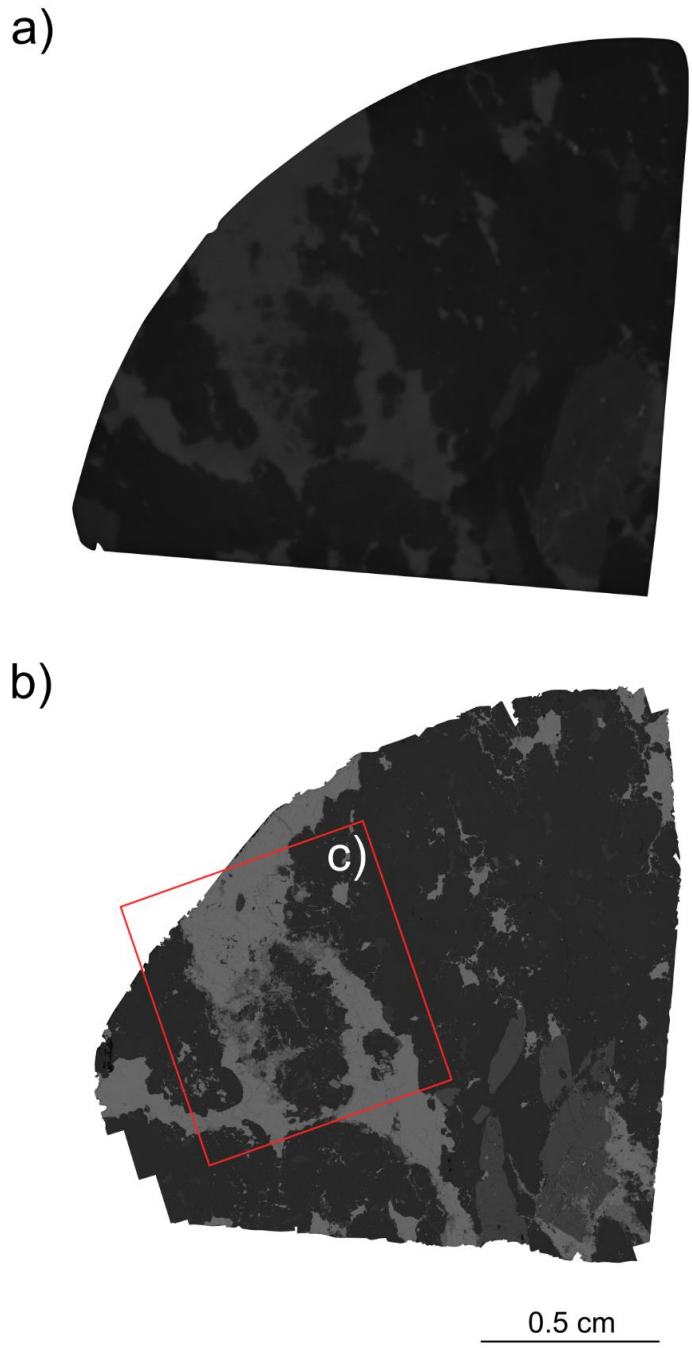
Mineral Liberation Analysis was carried out on a sulphide-rich epoxy mount to obtain a detailed overview of both sulphide phases and textures, and therefore optimize tomographic data processing. The polished mount was prepared from a drill core piece previously analyzed by 3D tomography to use it as a benchmark to differentiate between minerals with similar attenuation coefficients.

The MLA was performed on a FEI Quanta 600 FEG MLA combined with two Brucker Xflash X-ray detectors at the University of Johannesburg. Analyses were conducted at a working distance of 13 mm. The acceleration voltage was set at 25 kV and the current at the surface of the specimen at 10 nA. X-ray detectors were calibrated using a Cu standard. Calibration of the Back Scattered Electron (BSE) grey level was performed with Au, Cu and quartz standards. Collection time for sulphide and gangue phases were set at 10 ms and 30 ms, respectively. Map was created using the GXMAP mode, consisting of X-ray analysis according to a grid with a point spacing set at 23 µm.

4.4 Results

4.4.1 Spatial resolution

The MLA results assembled to produce the 2D attenuation image allowed the identification of the sulphide phases of interest as well as their textures, which in turn allowed the attribution of a grey level interval to the different minerals (Fig. 4.1). Mineral Liberation Analysis also revealed limited spatial resolution of the microCT (80 µm; Hoffman and De Beer, 2012). Small-scale mineralization features visible on the mineral map cannot be distinguished on the corresponding 2D linear attenuation projection. Therefore, only main trends and major features of the sulphide mineralization can be observed and interpreted with microCT analysis (Fig. 4.2).


a)
b)
c)
0.5 cm

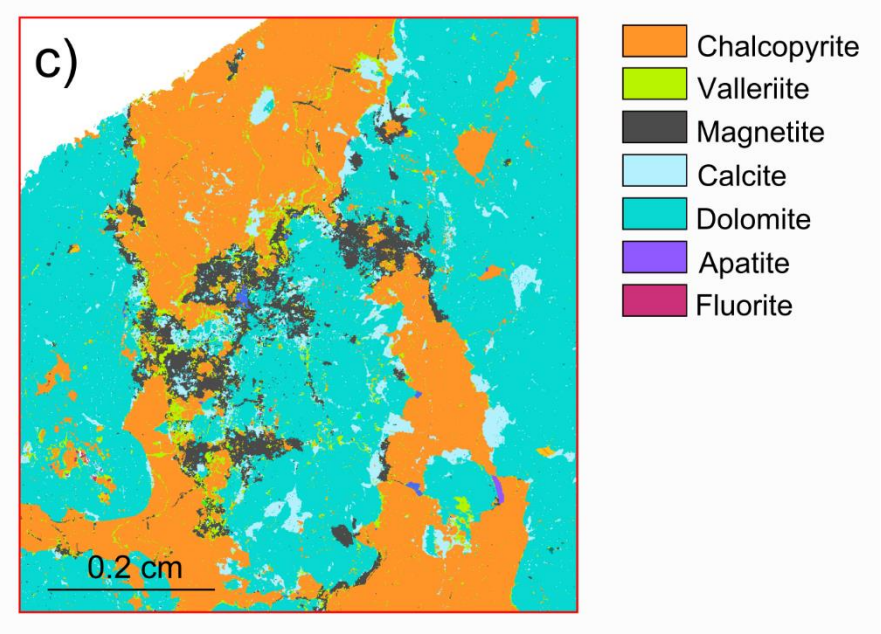


Figure 4.2: *(a) Raw microCT 2D projection of sulphide phases (medium grey) in a carbonatite matrix from the sample HD027 – 17 (Appendix H). (b)Electron microscopic picture of the same slice, showing higher spatial resolution. (c) High-resolution mineral map corresponding to a part of the picture (b).*

4.4.2 Mineral associations

According to combined microscopic observations and microCT results, three distinct types of sulphide phases can be observed with (i) gangue-hosted isolated Cu-sulphides, (ii) chalcopyrite veins, and (iii) secondary sulphides associated with the two first types (Fig. 4.3 and Table 4.1).

Copper-sulphides isolated in the gangue typically comprise fine-grained (up to 500 µm) dispersed chalcopyrite, locally associated with bornite within banded carbonatite and phoscorite (Figs. 4.3a, 4.3b, 4.4a, and 4.6a). Chalcopyrite is also present as small interstitial veinlets (~20 µm wide, maximum ~400 µm long) connected to the larger grains (Figs. 4.3c, 4.3d). Single bornite grains (~200 – 300 µm) are observed in association with chalcopyrite and locally with magnetite (Figs. 4.3a, 4.3b, 4.4c, 4.4d, 4.5d, 4.5e). Locally, bornite alteration and replacement by chalcocite can be observed (Fig. 4.5d and 4.5e). Chalcopyrite associated with bornite is mainly present as exsolution or replacement lamellae in the grains, but also at the contact with the surrounding gangue. Isolated Cu-sulphides can also be present as flat and elongate phases up to several mm long (Figs. 4.6a and 4.6b, Appendix I). Three-dimensional models indicate a length of > 10 mm in some cases, but observations are limited by the diameter of the drill core. The irregular but rounded surfaces of these elongate sulphide assemblages suggest a genetic link between these phases and dispersed chalcopyrite and bornite grains (Appendix I). Isolated

Cu-sulphides are also present as chalcopyrite accumulations (~3 mm thick in this study; Fig. 4.6a).

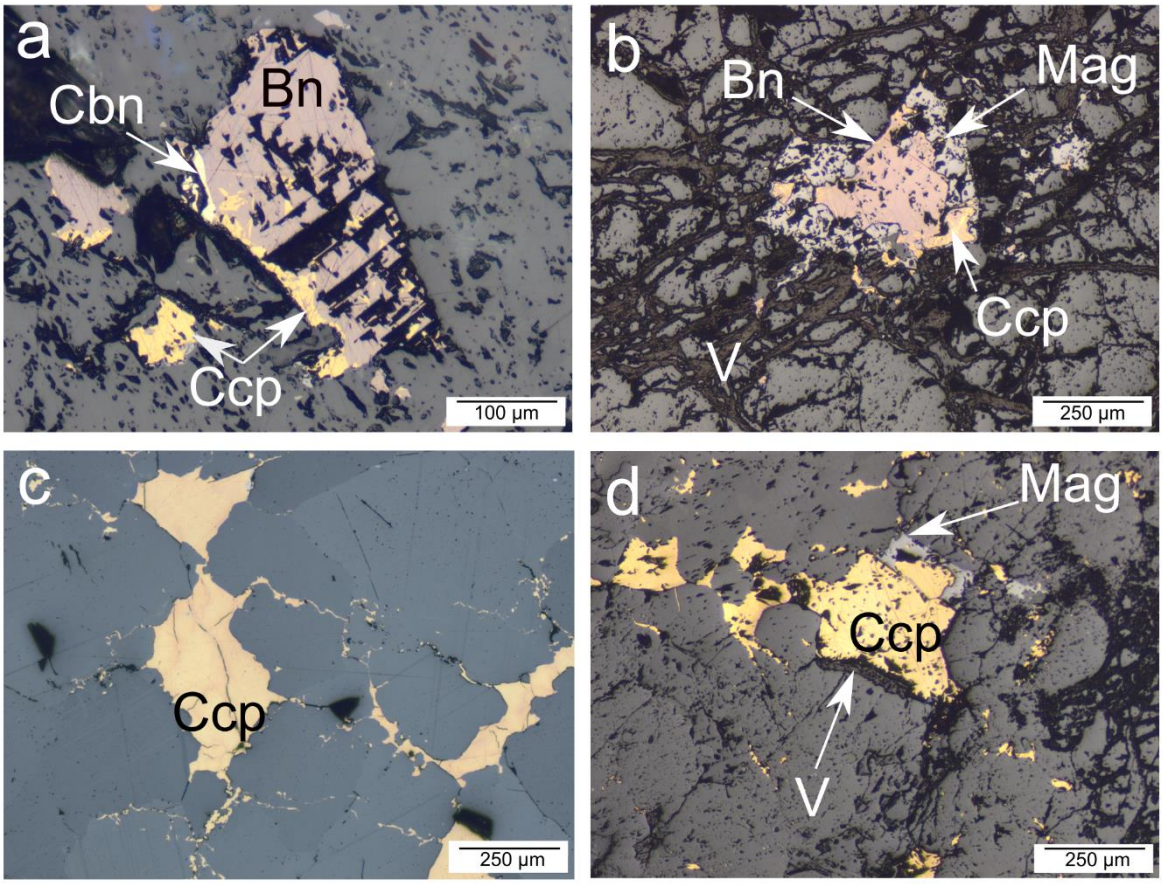


Figure 4.3: *Photomicrographs of different sulphide assemblages observed in the Loolekop Pipe. Bn = bornite, Cbn = cubanite, Ccp = chalcopyrite, Mag = magnetite, V = valleriite. (a) Typical bornite grain associated with chalcopyrite dispersed in the gangue. (b) Similar features to (a), with a valleriite-filled fracture network, and association of magnetite with bornite. (c) and (d) disseminated grains of chalcopyrite within gangue, with small chalcopyrite interstitial veinlets between gangue minerals.*

Table 4.1: *Summary of sulphide types and their respective textures within the Loolekop Pipe.*

Type	Textures	Corresponding sulphide associations
Sulphide layers	-Small-sized (< mm) subspherical grains	-Bornite and chalcopyrite grains (Figs. 4.3 and 4.6a)
	-Flat, elongate mm- to cm-long assemblages	-Chalcopyrite and bornite aggregates (Figs. 4.6a and 4.6b)
	- mm-thick accumulations (Fig. 4.6a)	-Chalcopyrite
Veins	-cm-wide veins (Fig. 4.6c)	-Chalcopyrite
	-Adjacent veinlet network (Fig. 4.6c)	-Chalcopyrite
Alteration	-In veinlets across primary sulphides and at grain boundaries (Fig. 4.6d, Appendix I)	-Valleriite across chalcopyrite and bornite
	-In small fractures in proximity to primary sulphides (Fig. 4.3b)	-Valleriite around chalcopyrite and bornite

The second major sulphide type is characterized by wide chalcopyrite veins (Figs. 4.5b, 4.5c and 4.6c). The width of such veins is highly variable and can reach ~1 cm in this study (Fig. 4.6c).

Microscopic observations and microCT analysis reveal the presence of secondary sulphides as late-stage valleriite associated with chalcopyrite and bornite as well as with magnetite (Figs. 4.3b, 4.3d, 4.5f and 4.6d). However, its distribution among the samples is heterogeneous. Some samples are valleriite-free (Figs. 4.6b and 4.6c), while others host a significant amount of this alteration mineral (Fig. 4.6d). According to microscopic observations, valleriite is very fine-grained (Figs. 4.3b and 4.5f). Valleriite can also be observed in veinlets across the gangue (Figs. 4.3b and 4.6b). MicroCT analysis reveals the presence of valleriite associated with all types of chalcopyrite and bornite mineralization (dispersed, elongated assemblages and cumulates), except the chalcopyrite veins (Fig. 4.6).

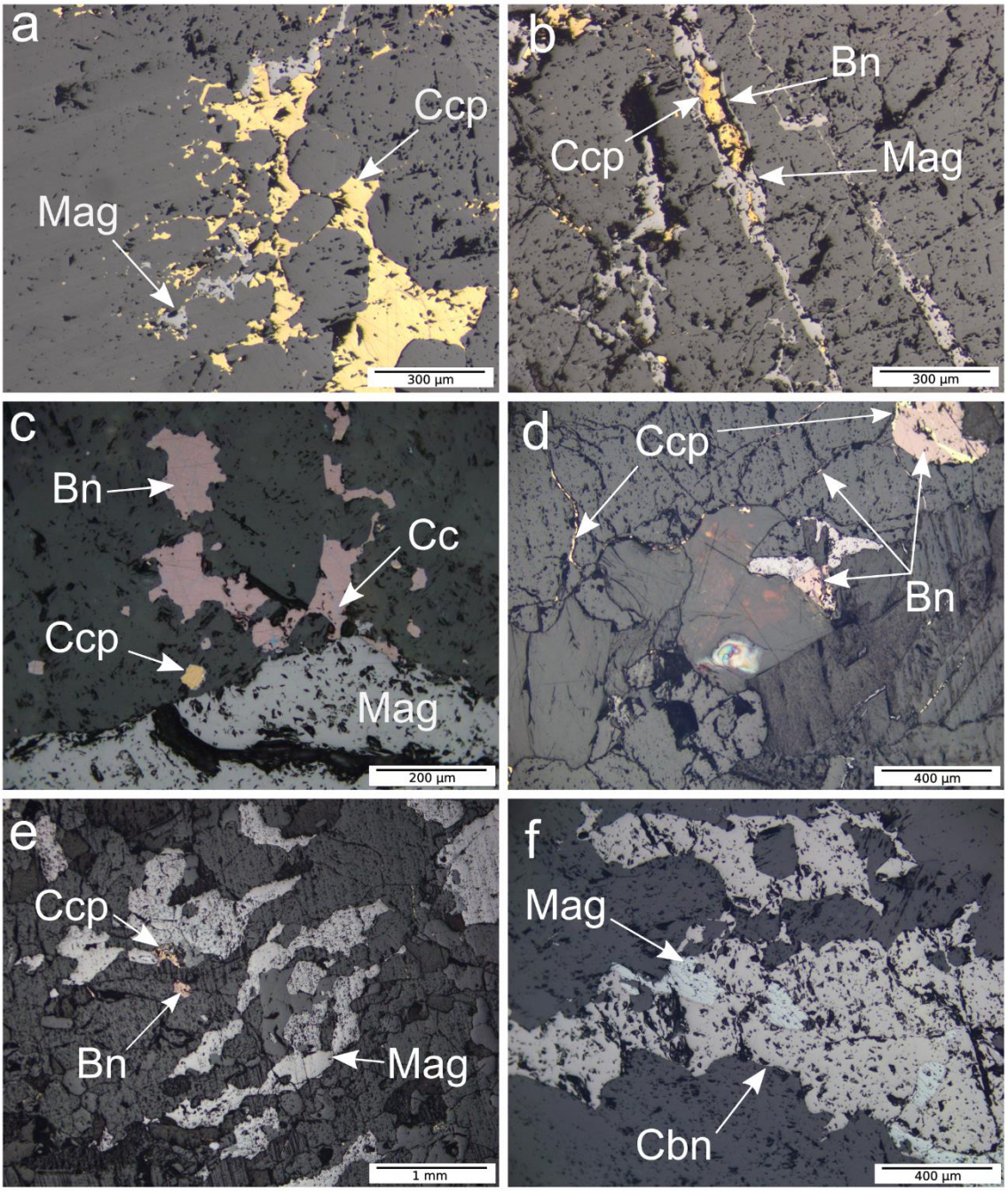


Figure 4.4: *Photomicrographs of different sulphide assemblages observed in the Loolekop Pipe. Bn = bornite, Cbn = cubanite, Ccp = chalcopyrite, Cc = chalcocite, Mag = magnetite. (a) Interstitial chalcopyrite and magnetite between gangue grains. (b) Parallel magnetite-filled veinlets, also hosting chalcopyrite in their axial zones. (c) Bornite grains with chalcocite alteration within the gangue close to magnetite. (d) and (e) Dispersed grains of magnetite and bornite with interstitial chalcopyrite veinlets with locally interstitial bornite veinlets across the gangue (top of picture d). Presence of small chalcopyrite interstitial veinlets between gangue minerals. (f) Assemblage of cubanite and magnetite within carbonate gangue.*

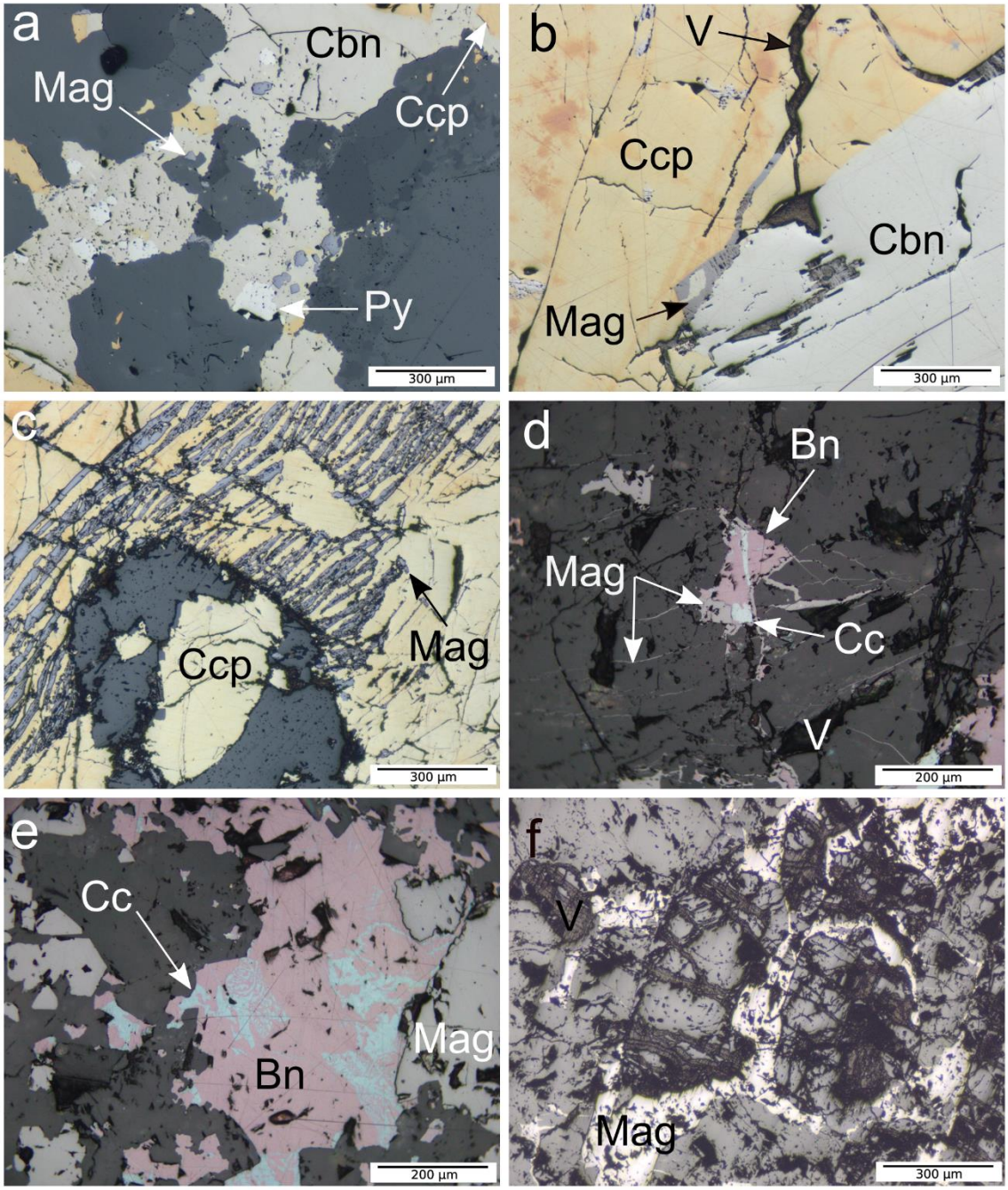


Figure 4.5: *Photomicrographs of several sulphide assemblages within the Loolekop Pipe. Bn = bornite, Cbn = cubanite, Ccp = chalcopyrite, Cc = chalcocite, Mag = magnetite, V = valleriite. (a) Complex assemblage of cubanite and chalcopyrite hosting both pyrite and magnetite. (b) Hydrothermal sulphide assemblages with both chalcopyrite and cubanite cut by late-stage veins filled by magnetite and valleriite. (c) Bornite, together with magnetite disseminated within the gangue. Bornite may host significant amounts of chalcocite. Gangue-hosted, parallel magnetite veinlets are observed. (f) Interstitial magnetite between gangue grains with late-stage valleriite.*

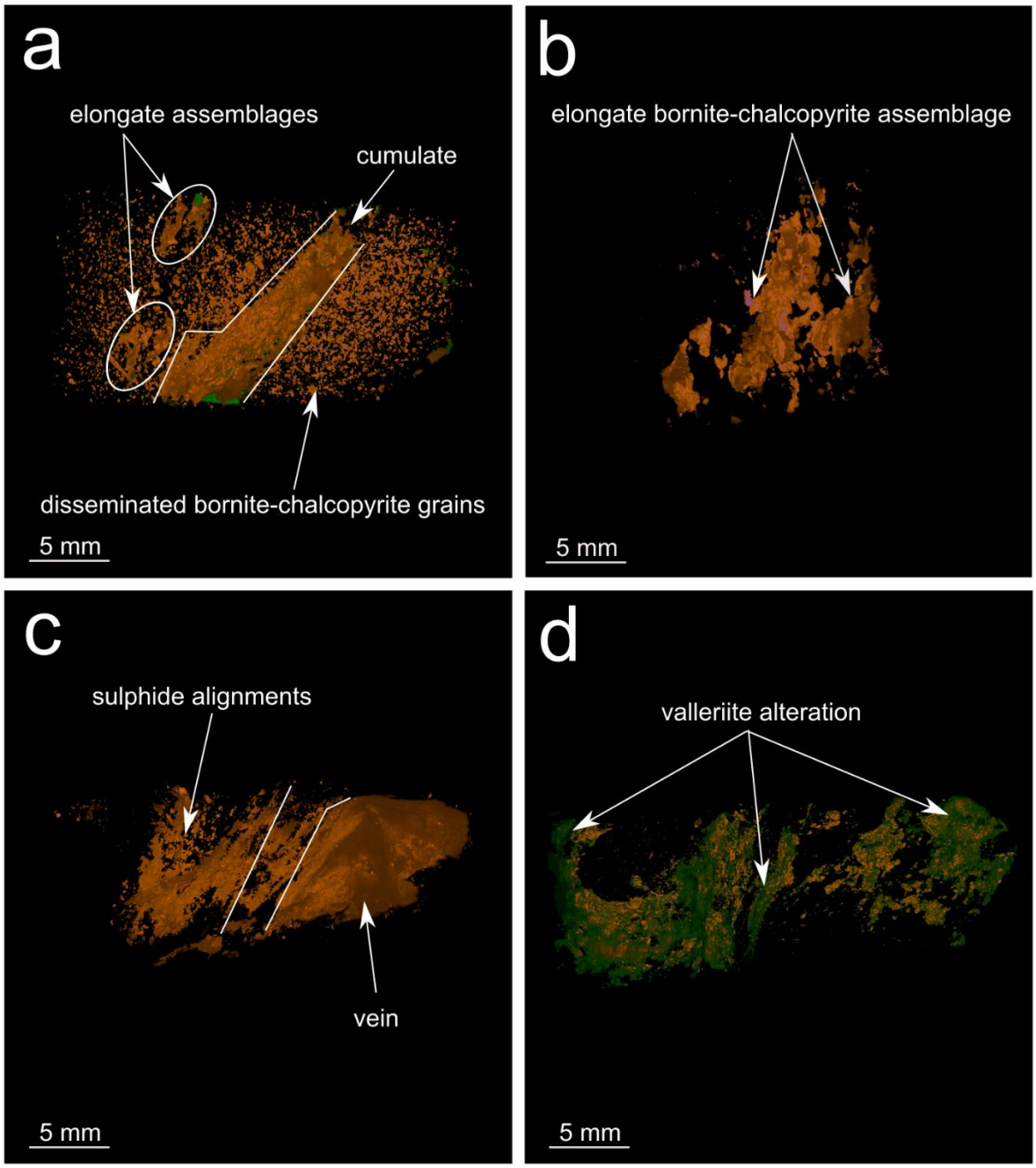


Figure 4.6: *Synthesis of the different types of primary sulphides. Picture (a) shows large patches of bornite (purple) and chalcopyrite (orange). Sulphide textures in (b) display alternating layers of sulphides with different textures. The sulphides in picture (c) show strong alteration leading to the formation of valleriite (green). Picture (d) displays a massive chalcopyrite vein at the top and underlying parallel sulphide layers.*

4.4.3 Planar sulphide layers

Dispersed sulphides form planar layers within the banded carbonatite – phoscorite sequence. Such layers are composed of either small grains, or mm- to cm-long, flat, elongated assemblages or mm-wide sulphide cumulates. Layers of a certain sulphide texture may be in

contact with layers of another (Fig. 4.6a). The alternation between dispersed sulphides layers and flat elongate chalcopyrite-bornite assemblages as well as sulphide cumulates are common and form macroscopic banding.

The orientation of such sulphide layers in the samples and the sub-horizontal dip of drill core samples suggest that they are sub-vertical and parallel to the banding in the interlayered phoscorite and banded carbonatite and the edges of the Loolekop Pipe (Appendices H and I).

4.5 Discussion

4.5.1 Textures and origin of magmatic sulphide mineralization

Characterization of sulphide textures enables the recognition of different types of mineralization (Figs. 4.3 to 4.6, Table 4.1). The first sulphide assemblage type, present in both banded carbonatite and phoscorite as layers of isolated Cu-sulphides, is of magmatic origin considering the specific texture of the ore minerals. As indicated by microCT results, small-size dispersed sulphides are isolated in their host rock without association with structural features, indicating a synchronous emplacement with carbonates, Fe oxides and silicates (Figs. 4.3a to 4.3d, 4.4a, 4.4c to 4.4f, 4.6a). In elongated assemblages, bornite is mainly present inside the aggregates (Appendix I, sample 22), making its recognition within the 3D model challenging. The relationship between bornite and chalcopyrite can only be effectively assessed by sequential observation of 2D attenuation projections or by optical microscopy (Figs. 4.3a, 4.3b, 4.4d and 4.4e, Appendix I). The lower resolution of microCT compared to electron microscope imagery does not permit the recognition of chalcopyrite exsolution or replacement in bornite as well as other micrometer-scale textural features (Fig. 4.2).

The presence of both chalcopyrite and bornite within banded carbonatite and phoscorite in the Loolekop Pipe indicates a magmatic origin of dispersed Cu-sulphides and sulphide cumulates. MicroCT results also show a clear dominance of chalcopyrite over bornite (Fig. 4.6), while microscopic observations rather indicate a bornite-dominated mineralization suggesting a heterogeneous distribution of the mineralization across the intrusive pipe. The relative proportions of bornite and chalcopyrite show a substantial variation between the different sulphide layers (Appendix I), suggesting the successive involvement of different sulphide liquids in the development of Cu-sulphide mineralization in the Loolekop Pipe. Sulphide liquids of different composition may have contributed to the formation of distinct sulphide assemblages during the emplacement of the banded carbonatite-phoscorite complex and cooling of the system (Cabri, 1973).

The sharp contact between chalcopyrite veins and gangue material suggests a hydrothermal origin of this ore phase (Fig. 4.6c, Appendix I). Only one occurrence has been observed in this study. Such a sulphide texture contrasts with isolated Cu-sulphides, which are characterized by an irregular contact between ore phases and gangue (Fig. 4.6a). It is unclear if the planar sulphide alignments parallel to the vein are of hydrothermal origin. The absence of dispersed grains and isolated cumulates suggests that such alignments resulted from the filling by sulphides of gaps within the gangue, possibly by precipitation during a fluid circulation cycle associated with mineral dissolution during the hydrothermal episode (Le Bras et al., 2020).

4.5.2 Sulphide layer formation processe(s)

Sub-vertical sulphide layers are parallel to the banding in the phoscorite and banded carbonatite (Figs. 2.2, 4.6 and 4.7, Appendix I), suggesting that the process responsible for this very specific feature may be the same as for the formation of the banded carbonatite – phoscorite sequence. Isolated sulphide layer textures do not show a clear spatial correlation, indicating the operation of several independent layer – forming events.

The involvement of different sulphide liquids combined with presence of sub-vertical phoscorite-carbonatite and sulphide bands suggests the successive emplacement of different magma pulses in the Loolekop Pipe, with decreasing Fe oxide, apatite and silicate contents from early to late stages of the intrusion process. Magma immiscibility during pulse emplacement is most likely responsible for the presence of the alternating banded carbonatite – phoscorite layers (Krasnova et al., 2004a and b; Giebel et al., 2019). The emplacement of a carbonatite – phoscorite sequence in several intrusion stages has likewise been observed for the Kovdor intrusion in the Kola Peninsula, Russia (Krasnova et al., 2004a). The preferential emplacement of phoscorite along the external boundaries of the Loolekop Pipe can be explained by density separation during rotational movement of the magma (Basson et al., 2017), based on the intersection of fractures and shear zones, and rotation of their segments relative to one another. Sub-vertical sulphide layers may have formed via the same process. Alternatively, a significant number of magma pulses of limited volume may have been emplaced near-simultaneously, each forming a banded carbonatite - phoscorite banding (Figs. 2.2b and c; Heaman and LeCheminant, 1993; Reischmann, 1995; Wu et al., 2011). In this case, textures may be linked to the emplacement conditions of the melt pulses. The chalcopyrite – bornite assemblage may be present as small, dispersed grains due to the emplacement of a limited volume of melt and, therefore, of sulphide liquid. The mm- to cm-scale elongated magmatic sulphide assemblages may have formed by emplacement of moderate melt/sulphide liquid volumes, forming large

sulphide patches with an irregular surface. This surface indicates that the assemblages may have formed by merging small sized grains together, most likely by magma flow, forming flat, elongated sulphide aggregates parallel to the layer strike. Sparse cm-wide cumulates (Fig. 4.6b) may have formed by the involvement of larger volumes of magma and sulphide liquid, pushing sulphides towards the contact with the rock that was emplaced during a previous melt pulse, and therefore forming mm-wide cumulates (Fig. 4.6a).

4.5.3 Formation of hydrothermal sulphides

Hydrothermal veins show a neat contact with the host rock, indicating that chalcopyrite precipitated along fractures during this stage (Palabora Mining Company Ltd Staff, 1976). Such sharp edges of hydrothermal veins can easily be distinguished from the magmatic cumulate texture, which rather shows an intricate association with the gangue. Sulphide planar alignments parallel to the veins can be observed in their immediate proximity. The corresponding 3D model does not show any link between such alignments and the hydrothermal vein itself. The resolution of microCT imagery may be insufficient to allow the identification of small fractures that may have acted as pathways for hydrothermal fluids within the host rock. A cogenetic link between hydrothermal vein and adjacent sulphide phases may be a reasonable assumption. Similar Fe isotope compositions between hydrothermal chalcopyrite and adjacent sulphide veinlets indicate precipitation of chalcopyrite from hydrothermal fluids into a network of veinlets along the contacts to hydrothermal mineralization, which lends further support to this hypothesis (Section 6.3.4.2) (Le Bras et al., 2020).

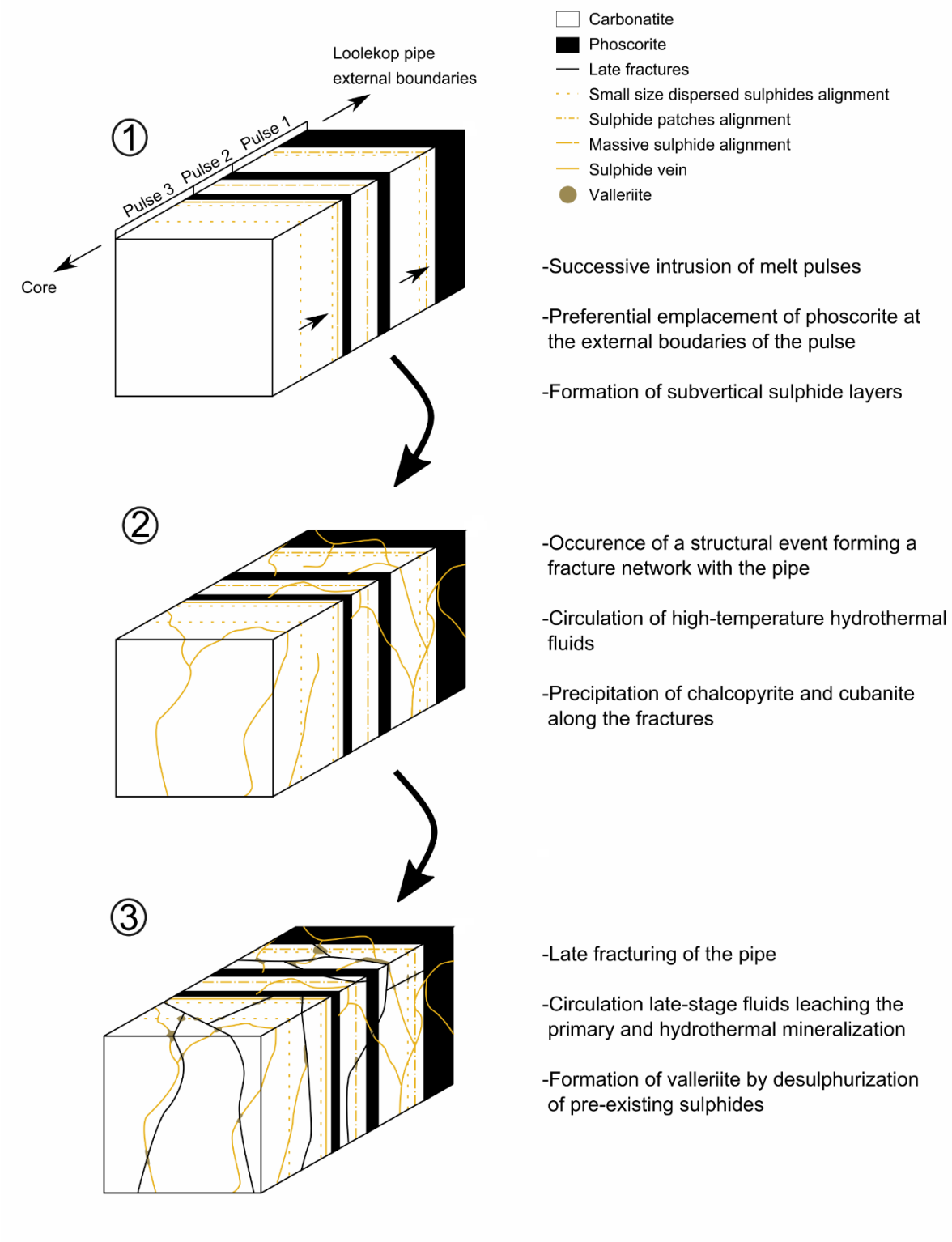


Figure 4.7: *Model of the sulphide mineralization formation within the Loolekop Pipe. The first step shows the successive intrusion of melt pulses, each forming phoscorite along their external boundaries and carbonatite towards the core of the intrusion as well as sub-vertical sulphide layers. The second step is characterized by a structural event and the precipitation of chalcopyrite from high-temperature hydrothermal fluids along the fractures. The third step shows the appearance of valleriite associated to late-stage fractures in chalcopyrite and bornite layers.*

4.5.4 Late-stage alteration characteristics

Three hypotheses exist regarding the origin of valleriite within the Loolekop Pipe: (i) alteration and replacement of magmatic and hydrothermal sulphides by valleriite (Lombaard et al., 1964; Palabora Mining Company Ltd Staff, 1976; Giebel et al., 2017; Milani et al., 2017a); (ii) dissolution of magmatic and hydrothermal sulphide phases and re-precipitation of dissolved material as valleriite (Giebel et al., 2017; Milani et al., 2017b); and (iii) deposition of a thin valleriite film on the primary sulphides (Palabora Mining Company Ltd Staff, 1976). The hypothesis (ii), through desulphurization of primary sulphides by an oxidizing fluid resulting in the formation of both valleriite and magnetite, represents the most likely possibility (Figs. 4.5a and 4.5b) (Le Bras et al., 2020).

Microscopic observations and microCT analysis show an alteration of magmatic sulphide by late-stage fluids as well as their dissolution and re-precipitation as valleriite along adjacent fractures (Figs. 4.3b and 4.6d, Appendix I, sample 57). A dissolution – (re)precipitation cycle related to late-stage fluid circulation is very likely, but valleriite may predominantly be the result of *in-situ* magmatic sulphide alteration as shown by the dominant presence of valleriite at the external boundaries and along fractures within magmatic sulphide phases (Figs. 4.3 and 4.6). Gangue-filled fractures in proximity to valleriite – magmatic sulphide assemblages support fluid circulation and *in-situ* replacement of primary sulphides by valleriite. Three-dimensional models do not show any major fractures filled with valleriite across the host rock (Appendix I, sample 53), implying a limited transport of the dissolved material.

Valleriite is heterogeneously distributed among the samples: some samples do not show any alteration of the chalcopyrite – bornite assemblages to valleriite. Circulation of late-stage fluids may have been facilitated by a structural event. The latter formed fault and shear zones in the pipe, postdating the emplacement of magmatic and hydrothermal mineralization (Fig. 4.7). The absence of fractures and veins, conversely, prevented fluid circulation and, consequently, the formation of valleriite, leaving primary sulphide assemblages intact.

4.5.5 Gas bubbles as potential carriers of sulphide liquid

Phlogopite dispersed within the carbonated gangue is seen to be surrounded by a sulphide aureole, most likely chalcopyrite and/or bornite (Fig. 4.8, Appendix I, sample 31). Valleriite is unlikely to occur in this context due to the relatively high brightness of the phase of interest. Iron sulphides are also not plausible since these phases remained at depth as indicated in Chapter 3. This rare feature, only observed in one sample, may suggest transport of a fraction of the sulphide liquid by exsolved gas bubbles, which further crystallized as gangue minerals

as suggested by the subspherical shape of the disseminated phlogopite (Mungall et al., 2015; Barnes et al., 2019). The lack of evidence for this feature may be explained by emplacement of one single pulse that was carrying gas bubbles.

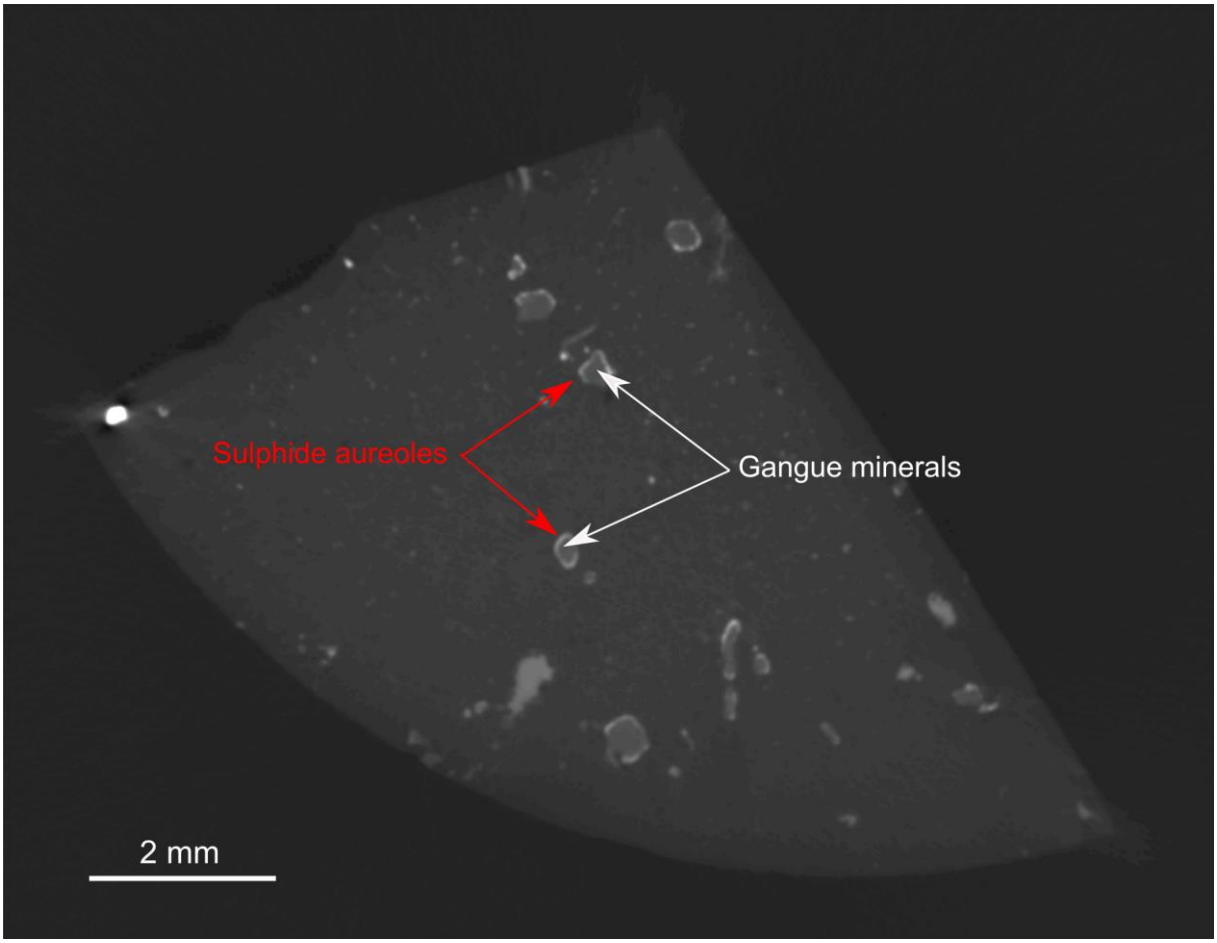


Figure 4.8: *Phlogopite (dark grey) surrounded by sulphide aureoles (light grey) in a calcite matrix.*

4.6 Conclusions

MicroCT analysis of several drill core samples, representing three major rock types (phoscorite, banded and transgressive carbonatites) within the Loolekop Pipe, reveal the presence of sub-vertical sulphide layers parallel to alternating bands of phoscorite and banded carbonatite. Such layers are composed of (i) small (< 1 mm) dispersed sulphides, (ii) elongate flat sulphide aggregates (> 1 mm) and (iii) chalcopyrite cumulates (mm-wide). The irregular and granular surface of elongate aggregates parallel to the layer axis suggests that they formed by accumulation of discrete sulphide grains. Modal proportions of bornite and chalcopyrite are highly variable from one layer to another, suggesting the presence of compositionally different sulphide liquids producing magmatic sulphide phases. The alternating distribution of banded carbonatite and phoscorite within the Loolekop Pipe and the involvement of several ore-

forming sulphide liquids reinforce the notion that the banded carbonatite – phoscorite complex, as well as the sulphide layers, are the result of emplacement of several magma pulses. Such pulses became more depleted in Fe-oxides, silicates and phosphate in the course of intrusive activity. Melt immiscibility, rotation and involvement of several magma pulses may have resulted in the formation of alternating bands of carbonatite and phoscorite. Formation of sub-vertical sulphide layers hosted by these two rock types is linked to the same processes. Sulphide textures formed in response to changing conditions during magma emplacement. Dispersed sulphide layers may have formed from a restricted amount of melt/sulphide liquid. Sulphide patches may be related to the association of dispersed sulphides from a moderate amount of melt/sulphide liquid, and sulphide cumulates from larger volumes of melt/sulphide liquid, pushing sulphide phases and phoscorite towards the external boundaries of the intrusive body.

High-temperature hydrothermal fluids precipitating large amounts of chalcopyrite along fractures across the Loolekop Pipe also circulated within small fracture networks adjacent to the hydrothermal vein itself, forming small-sized chalcopyrite veinlets in the host rocks.

Valleriite was derived from the alteration of pre-existing magmatic sulphides. No valleriite has been observed in fractures across the gangue, indicating a limited Cu mobility. The alteration is heterogeneously distributed across the Loolekop Pipe and was likely controlled by the presence of fractures. Only sulphides in proximity to fractures were affected by late-stage alteration and valleriite formation, leaving parts of the magmatic and hydrothermal sulphide layers unaltered.

Chapter 5

Copper and Iron Isotopic Analysis and Spatially Resolved Sampling: A New Method for Ore Characterization

5.1 Introduction

Over the years, Cu and Fe isotopic analysis has proved to be a useful tool for the characterization of various geological processes, such as partial melting, metasomatism or fractional crystallization (Dauphas et al., 2014; Zambardi et al., 2014; Liu et al., 2015; Savage et al., 2015; Dauphas et al., 2017; Moynier et al., 2017; Johnson et al., 2020). Copper and Fe isotopic compositional variation in sulphides and oxides has been used to characterize ore deposits through analysis of mineral separates. However, this method has a significant drawback: small-scale isotopic variations cannot be properly measured and, therefore, some ore-forming processes remain undetected. *In-situ* sampling techniques, combined with ion exchange chromatography for fraction purification prior to mass spectrometry, may solve this problem and provide spatially resolved results for optimized paragenetic interpretation.

Sulphide and oxide sampled by *in-situ* techniques, however, can contain significant amounts of Cu and Fe and, consequently, need specific chemical processing during chromatography to avoid isotopic fractionation during elution or poor recovery. Several ion exchange chromatography procedures already exist to handle silicate samples, but none are dedicated to sulphides or oxides. This chapter documents a new method specifically designed for the ion exchange separation of Cu and Fe fractions from sulphide and oxide ore-minerals. This method is then applied to processing and measurement of Cu and Fe isotopes from Cu-sulphides of the Loolekop Pipe as described in Chapter 6.

5.2 Background

5.2.1 Isotope fractionation processes

Iron isotope systematics have been extensively used to investigate different types of geological processes for a better understanding of Earth formation and evolution over time (Beard and Johnson, 1999; Schoenberg and von Blanckenburg, 2006; Weyer and Ionov, 2007; Chapman et al., 2009; Sossi et al., 2012; Dauphas et al., 2017; Johnson et al., 2020). Since the advent of multi collector (MC)-ICP-MS, in which mass bias is easier to correct for than in TIMS measurements (Thermal Ionization Mass Spectrometry), the use of Fe isotopes has expanded significantly over the last two decades (Beard and Johnson, 1999; Belshaw et al., 2000; Dauphas et al., 2009b; Millet et al., 2012). Several types of fractionation processes can account

for variations in Fe isotopic compositions in rocks and minerals. They can be divided in two categories: (i) kinetic and (ii) equilibrium processes (Dauphas et al., 2017; Johnson et al., 2020).

The first category consists of diffusion, thermal diffusion, condensation, evaporation, as well as various other kinetic processes. Diffusion is a simple process, which is based on the ability of light isotopes to move more easily than the heavy ones. This is also the case for thermal (or Soret) diffusion, where light isotopes move towards the high temperature parts of a system and the heavy towards the colder regions (Lundstrom, 2009; Zambardi et al., 2014). Such phenomenon can be characterized and quantified by the following equation:

$$\frac{D_j}{D_i} = \left(\frac{m_i}{m_j}\right)^{\beta} \quad (5.1)$$

where D_i and D_j are the diffusivities of two isotopes i and j, with m_i and m_j representing their masses, respectively. Beta (β) is between 0, where no fractionation occurs, and 0.5, where equipartition of monoatomic gas energy occurs (Dauphas et al., 2017). Soret diffusion can explain various Fe isotopic fractionation phenomena during geological processes and Fe isotopic compositions of different rock types. Richter et al. (2009a and b), Huang et al. (2010) and Zambardi et al. (2014) have suggested that Fe isotopic variations in magmatic suites may be related to thermal fractionation. Heavy Fe isotopes concentrate towards the cold area of a magmatic suite during differentiation.

Condensation processes are poorly constrained, and cannot therefore be properly quantified. However, evaporation can be characterized and modelled by the Hertz-Knudsen equation (Dauphas et al., 2017). Isotopic fractionation occurring during evaporation can be calculated as follows (Richter et al., 2002, 2007; Richter, 2004; Dauphas et al., 2015):

$$\Delta_{Evaporation} = \Delta_{Equilibrium} - \left(1 - \frac{P}{P_{Sat}}\right)\Delta_{Kinetic} \quad (5.2)$$

where P is the vapour partial pressure, P_{Sat} the pressure of saturation, $\Delta_{Equilibrium}$ the isotopic fractionation factor at equilibrium and $\Delta_{Kinetic}$ defined as:

$$\Delta_{Kinetic} = 1000\left(\frac{\gamma_i}{\gamma_j}\sqrt{\frac{m_j}{m_i}} - 1\right) \quad (5.3)$$

where γ_i and γ_j are the evaporation coefficients of isotopes i and j, and m_i and m_j, their masses, respectively.

High-temperature evaporation processes are rare. Most of them occur as stellar phenomena, such as Fe evaporation from solar nebulae (Mullane et al., 2005) or planet

collisions (Poitrasson et al., 2004). Isotopic fractionation related to chemical reaction kinetics is the least understood isotopic fractionation phenomenon. Most work thus far has focused on redox reactions under experimental conditions (Dauphas et al., 2017). Kinetic isotopic fractionations are complex processes, which are difficult to quantify and characterize. They are most likely the combination of several processes, which may produce isotopic fractionation such as redox and diffusion.

Equilibrium isotopic fractionation processes in mineral-mineral (Dauphas et al., 2004; Dauphas et al. 2007; Shahar et al., 2008), mineral-melt (Schuessler et al., 2007; Poitrasson et al., 2009; Shahar et al. 2015; Sossi and O'Neill, 2017), fluid-fluid (Welch et al., 2003; Hill and Schauble, 2008) and fluid-mineral pairs (Skulan et al., 2002; Wiesli et al. 2004; Wu et al., 2010; Saunier et al., 2011; Frierdich et al., 2014) can also be constrained by the use of Fe isotopic analysis. An equilibrium process is the isotope exchange between two phases until thermodynamic equilibrium is reached. In such processes, isotopic fractionation is directly related to Fe bond strength, coordination and redox state (Urey, 1947; Dauphas et al., 2017). Isotopic fractionation is dependent on the bond strength of Fe in its environment (Bigeleisen and Mayer, 1947). Heavy Fe isotopes are characterized by high valence and low coordination. According to O'Neil (1986), the isotopic equilibrium fractionation factor between two phases A and B is defined as:

$$\alpha_{A-B} = R_A^{i/j} / R_B^{i/j} \tag{5.4}$$

This coefficient formulates the fractionation between two phases (see above), with R being the abundance ratio between the rare isotope (i) and the abundant one (j). It can also be written as following:

$$\Delta_{A-B} = (\delta_A - \delta_B)_{Equilibrium} \approx 1000 ln\alpha_{A-B} \tag{5.5}$$

or, alternatively as:

$$\Delta_{A-B} = 1000(ln\beta_A - ln\beta_B) \tag{5.6}$$

The latter is based on calculations and is not measured, which is a significant advantage since the error is smaller. Such calculations are made using Density Functional Theory for the determination of 1000lnβ to compute the electronic orbitals and vibrational frequencies of chemical species (Blanchard et al., 2009; Rustad and Dixon, 2009; Fujii et al., 2014). Other calculation approaches exist such as the Hartree-Fock and Møller Plesset methods, as mentioned by Fujii et al. (2014). These methods and applications for β-factor calculations are

explained in detail in many studies (Anbar et al., 2005; Wells et al., 2005; Hill and Schauble, 2008; Ottonello and Zuccolini, 2009; Schauble et al., 2009).

In the case of equilibrium processes, Fe can help to characterize two types of systems. The first one consists of the complete exchange of isotopes between two phases and is referred to as a closed system (Johnson et al., 2020). According to Criss (1999), the isotopic fractionation values for this setting can be approximated as:

$$\delta^i E_A \approx \delta^i E_B - \Delta^i_{B-A} \tag{5.7}$$

where E is the element of interest, A and B are the two phases of the system, such that:

$$\Delta^i_{B-A} \approx 1000(\alpha_{B-A} - 1) \tag{5.8}$$

As mentioned above, several types of equilibrium processes occur in geological settings. The first type involves mineral-melt and mineral-mineral fractionation. Many studies focused on the fractionation of Fe isotopes between minerals and melts (Sossi et al., 2012; Williams et al., 2018; Ding et al., 2019; Peters et al., 2019), providing important information on the behaviour of isotopes during melting or fractional crystallization. In studies of natural isotopic fractionation between minerals and melt, experimental work has been successfully carried out under high pressure and temperature conditions for the determination of Fe isotopic fractionation in different systems (Shahar et al., 2008; Poitrasson et al., 2009; Sossi and O'Neill, 2017). The presence of significant amount of S in a metal-rich phase tends to encourage the fractionation of heavy isotopes in the latter (Poitrasson et al., 2009; Shahar et al., 2015). Mineral-mineral and mineral-melt fractionations are controlled, like most of the isotopic variation, by Fe coordination and valence in the minerals concerned and the associated redox reactions (Sossi and O'Neill, 2017). Mineral-fluid and fluid-fluid fractionation is particularly complex to quantify since it is difficult to reach equilibrium in such systems experimentally, and kinetic processes are most likely involved during the isotope fractionation processes. As for most of the equilibrium and kinetic fractionation processes, equilibrium between Fe^{2+} and Fe^{3+} in solution plays a significant role (Johnson et al., 2002; Welch et al., 2003), but temperature, more so than in other systems, plays a preponderant role and can produce a significant change in fractionation (Saunier et al., 2011).

The constant removal of a phase B from a system A during a Rayleigh fractionation process causes isotopic fractionation. Rayleigh fractionation occurs in open and closed systems, in both equilibrium and kinetic environments. The isotopic fractionation in such conditions is modelled according to the following equation (Rayleigh, 1902):

$$\frac{[R^{i/j}]}{[R^{i/j}]_i} = f^{(\alpha_{B-A}-1)} \quad (5.9)$$

where f is the remaining fraction of A and $[R^{i/j}]_i$ is the initial isotopic ratio. As mentioned by Johnson et al. (2020), the phases produced by a Rayleigh fractionation are isolated from the system and cannot be involved in further isotopic fractionation. The fact that the products are isolated suggests that large variations in isotopic composition will result.

High-temperature processes have been extensively investigated through Fe isotope systematics since the end of the 1990 with a specific focus on silicate Earth and mantle processes. It has been demonstrated that the Earth has a heavier Fe isotopic composition than chondrites (Poitrasson et al., 2004). This may be related to a vaporisation process that occurred during a hypothetical collision between Earth and another planet, which subsequently caused isotopic fractionation (Poitrasson et al., 2004). A recent study by Lesher et al. (2020) has suggested that the Fe isotopic fractionation process is related to Soret diffusion involving the mantle as cold end of the system and the earth core as its hot end. Multiple studies (Williams et al., 2005; Weyer and Ionov, 2007; Williams and Bizimis, 2014) have focused on the characterization of mantle processes at the origin of Fe isotopic fractionation, such as partial melting and metasomatism. Successive processes of depletion and re-fertilization may have initiated a heterogeneous mantle in terms of Fe isotopic composition. However, mantle values systematically overlap with the chondrite Fe isotopic range (Williams et al., 2005; Schoenberg and von Blanckenburg, 2006; Dauphas et al., 2007; Craddock and Dauphas, 2011; Poitrasson et al., 2013; Dauphas et al., 2017). Craddock et al. (2013) found similar Fe isotopic ratios in abyssal peridotite and chondrite. Williams and Bizimis (2014) have shown that partial melting events produce enrichment of the melt in heavy isotopes. To explain this Fe isotopic distribution, Weyer and Ionov (2007) proposed partial melting-related isotopic fractionation based on Rayleigh distillation of a peridotite source rock, and found a residue-melt Fe fractionation value of 0.1 - 0.3‰. By using an isotopic fractionation model exclusively driven by changes in Fe oxidation state during partial melting, Dauphas et al. (2009a) found similar fractionation values (0.24‰ at a 10% partial melting).

Iron isotope fractionation also occurs in crustal silicate rocks. The enrichment in heavy isotopes seems to be positively correlated with their SiO_2 content (Poitrasson and Freydier, 2005; Heimann et al., 2008): rhyolites and granites are enriched in heavy isotopes relative to other crustal rock types. Several explanations have been suggested to describe this feature. The first proposes Fe leaching by Cl-rich fluids, preferentially remobilizing light isotopes (Chapman et al., 2009). Isotopic fractionation through Soret diffusion has also been suggested (Zambardi

et al., 2014). However, the most likely option remains fractional crystallization combined with diffusion (Sossi et al., 2012).

Iron isotopes have been successfully used for the characterization of Fe-sulphide and oxide ore deposits (Graham et al., 2004; Wang et al., 2011, 2015; Weis, 2013; Wawryk and Foden, 2015; Hiebert et al., 2016; Zhu et al., 2016; Günther et al., 2017; Zhao et al., 2019). Variations of Fe isotopic composition in ore minerals have been useful to characterize the ore-forming mechanisms of a deposit, in particular the presence of low or high-temperature processes. Significant differences exist between Fe-bearing sulphides in terms of their Fe isotopic composition.

In a similar way, Cu isotope systematics have been used to characterize geological processes since the pioneering work of Maréchal et al. (1999) and the use of MC-ICP-MS instead of TIMS for isotopic analysis, with standard-sample bracketing (SSB) and elemental doping (Belshaw et al., 2000; Mason et al., 2004; Peel et al., 2008; Larner et al., 2011; Sossi et al., 2015). Copper isotopic fractionation mechanisms are similar to those that control Fe. As for Fe, many studies investigated Cu isotopic fractionation processes by determining the equilibrium constant for isotopic exchange lnβ by ab-initio calculations based on wave function of atoms (Fujii et al., 2013, 2014; Sherman et al., 2013). Such lnβ constants allow the direct calculation of isotopic fractionation between two phases without any measurements as described by Equation 5.6.

Copper isotope systematics have been used for the characterization of rocks and rock-forming processes (Ben Othman et al., 2006; Li et al., 2009; Fellows and Canil, 2012; Lee et al., 2012; Liu et al., 2015; Savage et al., 2015; Huang et al., 2017). Significant work has been done over the years on determining the Cu isotope composition of chondrites, revealing a wide variation range (Luck et al., 2003, 2005; Barrat et al., 2012). Such variations may be due to mixing of different components during early solar processes (Moynier et al., 2017). The silicate Earth also has wide Cu isotope compositional variations (Liu et al., 2015). Such variations, as with Fe isotopic ratios, depend on the different successive partial melting-metasomatic processes in the mantle, and, as with Fe, the Cu isotopic ratio for Bulk Silicate Earth is therefore particularly difficult to estimate (Moynier et al., 2017). Several studies focusing on Cu isotopic ratios in various rock types (komatiites, ocean island basalts, granites, peridotites) suggest limited Cu isotope fractionation during partial melting (Ben Othman et al., 2006; Li et al., 2009; Lee et al., 2012). Unlike igneous rocks whose Fe isotopic signatures are similar to that of the mantle, surficial processes, such as weathering, initiate very strong Cu isotopic fractionation.

Several studies (Graham et al., 2004; Fernandez and Borrok, 2009; Mathur et al., 2010; Ikehata et al., 2011; Asadi et al., 2015; Mathur and Fantle, 2015; Baggio et al., 2018; Kim et al., 2019; Zhao et al., 2019) have successfully investigated ore formation processes by measuring Cu isotopic variations. It is noted that magmatic mineralization is characterized by ~ -1‰ < δ^{65}Cu < ~ 1‰, while alteration minerals have an extremely wide Cu isotopic range (~ -16.5‰ to 10‰). The main parameter controlling Cu isotopic fractionation is most likely related to the distribution of its isotopes among minerals with Cu in different oxidation states through variations in Cu-anion bond strength and coordination of Cu species (Zhu et al., 2002; Ehrlich et al., 2004; Mathur et al., 2005). The large isotopic variation of supergene mineralization in many ore deposits affected by weathering processes supports the predominant role of redox reactions in Cu isotope variations (Asael et al., 2009; Mathur and Fantle, 2015; Baggio et al., 2018; Zhao et al., 2019). Despite a probable influence of phase equilibrium fractionation on Cu isotopic budget, the influence of such processes may not have been predominant (Markl et al., 2006a; Moynier et al., 2017).

5.2.2 Ion Exchange Chromatography

Ion exchange chromatography (IEC) was discovered in the middle of the 20th century and has been used since then to separate specific chemical elements from their host matrix (Kraus and Moore, 1953; Nelson and Kraus, 1958). This versatile process is used in various disciplines, from isotopic geochemistry for research purposes to industrial mining processes, where it is aimed at the recovery of materials of economic interest. Several variations of the separation procedure have been suggested, involving different types and volumes of acid at various concentrations.

Pioneering work by Maréchal et al. (1999) established separation of Fe, Cu and Zn by ion exchange chromatography, from several rock types and geological standards. Subsequently, several changes concerning the chemical procedure have been suggested (Chapman et al., 2006; Borrok et al., 2007; Larner et al., 2011; Sossi et al., 2015), as well as for MC-ICP-MS measurement parameters (Zhu et al., 2000; Weyer and Schwieters, 2003; Arnold et al., 2004; Mason et al., 2004; Millet et al., 2012; Liu et al., 2014; Chen et al., 2017). Much research focused on sulphide ore deposits, including mineralization processes in hypogene and supergene deposits, by Cu isotopic analysis, and successfully identified different crystallization/precipitation events (Markl et al., 2006a; Mathur et al., 2010). However, in most of the cases, ore deposits have not been investigated using coupled Cu and Fe isotopes, with

only a few exceptions (Graham et al., 2004), which may limit our understanding of the ore-forming processes.

The necessity to use combined Fe and Cu isotopes to characterize Cu-sulphide ore deposits is described in detail in the following parts of this chapter. In addition, a modified ion exchange chromatography procedure based on the work of both Maréchal et al. (1999) and Sossi et al. (2015) is also suggested to be applicable to sulphides from various Cu and Fe ore deposits.

5.3 Sampling

Various studies aiming at understanding the mineralization processes in a Cu ore deposit have used handpicked sulphides for Cu and/or Fe isotope analysis (Graham et al., 2004; Markl et al., 2006b; Mathur et al., 2010, Wang et al., 2011; Mathur et al., 2012; Asadi et al., 2015; Wang et al., 2017; Baggio et al., 2018). However, in the case of complex ore assemblages, where mineralogy can change at the scale of several hundred µm, such a procedure is inaccurate and does not take into account potential small-scale ore-forming processes. As a matter of fact, in the case of small-scale ore assemblage variations, corresponding isotopic fractionation processes cannot be detected by large-scale sampling. When using whole-rock or large sulphide samples, the resultant isotopic ratios will reflect an isotopic average of potentially many small-scale process(es) that affected the assemblage. The use of spatially resolved sampling, such as laser cutting and micro-drilling, may avoid this problem and improve the understanding of sulphide paragenesis in ore deposits.

5.3.1 Laser microtomy

Laser cutting as a sampling method has been considered in this study to solve the small-scale isotopic fractionation problems (Logue et al., 2018). Its high spatial resolution makes this method particularly relevant for complex assemblages. Several studies have already used a laser to perform *in-situ* stable isotope analysis, by connecting a mass spectrometer to the laser (Spötl et al., 2006; Chmeleff et al., 2008; Gilbert et al., 2014; Frick et al., 2016). However, such *in-situ* analysis does not separate the element(s) of interest from the matrix, which may cause major interferences during measurements. Ion exchange chromatography is the most suitable method to separate the analyte from a geological matrix.

The laser cutting method was employed in this study on a standard thin section to provide precise, controlled and spatially-resolved sampling of Cu-sulphides. Sulphide-rich areas were defined on drill-core pieces from which a 100 to 150 µm thick polished section was prepared.

Crystalbond 509 resin was used during the preparation of the thin section. This resin easily dissolves in acetone, making it possible to extract the area of interest from the rest of the thin section after laser cutting. In this study, we used a New Wave UP 213 (213 nm) laser with a Nd-YAG ESI Tempest-10 source. The most suitable sampling area is defined based on sulphide assemblage size and texture. Once cut, a small volume of acetone is applied to the area of interest and the resin below the sample subsequently dissolved. A small volume of acetone is necessary to avoid the dissolution of all the resin in the polished section. The extracted sample is then transferred into a drop of MilliQ H_2O and taken with a pipette for further processing.

Laser tuning is a necessary step to avoid melting or disaggregation of the target. Several parameters were optimized to determine the optimal laser cutting parameters for sulphides, such as the spot size (55, 30, 15 and 12 µm), the laser repetition rate (10, 12, 14, 16, 18 and 20 Hz), the energy output (50, 60, 70, 80 and 90%), and the number of passes over the designated path. The laser speed at the sample surface was fixed at 70 $\mu m.s^{-1}$ for an optimal comparison of the other parameters. It was observed during laser cutting tests that medium and high-energy output (>50%) and repetition rates (>12 Hz) trigger melting of the sample surface, as well as along the walls of a cut fragment. Since there are no homogeneous isotopic certified sulphide standards, it is impossible to test if the melting caused any isotopic fractionation by thermal diffusion. In comparison with the size of the samples, this effect could be negligible, but further investigations are necessary before ruling out the possible influence of this process. Spot size does not have any influence on the laser cutting efficiency, but affects acetone infiltration into the resin bed. Fast infiltration may promote the dissolution of acetone over a significant surface. On the other hand, if the cut is too narrow, the resin dissolution will be too slow or even insufficient to ensure optimal extraction of the sample. Optimal parameters for laser cutting are a repetition rate of 10 Hz combined with a 50% energy output to avoid eventual melting of the sample. Since both the repetition rate and the energy output have to be maintained at a low level, the number of passes has to be high to cut the entire sulphide/rock slice and reach the resin bed. Tests revealed that a minimum of 60 passes is necessary to reach the resin requiring a very long time (up to 7 h) to delineate the target.

The Crystalbond 509 resin was analyzed by ICP-MS to detect trace elements, which may cause problems during sample processing (Table 5.1). The presence of Cu and Zn at the ppm level in the resin requires careful cleaning of the resin from the sample, which given its sticky state once dissolved by acetone, can be delicate. Considering the usually small amount of sample extracted from the thin section, it is likely that the resin may affect the isotopic analysis results. After deliberating the abovementioned observations and required parameters, for

matters of convenience, time and cost optimization, laser cutting, despite its high spatial precision, is not the most suitable method for sulphide sampling, and was consequently not implemented for routine sulphide sampling for isotopic analysis in this study.

Table 5.1: *Trace element composition of the resin Crystalbond 509.*

Element	Resin Crystalbond 501 (ppm)
Li	0.024
P	16.102
Sc	0.033
Ti	0.138
V	0
Cr	0.726
Co	0.031
Ni	0.502
Cu	3.639
Zn	3.244
Ga	0
Rb	0.008
Sr	0.088
Y	0.002
Zr	0.167
Nb	0
Ba	0.084
Sn	0.121
Cs	0
La	0.153
Ce	0.058
Pr	0.005
Nd	0.031
Sm	0.004
Eu	0
Gd	0.004
Tb	0
Dy	0
Ho	0
Er	0
Tm	0
Yb	0
Lu	0
Hf	0.001
Ta	0
W	0.143
Pb	0.168
Th	0.006
U	0

5.3.2 Drilling

The second sampling technique investigated in this study is able to provide high spatial resolution. It utilizes a Dremel® 4000 drilling tool with a Dremel® diamond stainless steel drill bit (1 mm Ø) to drill into sulphide-rich drill core pieces mounted in epoxy resin. The procedure is as follows: first, the work space and the drilling tools are protected with plastic film in order to avoid any possible contamination of the sample by external material from surrounding surfaces or the metallic parts of the Dremel® Tool. Before drilling, a drop of 18.2 $M\Omega.cm^{-1}$ MilliQ H_2O is added onto the region of interest. The sulphide is then carefully drilled at 4000 rpm. The resulting MilliQ H_2O-hosted sulphide powder is taken in a pipette and transferred into a Savillex® 15 mL capacity beaker closed with a lid. The polished mount surface is rinsed three times with MilliQ H_2O to ensure that all of the drilled material is collected. The samples are then evaporated to dryness and weighed before being dissolved. Between samples, the drill bit was placed in an ultrasonic bath for 30 minutes before being rinsed successively with both MilliQ H_2O and acetone.

The drilling technique, despite a lower resolution than laser cutting, is easier to carry out since it does not require heavy equipment, is comparatively fast and can be performed directly in a dedicated space in the chemistry lab, limiting potential sample contamination. However, this method is limited in terms of spatial resolution by the diameter of the drill bit, which may be too wide for some complex mineral assemblages. Moreover, sulphide assemblages are visible only on the surface of polished mounts, and their nature may be different below that surface. The laser technique, due to the use of a thin section instead of a polished mount, avoids this problem. A potential issue for polished mount drilling may be sample contamination by the drill bit itself. This problem is exclusively related to the type and quality of the drill bit used, and can be consequently fixed by changing the drill bit. During implementation of the technique, quality control was considered to be necessary to evaluate contamination of the sample by the drill bit (Table 5.2). Quality control was achieved by drilling into a natural quartz crystal. Both the sampled material and an undrilled piece of quartz were analyzed for trace element concentrations with a Thermo Scientific iCAP ICP-MS for comparison. No perceptible difference in element concentrations was determined for nearly all the analyzed elements, indicating the reliability of this technique. In fact, a natural sample may have a slightly heterogeneous trace element composition and variations of Cu and Zn contents. The higher Ni content in the drilled sample may suggest the presence of Ni-rich inclusions in the natural material. Contamination of the sample by the drill bit during drilling causing the Ni anomaly cannot be entirely ruled out.

Table 5.2: *Trace element composition of drilled natural quartz against the composition of undrilled sample.*

Element	Drilled (ppm)	Non-drilled (ppm)
Li	5.031	6.358
P	5.785	4.749
Sc	0.043	0.024
Ti	5.705	3.778
V	0.234	0.1
Cr	1.164	1.308
Co	0.056	0.066
Ni	217.001	3.374
Cu	2.612	3.586
Zn	6.4	4.737
Ga	0.04	0.036
Rb	0.276	0.131
Sr	2.339	0.634
Y	0.029	0.017
Zr	0.281	0.406
Nb	0.021	0.011
Sn	0.155	1.032
Cs	0.037	0.007
Ba	2.558	1.66
La	0.177	0.138
Ce	0.052	0.363
Pr	0.007	0.007
Nd	0.031	0.028
Sm	0.005	0.006
Eu	0.002	0.001
Gd	0.005	0.006
Tb	0.001	0.001
Dy	0.005	0.004
Ho	0.001	0.001
Er	0.004	0.004
Tm	0.001	0.001
Yb	0.005	0.004
Lu	0.001	0.001
Hf	0.024	0.012
Ta	0.019	0.013
W	0.089	0.048
Pb	0.3	4.131
Th	0.011	0.02
U	0.011	0.008

5.4 Chromatography mechanisms and method choice

The separation of Cu, Fe and Zn from a matrix by ion exchange chromatography is based on the different adsorption properties of these metals with respect to a polymer-composed resin. Their adsorption is dependent on the molarity of the acid (HCl for this procedure) used for the elution (Table 5.3). Elements can therefore be adsorbed and eluted by successive changes of HCl concentration, exploiting these characteristics (Kraus and Moore, 1953). The equilibrium factor D, defined as the mass of an element on resin divided by the mass of this element in solution multiplied by 100, is also an important parameter to determine the behaviour of chemical elements during the ion exchange chromatography. The AG MP-1 resin is the most commonly used medium for the separation of Cu, Fe and Zn by ion exchange chromatography (Maréchal et al., 1999; Archer and Vance, 2004; Borrok et al., 2007; Dauphas et al., 2017). It is well accepted that the AG MP-1 resin has an excellent retention capacity for Cu (van der Walt et al., 1985) and is therefore used when all Fe and Cu has to be recovered for independent isotopic analysis (Liu et al., 2014). However, if the purpose is also to separate Cu from Fe, the equilibrium factor ratio D_{Fe}/D_{Cu} must be the determining criterion for the selection of the resin and the chromatography procedure. According to van der Walt et al. (1985), the AG1-X8 resin is the optimal resin to fulfil such requirements. AG1 resins are able to strongly retain Fe in its ferric form. Despite a lower retention of Cu in the AG1 resins, careful examination of the Cu elution timing relative to the matrix makes their use possible. The presence of a significant tail of the matrix elution peak is due to the presence of matrix-derived cations in some test samples, therefore a second chromatography procedure needs to be systematically performed to obtain pure Cu and Fe fractions. The D factors for the elements of interest when applying the AG1-X8 resin range from 13.1 to 21.2 for Cu^{2+} and from 340 to 3400 for Fe^{3+} at 6 mol L^{-1} HCl (Table 5.3; van der Walt et al., 1985). It has been demonstrated that the sample composition influences the first elution step: Sossi et al. (2015) mentions that the breakthrough point of the resin is different for two different standards, which implies that the matrix-hosted cations eluting immediately are responsible for such a phenomenon. In the case of pure sulphides, such a problem may be considered negligible due to the trace-level of other chemical elements. However, in case of complex sulphide assemblages associated with gangue, such processes have to be taken in account. This possibility highlights the importance of mm- to µm-scale spatially resolved sampling.

Table 5.3: *Distribution coefficients D for Cu and Fe for several ion exchange resins depending on the molarity of eluting acid (modified after van der Walt et al., 1985).*

Resin	Ion	HCl molarity (mol L^{-1})				
		3	5	7	8	9
AG MP-1						
	Cu^{2+}	13.2	27.2	39.9	39.0	36.4
	Fe^{3+}	19.6	158	1390	3100	3800
AG1-X2						
	Cu^{2+}	3.8	8.6	14.4	15.2	14.6
	Fe^{3+}	5.0	30.0	256	570	1170
AG1-X4						
	Cu^{2+}	2.3	7.4	15.4	15.6	15.8
	Fe^{3+}	9.7	75	694	1550	2740
AG1-X8						
	Cu^{2+}	4.0	13.1	21.2	23.1	21.2
	Fe^{3+}	35.6	340	3400	7500	$>10^4$
AG1-X10						
	Cu^{2+}	4.2	15.2	23.1	25.7	23.6
	Fe^{3+}	31.0	319	2700	7200	$>10^4$

The complexity of sulphide assemblages, natural ones being typically heterogeneous in composition, makes the calculation of the maximum amount of material, which can be put on the resin, challenging. Therefore, extra care is required when calculating the maximum amount of sulphide sample to be loaded on the resin. Indeed, the exact nature of the sample remains unclear, because only the surface of the sulphide is exposed during drilling. The amount of Cu and Fe passing through the resin can only be approximated in the case of natural sulphides in complex assemblages. It implies that the breakthrough point must be maximized to avoid overloading. If the sample amount exceeds the resin capacity, it would initiate the early elution of fractions of interest, as well as induce isotopic fractionation. It has to be highlighted that such approximation requires quantitative analysis prior to mass spectrometry to optimize dilution. In the case of a bornite-dominated sample, the optimal sample amount for chromatography needs to be calculated assuming the ideal bornite composition (Cu_5FeS_4). As a matter of fact, under oxidized conditions and after conversion to chloride form, Cu reacting with the resin will be $CuCl^{2-}_4$ (Anbar et al., 2000; Maréchal and Albarède, 2002). This ion will consequently occupy two sites in the resin according to the following reaction:

$$2(R\text{-}Cl^-) + CuCl^{2-}_4 \Leftrightarrow 2R\text{-}CuCl^{2-}_4 + 2Cl^- \qquad (5.10)$$

Iron, on the other hand, will form $FeCl^-_4$ species in chloride form and in an oxidized environment and will bond to the resin as described by the following reaction:

$$R\text{-}Cl^- + FeCl^-_4 \Leftrightarrow R - FeCl^-_4 + Cl^- \quad (5.11)$$

The use of H_2O_2 during the elution of the matrix and Cu is essential to keep the elements of interest oxidized and therefore to prevent their early elution. This is particularly relevant for Fe, which needs to be in trivalent state to be properly fixed onto the resin (van der Walt et al., 1985; Dauphas et al., 2017). Willbold et al. (2015) suggested the addition of ascorbic acid in the eluent(s) to avoid resin overloading and to optimize separation. However, such a procedure would reduce Fe^{3+} to Fe^{2+}, making the complete retention of Fe impossible.

5.5 Chemistry

The chemical Cu and Fe separation procedure for sulphides described in this section is based on the Cu and Fe ion exchange chemistry outlined by Maréchal et al. (1999) and Sossi et al. (2015). Changes were implemented to adapt to the sample types specific to Phalaborwa and to optimize the procedure for increasing element adsorption on the resin due to the presence of significant amounts of both Cu and Fe in the samples.

5.5.1 Material

The sample processing was performed entirely in the WIGL (Wits Isotope Geoscience Lab) facility at the University of the Witwatersrand. Laminar flow class 100 hoods were utilized for sample digestion and evaporation, whereas a laminar flow class 10 hood exclusively dedicated for the Cu-Fe separation was used for the ion exchange chromatography. The reagents used during the chemical separation procedure were produced from double distilled Merck® HCl, HF and HNO_3 diluted with 18.2 MΩ cm^{-1} MilliQ H_2O. Dissolution was performed in dedicated 15 mL perfluoroalkoxy-alkane (PFA) Savillex® closed beakers to avoid any potential cross contamination with other sample types. 25 mL capacity PFA Savillex® open beakers were used for fraction collection during the ion exchange chromatography. BioRad® 0.8 x 4 polyprep columns were selected for the chromatography. Eluents containing H_2O_2 were prepared only a few hours prior to ion exchange chromatography due to the instability of H_2O_2 in solution.

Pipette tips, centrifuge tubes, as well as chromatography columns, were washed with 5% HNO_3. The PFA vessel was refluxed with 6 mol L^{-1} HNO_3, and subsequently cleaned in PFA jars with successive batches of soapy MilliQ H_2O and 50% HNO_3 at 100°C for 48 and 72h, respectively.

The standard used for Fe measurements was IRMM-524b, prepared in the WIGL. A suitable piece of IRMM-524b wire was dissolved in concentrated HNO_3 and the resulting solution diluted to reach a 2% HNO_3 concentration at 100 ppm. The standard IRMM-524b was subsequently normalized to IRMM-014 during measurement result processing (Dauphas et al., 2017). The Cu standard used for the measurements was NIST SRM-976 in a 2% HNO_3 solution. Copper NIST SRM-976 was prepared according to the same method as for IRMM-524b, but diluted to 10 ppm in 2% HNO_3.

5.5.2 Dissolution

The samples were digested in sulphide-dedicated 15 mL Savillex® PFA closed beakers with a 12 mL mixture of 1HCl:0.5HF:0.2HNO_3, with concentrations of 10 mol L^{-1}, 23 mol L^{-1}, 12.5 mol L^{-1}, respectively (Sossi et al., 2015). The beakers were left for 48 hours on a hotplate at 130°C. The bottom of the dissolution beakers was then carefully examined to detect potentially undissolved material. The beakers were left an additional 36 hours if any solid residue was visible. The beakers were left to cool down, opened and dried down on a hotplate at 95°C until evaporation was complete. Every 4-6 hours, 0.5 mL of concentrated HNO_3 was added to the mixture to avoid the formation of insoluble fluorides. In addition, HNO_3 offers the advantage of maintaining sample oxidation. A mixture of HNO_3 with $HClO_4$ and/or H_2O_2 may also be an option to oxidize the solution. Some laboratories perform successive cycles of dissolution-evaporation to avoid the formation of fluorides (Dauphas et al., 2017). However, the addition of supplementary acid may significantly raise the procedural blank level.

5.5.3 Ion exchange chromatography

The modified chemical separation is based on the procedure published by Sossi et al. (2015) using 1 mL BioRad® AG1-X8 (200-400 mesh) resin with 0.8 x 4 BioRad® polyprep columns (Table 5.4). Minor changes were introduced to the separation procedure. In order to keep Fe oxidized, 0.001% of H_2O_2 was added to 6 mol L^{-1} HCl during the elution of the matrix and Cu (Maréchal et al., 1999). One mL of AG1-X8 (200-400 mesh) was added in the columns the day before the chromatography was performed. Volume loss must be taken into account as the resin compacts overnight and the volume is usually reduced by ~10% in this procedure. If necessary, the remaining space is filled up and left to settle. The resin has been successively washed with 10 mL of 3 mol L^{-1} HNO_3, MilliQ H_2O, as well as washed and conditioned with 10 mL of 6 mol L^{-1} HCl + 0.001% H_2O_2. The samples were remobilized in 1 mL 6 mol L^{-1} HCl + 0.001% H_2O_2 and the beakers heated for 30 to 45 min at 35°C to ensure optimal uptake. The

beakers were left to cool down, and the samples loaded on the resin once the 10 mL of 6 mol L^{-1} HCl + 0.001% H_2O_2 for resin cleaning and conditioning was eluted (Table 5.4). The matrix was then eluted by 5 mL 6 mol L^{-1} HCl + 0.001% H_2O_2 (Fig. 5.1, Table 5.4). After elution of the matrix, 2 x 7 mL of 6 mol L^{-1} HCl were successively added to elute the Cu fraction, followed by the addition of 2 x 4 plus 1 mL of 0.5 mol L^{-1} HCl for the elution of Fe in the same beaker as Cu in preparation for a second chromatographic pass. Zinc was then eluted in the waste with 5 mL 3 mol L^{-1} HNO_3.

The collected Cu and Fe fractions were then dried down and remobilized with 1 mL 6 mol L^{-1} HCl + 0.001% H_2O_2. The ion exchange chromatography procedure described above was repeated once for further purification (Savage et al., 2015; Dauphas et al., 2017). Copper and Fe fractions were collected separately during the second stage. The Cu and Fe fractions were then evaporated, dissolved in 1 mL 12.5 mol L^{-1} HNO_3 + 0.001% H_2O_2 to remove eventual organic material from the resin and to ensure the total removal of Cl, which may cause interference during the measurements. Fractions were then dried down and taken up into 1 mL of 2% HNO_3 for Cu and 0.2% HNO_3 for Fe fractions from which the appropriate dilution was performed for the MC-ICP-MS measurements.

Table 5.4: *Ion exchange chromatography procedure implemented for Cu and Fe separation from sulphides. Procedure modified from Maréchal et al. (1999) and Sossi et al. (2015).*

Step	Eluent	Volume
Cleaning	HNO_3 3 mol L^{-1}	10 mL
	MilliQ H_2O	10 mL
Cleaning and conditioning	HCl 6 mol L^{-1} + 0.001% H_2O_2	10 mL
Sample loading	HCl 6 mol L^{-1} + 0.001% H_2O_2	1 mL
Matrix elution	HCl 6 mol L^{-1} + 0.001% H_2O_2	5 mL
Cu elution	HCl 6 mol L^{-1} + 0.001% H_2O_2	7 mL
	HCl 6 mol L^{-1} + 0.001% H_2O_2	7 mL
Fe elution	HCl 0.5 mol L^{-1}	4 mL
	HCl 0.5 mol L^{-1}	4 mL
	HCl 0.5 mol L^{-1}	1 mL
Zn elution	HNO_3 3 mol L^{-1}	5 mL

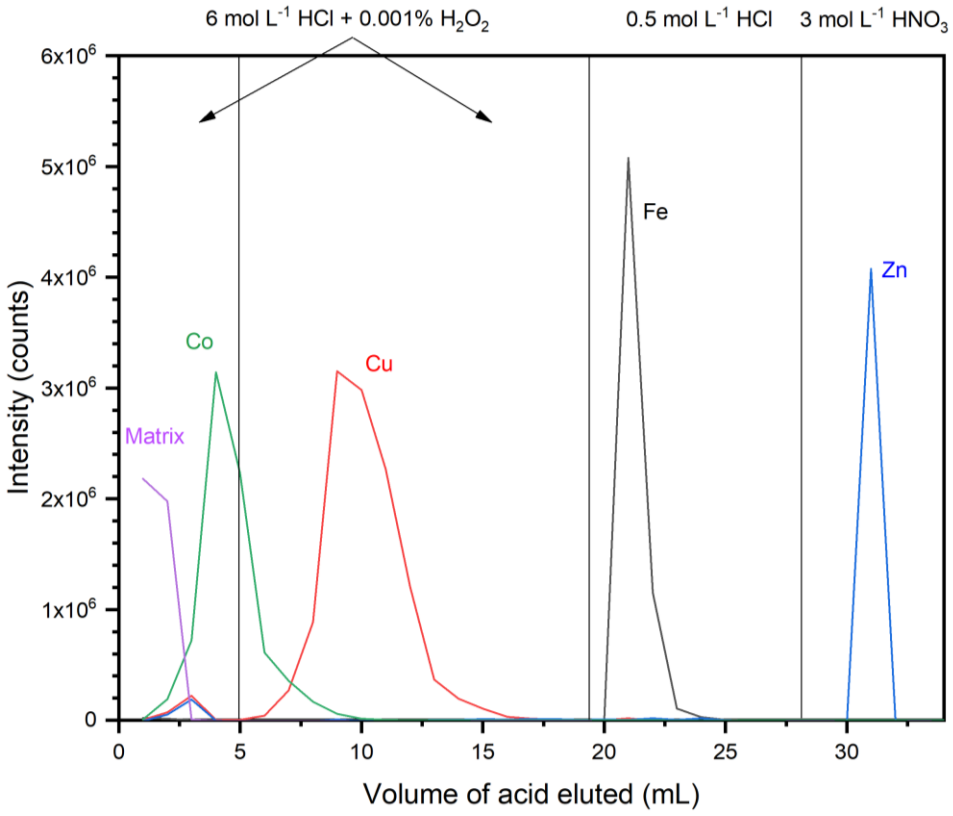


Figure 5.1: *Elution curve for the ion exchange chromatography procedure described in Table. 5.4 for Cu and Fe separation.*

5.6 Measurements

5.6.1 Copper

Copper fractions were diluted to 1 ppm mL^{-1} and measured using the MC-ICP-MS instrument at the University of Johannesburg. Fractions were measured on a Nu Plasma II instrument using wet plasma set-up equipped with a self-aspirating Expansion MicroMist U-series nebulizer with an uptake rate of 200 µL min^{-1}. The nebulizer was coupled to a Peltier Glass Expansion Twister Spray Chamber cooled at 7°C. Cup configuration is described in Table 5.5, with a mass separation of 0.5 amu.

Table 5.5: *Cup configuration of Nu Plasma II MC-ICP-MS for Cu measurements.*

Cup	L6	L5	L4	L3	L2	L1	Ax	H1	H2	H3	H4	H5	H6
		^{60}Ni				^{62}Ni		^{63}Cu		$^{64}Ni + {}^{64}Zn$		^{65}Cu	^{66}Zn

All measurements were performed in low resolution mode with a sensitivity of 14 V ppm^{-1} mL^{-1}. Detailed device parameters are described in Table 5.6. Copper fractions must be Na-free for measurements due to potential $^{23}Na^{40}Ar^{+}$ and $^{25}Na^{40}Ar^{+}$ interferences.

Table 5.6: *Characteristics of Nu Plasma II and Thermo Scientific Neptune Plus MC-ICP-MS for measurements of Cu and Fe, respectively.*

Device	Nu Plasma II	Thermo Scientific Neptune Plus
RF Power	1300 W	1200 W
Acceleration voltage	6000 V	-2000 V
Sampler cone	1.15 mm Ø , Ni	Jet 1.1 mm Ø , Ni
Skimmer cones	0.6 mm Ø	H-type 0.8 mm Ø, Ni
Coolant Ar gas flow	13 L m^{-1}	12.5 L m^{-1}
Auxiliary Ar gas flow	0.8 L m^{-1}	0.7-1 L m^{-1}
Nebulizer	200 µL min^{-1}	200 µL min^{-1}
Analyte solution	2% HNO_3	0.2% HNO_3
Sample uptake time	60 s	130 s
Wash time	400 s	300 s
Cycles per analysis	40	40
Blocks per analysis	1	1
Integration time per cycle	10 s	4.194 s

The mass bias was corrected using the SSB technique and by doping the sample with 1 ppm mL^{-1} Ni (Inorganic Ventures™ single solution). The exponential law was used for the correction of $^{65}Cu/^{63}Cu$ by $^{62}Ni/^{60}Ni$. Nickel is particularly useful as a doping element due to its different ionization behaviour compared to Cu. Measurements of Cu isotopes with the MC-ICP-MS must be corrected by element doping by exponential law according to the following equation:

$$\left(\frac{^{65}Cu}{^{63}Cu}\right)_{Measured} = \left(\frac{^{65}Cu}{^{63}Cu}\right)_{True} \times \left(\frac{M_{^{65}Cu}}{M_{^{63}Cu}}\right)^{\beta} \quad (5.12)$$

with β the mass independent fractionation factor defined as:

$$\beta = ln\left[\frac{\left(\frac{^{62}Ni}{^{60}Ni}\right)_{Measured}}{\left(\frac{^{62}Ni}{^{60}Ni}\right)_{Reference}}\right] / ln\left(\frac{M_{^{62}Ni}}{M_{^{60}Ni}}\right) \quad (5.13)$$

The Cu isotopic ratios in the sample are normalized by the average of the Cu isotopic ratios of the bracketing NIST SRM-976 standards according to the following formula:

$$\delta^{65}Cu = 1000 \times \left[\frac{\left(\frac{^{65}Cu}{^{63}Cu}\right)_{Sample}}{\left(\frac{\left(\frac{^{65}Cu}{^{63}Cu}\right)_{Standard\ 1} + \left(\frac{^{65}Cu}{^{63}Cu}\right)_{Standard\ 2}}{2}\right)} - 1\right] \quad (5.14)$$

with Standard 1 the bracketing NIST SRM-976 measurement before, and Standard 2 the bracketing NIST SRM-976 measurement after the measurement of the sample.

5.6.2 Iron

Iron isotopes are difficult to measure due to presence of $^{14}N^{40}Ar^{+}$, $^{16}O^{40}Ar^{+}$ and $^{1}H^{16}O^{40}Ar^{+}$ interferences overlapping with the Fe peaks. Peaks are almost superposed and measurements have to be done on a narrow shoulder of the Fe peaks (Dauphas et al., 2017).

Iron fractions were measured with a Thermo Scientific Neptune Plus at the CNRS-Ecole Normale Supérieure de Lyon in France. The Thermo Scientific Neptune Plus instrument was used in medium resolution and wet plasma. Technical details concerning the device set up are given in Table 5.6. The Fe fractions were diluted to 1 ppm mL^{-1}. The masses ^{54}Fe, ^{56}Fe, ^{57}Fe, ^{58}Ni and ^{62}Ni were measured simultaneously. The resolution was 15 $V.ppm^{-1}$ mL^{-1} with a progressive drift to 11 V ppm^{-1} mL^{-1} at the end of the measurement session (about. 56 h). Quality control of the results is given by a three-isotope correlation graph in Fig. 5.2.

As with Cu, the SSB technique was used to correct mass bias, combined with a Ni spike (Poitrasson and Freydier, 2005). One single sample was measured between each standard. Correction of the Fe isotopic ratios by Ni doping was done using the exponential mass fractionation law as follows:

$$\left(\frac{^{56}Fe}{^{54}Fe}\right)_{Measured} = \left(\frac{^{56}Fe}{^{54}Fe}\right)_{True} \times \left(\frac{M_{^{56}Fe}}{M_{^{54}Fe}}\right)^{\beta} \quad (5.15)$$

with β the mass independent fractionation factor defined as:

$$\beta = ln\left[\frac{\left(\frac{^{62}Ni}{^{60}Ni}\right)_{Measured}}{\left(\frac{^{62}Ni}{^{60}Ni}\right)_{Reference}}\right] / ln\left(\frac{M_{^{62}Ni}}{M_{^{60}Ni}}\right) \quad (5.16)$$

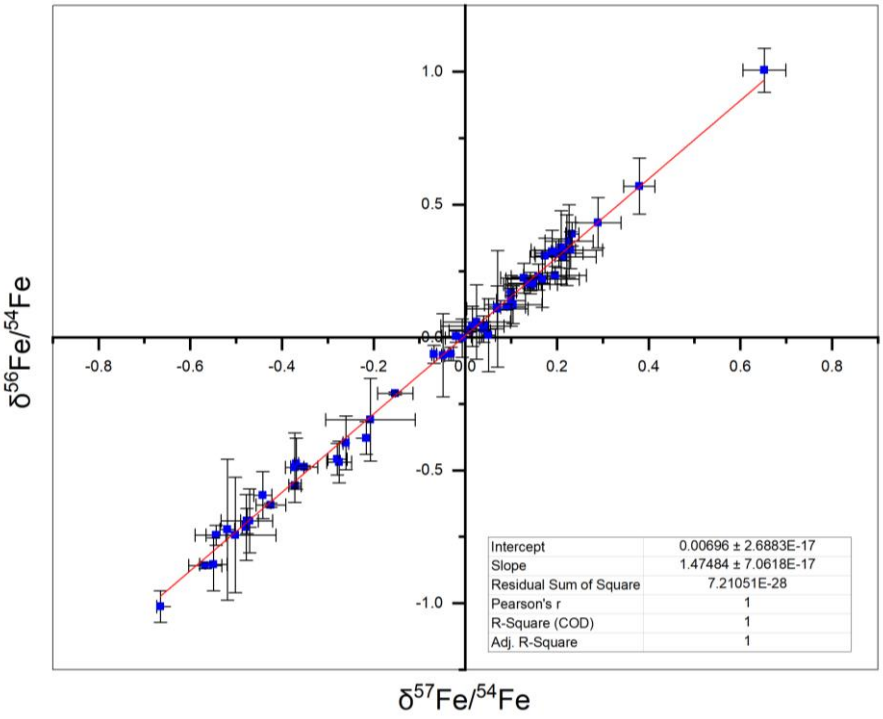


Figure 5.2: *Three Fe isotopes correlation graph for measurement quality control.*

Isotopic variations relative to the bracketing standard IRMM-014, known to have the same isotopic composition as chondrite (Craddock and Dauphas, 2011), are reported according to the following equation:

$$\delta^{56}Fe = 1000 \times \left[\frac{\left(\frac{^{56}Fe}{^{54}Fe}\right)_{Sample}}{\left(\frac{\left(\frac{^{56}Fe}{^{54}Fe}\right)_{Standard\ 1} + \left(\frac{^{56}Fe}{^{54}Fe}\right)_{Standard\ 2}}{2}\right)} - 1\right] \quad (5.17)$$

5.6.3 Optimization

Various Cu solution concentrations were tested to optimize the signal stability (100 ppb, 150 ppb, 300 ppb and 1 ppm). Measurements show that a concentration of 1 ppm resulted in an optimal signal stability without saturating the Faraday cups (empiric limit at 20 V ppm^{-1} mL^{-1}). Measurements with a sample concentration below 1 ppm did not produce satisfactory results.

Iron isotopic measurements on the Thermo Scientific Neptune Plus revealed that the Ni doping of the fractions is inefficient for this study. It produces instability during the measurements, resulting in a higher error than for the uncorrected Fe isotopic ratios. The absence of elements other than Cu and Fe in the sulphides precludes any potential matrix effect. Furthermore, since the IEC has been performed twice to ensure high purity of the fraction, no element other than Fe and Cu has been detected in the standards using mass scan. Therefore, the uncorrected Fe isotopic ratios have been used for processing and interpretation.

5.7 Conclusions

Two different *in-situ* sampling techniques were tested: laser microtomy and drilling. The laser-based sampling method tested on a thin section proved to be inconvenient, as it requires a dedicated laser facility, as well as the transportation of the sample from the laser room to the chemistry laboratory, and the resin used for the thin section is especially challenging to handle. The drilling technique is significantly more convenient as it can be implemented directly in the chemistry laboratory, as long as all the exposed metal surfaces are protected against contamination and the drilling done in a dedicated room. Drilling can be carried out on a simple polished mount (Fig. 5.3). The powder obtained by drilling is easier to handle than a micrometer-sized piece of thin section. Therefore, drilling is preferred to laser cutting.

The isotope separation procedure preferred for sulphide processing is based on the method developed by Sossi et al. (2015) due to the use of the AG1-X8 resin. This resin is the most suitable medium due to its propensity to preferentially adsorb the elements of interest in this study (Table 5.3). However, in contrast to the original method, H_2O_2 was used during resin conditioning, sample loading as well as matrix and Cu elution to maintain Fe in an oxidized state (Fig. 5.1, Table 5.4). It was also observed that one chromatographic separation is not sufficient to obtain a satisfactory purity of the fractions and that a second is necessary. The fraction purity obtained after two chromatographic runs make the addition of a Ni spike unnecessary and even counterproductive, since it resulted in signal instability during the Fe measurements.

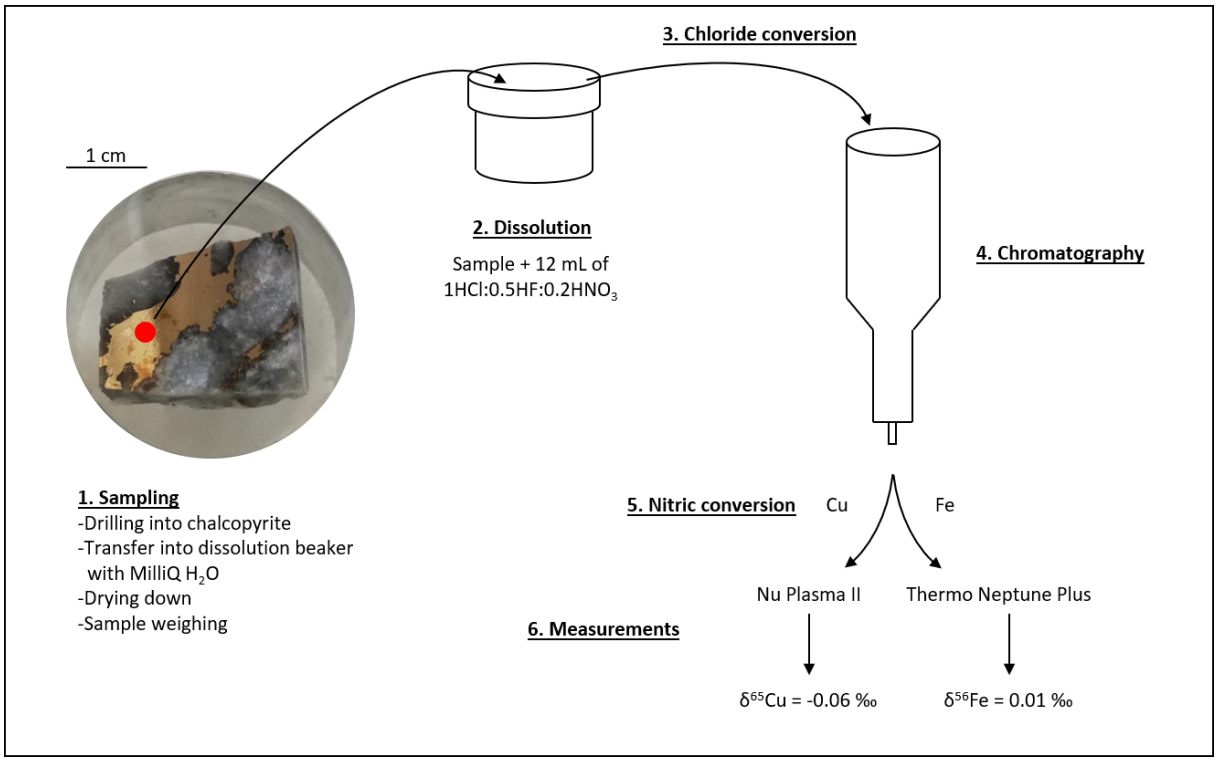


Figure 5.3: *Summary of the procedure, from sampling to measurement, for sulphide Cu and Fe isotopic ratio determination.*

The measurement of samples obtained exclusively by micro-drilling may not be able to detect the presence, or absence, of large-scale isotopic fractionation processes. It is therefore necessary for characterization of ore deposits by isotope ratio analysis to use these two sample types to obtain a comprehensive overview of all the chemical and physical processes involved in the development of mineralization.

Chapter 6

Copper and Iron Isotope Variations in Cu-sulphides from the Phalaborwa Carbonatite: A Fingerprint for Ore-Forming Processes

This chapter was submitted as a manuscript to *Mineralium Deposita* entitled "Cu and Fe isotope variations in Cu-sulphides from the Phalaborwa carbonatite: a fingerprint for ore-forming processes." by Loic Y. Le Bras, Robert Bolhar, Henriette Ueckermann, Paul A. M. Nex, Emmanuelle Albalat, Vincent Balter and Grant M. Bybee. Manuscript reference: MIDE-D20-00114.

6.1 Introduction

The Loolekop Cu-sulphide deposit in the PIC has been studied since the mid-20th century, but some aspects of ore crystallization/precipitation have remained poorly constrained (Forster, 1958; Lombaard et al., 1964; Groves and Vielreicher, 2001). For instance, despite recent suggestions of a mantle source for sulphide material, the final stages of the ore-forming process(es) remain unclear (Le Bras et al., 2020).

Stable isotope geochemistry has been used over the last two decades for the characterization of magmatic, hydrothermal and supergene processes (Larson et al., 2003; Graham et al., 2004; Lv et al., 2016). The development of high-precision analytical instrumentation, in particular MC-ICP-MS, combined with measurement techniques, such as standard-sample bracketing and the addition of double spike, has contributed to a significant increase in precision and accuracy (Maréchal et al., 1999; Peel et al., 2008; Dauphas et al., 2017; Moynier et al., 2017; Johnson et al., 2020). For standard-sample bracketing one single sample is measured between each standard.

Copper isotopes have been successfully used for twenty years in economic geology for ore deposit characterization (Maréchal et al., 1999; Graham et al., 2004; Mathur and Fantle, 2015; Moynier et al., 2017 and references therein). Isotopic fractionation related to redox reactions, sorption, aqueous complexation and weathering may be fingerprinted by Cu isotopic analysis. Several studies used Cu isotopes to examine the role of redox reactions in sulphide ore-forming processes since Cu isotope fractionation is diagnostic of fluid-induced chemical reactions (Markl et al., 2006a; Asael et al., 2009; Ikehata et al., 2011; Mathur et al., 2012; Mathur and Fantle, 2015). Likewise, the Cu isotope composition of a particular sulphide phase provides information about the physical and chemical conditions (such as the redox status of

base metal-bearing sulphide liquid or melt) at the time of sulphide crystallization (Lee et al., 2012). During redox reactions, Cu isotope fractionation is driven by changes in Cu oxidation state. For instance, Cu^{2+} preferentially mobilizes ^{65}Cu and is, therefore, heavier than Cu^{+}. As the Cu isotope composition of sulphides changes in response to variations in Cu oxidation state, it is possible to track the formation processes of sulphide ore deposits and their evolution over time. Copper isotope variations within different types of magmatic and high-temperature hydrothermal ore deposits have been investigated (Larson et al., 2003; Markl et al., 2006a; Ikehata et al., 2011; Zhao et al., 2019), enabling the discrimination of hypogene ($\delta^{65}Cu = 0.0 \pm 1‰$), supergene and secondary mineralization ($\delta^{65}Cu$ = -3 to more than 6‰, typically) (Fig. 6.1; Mathur and Fantle, 2015; Baggio et al., 2018). During supergene and alteration processes, Cu isotope fractionation is driven by changes in Cu redox state impacted by Eh-pH characteristics of the fluids involved (Asael et al. 2009).

Iron isotopes are also sensitive to changing redox conditions (Sossi et al., 2012; Zhao et al., 2019), although fractionation is more restricted relative to Cu. Iron isotopes effectively characterize kinetic (e.g. chemical diffusion; Schauble, 2004) and equilibrium (bonding difference-driven; Bilenker et al., 2016) isotope fractionation processes, including Rayleigh distillation (Dauphas et al., 2017) and several other geological processes, such as fluid exsolution (Poitrasson and Freydier, 2005), fractional crystallization (Dauphas et al., 2014; Foden et al., 2015) and partial melting (Weyer and Ionov, 2007; Dauphas et al., 2014). It may, therefore, be possible to characterize crystallization conditions, metasomatism and partial melting processes due to their influence on Fe redox states, and consequently, on Fe isotope ratios (Weyer and Ionov, 2007; Telus et al., 2012; Poitrasson et al., 2013). Since rocks possess specific $\delta^{56}Fe$ signatures, it is possible to identify the source material from which the rock is derived as well as the potential mixing processes of different components in a melt (Williams and Bizimis, 2014; Nebel et al., 2019). Iron isotopes are also useful for distinguishing compositional variations related to source heterogeneities in the mantle (Williams and Bizimis, 2014). Like Cu, Fe isotopes are particularly useful for the identification of ore-forming mechanisms of certain deposits, for instance, by being able to make the distinction between magmatic and hydrothermal ore crystallization/precipitation (Graham et al., 2004; Wawryk and Foden, 2015). Large variations of sulphidic Fe isotope compositions in different deposits of the same type indicate a strong influence of local geology, making it difficult to constrain a Fe isotope variation range for specific categories of ore-deposits (Fig. 6.2).

As there is a difference in the behaviour of Cu and Fe in terms of isotopic fractionation, a combination of the two will give a comprehensive dataset when applied to sulphide analysis for a better understanding of the ore-forming processes in the Loolekop Cu deposit.

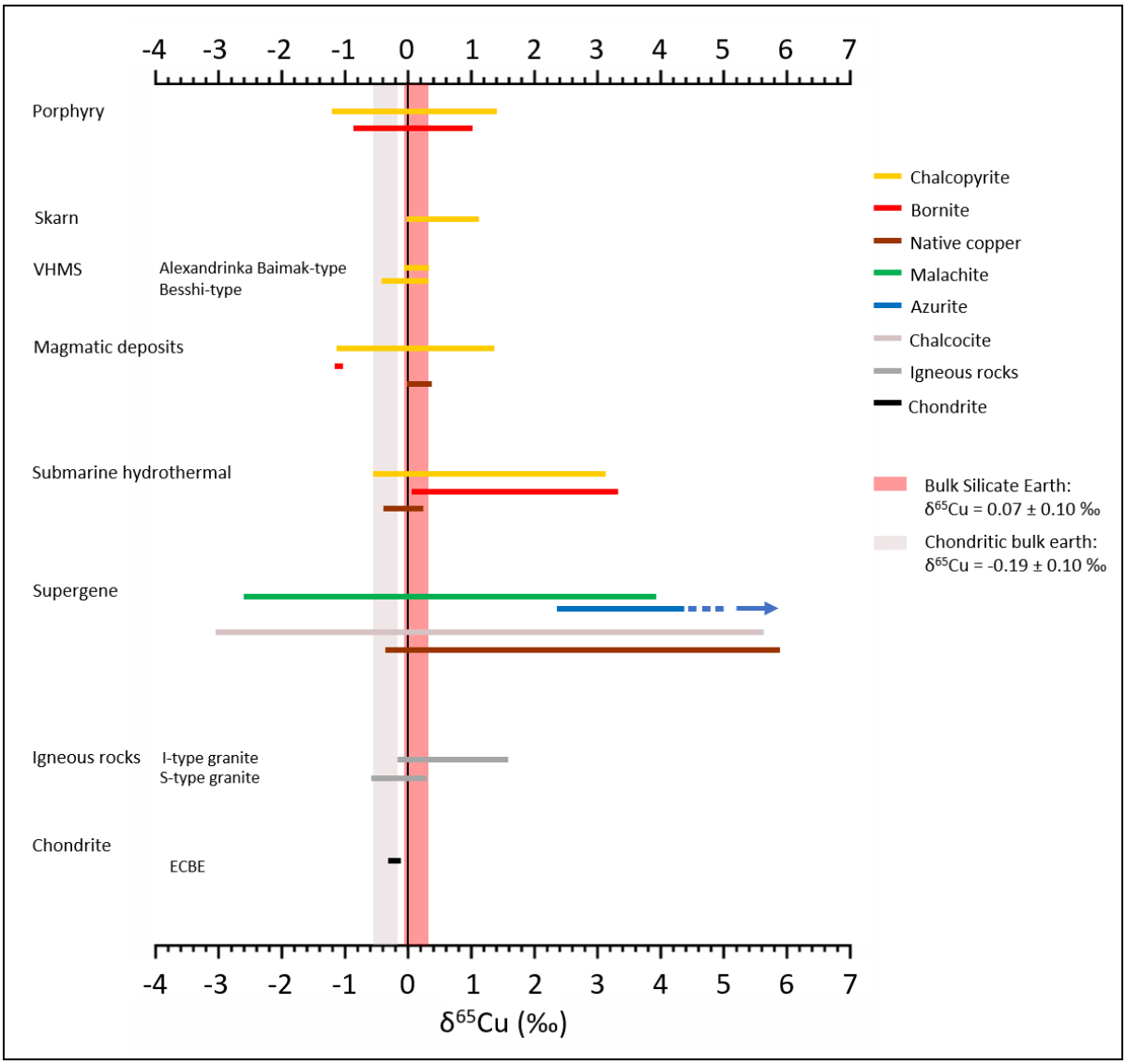


Figure 6.1: *Summary of $\delta^{65}Cu$ variations for different sulphide ore deposit types and locations worldwide as well as values for chondrites and Bulk Silicate Earth. Porphyry $\delta^{65}Cu$ values were published by Maréchal et al. (1999), Larson et al. (2003), Graham et al. (2004), Mathur et al. (2009, 2012) and Mirnejad et al. (2010). Skarn-type deposit $\delta^{65}Cu$ values were measured by Wang et al. (2017). Values of $\delta^{65}Cu$ values for Alexandrinka and Besshi Volcanic Hosted Massive Sulphide (VHMS) deposits were summarized from Mason et al. (2005) and Ikehata et al. (2011), respectively. Magmatic deposit $\delta^{65}Cu$ values were taken from Larson et al. (2003) and Zhao et al. (2019). Submarine hydrothermal $\delta^{65}Cu$ values were published by Zhu et al. (2000) and Rouxel et al. (2004). $\delta^{65}Cu$ variation for supergene minerals was published by Maréchal et al. (1999), Zhu et al. (2000), Larson et al. (2003), Mathur et al. (2009), Mirnejad et al. (2010) and Ikehata et al. (2011). Granite $\delta^{65}Cu$ values were published by Li et al. (2009). Enstatite Chondrite Bulk Earth (ECBE), Chondrite Bulk Earth (CBE) and Bulk Silicate Earth (BSE) $\delta^{65}Cu$ values were published by Savage et al. (2015).*

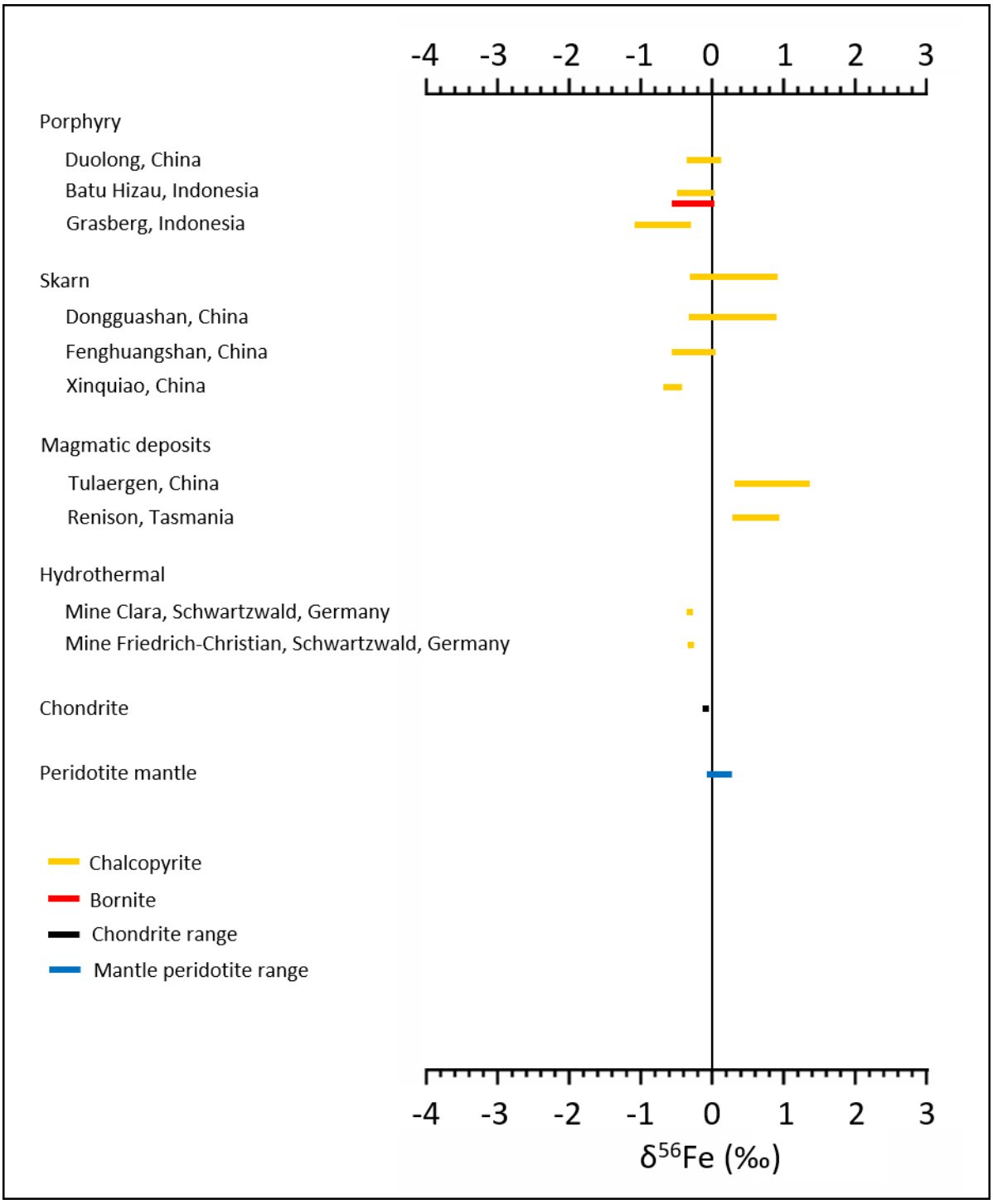


Figure 6.2: *Summary of $\delta^{56}Fe$ variations for different sulphide ore deposit types and locations worldwide as well as values for chondrites and mantle peridotites. Porphyry $\delta^{56}Fe$ values were published by Graham et al. (2004), Wawryk and Foden (2017) and J.-X. Li et al. (2018). Skarn-type deposit $\delta^{56}Fe$ values were measured by Wang et al. (2011, 2015). Values of $\delta^{56}Fe$ values for hydrothermal deposits were published by Markl et al. (2006b). Magmatic deposit $\delta^{56}Fe$ values were taken from Wawryk and Foden (2015) and Zhao et al. (2019). Chondrite $\delta^{56}Fe$ values were published by Poitrasson et al. (2004), Mullane et al. (2005), Needham et al. (2009), Craddock and Dauphas (2011) and Hezel et al. (2018). Peridotite mantle $\delta^{56}Fe$ values were summarized from Zhu et al. (2002), Beard and Johnson (2004), Williams et al. (2004, 2005), Weyer et al. (2005), Schoenberg and von Blanckenburg (2006), Weyer and Ionov (2007), Zhao et al. (2010, 2012), Huang et al. (2011) and Poitrasson et al. (2013).*

6.2 Methods

6.2.1 Sampling

Pieces of drill core were collected at the drill core yard of the Palabora Mining Company. These samples were selected according to their sulphide content. Care was taken to collect samples from all the rock types present in the Loolekop intrusion. Two different methods were used for sulphide sampling. The first method involved handpicking of sulphide assemblages from crushing pieces of drill core. The assemblages were subsequently examined under a binocular microscope to identify the sulphide phases and weighed. The second method involved *in-situ* drilling into polished epoxy mounts of sulphide-rich drill core pieces at 4000 rpm with a Dremel® 4000 drill and a 1 mm diameter diamond drill bit (Chapter 5). Microscopic observations before drilling helped to determine the nature of the sampled sulphide assemblage. To avoid any loss or contamination of material, the mounts were drilled through a MilliQ H_2O droplet placed on the spot of interest. After drilling, the MilliQ H_2O drop with powdered sulphide material was collected and the surface rinsed three times to ensure that all the drilled material was sampled. The resulting solution was dried down and the residue weighed. The diamond drill bit was cleaned in an ultrasonic bath for 30 min between samples and rinsed successively with MilliQ H_2O and acetone.

6.2.2 Chemical separation

Chemical processing took place in the ultra-clean, metal-free Wits Isotope Geoscience Laboratory (WIGL) in the School of Geosciences at the University of the Witwatersrand. The reagents used for both the dissolution and the IEC were made from double distilled Merck® acids and MilliQ H_2O 18.2 MΩ cm^{-1} (3 ppb TOC). The PFA dissolution beakers were cleaned successively with soapy MilliQ H_2O and 50% HNO_3 for 48 hours and 72 hours, respectively. Pipette tips, columns and centrifuge tubes were washed with 5% HNO_3. The samples were dissolved in 15 mL Savillex® PFA beakers with a mixture of 1HCl:0.5HF:0.2HNO_3 at concentrations of 10 mol L^{-1}, 23 mol L^{-1} and 12.5 mol L^{-1}, respectively. The beakers were left on a hotplate at 130°C for 48 hours. Heating was continued for an additional 36 hours if solid residue was visible at the bottom of the beaker. The samples were then evaporated to dryness, with the addition of 0.5 mL 12.5 mol L^{-1} HNO_3 every 4 to 6 hours to avoid the formation of insoluble fluorides. The samples were taken up in 10 mol L^{-1} HCl and dried down again, and were then dissolved with 1 mL of 6 mol L^{-1} HCl + 0.001% H_2O_2, heated at 35°C and left to cool. The element separation procedure of Cu and Fe from the matrix is based on the methods

described by Maréchal et al. (1999) and Sossi et al. (2015). The different steps of the ion exchange chromatography are summarized in Table 6.1. The ion exchange chromatography was performed under class 10 laminar air-flow conditions. The procedure used 10 mL capacity BioRad® Poly-Prep columns (0.8 x 4 cm) filled with 1 mL of analytical grade BioRad® AG1-X8 200-400 mesh resin, with 1.2 meq mL^{-1} capacity, in chloride form. To ensure the purity of the analyte fractions, the procedure was repeated once (Huang et al., 2017). After the second chromatography, the eluted fractions were collected in 25 mL PFA open beakers, evaporated to dryness, dissolved in 1 mL 12.5 mol L^{-1} HNO_3 + 0.001% H_2O_2 and dried down again. Both HNO_3 and H_2O_2 were added to ensure the removal of potential organic material from the resin. The fractions were then dissolved in 1 mL of HNO_3 of suitable molarity and diluted to a concentration appropriate for isotope ratio measurements.

Table 6.1: *Ion exchange chromatography procedure for separation of Cu, Fe and Zn for 1 ml of AG1-X8 (200-400 mesh) resin used with 0.8 X 7 cm columns.*

Step	Solvent	Volume of acid (ml)
Cleaning	3 mol L^{-1} HNO_3	10
Cleaning	Milli-Q H_2O	10
Cleaning & conditioning	6 mol L^{-1} HCl	10
Sample	6 mol L^{-1} HCl + 0.001% H_2O_2	1
Matrix elution	6 mol L^{-1} HCl + 0.001% H_2O_2	5
Cu elution	6 mol L^{-1} HCl + 0.001% H_2O_2	14
Fe elution	0.5 mol L^{-1} HCl + 0.001% H_2O_2	9
Zn elution	3 mol L^{-1} HNO_3	5

6.2.3 MC-ICP-MS measurements

The Cu isotopic compositions were measured on a Nu Plasma II MC-ICP-MS instrument at the University of Johannesburg. The Cu fractions were diluted to 1 ppm. The standard-sample bracketing method and an internal Ni correction were used to correct instrumental biases (Mason et al., 2004; Peel et al., 2008). The solution used for internal correction is a Ni standard from Inorganic Ventures™, which was added at the same concentration as the analyte. Prior to the measurement of both the standard and unknown samples, the background was measured at a half-mass offset from the peak position and subtracted from the peak. The NIST SRM-976 reference solution was used to normalize the ratios as described by equation 6.1:

$$\delta^{65}Cu = \left[\left({}^{65}Cu/{}^{63}Cu\right)_{Sample}/\left({}^{65}Cu/{}^{63}Cu\right)_{NIST\ SRM-976} - 1\right] \times 1000 \qquad (6.1)$$

The Fe isotopic compositions were performed using a Thermo Fisher Scientific Neptune Plus MC-ICP-MS at the Ecole Normale Supérieure de Lyon. The Fe fractions were dissolved

in 0.2% HNO_3 and diluted to a concentration of 1 ppm. The analysis was performed in wet plasma at medium resolution with Jet interface. The standard-sample bracketing method and an internal Ni correction were used to correct instrumental biases. No correction for Cr has been implemented. The IRMM-014 reference solution was used to normalize the ratios as described by equation 6.2:

$$\delta^{56}Fe = \left[\left({}^{56}Fe/{}^{54}Fe\right)_{Sample}/\left({}^{56}Fe/{}^{54}Fe\right)_{IRMM-014} - 1\right] \times 1000 \qquad (6.2)$$

Iron isotopic analysis yielded small errors (mean ± 2SD), an optimal correlation between $^{56}Fe/^{54}Fe$ and $^{57}Fe/^{54}Fe$ showing expected mass fractionation (Fig. 6.3), and an excellent reproducibility of the certified reference material (Table 6.2).

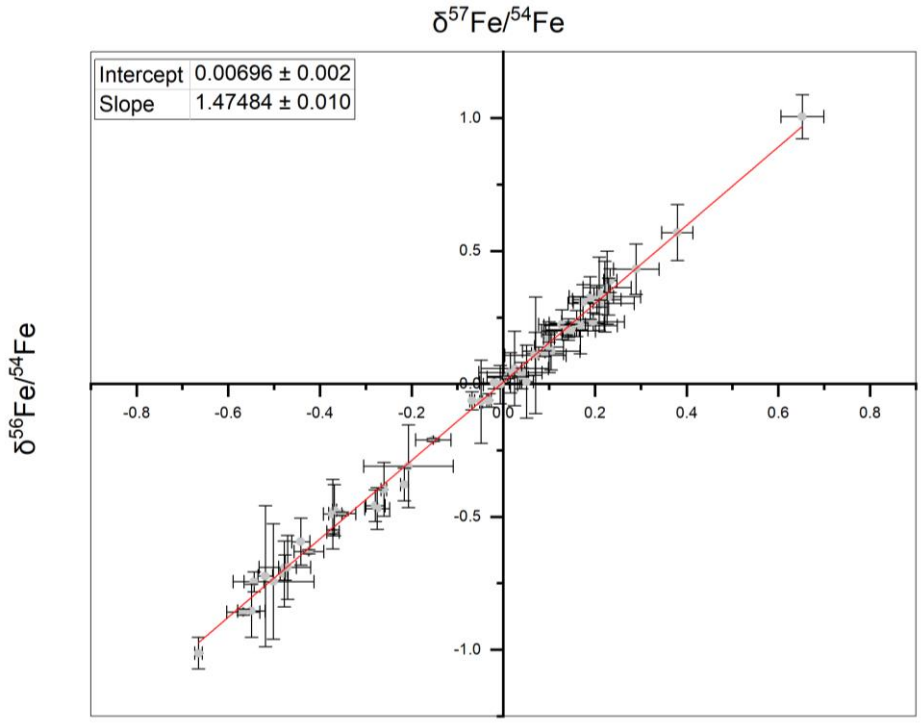


Figure 6.3: *Iron three-isotope plot of δ-values for sulphides. The slope is close to the theoric value (1.475). Uncertainties are ±2 SD.*

Table 6.2: *Measured Fe and Cu isotopic composition of geologic standards and comparison with the recommended values (Fe values from Craddock and Dauphas; 2011; Cu values from Sossi et al., 2015).*

Standard		δ^{56}Fe (‰) (n=2)	Error (±)	δ^{65}Cu (‰) (n=1)	Error (±)
BHVO-2	measured	0.13	0.05	0.14	-
	recommended	0.11	0.01	0.09	0.05
BIR-1a	measured	0.05	0.01	0.03	-
	recommended	0.05	0.02	-0.00	0.05
W2	measured	0.04	0.03	-	-
	recommended	0.06	0.01	-	-

6.3 Results

6.3.1 Mineral association

Microscopic observations reveal the presence of both primary and alteration-related sulphide phases. Two main types of primary sulphide assemblages are present in the Loolekop Pipe, namely magmatic and hydrothermal assemblages.

6.3.2 Magmatic and hydrothermal assemblages

The earliest primary magmatic sulphide phase occurs as two different assemblage types. The first assemblage is composed of banded carbonatite- and phoscorite-hosted bornite associated with chalcopyrite. Chalcopyrite can be found as lamellae or patches within bornite, sometimes occupying a significant part of the grain as well as disseminated grains within the gangue together with cubanite (Figs. 6.4a and 6.4b). Chalcopyrite laths and patches in bornite may be related to reheating of the pipe during emplacement of the transgressive carbonatite or hydrothermal fluid circulation (Cabri et al., 1973). The amount of bornite and chalcopyrite varies significantly among the samples. Both phases are disseminated within the host rock and are mostly absent along fractures or veins within the transgressive carbonatite. This feature indicates that the disseminated sulphides may have formed during emplacement of the phoscorite-banded carbonatite sequence, hence they are interpreted as magmatic (Le Bras et al., 2020). These sulphides show a preferential association with phoscorite- and banded carbonatite-hosted cumulates composed of magnetite and minor apatite and silicates, which may be related to combined magmatic flow and density contrasts during the simultaneous emplacement of both banded carbonatite and phoscorite. The size of the sulphide assemblages is variable and ranges from 10 µm to one cm.

The second primary magmatic sulphide type is composed of mm- to cm-wide hydrothermal chalcopyrite veins crosscutting/intruding the transgressive carbonatite, but also the other rock types of the Loolekop Pipe to a smaller extent. These veins indicate (i) the

occurrence of a structural event postdating the emplacement of banded carbonatite and phoscorite (Basson et al., 2017) and (ii) a subsequent fluid circulation episode followed by the precipitation of chalcopyrite along fractures. A previous study reported m-wide hydrothermal vein networks, mainly present in the centre of the intrusion (Palabora Mining Company Ltd Staff, 1976). Cubanite exsolutions and phases associated with vein-hosted chalcopyrite (Figs. 6.4c and 6.4d) are an indicator of chalcopyrite precipitation from a high-temperature hydrothermal fluid. The veins also host very rare pyrite (up to 200 μm; Fig. 6.4d).

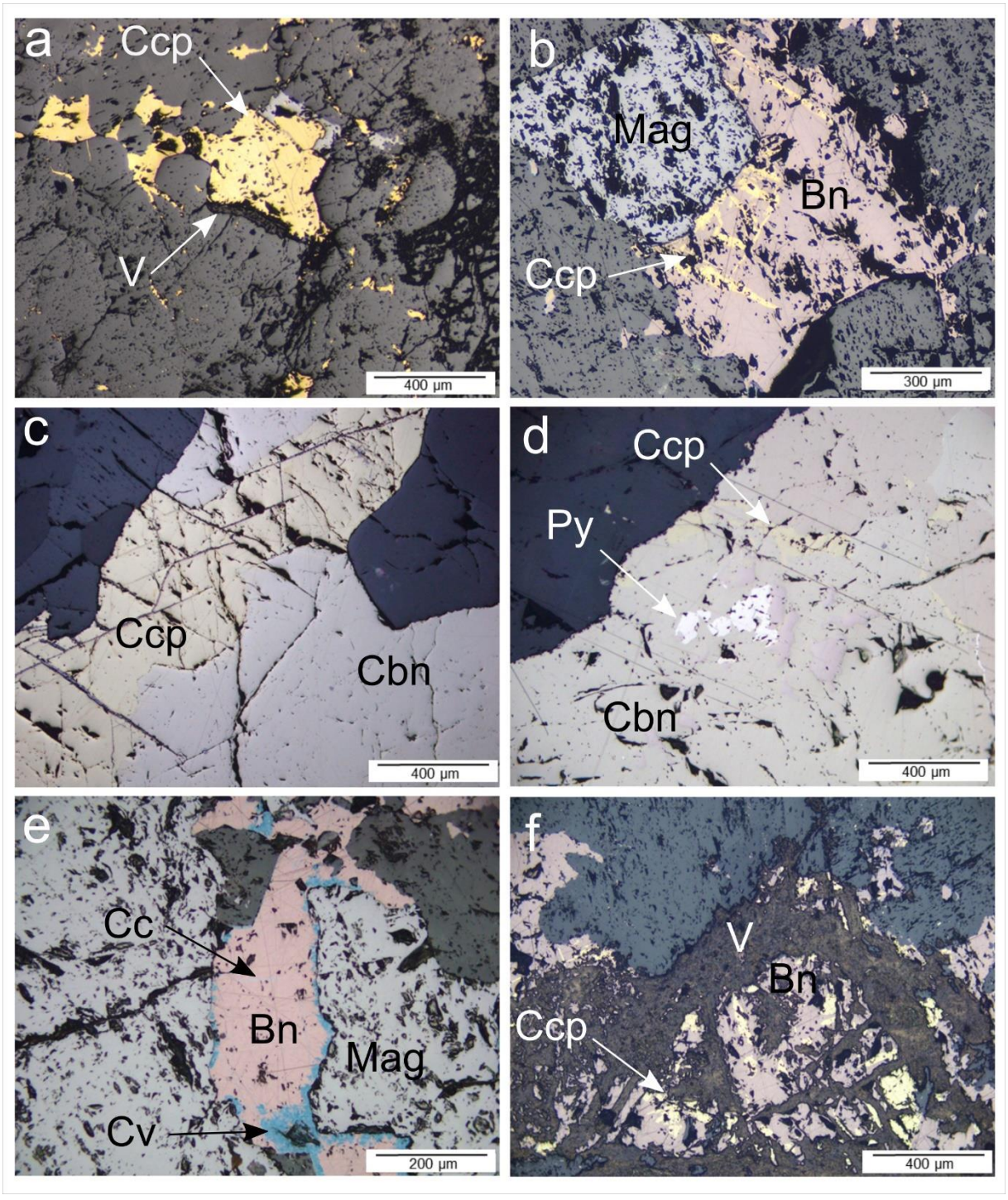


Figure 6.4: *Photomicrographs of the different sulphide phases present in the Loolekop Pipe. Bn=bornite, Py=pyrite, V=valleriite, Cbn=cubanite, Cc=chalcocite, Cv=covellite, Mag=magnetite. (a) and (b) Primary magmatic chalcopyrite and chalcopyrite-bornite assemblages, disseminated into carbonate gangue and associated with Fe-oxides in both the phoscorite and the banded carbonatite. (c) and (d) Hydrothermal vein-hosted sulphide assemblages composed of chalcopyrite and cubanite (c). These veins may locally host pyrite (d). (e) Alteration of bornite as thin veinlets of chalcocite and covellite replacement at the outer edges of the mineral. (f) Alteration of primary bornite-chalcopyrite assemblage and replacement by late-stage valleriite.*

6.3.3 Alteration phases

Two types of Cu-sulphide alteration can be observed in the Loolekop Pipe. The first one consists of local replacement of primary banded carbonatite- and phoscorite-hosted bornite by chalcocite in veinlets within the primary magmatic assemblage (Fig. 6.4e). Chalcocite and covellite are also present along the edges of bornite grains in variable amounts. Such textures fluid-aided alteration of the magmatic phases postdating the precipitation of primary sulphides and emplacement of banded carbonatite and phoscorite. The main secondary Cu-sulphide alteration phase is valleriite [$(Fe^{2+},Cu)_4(Mg,Al)_3S_4(OH,O)_6$] that precipitated in veins within all the rock types. Valleriite is present within and around primary sulphides and magnetite as a replacement phase, as well as along fractures within the host rock (Fig. 6.4f). The alteration is often intense and left barely recognizable relics of the primary bornite and chalcopyrite.

6.3.4 Copper isotopes

The Cu isotope compositions of sulphides are reported in Tables 6.3 and 6.4 as well as in the Appendix J and displayed in Fig. 6.5. The δ^{65}Cu variations do not seem to be related to mineral assemblages. Results for drilled and separate micro-samples are described below.

6.3.4.1 Sulphide separates

The δ^{65}Cu values for the sulphide separates from phoscorite, banded carbonatite and transgressive carbonatite range from -0.64 to 0.39‰. The values cluster mainly between -0.5 and -0.3‰ (Fig. 6.5a). A less well-defined abundance peak occurs between -0.2 and 0.4‰ (Fig. 6.5a). The Cu isotopic ratios do not seem to be dependent on the sulphide textures. Chalcopyrite values range from -0.64 to 0.39‰, while bornite values are -0.59, -0.39, -0.38, -0.16 and 0.05‰ (Table 6.3).

Table 6.3: *Cu and Fe isotopic compositions of different sulphide separates from the Loolekop Pipe sampled from whole-rocks. Sulphides are abbreviated as bn = bornite, ccp = chalcopyrite, v = valleriite.*

Sample n°	Rock type	Sulfide	Texture	δ^{65}Cu (‰)	2SD	n	δ^{56}Fe (‰)	2SD	n
9	PC[a]	Bn	Vein-hosted	0.05	0.08	3	-0.50	0.09	2
		Ccp	Disseminated	0.31	0.07	3	0.09	0.04	2
		Ccp	Disseminated	0.39	0.08	4	-0.05	0.00	2
13	TC[b]	Ccp	Vein-hosted	0.34	0.18	4	-0.26	0.01	2
21	BC/PC[c]	Ccp	Disseminated	-0.08	0.00	3	0.14	0.05	2
		Ccp	Disseminated	-0.13	0.16	3	0.17	0.08	2
25	BC	Bn	Disseminated	-0.59	0.02	3	0.07	0.01	2
		Ccp	Disseminated	-0.64	0.11	3	-0.03	0.01	2
27	BC	Ccp	Disseminated	0.22	0.03	3	0.22	0.08	2
		Ccp	Disseminated	0.19	0.13	4	0.19	0.00	2
33	BC	Ccp	Disseminated	-0.31	0.07	3	0.38	0.03	2
		Ccp	Disseminated	-0.11	0.09	4	0.15	0.02	2
36	BC	Bn	Disseminated	-0.38	0.10	2	-0.07	0.01	2
		Ccp	Disseminated	-0.46	0.15	2	0.23	0.01	2
41	BC	Ccp	Disseminated	-0.39	0.09	2	0.16	0.06	2
		Ccp	Disseminated	-0.48	0.05	3	-0.02	0.03	2
		Ccp	Disseminated	-0.30	0.18	4	0.02	0.07	2
42	BC	Ccp	Vein-hosted	-0.49	0.02	2	-0.22	0.01	2
		Ccp	Vein-hosted	-0.01	0.24	4	-0.37	0.02	2
43	BC	Bn	Disseminated	-0.16	0.14	4	-0.55	0.03	2
		Ccp	Disseminated	-0.08	0.05	3	0.21	0.01	2
51	TC	Ccp	Vein-hosted	-0.49	0.05	2	-0.28	0.01	2
		Ccp	Vein-hosted	-0.46	0.04	3	-0.35	0.01	2
58	TC	Ccp	Vein-hosted	-0.40	0.04	2	-0.57	0.02	2
		Ccp	Vein-hosted	-0.46	0.05	3	-0.66	0.00	2
		Ccp	Vein-hosted	-0.30	0.02	3	-0.48	0.03	2
		Ccp	Vein-hosted	-0.39	0.01	3	-0.42	0.02	2

[a]Phoscorite
[b]Transgressive carbonatite
[c]Banded carbonatite

6.3.4.2 *In-situ* drilling

Magmatic chalcopyrite disseminated in carbonate gangue shows a wide range of Cu isotopic compositions, from -1.21 to 0.76‰; (Fig. 6.5b and Table 6.4). There is no correlation between δ^{65}Cu values and textures or mineral assemblage. A single sample shows internal isotopic fractionation between two distinct phases, with one phase characterized by δ^{65}Cu = 0.05‰ and the adjacent one by δ^{65}Cu = -1.21‰. Hydrothermal sulphide Cu isotope values range widely (δ^{65}Cu = -0.73 to 0.55‰). Sulphides in the three polished mounts show spatial variation in Cu isotope compositions (Fig. 6.5b). Samples were collected both by drilling directly into a hydrothermal vein-hosted sulphide (-0.73‰) as well as into phases in immediate proximity. The area adjacent to the hydrothermal vein is further named transition zone. Sulphides from the transition zones were collected by drilling into two different mounts (0.19 and 0.31‰ for the first one; 0.42 and 0.55‰ for the second) in the same area of the vein network. Late-stage valleriite occurs as a replacement product of primary sulphides. The drilled valleriites show similar δ^{65}Cu signatures to primary sulphides indicating an absence of Cu isotope fractionation during the alteration process (Fig. 6.5b).

Table 6.4: *Cu and Fe isotopic compositions of sulphides in the Loolekop Pipe drilled into polished mounts from different assemblages. Sulphides are abbreviated as bn = bornite, ccp = chalcopyrite, v = valleriite.*

Sample n°	Rock type	Sulfide	Texture	δ^{65}Cu (‰)	2SD	n	δ^{56}Fe (‰)	2SD	n
6	PC[a]	Ccp	Dispersed	0.76	0.01	3	-0.15	0.04	2
9	PC	Bn	Vein-hosted	0.19	0.01	3	-0.44	0.02	2
		Ccp	Vein-hosted	0.31	0.04	3	-0.37	0.00	2
		V	Late-stage	0.31	0.02	3	0.10	0.03	2
13	TC[b]	Bn	Vein-hosted	0.55	0.03	3	-0.54	0.02	2
		Ccp	Vein-hosted	0.42	0.04	3	-0.47	0.02	2
		V	Late-stage	0.36	0.06	3	-0.21	0.10	2
18	BC[c]	Ccp	Dispersed	0.05	0.07	2	-0.01	0.04	2
21	BC/PC	Ccp	Dispersed	-0.06	0.06	2	0.01	0.05	2
25	BC	Ccp	Dispersed	-0.73	0.13	2	0.02	0.07	2
27	BC	Cbn	Dispersed	-1.21		1	0.21	0.07	2
		Ccp	Dispersed	0.05	0.14	2	0.23	0.01	2
33	BC	Ccp	Dispersed	-0.45	0.01	2	0.23	0.05	2
51	TC	Ccp	Vein-hosted	-0.73	0.01	2	-0.37	0.01	2

[a]Phoscorite
[b]Transgressive carbonatite
[c]Banded carbonatite

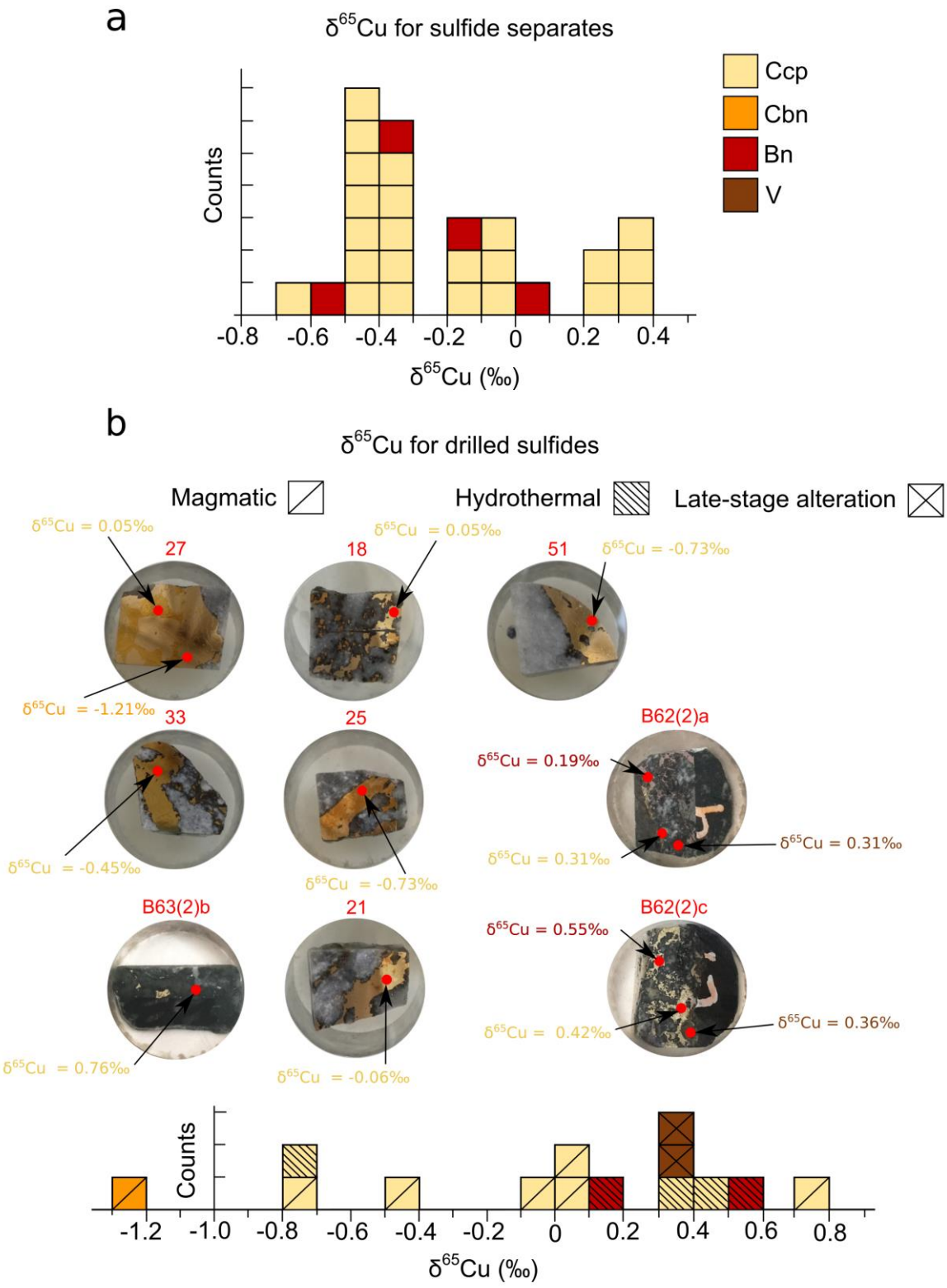


Figure 6.5: *Cu isotopic compositions. (a) Histogram showing Cu isotopic compositions of sulphide separates. (b) Copper isotopic composition of magmatic, hydrothermal and late-stage alteration sulphides sampled by drilling into polished mounts.*

6.3.5 Iron isotopes

Iron isotope analysis was also performed on both drilled and hand-picked Cu-sulphides (Fig. 6.6, Appendix J). Additionally, whole-rock powdered samples and magnetite separates from different rock types were included for Fe isotope measurements. Copper and Fe isotopic ratios do not show any correlation with either mineral separates or drilled samples (Tables 6.3 and 6.4).

6.3.5.1 Whole-rock analysis

The Fe isotopic ratios of the four rock types of the Loolekop Pipe can be divided into two groups (Table 6.5). The first group, including banded carbonatite, phoscorite and micaceous clinopyroxenite, is slightly enriched in heavy isotopes and exhibits little variation in δ^{56}Fe (0.04 to 0.14‰; Fig. 6.6a and Table 6.5). The second group includes only transgressive carbonatite, which is significantly enriched in ^{54}Fe relative to the three other rock types (-0.27‰).

Table 6.5: *Fe isotopic compositions of the different rock types of the Loolekop Pipe.*

Sample n°	Rock type	δ^{56}Fe (‰)	2SD
1	BC[a]	0.04	0.00
4	TC[b]	-0.27	0.03
10	PC[c]	0.14	0.01
15	MP[d]	0.10	0.06

[a]Banded carbonatite
[b]Transgressive carbonatite
[c]Phoscorite
[d]Micaceous clinopyroxenite

6.3.5.2 Sulphide separates

Iron isotope compositions of sulphides show significant variation (δ^{56}Fe = -0.66 - 0.38‰; Fig. 6.6a and Table 6.3). The distribution of Fe isotope ratios defines two groups of δ^{56}Fe for chalcopyrite (-0.66 to -0.22‰ and -0.07 to 0.38‰). Bornite δ^{56}Fe values are also concentrated in two clusters, overlapping with values for chalcopyrite, specifically at -0.55 and -0.50‰ for the negative cluster (cluster A) and -0.07, 0.07 and 0.16‰ for the cluster approaching zero (cluster B). No correlation of δ^{56}Fe with the sulphide assemblage types can be observed. However, sulphides with negative δ^{56}Fe values overlap with values for transgressive carbonatite, while sulphides plotting from near-zero to slightly positive δ^{56}Fe-values overlap with the values measured for banded carbonatite, phoscorite and micaceous clinopyroxenite.

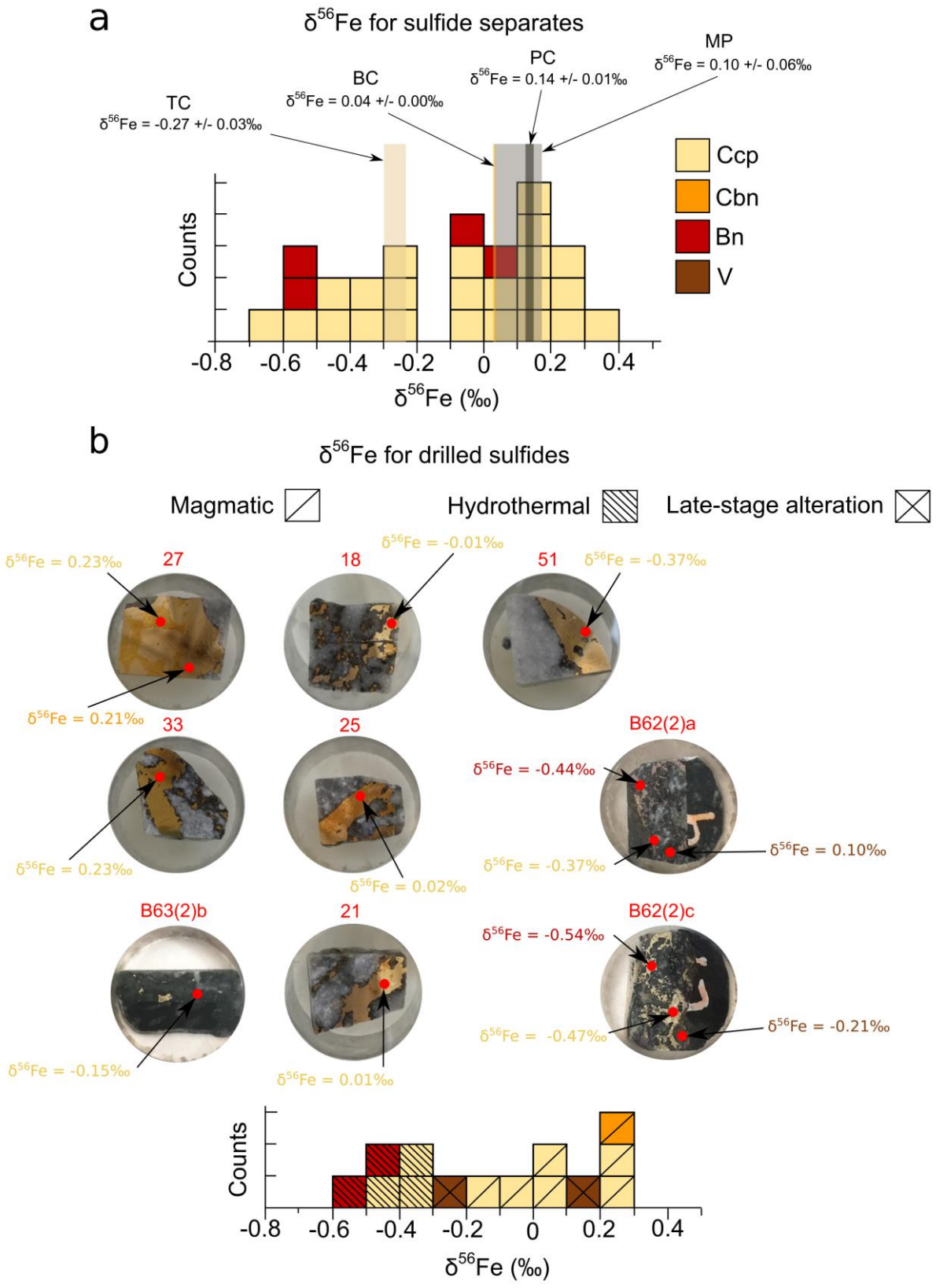


Figure 6.6: *Fe isotope ratio analyses. (a) Histogram showing Fe isotopic compositions of sulphide separates as well as whole-rocks. (b) Iron isotopic compositions of magmatic, hydrothermal and late-stage alteration sulphides sampled by drilling into polished mounts.*

6.3.5.3 *In-situ* drilling

Sulphide assemblages do not appear to be correlated with the Fe isotopic composition of sulphides. However, there is a clear influence of the mineralization type (magmatic, hydrothermal, late-stage alteration). Disseminated grains of magmatic chalcopyrite in carbonates are slightly enriched in heavy Fe isotopes with δ^{56}Fe ranging from -0.01 to 0.23‰, with one exception at -0.15‰ (Fig. 6.6b). The large magmatic, two-phase sulphide grain has a homogeneous Fe isotopic composition (δ^{56}Fe = 0.23 and 0.21‰), which contrasts with the significant Cu isotope fractionation. Both hydrothermal bornite and chalcopyrite from the transition zone have δ^{56}Fe values clustering between -0.37 and -0.54‰. The Fe isotopic composition is homogeneous and does not show significant spatial variations between different areas of the stockwork. Contrary to Cu, Fe isotopic compositions of secondary valleriite do not reflect the composition of the parent sulphide, as shown by *in-situ* Fe isotope analysis of valleriite and adjacent magmatic sulphides (Fig. 6.6b and Table 6.4).

6.3.5.4 Magnetite separates

Magnetite separates from transgressive carbonatite, banded carbonatite, phoscorite and micaceous clinopyroxenite have homogeneous Fe isotopic compositions (Table 6.6). The isotopic ratios cluster within a relatively narrow range of values, slightly enriched in heavy isotopes (δ^{56}Fe = 0.07 - 0.29‰).

Table 6.6: *Fe isotopic composition of magnetites (Mag) sampled in the different rock types of the Loolekop Pipe. Rock types are abbreviated as banded carbonatite = BC, phoscorite = PC and transgressive carbonatite = TC.*

Sample n°	Rock type	Mineral	δ^{56}Fe (‰)	2SD
29	BC[a]	Mag	0.20	0.05
35	TC[b]	Mag	0.14	0.06
37	BC/PC[c]	Mag	0.29	0.05
44	PC	Mag	0.17	0.02
45	BC	Mag	0.20	0.07
46	PC	Mag	0.10	0.01
59	BC	Mag	0.07	0.07

[a]Banded carbonatite
[b]Transgressive carbonatite
[c]Phoscorite

6.4 Discussion

Textural observations suggest the presence of several sulphide assemblage types implying the presence of multiples cycles of Cu-sulphide crystallization/precipitation. The use of combined Cu and Fe isotopes aims to identify the sulphide material source and characterize the successive ore-forming processes.

6.4.1 Partial melting and mantle origin

Whole-rock Fe isotope compositions for banded carbonatite, phoscorite and micaceous clinopyroxenite overlap the average composition of mantle rocks (0.002 ± 0.224‰; Beard and Johnson, 2004; Schoenberg and von Blanckenburg, 2006; Weyer et al., 2005; Williams et al., 2005; Weyer and Ionov, 2007; Dauphas et al., 2009a; Zhao et al., 2010, 2012, 2015; Huang et al., 2011; Craddock et al., 2013; Williams and Bizimis, 2014). The whole-rock Fe isotope composition for these three rock types also reflects the Fe isotopic composition of both gangue minerals (oxides, silicates) and sulphides. Since the transgressive carbonatite is almost exclusively composed of calcite and dolomite, whole-rock Fe isotope compositions are largely controlled by these sulphide-free minerals. Conversely, the Fe isotope composition is strongly influenced by Cu-sulphides if present. The heavy Fe isotope enrichment of phoscorite and micaceous clinopyroxenite relative to the average mantle composition is related to small degrees of partial melting of the mantle (Williams et al., 2005; Weyer and Ionov, 2007; Dauphas et al., 2014; Foden et al., 2018), and to the modal abundance of Fe-oxides and silicates in these rocks. Iron isotope fractionation is directly controlled by the initial Fe^{3+}/Fe^{2+} ratio and the degree of partial melting. A small degree of partial melting produces strong isotopic fractionation since heavy Fe isotopes preferentially partition into the melt, due to the higher incompatibility and isotopic mass of Fe^{3+} when compared to Fe^{2+} (Schoenberg and von Blanckenburg, 2006; Dauphas et al., 2009a). This may explain the enrichment in heavy isotopes in the banded carbonatite, phoscorite and micaceous clinopyroxenite. According to Le Bras et al. (2020), the low PGE contents in the different sulphide phases confirm this hypothesis. Another possible mechanism for the enrichment of the Loolekop rocks in heavy Fe isotopes may be partial melting of an oxidized source. Several studies suggested the presence of a metasomatized sub-continental lithospheric mantle beneath the Kaapvaal Craton (Kobussen et al., 2009; Hanger et al., 2015; Bolhar et al., 2020). Metasomatism may explain melt oxidation as the cause for the enrichment in heavy Fe. Considering the results of Bolhar et al. (2020) and Le Bras et al. (2020), it is likely that both events occurred in tandem.

6.4.2 Hypogene origin and isotopic fractionation between primary sulphides

Normalized Cu isotopic ratios overlap with the magmatic-hydrothermal/hypogene range (-1 to 1‰; Figs. 6.1, 6.4 and 6.5; Larson et al., 2003; Graham et al., 2004; Mirnejad et al., 2010; Mathur et al., 2012), suggesting that Cu-sulphide mineralization within the Loolekop Pipe is not related to supergene processes. Globally, low-temperature isotopic fractionation processes are characterized by significant δ^{65}Cu variations (-16.5 to 9‰; Maréchal et al., 1999; Zhu et al., 2000; Larson et al., 2003; Mathur et al., 2009; Mirnejad et al., 2010; Ikehata et al., 2011), indicating that (i) the sulphide phases from the Loolekop Pipe formed at high- or medium-temperatures (350 to 600°C) and (ii) sulphide assemblages were not affected by postdating major isotopic fractionation processes.

The Fe isotopic ratios of sulphide separates define two clusters (A and B) independent of the ore-assemblage (Fig. 6.6a). The first cluster overlaps with the transgressive carbonatite Fe isotopic composition (cluster A), while the second one is similar in its Fe isotopic composition to the banded carbonatite, phoscorite and micaceous clinopyroxenite (cluster B). The two clusters document distinct Cu-sulphide-forming processes. The similar Fe isotope composition between sulphides and banded carbonatite, phoscorite, and micaceous clinopyroxenite, to a larger extent (cluster B), further indicates that such sulphides were not affected by any late, low-temperature fractionation process(es) after the system became closed with regard to isotopic exchange. Consequently, their initial Fe isotopic composition was preserved.

Dispersed sulphide assemblages appear to be specific to banded carbonatite- and phoscorite-hosted Cu mineralization based on petrographic evidence, and are enriched in heavy Fe isotopes. This observation is consistent with the existence of a distinct data cluster representing the banded carbonatite, phoscorite and micaceous clinopyroxenite (cluster B). Such a feature confirms the magmatic nature of dispersed sulphides within phoscorite and banded carbonatite. Their Fe isotope composition exhibits a mantle signature and suggests isotopic equilibration at depth without any effects from postdating fractionation processes. Vein-hosted sulphides (cluster A) differ from the dispersed phases (cluster B) by slight enrichment in ^{54}Fe, suggests a distinct mineralization process when compared to dispersed sulphides.

Considering the significant variation of δ^{65}Cu in the sulphides, which correlates with neither δ^{56}Fe values nor the mineralization type, it seems that a specific isotopic fractionation process occurred either during or after the formation of Cu-sulphides. It has been established that Cu isotope fractionation is strongly influenced by the redox state of Cu (Asael et al., 2009;

Lv et al., 2016; Moynier et al., 2017; Kim et al., 2019). Moreover, irrespective of detailed studies on the oxidation state of Cu in chalcopyrite, the valence of Cu in this and other phases remains debatable (Folmer and Jellinek, 1980; Goh et al., 2006; Pearce et al., 2006). The complexity of the sulfide assemblages, combined with potential variations in the Cu valence in Cu-sulphides postdating the isotopic closure of the system, may explain the large variation of Cu isotope compositions and the absence of correlation between sulphide type and Cu isotopic ratios. The Fe-S bond is stronger than the Cu-S bond in sulphides, making Cu isotope fractionation more sensitive to physical and chemical changes in the environment (Bachinski, 1969). Hence, the Fe isotopic signature may be preserved during redox processes due to its robustness, explaining the absence of correlation between the measured Fe and Cu isotope distributions. The formation of intricate bornite-chalcopyrite assemblages related to the reheating of the pipe by the emplacement of transgressive carbonatite may have been responsible for the significant variations of Cu isotope compositions in the primary phase.

6.4.3 Hydrothermal assemblage source and formation processes.

Hydrothermal vein-hosted chalcopyrite shows significant ^{54}Fe isotope enrichment (Fig. 6.6b). Three scenarios may explain this feature. The first scenario involves the leaching of a large, deep-seated iss phase, which may have crystallized synchronously with bornite and chalcopyrite, followed by reprecipitation of mobilized material into chalcopyrite along fractures forming Cu-sulphide veins. The second scenario involves the leaching of a significant amount of deep-seated primary magmatic assemblages. However, when comparing the proportions of primary magmatic with hydrothermal assemblages, leaching would have required an excessive amount of sulphide. Such amounts are not observed in either banded carbonatite or phoscorite. This would suggest a massive settling of magmatic assemblages at depth. The third option would involve massive leaching and breakdown of deep-seated magnetite. However, textural evidence regarding this scenario remains elusive. The preferential mobilization of Fe^{2+}, which naturally tends to be a light Fe isotope carrier, would have produced an isotopically light, Fe-bearing fluid from which ^{54}Fe-enriched chalcopyrite and cubanite were precipitated along large veins within the pipe (Polyakov and Mineev, 2000; Rouxel et al., 2003; Debret et al., 2016). The greater abundance of magnetite relative to magmatic sulphides within the Loolekop Pipe suggests that this is the most likely scenario (Palabora Mining Company Ltd Staff, 1976; Vielreicher et al., 2000). In this configuration, the involvement of oxidizing fluids can be ruled out since such fluids precipitated sulphides enriched in heavy Fe isotopes and appear to be

contradictory to the conclusion made by Le Bras et al. (2020). It is more likely that several fluids have been involved.

Copper and Fe isotope compositions of sulphides in the transition zone between hydrothermal veins and the host rock reveal several important features. Their negative δ^{56}Fe values (Fig. 6.6b) are similar to those in massive hydrothermal vein-hosted chalcopyrite and suggest that both assemblages precipitated from an isotopically similar hydrothermal fluid. Such observations explain the presence of bornite with negative δ^{56}Fe values (Fig. 6.6b), which overlap with the Fe isotope composition of transgressive carbonatite (Tables 6.4 and 6.5). Results also show that bornite-chalcopyrite assemblages can precipitate during the hydrothermal stage of sulphide crystallization/precipitation (Figs. 6.4b and 6.5b, Table 6.4). Despite the fact that the assemblages are typical of primary sulphides, their proximity to hydrothermal veins and their isotopic composition indicate their hydrothermal origin.

6.4.4 Fluid circulation and valleriite formation

Copper-sulphide assemblage textures show that valleriite is the result of primary sulphide alteration, most likely related to fluid circulation (Lombaard et al., 1964; Palabora Mining Company Ltd Staff, 1976; Milani et al., 2017a, b; Le Bras et al., 2020). This is indicated by the presence of valleriite veins within the gangue (Fig. 6.4f). The small surface of pure valleriite exposed within the mounts made the sampling difficult. Drilling into polished mounts after microscopic observations led to the discovery of primary sulphide phases entirely replaced by secondary valleriite (Figs. 6.4b and 6.5b). Results reveal similar δ^{65}Cu values for valleriite and spatially associated, unaltered primary sulphides, indicating the absence of fractionation during secondary processes. Since it is known that Cu isotope fractionation during leaching of chalcopyrite is negligible (Albarède, 2004), a similar isotopic signature would confirm petrographic observations, implying that valleriite results from the *in-situ* replacement of primary sulphides. The absence of analytically resolvable fractionation during bornite leaching indicates a restricted influence of the late-stage oxidizing fluid on the isotope composition of valleriite. Due to the chemical composition of valleriite, fluids may have circulated through the different rocks of the Loolekop Pipe, dissolving dolomite, calcite and magnetite and causing the enrichment of fluids in Mg and Al. Fluid circulation in the surrounding micaceous clinopyroxenite is also a likely scenario. Two valleriite samples analyzed in this study may be the result of chalcopyrite alteration, which would explain the absence of Cu isotope fractionation during replacement. However, since the spots have been chosen to be as primary sulphide-free as possible, it is not possible to identify the precursor phase for valleriite alteration.

6.4.5 Origin of magnetite

Magnetite has similar Fe isotopic composition compared to primary magmatic sulphides and whole-rock banded carbonatite, phoscorite and micaceous clinopyroxenite (Tables 6.5 and 6.6). This indicates a magmatic origin of the Fe-oxide mineralization (Günther et al., 2017; Milani et al., 2017a). Near-mantle isotopic values suggest that magnetite may not be the result of the oxidation of a Fe-rich phase during ascent of melt(s) and emplacement of the Loolekop Pipe, but was rather formed shortly after partial melting in an oxidizing environment, while the system was still being supplied with magma. If no exchange between the melt and the mantle existed, and if the melt pulse was already ascending into the pipe during crystallization of magnetite, the Fe isotopic composition of both the melt(s) and magnetite would have been significantly different from mantle values. Two important conclusions can be drawn. Firstly,

the melt(s), which gave rise to phoscorite and banded carbonatite, were mantle-derived as suggested in previous studies (Milani et al., 2017a; Bolhar et al., 2020). Secondly, the presence of very early-crystallized magnetite suggests that differentiation of phoscorite and banded carbonatite may have been related to magma flow (Basson et al., 2017).

6.4.6 Model for Cu mineralization

A previous PGE and trace element study of Cu-sulphides indicated that the formation of an iss-mss system was critical to Cu-sulphide mineralization in the Loolekop pipe (Le Bras et al., 2020). This model suggests (i) the transformation of a Cu-rich sulphide liquid into an iss, (ii) the exsolution from the latter of a second Cu-rich sulphide liquid forming the magmatic assemblages, followed by (iii) remobilization of the iss by a hydrothermal fluid and the precipitation of chalcopyrite along veins, and finally (iv) the alteration of magmatic and hydrothermal Cu-minerals and their replacement by valleriite. Formation of primary magmatic sulphides can be explained by the separation of the mantle-derived Cu-, Fe- and S-bearing immiscible liquid during its ascent and the emplacement of banded carbonatite and phoscorite into the Loolekop Pipe (Fig. 6.7a; Ebel and Naldrett, 1997). During cooling, the liquid may have precipitated bornite and an iss phase at 600°C (Fig. 6.7b; Cabri et al., 1973). The presence of isolated chalcopyrite can be explained by co-precipitation, during further cooling, of bornite, chalcopyrite as well as an iss (Fig. 6.7c; Sugaki et al., 1975). Such a genetic model for magmatic sulphide formation is in accordance with the absence of Fe isotope fractionation relative to mantle values. The iss may have subsequently transformed into a multi-phase sulphide assemblage composed of cubanite and chalcopyrite accompanied by strong Cu isotope fractionation between these two minerals (Figs. 6.4b and 6.6c). Contrary to conclusions based on trace element and platinum-group element geochemistry (Le Bras et al., 2020), a new model is proposed concerning the precipitation of chalcopyrite along hydrothermal veins. The hypothesis of iss remobilization by hydrothermal fluids and the precipitation of chalcopyrite within a stockwork remains possible, but considering the significant amount of hydrothermal chalcopyrite relative to primary mineralization, the source might be different from the iss (Hanekom et al., 1965; Palabora Mining Company Ltd Staff, 1976; Vielreicher et al., 2000). Leaching and breakdown of magnetite is a plausible option considering the importance of hydrothermal mineralization. However, remobilization by high-temperature magmatic fluids of both primary magmatic phases and magnetite is the most likely scenario (Polyakov and Mineev, 2000; Rouxel et al., 2003). Variations of Fe and Cu isotope compositions in valleriite relative to primary sulphides suggest alteration by late-stage fluids. Conservation of the Cu isotopic

signature of parent sulphides and the presence of significant variations in Fe isotopic composition suggest the intervention of Fe-bearing fluids, which may have caused changes of isotopic compositions, the variability of which may be controlled by the intensity of the alteration.

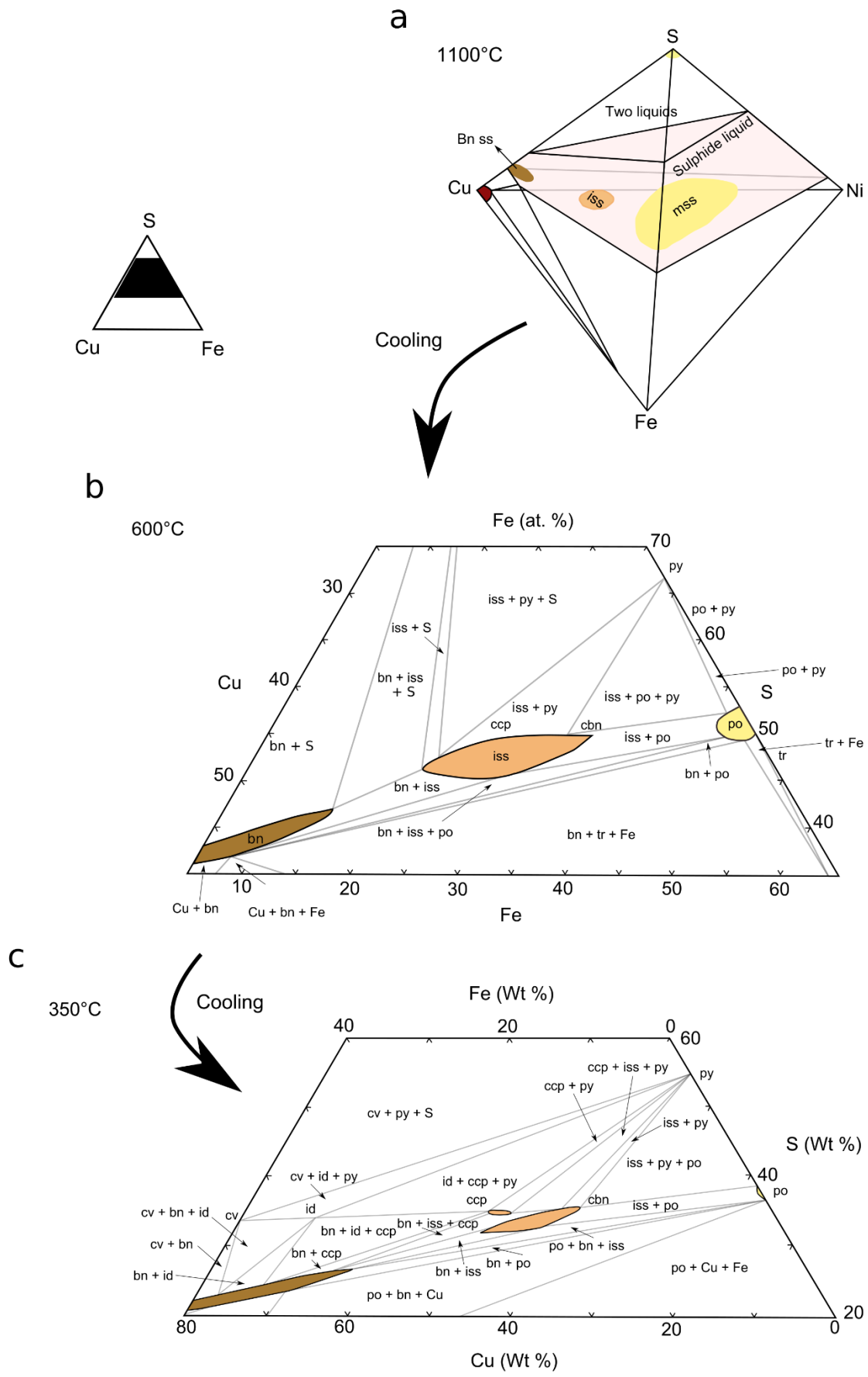


Figure 6.7: *Evolution of sulphide phases in the Cu-Fe-S system during cooling of a sulphide liquid, with a focus on the central portion of the Cu-Fe-S system. The sulphide liquid at the origin of the monosulphide solid solution (mss) and intermediary solid solution (iss) also crystallized directly as bornite (bn), chalcopyrite (ccp), pyrrhotite (po), pyrite (py), troilite (tr) and cubanite (cbn), mostly as complex assemblages. Modified after Ebel and Naldrett (1997) (a), Cabri (1973) (b) and Sugaki et al. (1975) (c).*

6.5 Conclusions

Copper and Fe isotope compositions of primary sulfides range from -1.21 to 0.76 ‰ and -0.55 to 0.38 ‰, respectively, suggesting a magmatic/hydrothermal origin of the mineralization without any alteration caused by circulation of late, oxidizing (supergene) or reducing fluids, also consistent with primary sulphide textures (sections 3.4.1 and 3.4.2). Moreover, δ^{56}Fe values of both primary sulphides (-0.1 to 0.4‰) and banded carbonatite, phoscorite and micaceous clinopyroxenite (from 0.04 to 0.10‰) overlap with typical mantle values (0.002 ± 0.224‰; Johnson et al., 2020), suggesting a mantle origin of both the primary sulphide material and the rocks of the Loolekop Pipe. Considering the higher resilience of the Fe isotopic system relative to Cu isotopes due to stronger Fe-S bonds compared to Cu-S bonds in sulphide structures, Fe isotopic signatures of primary sulphides appear to have remained unaffected by fractionation after the development of magmatic mineralization comprising dispersed sulphides.

Slight enrichment in heavy Fe isotope in magmatic sulphide assemblages, combined with the presence of dispersed chalcopyrite, chalcopyrite-bornite and chalcopyrite-cubanite assemblages in banded carbonatite and phoscorite, points to early cogenetic precipitation of bornite, chalcopyrite and an iss phase, which evolved independently from each other during the emplacement of the rocks and the cooling of the pipe. The near-zero δ^{65}Cu values of pure isolated chalcopyrite in the gangue indicate that chalcopyrite formed at the same time as both the bornite and the iss phase and was not affected by post-crystallization fractionation processes. The iss phase may have evolved into a chalcopyrite-cubanite assemblage during further cooling of the system prior to the intrusion of transgressive carbonatite. Highly variable δ^{65}Cu values contrast with relatively uniform δ^{56}Fe values. Such features suggest the occurrence of redox-related isotopic fractionation affecting sulphides phases, like chalcopyrite/bornite exsolution or replacement. The reheating of the Loolekop Pipe through emplacement of transgressive carbonatite or high-temperature hydrothermal fluid circulation was probably responsible for the exsolution of chalcopyrite from bornite or replacement of bornite by chalcopyrite leading to significant Cu isotope fractionation.

The negative δ^{56}Fe values of both hydrothermal vein-hosted chalcopyrite and chalcopyrite-bornite assemblages, which precipitated in proximity to the vein itself, suggest that such assemblages are the result of sulphide precipitation along fractures within the Loolekop Pipe. High-temperature fluids may have reacted with deep-seated magnetite, triggering its breakdown and the preferential remobilization of isotopically light Fe^{2+} into

hydrothermal fluids, from which ^{54}Fe-enriched chalcopyrite precipitated. Precipitation of chalcopyrite also requires the leaching of deep-seated primary Cu-sulphides.

Valleriite does not show any variability in δ^{65}Cu as compared to texturally-adjacent sulphides. The circulation of a high-temperature fluid along fractures also appears unlikely due to the strong influence of such fluids on Cu isotopic composition. Valleriite most likely resulted from fluid-induced alteration and replacement of magmatic and hydrothermal sulphide assemblages.

Chapter 7
Discussion and Conclusions

This chapter summarizes the results and discussions of previous Chapters 3, 4 and 6 and presents a revised metallogenetic model.

7.1 Methods and tools

Several methods used in this study required development and optimization due to the nature and complexity of the sulphide assemblages on the Loolekop Pipe of the Phalaborwa Igneous Complex. Copper and Fe isotope analysis require spatially resolved sampling of Cu-sulphides. It was therefore necessary to develop a new versatile sampling technique and implement an ion exchange chromatography procedure for Cu and Fe separation suitable for Cu-sulphide processing (Sections 5.3 to 5.6; Fig. 5.3).

Two *in-situ* sampling methods were tested: (i) laser cutting of sulphide phases in thin sections (Section 5.3.1) and (ii) polished mount drilling with a Dremel® tool (Section 5.3.2). Laser cutting was shown to be impractical due to the need of a specific facility separated from the chemistry lab itself, and the increased the risk of contamination by external material during sample transfer. Moreover, sampling time is particularly long due to the use of low energy (50% output) and frequency (12 Hz) for the laser to avoid melting of the sample surface, potentially causing isotopic fractionation. Therefore, drilling into sulphide-rich pieces of drill core mounted into epoxy resin was the preferred method. Tests did not reveal contamination from the drill bit (Section 5.3.2). Prior to drilling, a drop of MilliQ H_2O was placed on the sulphide of interest on the surface of the polished mount to trap the powder sample into a liquid phase, drastically reducing risks of contamination and simplifying sample handling.

Sulphides typically have a high content in the elements of interest (Cu and Fe), and therefore may pose problems when being processed due to a significant risk of resin saturation during ion exchange chromatography which may produce isotopic fractionation during elution. Therefore, such samples require careful handling during elemental separation (Section 5.5). The procedure implemented for Cu-sulphide processing uses 1 mL AG1-X8 (200-400 mesh) resin in BioRad polyprep columns (0.8 x 4 cm) (Table 5.4). The elution scheme is based on the procedure published by Sossi et al. (2015), modified to keep Fe in an oxidized form by adding H_2O_2 at 0.001% to the acids during early phases of IEC, thus optimizing Fe retention in the resin. The use of limited volumes of acid for the IEC lowers the blank level and reduces running costs. The use of the AG1-X8 resin was the decisive criterion for the use of this procedure. This

resin has the highest D_{Fe}/D_{Cu} ratio for HCl at a concentration between 5 and 7 mol L^{-1}, and is therefore the most suitable for the separation of Fe and Cu (Table 5.3, van der Walt et al., 1985).

Despite a sulphide-dedicated setup, the sampling method described in Sections 5.3 to 5.5 suffers from some limitations. In case of complex sulphide assemblages, the exact nature of the drilled material cannot be determined with certainty since mineral interrelations below the sample surface are not observable (Figs. 6.4 and 6.5). It may produce erroneous calculations for the determination of the suitable amount of material for ion exchange chromatography, potentially causing resin saturation.

7.2 Copper-sulphide classification

A careful observation of mineral associations and textures by optical microscopy, MLA and microCT allowed the identification of magmatic, hydrothermal and secondary Cu-sulphides (Sections 3.3.1, 3.3.2 and 4.4).

7.2.1 Magmatic assemblages

Early Cu-sulphide phases are isolated in both banded carbonatite and phoscorite within the Loolekop Pipe. MicroCT results revealed that they form sub-vertical layers parallel to banded carbonatite and phoscorite (Fig. 4.6). Three main textures were observed in these layers with (i) sub mm dispersed bornite and chalcopyrite, (ii) mm to cm elongated sulphide aggregates and (iii) mm-wide sulphide cumulates (Figs. 3.1 to 3.3, 4.3 to 4.6).

Dispersed bornite grains often host chalcopyrite, either as lamellae or patches (Figs. 3.1a, 3.2, 3.3, 4.3a, 4.3b, 4.4c and 4.4d). The size of these assemblages is highly variable and ranges from 10 µm to 500 µm, according to microscopic observations and mineral maps. Bornite can be observed together with chalcocite (Figs. 4.5c and 4.5d). The latter occurs either as veinlets within the bornite grains or as an alteration phase replacing bornite along the edges of the assemblages associated with covellite (Fig. 3.1b). Chalcopyrite may occur as disseminated grains within the gangue, like bornite (Figs. 4.4a). Some chalcopyrite veinlets (~10 µm wide) may occur between gangue minerals, associated with the dispersed sulphide phases (Figs. 4.3c and 4.3d). Rare chalcopyrite and cubanite assemblages can be observed dispersed within the gangue (Figs. 4.4f and 4.5a). They form separated phases in a single grain (Figs. 6.4b and 6.5b). The grain observed in this study has a diameter of up to several cm, with chalcopyrite and cubanite having a diameter of several mm.

Elongate sulphide assemblages show an irregular surface (Fig. 4.6b), suggesting that they result from the merging of dispersed sulphides. Such aggregates are composed of both bornite

and chalcopyrite as shown by microCT analysis results (Appendix I). Their elongation axis is parallel to the sulphide layer plane. Unfortunately, the resolution of microCT does not allow detailed identification of sulphide assemblages (Fig. 4.2). However, the fact that such assemblages may result from the clustering of dispersed sulphide phases suggests a mineralogical makeup similar to dispersed grains.

Only one occurrence of magmatic sulphide cumulate was observed in this study and is exclusively composed of chalcopyrite (Fig. 4.6a; Appendix I). The irregular shape of the contact between cumulate and gangue indicates that its formation is similar to elongated aggregates.

7.2.2 Hydrothermal mineralization

Hydrothermal assemblages are characterized by chalcopyrite veins hosted by a vast fracture network within the core of the Loolekop Pipe, mainly in the transgressive carbonatite (Figs. 3.1d, 3.1e, 3.1f and 4.6c). However, such veins may also be present in banded carbonatite and phoscorite, and may extend towards the pipe boundaries. Veins observed in this study may reach a cm-scale width (Figs. 3.1d, 3.1e, 3.1f). The contact between the veins and the host rocks ranges from sharp to gradational. A typical gradational transition is characterized by a dense network of small (10 – 100 μm) veinlets filled by chalcopyrite and bornite. The transition zones observed in this study range from 1 to 2 cm wide.

Cubanite is frequently associated with chalcopyrite, either as exsolution lamellae or as a large and discrete phase in hydrothermal veins (Figs. 3.1d and 3.1e). Such phases may have a diameter of several mm. Some rare pyrite and pyrrhotite occur in the veins, as inclusions in chalcopyrite and at the margins of different vein-hosted sulphide phases (Fig. 3.1f).

7.2.3 Late-stage alteration phases

Textures and mineral associations in all the rock types of the Loolekop Pipe show a late-stage alteration phase that developed after formation of both magmatic and hydrothermal sulphides, in the form of valleriite [$(Fe^{2+},Cu)_4(Mg,Al)_3S_4(OH,O)_6$]. Flow textures indicate the involvement of fluids in the ore-forming process (Fig. 3.3). Valleriite is systematically present as small-grained crystals (Figs 3.1c and 4.6d). Despite the occurrence of such alteration within the whole intrusive pipe, large parts of magmatic and hydrothermal mineralization remain intact (Figs. 4.6a, 4.6b and 4.6c). According to microscopic observations and MLA, two different types of valleriite seem to exist within the Loolekop Pipe. One type represents an association of valleriite with magmatic and hydrothermal sulphides along small fractures and at their boundaries (Figs. 3.3 and 6.3f). Another type is characterized by the presence of valleriite along

fractures in the gangue (Fig. 4.3b). However, microCT results do not show traces of valleriite along major fractures within the gangue (Appendix I), suggesting that such valleriite veinlets form exclusively in the immediate proximity of primary sulphides.

The presence of valleriite in veins in the different rock types around magmatic and hydrothermal sulphide assemblages suggests the occurrence of a structural event postdating the hydrothermal cycle and allowing late-stage fluids to circulate into the pipe. Such veins also indicate that valleriite precipitated from dissolved material along fractures (Figs. 3.1c, 4.3b and 6.3f). The absence of large valleriite veins in banded carbonatite and phoscorite as shown by microCT results indicates that valleriite veins are the result of a local process occurring in the proximity of primary sulphides.

7.3 A revised model

The results and conclusions of Chapters 3, 4 and 6 are combined as a revised model for Cu mineralization within the Loolekop Pipe based on sulphide textures, trace and platinum-group element contents, and Cu and Fe isotope compositions of the sulphides.

7.3.1 Mantle source, partial melting and intrusive processes

Low PGE contents (Appendix F) and near-mantle Fe isotope composition (δ^{56}Fe between 0 to 0.4‰; Tables 6.3 and 6.4) of banded carbonatite- and phoscorite-hosted Cu-sulphide phases reveal a mantle origin of the Cu mineralization, involving low-degree partial melting, according to a calculated fractionation model driven by the redox state of Fe (± 10%; Dauphas et al., 2017).

According to Rudashevsky et al. (2004), Cu-sulphides hosted in both banded carbonatite and phoscorite are associated with minor amounts of sperrylite ($PtAs_2$). The presence of this Pt-arsenide, combined with a Pt depletion relative to Pd in sulphide phases, suggests early complexation of Pt with As.

The Loolekop Pipe shows sub-vertical alternation of banded carbonatite and phoscorite (Fig. 7.1). The preferential emplacement of phoscorite along the edges of the Loolekop Pipe (Fig. 2.2), together with a progressive transition from phoscorite along the contact with micaceous clinopyroxenite to banded carbonatite towards the core of the intrusion, suggests that these two rocks resulted from immiscibility during the ascent and emplacement of several magma pulses, combined with a rotation/torsion of the intrusive volume (Krasnova et al., 2004b; Basson et al., 2017; Barbosa et al., 2020). This phenomenon may be related to depressurization during the magma ascent (Giebel et al., 2019), followed by rotational magma

flow inducing preferential emplacement of higher density rocks along the outer parts of the pipe. Basson et al. (2017) suggested that the pipe underwent torsion of the intruding volume related to the intersection of structural features that were rotated relative to one another. Such a mechanism may have caused the structural assembly of the banded carbonatite – phoscorite sequence.

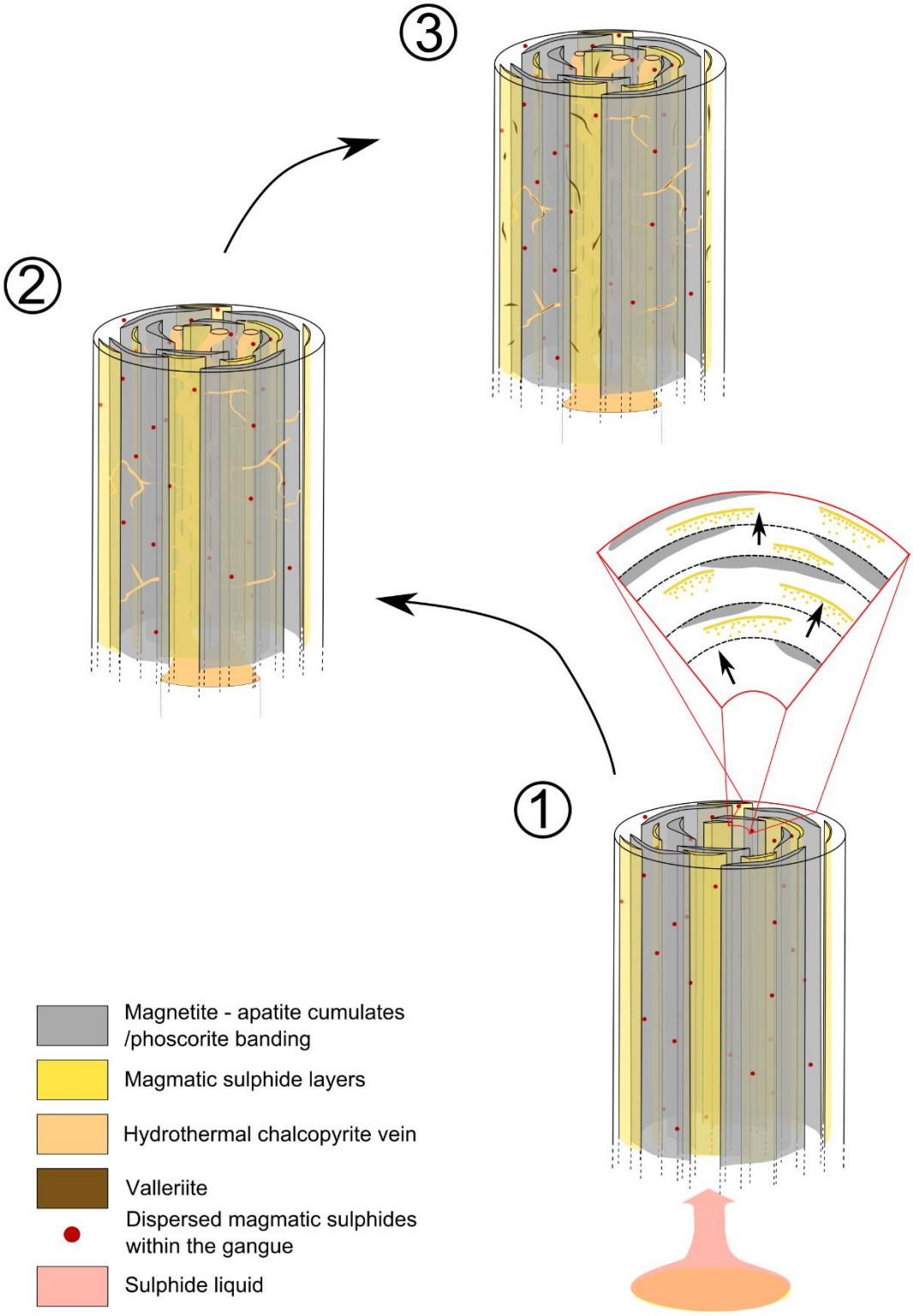


Figure 7.1: *Simplified model illustrating the various ore-forming processes for Cu-sulphides in the Loolekop Pipe.*

7.3.2 Early sulphide formation mechanisms

The enrichment of PPGEs over IPGEs in Cu-sulphides indicates the presence of an mss – iss system (Section 3.4.2; Figs. 3.7 and 3.9). It is proposed that during the ascent a sulphide liquid formed an IPGE-enriched mss and a Cu-rich sulphide liquid, the latter forming the Cu-mineralization in the Loolekop Pipe during further ascent and cooling of the system (Cabri, 1973; Sugaki et al., 1975). The similar Fe isotope compositions of all the banded carbonatite- and phoscorite-hosted sulphide phases suggest their co-precipitation during ascent and cooling of the pipe (Fig. 6.6). Bornite and an iss phase may have precipitated at high temperature (600°C), evolving to the co-precipitation of bornite, chalcopyrite and iss at lower temperatures (350°C) (Section 6.4.2; Fig. 6.7). The precipitated iss phase evolved during further cooling forming chalcopyrite-cubanite aggregates, but also chalcopyrite and (rare) cubanite grains (Cabri, 1973; Fleet, 2006). It was suggested in Section 3.4.2 that a sulphide liquid may have exsolved from a massive iss phase and formed phoscorite- and banded carbonatite-hosted bornite and chalcopyrite. However, light Fe isotope signatures of hydrothermal chalcopyrite reveal the absence of this phase since it would have resulted in a much higher Cu content in hydrothermal sulphides (Section 6.4.3, Fig. 6.6).

As revealed by microCT analysis, banded carbonatite- and phoscorite-hosted Cu-sulphide assemblages are present as sub-vertical layers within the host rock (Fig. 7.1). These layers have different Cu-sulphide modal proportions and differ texturally from one to another, suggesting the involvement of several sulphide liquids of distinct chemical composition (Fig. 6.7; Cabri, 1973). Alternating banded carbonatite, phoscorite and sulphide bands indicate the successive emplacement of magma pulses, each carrying a compositionally distinct sulphide liquid.

An interesting observation concerns the primary Cu-sulphide mineralization within the Loolekop Pipe and the presence of primary bornite. In other Cu-sulphide deposits, bornite is the outcome of a chalcopyrite transformation by retrograde reaction (Cawthorn and Meyer, 1993). The presence of chalcopyrite lamellae in bornite is consistent with the formation of primary bornite from a Cu-rich sulphide liquid and the exsolution of chalcopyrite from bornite, or the replacement of bornite by chalcopyrite by a low-temperature (~150°C) retrograde reaction (K. Li et al., 2018), most likely related to the emplacement of transgressive carbonatite and/or the circulation of high-temperature hydrothermal fluids in the Loolekop Pipe. As a matter of fact, this may have caused reheating of the Loolekop Pipe and the exsolution or replacement of chalcopyrite (Durazzo and Taylor, 1982; K. Li et al. 2018). The presence of isolated chalcopyrite in the gangue may also be the result of the total replacement of bornite by

chalcopyrite during retrograde reaction, i.e., not exclusively direct precipitation from the Cu-rich sulphide liquid (Figs. 4.3c and 4.3d).

Variable Cu isotope compositions of primary sulphide phases suggest operation of post-crystallization isotopic fractionation processes (Sections 6.4.3 and 6.4.4; Fig. 6.5). The absence of correlation between Cu and Fe isotope ratios and the small variations in Fe isotope compositions indicate a fractionation process that was short and occurred over a limited T range (Figs. 6.4 and 6.5). In fact, the Fe isotopic system is more resistant than Cu in sulphides to physical and chemical changes in the environment, explaining the observed variations in isotopic composition (Bachinski, 1969). The different Cu isotope signatures may be related to the exsolution of chalcopyrite from bornite and/or the replacement of bornite by chalcopyrite as well as the evolution of the iss to cubanite and chalcopyrite.

7.3.3 A complex hydrothermal ore-forming process

It was initially suggested that hydrothermal chalcopyrite veins resulted in the re-precipitation of dissolved material derived from primary sulphide leaching, which would have remained at depth (Section 3.4). However, when comparing the amount of primary sulphides to chalcopyrite veins (Appendices C and D), it is very unlikely that primary sulphides represent a volume large enough to form chalcopyrite by dissolution – re-precipitation. The light Fe isotope composition of hydrothermal sulphides rather suggests reaction of high temperature fluids with magnetite, triggering its breakdown and the preferential remobilization of light Fe, which subsequently precipitated as chalcopyrite along a large vein network within the core of the pipe (Fig. 6.6). The large amount of magnetite available in the Loolekop Pipe and the light Fe isotope composition of hydrothermal chalcopyrite (δ^{56}Fe from -0.8 to -0.3‰) support this interpretation (Appendix J) (Johnson et al., 2020). Leaching of magmatic Cu-sulphide phases may have contributed to the formation of hydrothermal mineralization by increasing the dissolved Cu budget. Leaching of magnetite and magmatic Cu-sulphide phases at depth is therefore the most likely source of dissolved hydrothermal chalcopyrite-forming material. However, this hypothesis involves gravity settling of banded carbonatite- and phoscorite-hosted magmatic phases before the solidification of the system. The presence of cubanite exsolution lamellae in chalcopyrite veins indicates high-temperature fluid circulation (Ramdohr, 1969). It is therefore very likely that fluids are of magmatic origin.

7.3.4 Late stage alteration

Textures and mineral assemblages suggest that in the Loolekop Pipe valleriite is the result of the alteration of magmatic and hydrothermal sulphides (Figs. 3.1 to 3.3, 4.3b and 4.6d). However, the presence of valleriite along fractures within the host rocks in the proximity of primary sulphides indicates limited remobilization of sulphide material by late stage fluids and subsequent re-precipitation (Figs. 3.3c, 4.3b and 4.6d). Similar Cu isotope composition of primary sulphides and valleriite confirm that the latter formed by alteration and eventual replacement of magmatic and hydrothermal sulphide phases (Fig. 6.5). Iron isotope compositions of valleriite and primary sulphide are significantly different (Fig. 6.6). Since Cu isotopes are more responsive than Fe to redox processes in sulphide systems (Bachinski, 1969), this difference may imply the presence of Fe of different isotopic composition in the alteration fluids, combined with heterogeneous alteration intensity affecting primary sulphide phases within the Loolekop Pipe. The association of valleriite with magnetite suggests that alteration of magmatic and hydrothermal sulphides by late-stage fluids may have resulted in the formation of valleriite and magnetite through desulphurization by fluids of the primary Cu-sulphide phases (Figs. 3.3c to 3.3f, 4.5a to 4.5c). However, the observation that magnetite is not always present indicates circulation of several late-stage fluids, some of which triggers the exclusive replacement of primary sulphide by valleriite without any trace of isotope fractionation.

7.4 Perspectives

The presence of several sulphide liquids and sub-vertical alternation of phoscorite and banded carbonatite units suggests the involvement of several magma pulses and indicates similar emplacement processes for phoscorite and carbonatite in the Loolekop Pipe, the Kovdor Complex (Krasnova et al., 2004a), as well as the Salitre Complex (Barbosa et al., 2020). With the exception of the rotational movement interpreted to have affected the Loolekop Pipe, formation of the phoscorite – carbonatite complex appears to be similar at these intrusions. Likewise, a mantle origin of the carbonates and phoscorite forming-material is established by similar PGE concentrations for Primitive Mantle and Loolekop rocks. The high PGM contents within the Kovdor complex also indicate a mantle origin (Bulakh et al., 1998; Rudashevsky et al., 2004). Similarly, the Loolekop Pipe hosts a classic phoscorite – carbonatite sequence (Russell et al., 1954).

What makes the Loolekop Pipe unique is the presence of both magmatic and hydrothermal Cu-sulphides of economic significance. Copper-sulphides have also been observed within the Salmagorskii Ring Igneous Complex carbonatite, but appear to be both

secondary in nature and occurring in small amounts (Korobeinikov et al., 1998). Considering the classic emplacement process of the phoscorite – carbonatite sequence within the Loolekop Pipe and the presence of magmatic Cu-sulphides hosted in these rocks, it seems that Cu was most likely derived from partial melting of a heterogeneous mantle. Partial melting may have mobilized a sulphide phase significantly enriched in Cu, which may have crystallized phoscorite- and banded carbonatite-hosted sulphide assemblages.

The most unusual feature of the Cu-sulphide phases within the Loolekop Pipe appears to be the possible leaching of both sub-vertical magmatic sulphide and magnetite layers, and the subsequent precipitation of chalcopyrite along fractures in the core of the pipe. Various studies reported hydrothermal sulphides resulting from leaching of disseminated magmatic sulphides (Fontboté et al., 2017; Hu et al., 2020), non-sulphide minerals (Li et al., 2019; Liu et al., 2019) or large rock volumes, accompanied by base metal-enrichment of hydrothermal fluids (Walter et al., 2019). This feature is exceptional and opens new perspectives regarding hydrothermal ore-forming processes. Other magnetite- and Cu-sulphide-rich deposits such as in Duolong in Tibet, Renison in Tasmania, and Butte in Montana, may have formed by similar ore-forming processes (Rusk et al., 2008; Wawryk and Foden, 2015; J.-X. Li et al., 2018) and therefore deserve to be investigated using Cu and Fe isotope systematics.

The data produced in this study represent, so far, the only Cu and isotope compositions of carbonatite-hosted sulphides of magmatic, hydrothermal and alteration origin. This is of a significant interest to researchers studying economic geology using stable isotope analysis. The presence of magmatic, hydrothermal and alteration sulphides provides fundamental insights in the isotope and trace element fractionation mechanisms in the course of staged metallogenesis.

The new spatially-resolved sampling technique developed in this study is an alternative to laser ablation-based analysis. The latter is expensive and has the significant drawback as matrix cannot be easily separated from sulphides, or to any other mineral of interest, which could result in spurious isotope ratio analysis. In addition to being more accurate, the technique detailed in the thesis is particularly cost-effective, offering significant potential for future economic geology-related projects, but also for any research project requiring small-scale spatially-resolved sampling. Spatially-resolved isotopic analysis revealed significant isotopic fractionation at the >mm scale. This feature clearly indicates the importance of this technique for ore characterization by isotopic ratio analysis. As a matter of fact, studies based exclusively on mineral separate and whole-rock isotopic analysis may not be able to detect small-scale ore-forming processes necessary for a comprehensive understanding of ore deposit formation.

This study enabled the characterization of one aspect of the ore formation. However, only one method may be insufficient for late-stage alteration characterization. Conclusions based on isotopic and PGE data allow two different interpretations regarding fluid-related mechanisms in the Loolekop Pipe, revealing more complexity than may have been expected. This clearly shows that investigation of a geological phenomenon ideally relies on multiple analytical methods.

References

Agangi, A., Hofmann, A., Hegner, E., Xie, H., Teschner, C., Slabunov, A., Svetov, S. A. (2020) The Mesoarchaean Dominion Group and the onset of intracontinental volcanism on the Kaapvaal craton – geological, geochemical and temporal constraints. *Gondwana Research* 84:131-150. doi: 10.1016/j.gr.2020.03.005.

Albarède, F. (2004) The stable isotope geochemistry of copper and zinc. *Reviews in Mineralogy & Geochemistry* 55:409-427. doi: 10.2138/gsrmg.55.1.409.

Anbar, A. D., Jarzecki, A. A., Spiro, T. G. (2005) Theoretical investigation of iron isotope fractionation between $Fe(H_2O)_6^{3+}$ and $Fe(H_2O)_6^{2+}$: Implications for iron stable isotope geochemistry. *Geochimica et Cosmochimica Acta* 69:825-837. doi: 10.1016/j.gca.2004.06.012.

Anbar, A. D., Roe, J. E., Barling, J., Nealson, K. H. (2000) Nonbiological fractionation of iron isotopes. *Science* 288:126-128. doi: 10.1126/science.288.5463.126.

Archer, C., Vance, D. (2004) Mass discrimination correction in multiple-collector plasma source mass spectrometry: an example using Cu and Zn isotopes. *Journal of Analytical Atomic Spectrometry* 19:656-665. doi: 10.1039/B315853E.

Armstrong, R. A., Compston, W., De Wit, M. J., Williams, I. S. (1990) The stratigraphy of the 3.5-3.2 Ga Barberton Greenstone Belt revisited: a single zircon ion microprobe study. *Earth and Planetary Science Letters* 101:90-106.

Arnold, G. L., Weyer, S., Anbar, A. D. (2004) Fe isotope variations in natural materials measured using high mass resolution multiple collector ICPMS. *Analytical Chemistry* 76:322-327. doi: 10.1021/ac034601v.

Asadi, S., Mathur, R., Moore, F., Zarasvandi, A. (2015) Copper isotope fractionation in the Meiduk porphyry copper deposit, Northwest of Kerman Cenozoic magmatic arc, Iran. *Terra Nova* 27:36-41. doi: 10.1111/ter.12128.

Asael, D., Matthews, A., Oszczepalski, S., Bar-Matthews, M., Halicz, L. (2009) Fluid speciation controls of low temperature copper isotope fractionation applied to the Kupferschiefer and Timna ore deposits. *Chemical Geology* 262:147-158. doi: 10.1016/j.chemgeo.2009.01.015.

Augé, T., Petrunov, R., Bailly, L. (2005) On the origin of the PGE mineralization in the Elatsite Porphyry Cu-Au Deposit, Bulgaria: comparison with the Baula-Nuasahi Complex, India and other alkaline PGE-rich porphyries. *The Canadian Mineralogis*t 43:1355-1372. doi: 10.2113/gscanmin.43.4.1355.

Bachinski, D. J. (1969) Bond strength and sulfur isotopic fractionation in coexisting sulfides. *Economic Geology* 64:56-65.

Baggio, S. B., Hartmann, L. A., Lazarov, M., Massonne, H.-J., Theye, T., Viefhaus, T. (2018) Origin of native copper in the Paraná volcanic province, Brazil, integrating Cu stable isotopes in a multi-analytical approach. *Mineralium Deposita* 53:417-434. doi: 10.1007/s00126-017-0748-2.

Ballhaus, C., Sylvester, P. J. (2000) Noble metal enrichment processes in the Merensky Reef, Bushveld Complex. *Journal of Petrology* 41:545-561. doi: 10.1093/petrology/41.4.545.

Barbosa, E. S. R., Brod, J. A., Cordeiro, P. F. O., Junqueira-Brod, T. C., Santos, R. V., Dantas, E. L. (2020) Phoscorites of the Salitre I complex: Origin and petrogenetic implications. *Chemical Geology* 535. doi: 10.1016/j.chemgeo.2020.119463.

Barnes, S.-J. (2016) Chalcophile Elements In: White, W. M. (ed) Encyclopedia of Geochemistry. Springer International Publishing, Switzerland, pp 1-5.

Barnes, S. J., Beresford, S. W., Le Vaillant, M. (2016) Interspinifex Ni sulfide ore from the Coronet Shoot, Kambalda: Characterization using microbeam X-ray fluorescence mapping and 3-D X-ray computed tomography. *Economic Geology* 111:1509-1517. doi: 10.2113/econgeo.111.6.1509.

Barnes, S.-J., Cox, R. A., Zientek, M. L. (2006) Platinum-group element, gold, silver and base metal distribution in compositionally zoned sulfide droplets from the Medvezky Creek Mine, Noril'sk, Russia. *Contributions to Mineralogy and Petrology* 152:187-200. doi: 10.1007/s00410-006-0100-9.

Barnes, S. J., Fiorentini, M. L., Austin, P., Gessner, K., Hough, R. M., Squelch, A. P. (2008) Three-dimensional morphology of magmatic sulfides sheds light on ore formation and sulfide melt migration. *Geology* 36:655-658. doi: 10.1130/g24779a.1.

Barnes, S. J., Le Vaillant, M., Godel, B., Lesher, C. M. (2019) Droplets and bubbles: solidification of sulphide-rich vapour-saturated orthocumulates in the Norilsk-Talnakh Ni–Cu–PGE ore-bearing intrusions. *Journal of Petrology* 60:269-300. doi: 10.1093/petrology/egy114.

Barnes, S.-J., Makovicky, E., Makovicky, M., Rose-Hansen, J., Karup-Moller, S. (1997) Partition coefficients for Ni, Cu, Pd, Pt, Rh, and Ir between monosulfide solid solution and sulfide liquid and the formation of compositionally zoned Ni-Cu sulfide bodies by fractional crystallization of sulfide liquid. *Canadian Journal of Earth Sciences* 34:366-374.

Barnes, S.-J., Prichard, H. M., Cox, R. A., Fisher, P. C., Godel, B. (2008) The location of the chalcophile and siderophile elements in platinum-group element ore deposits (a textural, microbeam and whole rock geochemical study): Implications for the formation of the deposits. *Chemical Geology* 248:295-317. doi: 10.1016/j.chemgeo.2007.08.004.

Barnes, S.-J., Ripley, E. M. (2016) Highly siderophile and strongly chalcophile elements in magmatic ore deposits. In: Harvey, J., Day, J. M. D. (eds) Highly Siderophile and Strongly Chalcophile Elements in High-Temperature Geochemistry and Cosmochemistry. Mineralogical Society of America & Geochemical Society, pp 725-774.

Barnes, S.-J., van Achterbergh, E., Makovicky, E., Li, C. (2001) Proton microprobe results for the partitioning of platinum-group elements between monosulphide solid solution and sulphide liquid. *South African Journal of Geology* 104:275-286.

Barrat, J.-A., Zanda, B., Moynier, F., Bollinger, C., Liorzou, C., Bayon, G. (2012) Geochemistry of CI chondrites: Major and trace elements, and Cu and Zn isotopes. *Geochimica et Cosmochimica Acta* 83:79-92. doi: 10.1016/j.gca.2011.12.011.

Basson, I., Lourens, P., Paetzold, H.-D., Thomas, S., Brazier, R., Molabe, P. (2017) Structural analysis and 3D modelling of major mineralizing structures at the Phalaborwa copper deposit. *Ore Geology Reviews* 83:30-42. doi: 10.1016/j.oregeorev.2016.12.002.

Beard, B. L., Johnson, C. M. (1999) High precision iron isotope measurements of terrestrial and lunar material. *Geochimica et Cosmochimica Acta* 63:1653-1660.

Beard, B. L., Johnson, C. M. (2004) Inter-mineral Fe isotope variations in mantle-derived rocks and implications for the Fe geochemical cycle. *Geochimica et Cosmochimica Acta* 68:4727-4743. doi: 10.1016/j.gca.2004.04.023.

Belshaw, N. S., Zhu, X. K., Guo, Y., O'Nions, R. K. (2000) High precision measurement of iron isotopes by plasma source mass spectrometry. *International Journal of Mass Spectrometry* 197:191-195.

Ben Othman, D., Luck, J. M., Bodinier, J. L., Arndt, N. T., Albarède, F. (2006) Cu–Zn isotopic variations in the Earth's mantle. *Geochimica et Cosmochimica Acta* 70:A46. doi: 10.1016/j.gca.2006.06.201.

Bezmen, N. I., Asif, M., Brügmann, G. E., Romanenko, I. M., Naldrett, A. J. (1994) Distribution of Pd, Rh, Ru, Ir, Os, and Au between sulfide and silicate metals. *Geochimica et Cosmochimica Acta* 58:1251-1260.

Bigeleisen, J., Mayer, M. G. (1947) Calculation of equilibrium constants for isotopic exchange reactions. *The Journal of Chemical Physics* 15:261-267. doi: 10.1063/1.1746492.

Bilenker, L. D., Simon, A. C., Reich, M., Lundstrom, C. C., Gajos, N., Bindeman, I., Barra, F., Munizaga, R. (2016) Fe–O stable isotope pairs elucidate a high-temperature origin of Chilean iron oxide-apatite deposits. *Geochimica et Cosmochimica Acta* 177:94-104. doi: 10.1016/j.gca.2016.01.009.

Blanchard, M., Poitrasson, F., Méheut, M., Lazzeri, M., Mauri, F., Balan, E. (2009) Iron isotope fractionation between pyrite (FeS2), hematite (Fe2O3) and siderite (FeCO3): A first-principles density functional theory study. *Geochimica et Cosmochimica Acta* 73:6565-6578. doi: 10.1016/j.gca.2009.07.034.

Blundell, D. J., Karnkowski, P. H., Alderton, D. H. M., Oszczepalski, S., Kucha, H. (2003) Copper mineralization of the polish Kupferschiefer: a proposed basement fault-fracture system of fluid flow. *Economic Geology* 98:1487-1495. doi: 10.2113/gsecongeo.98.7.1487.

Bockrath, C., Ballhaus, C., Holzheid, A. (2004) Fractionation of the platinum-group elements during mantle melting. *Science* 305:1951-1953. doi: 10.1126/science.1100160.

Bolhar, R., Whitehouse, M. J., Milani, L., Magalhães, N., Golding, S. D., Bybee, G., Le Bras, L., Bekker, A. (2020) Atmospheric S and lithospheric Pb in sulphides from the 2.06 Ga Phalaborwa phoscorite-carbonatite complex, South Africa. *Earth and Planetary Science Letters* 530:115939. doi: 10.1016/j.epsl.2019.115939.

Borrok, D. M., Wanty, R. B., Ridley, W. I., Wolf, R., Lamothe, P. J., Adams, M. (2007) Separation of copper, iron, and zinc from complex aqueous solutions for isotopic measurement. *Chemical Geology* 242:400-414. doi: 10.1016/j.chemgeo.2007.04.004.

Bowen, T. B., Marsh, J. S., Bowen, M. P., Eales, H. V. (1986) Volcanic rocks of the Witwatersrand triad, South Africa. I: Description, classification and geochemical stratigraphy. *Precambrian Research* 31:297-324.

Brown, A. C. (2014) Low-temperature sediment-hosted copper deposits. In: Scott SD (ed) Geochemistry of Mineral Deposits. 2nd edn. Elsevier, pp 251-268.

Bulakh, A. G., Rudashevsky, N. S., Karchevsky, P. I. (1998) Gold, silver, sulphides and rare-earth minerals in carbonatites of the Loolekop deposit (RSA). *Zapiski Vserossiyskogo Mineralogicheskogo Obshchestva* 3:45-54.

Cabri, L. J. (1973) New data on phase relations in the Cu-Fe-S system. *Economic Geology* 68:443-454.

Cabri, L. J., Hall, S. R., Szymanski, J.T., Stewart, J. M. (1973) On the transformation of cubanite. *The Canadian Mineralogist* 12:33-38.

Catuneanu, O., Eriksson, P. G. (1999) The sequence stratigraphic concept and the Precambrian rock record: an example from the 2.7–2.1 Ga Transvaal Supergroup, Kaapvaal craton. *Precambrian Research* 97:215-251.

Cawthorn, R. G. (2015) The Bushveld Complex, South Africa In: Charlier, B., Namur, O., Latypov, R. M., Tegner, C. (eds) Layered Intrusions. Springer, Dordrecht, pp 517-587.

Cawthorn, R. G., Meyer, F. M. (1993) Petrochemistry of the Okiep copper district basic intrusive bodies, Northwestern Cape Province, South Africa. *Economic Geology* 88:590-605.

Cawthorn, R. G., Walraven, F. (1998) Emplacement and crystallization time for the Bushveld Complex. *Journal of Petrology* 39:1669-1687.

Chapman, J. B., Mason, T. F. D., Weiss, D. J., Coles, B. J., Wilkinson, J. J. (2006) Chemical separation and isotopic variations of Cu and Zn from five geological reference materials. *Geostandards and Geoanalytical Research* 30:5-16. doi: 10.1111/j.1751-908X.2006.tb00907.x.

Chapman, J. B., Weiss, D. J., Shan, Y., Lemburger, M. (2009) Iron isotope fractionation during leaching of granite and basalt by hydrochloric and oxalic acids. *Geochimica et Cosmochimica Acta* 73:1312-1324. doi: 10.1016/j.gca.2008.11.037.

Chen, K.-Y., Yuan, H.-L., Liang, P., Bao, Z.-A., Chen, L. (2017) Improved nickel-corrected isotopic analysis of iron using high-resolution multi-collector inductively coupled plasma mass spectrometry. *International Journal of Mass Spectrometry* 421:196-203. doi: 10.1016/j.ijms.2017.07.002.

Chmeleff, J., Horn, I., Steinhoefel, G., von Blanckenburg, F. (2008) In situ determination of precise stable Si isotope ratios by UV-femtosecond laser ablation high-resolution multi-collector ICP-MS. *Chemical Geology* 249:155-166. doi: 10.1016/j.chemgeo.2007.12.003.

Clendenin, C., Charlesworth, E., Maske, S. (1988) An early Proterozoic three-stage rift system, Kaapvaal craton, South Africa. *Tectonophysics* 145:73-86.

Cnudde, V., Boone, M. N. (2013) High-resolution X-ray computed tomography in geosciences: A review of the current technology and applications. *Earth-Science Reviews* 123:1-17. doi: 10.1016/j.earscirev.2013.04.003.

Coward, M. P., Spencer, R. M., Spencer, C. E. (1995) Development of the Witwatersrand Basin, South Africa In: Coward, M. P., Ries, A. C. (eds) Early Precambrian Processes. Geological Society Special Publication, pp 243-269.

Craddock, P. R., Dauphas, N. (2011) Iron isotopic compositions of geological reference materials and chondrites. *Geostandards and Geoanalytical Research* 35:101-123. doi: 10.1111/j.1751-908X.2010.00085.x.

Craddock, P. R., Warren, J. M., Dauphas, N. (2013) Abyssal peridotites reveal the near-chondritic Fe isotopic composition of the Earth. *Earth and Planetary Science Letters* 365:63-76. doi: 10.1016/j.epsl.2013.01.011.

Craig, J. R., Vaughan, D. J. (1994) Ore Microscopy and Ore Petrography - 2nd ed. John Wiley & Sons.

Criss, R. E. (1999) Principles of stable isotope distribution. Oxford University Press, USA.

Crow, C., Condie, K. C. (1987) Geochemistry and origin of late Archean volcanic rocks from the Rhenosterhoek Formation, Dominion Group, South Africa. *Precambrian research* 37:217-229.

Crow, C., Condie, K. C. (1988) Geochemistry and origin of late Archean volcanics from the Ventersdorp Supergroup, South Africa. *Precambrian Research* 42:19-37.

Dare, S. A. S., Barnes, S.-J., Prichard, H. M. (2010) The distribution of platinum group elements (PGE) and other chalcophile elements among sulfides from the Creighton Ni-Cu-PGE sulfide deposit, Sudbury, Canada, and the origin of palladium in pentlandite. *Mineralium Deposita* 45:765-793. doi: 10.1007/s00126-010-0295-6.

Dare, S. A. S., Barnes, S.-J., Prichard, H. M., Fisher, P. C. (2011) Chalcophile and platinum-group element (PGE) concentrations in the sulfide minerals from the McCreedy East deposit, Sudbury, Canada, and the origin of PGE in pyrite. *Mineralium Deposita* 46:381-407. doi: 10.1007/s00126-011-0336-9.

Dauphas, N., Craddock. P. R., Asimow, P. D., Bennett, V. C., Nutman, A. P., Ohnenstetter, D. (2009a) Iron isotopes may reveal the redox conditions of mantle melting from Archean to Present. *Earth and Planetary Science Letters* 288:255-267. doi: 10.1016/j.epsl.2009.09.029.

Dauphas, N., John, S. G., Rouxel, O. (2017) Iron isotope systematics In: Teng, F.-Z., Watkins, J. M., Dauphas, N. (eds) Non-Traditional Stable Isotopes. *Reviews in Mineralogy & Geochemistry* 82:415-510. doi: 10.2138/rmg.2017.82.11.

Dauphas, N., Poitrasson, F., Burkhardt, C., Kobayashi, H., Kurosawa, K. (2015) Planetary and meteoritic Mg/Si and δ30Si variations inherited from solar nebula chemistry. *Earth and Planetary Science Letters* 427:236-248. doi: 10.1016/j.epsl.2015.07.008.

Dauphas, N., Pourmand, A., Teng, F.-Z. (2009b) Routine isotopic analysis of iron by HR-MC-ICPMS: How precise and how accurate? *Chemical Geology* 267:175-184. doi: 10.1016/j.chemgeo.2008.12.011.

Dauphas, N., Roskosz, M., Alp, E. E., Neuville, D. R., Hu, M. Y., Sio, C. K., Tissot, F. L. H., Zhao, J., Tissandier, L., Médard, E., Cordier, C. (2014) Magma redox and structural controls on iron isotope variations in Earth's mantle and crust. *Earth and Planetary Science Letters* 398:127-140. doi: 10.1016/j.epsl.2014.04.033.

Dauphas, N., Van Zuilen, M., Busigny, V., Lepland, A., Wadhwa, M., Janney, P. E. (2007) Iron isotope, major and trace element characterization of early Archean supracrustal rocks from SW Greenland: Protolith identification and metamorphic overprint. *Geochimica et Cosmochimica Acta* 71:4745-4770.

Dauphas, N., Van Zuilen, M., Wadhwa, M., Davis, A. M., Marty, B., Janney, P. E. (2004) Clues from Fe isotope variations on the origin of early Archean BIFs from Greenland. *Science* 306:2077-2080.

de Ronde, C. E. J., De Wit, M. J. (1994) Tectonic history of the Barberton greenstone belt, South Africa: 490 million years of Archean crustal evolution. *Tectonics* 13:983-1005.

de Wit, M. J. (1982) Gliding and overthrust nappe tectonics in the Barberton Greenstone Belt. *Journal of Structural Geology* 4:117-136.

Debret, B., Millet, M. A., Pons, M. L., Bouilhol, P., Inglis, E., Williams, H. (2016) Isotopic evidence for iron mobility during subduction. *Geology* 44:215-218. doi: 10.1130/g37565.1.

Ding, X., Ripley, E. M., Wang, W., Li, C., Huang, F. (2019) Iron isotope fractionation during sulfide liquid segregation and crystallization at the Lengshuiqing Ni-Cu magmatic sulfide deposit, SW China. *Geochimica et Cosmochimica Acta* 261:327-341. doi: 10.1016/j.gca.2019.07.015.

Durazzo, A., Taylor, L. A. (1982) Experimental exsolution textures in the system bornite-chalcopyrite: genetic implications concerning natural ores. *Mineralium Deposita* 17:79-97.

Dutrizac, J. E. (1976) Reactions in cubanite and chalcopyrite. *The Canadian Mineralogist* 14:172-181.

Eales, H. V., Cawthorn, R. G. (1996) The Bushveld Complex. *Developments in Petrology* 15:181-229.

Ebel, D. S., Naldrett, A. J. (1997) Crystallization of sulfide liquids and the interpretation of ore composition. *Canadian Journal of Earth Sciences* 34:352-365.

Eglington, B. M., Armstrong, R. A. (2004) The Kaapvaal Craton and adjacent orogens, southern Africa: a geochronological database and overview of the geological development of the craton. *South African Journal of Geology* 107:13-32. doi: 10.2113/107.1-2.13.

Ehrlich, S., Butler, I., Halicz, L., Rickard, D., Oldroyd, A., Matthews, A. (2004) Experimental study of the copper isotope fractionation between aqueous Cu(II) and covellite, CuS. *Chemical Geology* 209:259-269.

El Desouky, H. A., Muchez, P., Boyce, A. J., Schneider, J., Cailteux, J. L. H., Dewaele, S., von Quadt, A. (2010) Genesis of sediment-hosted stratiform copper–cobalt mineralization at Luiswishi and Kamoto, Katanga copperbelt (Democratic Republic of Congo). *Mineralium Deposita* 45:735-763. doi: 10.1007/s00126-010-0298-3.

Eriksson, S. C. (1982) Aspects of the petrochemistry of the Phalaborwa Complex, Northeastern Transvaal, South Africa. Faculty of Science. University of the Witwatersrand.

Eriksson, S. C. (1989) Phalaborwa: a saga of magmatism, metasomatism and miscibility In: Carbonatites: Genesis and evolution. Unwin Hyman, London, pp 221-254.

Eriksson, P. G., Altermann, W. (1998) An overview of the geology of the Transvaal Supergroup dolomites (South Africa). *Environmental Geology* 36:179-188.

Farmer, G. L., Perry, F. V., Semken, S., Crowe, B., Curtis, D., DePaolo, D. J. (1989) Isotopic evidence on the structure and origin of subcontinental lithospheric mantle in southern Nevada. *Journal of Geophysical Research* 94:7885-7898. doi: 10.1029/JB094iB06p07885.

Fellows, S. A., Canil, D. (2012) Experimental study of the partitioning of Cu during partial melting of Earth's mantle. *Earth and Planetary Science Letters* 337-338:133-143. doi: 10.1016/j.epsl.2012.05.039.

Fernandez, A., Borrok, D. M. (2009) Fractionation of Cu, Fe, and Zn isotopes during the oxidative weathering of sulfide-rich rocks. *Chemical Geology* 264:1-12. doi: 10.1016/j.chemgeo.2009.01.024.

Foden, J., Sossi, P. A., Nebel, O. (2018) Controls on the iron isotopic composition of global arc magmas. *Earth and Planetary Science Letters* 494:190-201. doi: 10.1016/j.epsl.2018.04.039.

Foden, J., Sossi, P. A., Wawryk, C. M. (2015) Fe isotopes and the contrasting petrogenesis of A-, I- and S-type granite. *Lithos* 212-215:32-44. doi: 10.1016/j.lithos.2014.10.015.

Folmer, J. C. W., Jellinek, F. (1980) The valence of copper in sulphides and selenides: an X-ray photoelectron spectroscopy study. *Journal of the Less-Common Metals* 76:153-162.

Fontboté, L., Kouzmanov, K., Chiaradia, M., Pokrovski, G. S. (2017) Sulfide minerals in hydrothermal deposits. *Elements* 13:97-103. doi: 10.2113/gselements.13.2.97.

Forster, I. F. (1958) Paragenetical Ore Mineralogy of the Loolekop-Phalaborwa Carbonatite Complex, Eastern Transvaal. *South African Journal of Geology* 61:359-365.

Frick, D. A., Schuessler, J. A., von Blanckenburg, F. (2016) Development of routines for simultaneous in situ chemical composition and stable Si isotope ratio analysis by femtosecond laser ablation inductively coupled plasma mass spectrometry. *Analytical Chimica Acta* 938:33-43. doi: 10.1016/j.aca.2016.08.029.

Frierdich, A. J., Beard, B. L., Scherer, M. M., Johnson, C. M. (2014) Determination of the Fe(II)aq–magnetite equilibrium iron isotope fractionation factor using the three-isotope method and a multi-direction approach to equilibrium. *Earth and Planetary Science Letters* 391:77-86. doi: 10.1016/j.epsl.2014.01.032.

Fujii, T., Moynier, F., Abe, M., Nemoto, K., Albarède, F. (2013) Copper isotope fractionation between aqueous compounds relevant to low temperature geochemistry and biology. *Geochimica et Cosmochimica Acta* 110:29-44. doi: 10.1016/j.gca.2013.02.007.

Fujii, T., Moynier, F., Blichert-Toft, J., Albarède, F. (2014) Density functional theory estimation of isotope fractionation of Fe, Ni, Cu, and Zn among species relevant to geochemical and biological environments. *Geochimica et Cosmochimica Acta* 140:553-576. doi: 10.1016/j.gca.2014.05.051.

Giebel, R. J., Gauert, C. D. K., Marks, M. A. W., Costin, G., Markl, G. (2017) Multi-stage formation of REE minerals in the Palabora Carbonatite Complex, South Africa. *American Mineralogist* 102:1218-1233. doi: 10.2138/am-2017-6004.

Giebel, R. J., Marks, M. A. W., Gauert, C. D. K., Markl, G. (2019) A model for the formation of carbonatite-phoscorite assemblages based on the compositional variations of mica and apatite from the Palabora Carbonatite Complex, South Africa. *Lithos* 324-325:89-104. doi: 10.1016/j.lithos.2018.10.030.

Gilbert, S. E., Danyushevsky, L. V., Rodemann, T., Shimizu, N., Gurenko, A., Meffre, S., Thomas, H., Large, R. R., Death, D. (2014) Optimisation of laser parameters for the analysis of sulphur isotopes in sulphide minerals by laser ablation ICP-MS. *Journal of Analytical Atomic Spectrometry* 29:1042-1051. doi: 10.1039/c4ja00011k.

Godel, B., Barnes, S. J., Barnes, S.-J., Maier, W. D. (2010) Platinum ore in three dimensions: Insights from high-resolution X-ray computed tomography. *Geology* 38:1127-1130. doi: 10.1130/g31265.1.

Goh, S. W., Buckley, A. N., Lamb, R. N., Rosenberg, R. A., Moran, D. (2006) The oxidation states of copper and iron in mineral sulfides, and the oxides formed on initial exposure of chalcopyrite and bornite to air. *Geochimica et Cosmochimica Acta* 70:2210-2228. doi: 10.1016/j.gca.2006.02.007.

Goldschmidt, V. M. (1937) The principles of distribution of chemical elements in minerals and rocks. The seventh Hugo Müller Lecture, delivered before the Chemical Society on March 17th, 1937. *Journal of the Chemical Society (Resumed)* 655-673.

Graham, S., Pearson, N. J., Jackson, S., Griffin, W. L., O'Reilly, S. Y. (2004) Tracing Cu and Fe from source to porphyry: in situ determination of Cu and Fe isotope ratios in sulfides from the Grasberg Cu-Au deposit. *Chemical Geology* 207:147-169. doi: 10.1016/j.chemgeo.2004.02.009.

Groves, D. I., Vielreicher, N. M. (2001) The Phalaborwa (Palabora) carbonatite-hosted magnetite-copper sulfide deposit, South Africa: an end-member of the iron-oxide copper-gold-rare earth element deposit group? *Mineralium Deposita* 36:189-194.

Günther, T., Klemd, R., Zhang, X., Horn, I., Weyer, S. (2017) In-situ trace element and Fe-isotope studies on magnetite of the volcanic-hosted Zhibo and Chagangnuoer iron ore deposits in the Western Tianshan, NW China. *Chemical Geology* 453:111-127. doi: 10.1016/j.chemgeo.2017.02.001.

Hanekom, H. J., Van Standen, C. M., Smit, P. J., Pike, D. R. (1965) The Geology of Palabora Igneous Complex, South Africa. Geological Survey Handbook Memoir 54.

Hanger, B. J., Yaxley, G. M., Berry, A. J., Kamenetsky, V. S. (2015) Relationships between oxygen fugacity and metasomatism in the Kaapvaal subcratonic mantle, represented by garnet peridotite xenoliths in the Wesselton kimberlite, South Africa. *Lithos* 212-215:443-452. doi: 10.1016/j.lithos.2014.09.030.

Hartzer, F. J. (1995) Transvaal Supergroup inliers: geology, tectonic development and relationship with the Bushveld complex, South Africa. *Journal of African Earth Sciences* 21:521-547.

Heaman, L. M., LeCheminant, A. N. (1993) Paragenesis and U-Pb systematics of baddeleyite (ZrO_2). *Chemical Geology* 110:95-126.

Heimann, A., Beard, B. L., Johnson, C. M. (2008) The role of volatile exsolution and sub-solidus fluid/rock interactions in producing high 56Fe/54Fe ratios in siliceous igneous rocks. *Geochimica et Cosmochimica Acta* 72:4379-4396. doi: 10.1016/j.gca.2008.06.009.

Heinrich, E. W. (1970) The Palabora carbonatitic complex – a unique copper deposit. *The Canadian Mineralogist* 10:585-598.

Helmy, H. M., Ballhaus, C., Wohlgemuth-Ueberwasser, C. C., Fonseca, R. O. C., Laurenz, V. (2010) Partitioning of Se, As, Sb, Te and Bi between monosulfide solid solution and sulfide melt - Application to magmatic sulfide deposits. *Geochimica et Cosmochimica Acta* 74:6174-6179.

Heubeck, C., Lowe, D. R. (1994) Depositional and tectonic setting of the Archean Moodies Group, Barberton greenstone belt, South Africa. *Precambrian Research* 68:257-290.

Hezel, D. C., Wilden, J. S., Becker, D., Steinbach, S., Wombacher, F., Harak, M. (2018) Fe isotope composition of bulk chondrules from Murchison (CM2): Constraints for parent body alteration, nebula processes and chondrule-matrix complementarity. *Earth and Planetary Science Letters* 490:31-39. doi: 10.1016/j.epsl.2018.03.013.

Hiebert, R. S., Bekker, A., Houlé, M. G., Wing, B. A., Rouxel, O. J. (2016) Tracing sources of crustal contamination using multiple S and Fe isotopes in the Hart komatiite-associated Ni–Cu–PGE sulfide deposit, Abitibi greenstone belt, Ontario, Canada. *Mineralium Deposita* 51:919-935. doi: 10.1007/s00126-016-0644-1.

Hill, P. S., Schauble, E. A. (2008) Modeling the effects of bond environment on equilibrium iron isotope fractionation in ferric aquo-chloro complexes. *Geochimica et Cosmochimica Acta* 72:1939-1958. doi: 10.1016/j.gca.2007.12.023.

Hitzman, M. W., Broughton, D. W. (2017) Discussion: "Age of the Zambian Copperbelt" by Sillitoe et al. (2017) Mineralium Deposita. *Mineralium Deposita* 52:1273-1275. doi: 10.1007/s00126-017-0767-z.

Hoffman, J. W., De Beer, F. C. (2012) Characteristics of the micro-focus X-ray tomography facility (MIXRAD) at Necsa in South Africa. *Proceedings 18th World Conference on Nondestructive Testing*. pp 16-20.

Holwell, D. A., McDonald, I. (2010) A review of the behaviour of Platinum Group Elements within natural magmatic sulfide ore systems. *Platinum Mineral Review* 54:26-36. doi: 10.1595/147106709X480913.

Hu, H.-L., Fan, H.-R., Santosh, M., Liu, X., Cai, Y.-C., Yang, K.-F. (2020) Ore-forming processes in the Wang'ershan gold deposit (Jiaodong, China): Insight from microtexture, mineral chemistry and sulfur isotope compositions. *Ore Geology Reviews* doi: 10.1016/j.oregeorev.2020.103600.

Huang, F., Chakraborty, P., Lundstrom, C. C., Holmden, C., Glessner, J. J., Kieffer, S. W., Lesher, C. E. (2010) Isotope fractionation in silicate melts by thermal diffusion. *Nature* 464:396-400. doi: 10.1038/nature08840.

Huang, J., Huang, F., Wang, Z., Zhang, X., Yu, H. (2017) Copper isotope fractionation during partial melting and melt percolation in the upper mantle: Evidence from massif peridotites in Ivrea-Verbano Zone, Italian Alps. *Geochimica et Cosmochimica Acta* 211:48-63. doi: 10.1016/j.gca.2017.05.007.

Huang, F., Zhang, Z., Lundstrom, C. C., Zhi, X. (2011) Iron and magnesium isotopic compositions of peridotite xenoliths from Eastern China. *Geochimica et Cosmochimica Acta* 75:3318-3334. doi: 10.1016/j.gca.2011.03.036.

Ikehata, K., Notsu, K., Hirata, T. (2011) Copper isotope characteristics of copper-rich minerals from Besshi-type volcanogenic massive sulfide deposits, Japan, determined using a femtosecond LA-MC-ICP-MS. *Economic Geology* 106:307-316. doi: 10.2113/econgeo.106.2.307.

Jackson, M. C. (1992) A review of the late Archaean volcano-sedimentary Dominion Group and implications for the tectonic setting of the Witwatersrand Supergroup, South Africa. *Journal of African Earth Sciences* 15:169-186.

Jahn, B.-M., Condie, K. C. (1995) Evolution of the Kaapvaal Craton as viewed from geochemical and Sm-Nd isotopic analyses of intracratonic pelites. *Geochimica et Cosmochimica Acta* 59:2239-2258.

Johnson, C. M., Beard, B. L., Weyer, S. (2020) Iron Geochemistry: An Isotopic Perspective. Springer. doi: 10.1007/978-3-030-33828-2.

Johnson, C. M., Skulan, J. L., Beard, B. L., Sun, H., Nealson, K. H., Braterman, P. S. (2002) Isotopic fractionation between Fe(III) and Fe(II) in aqueous solutions. *Earth and Planetary Science Letters* 195:141-153. doi: 10.1016/S0012-821X(01)00581-7.

Jowett, E. C. (1992) Role of organics and methane in sulfide ore formation, exemplified by Kupferschiefer Cu-Ag deposits, Poland. *Chemical Geology* 99:51-63.

Kim, Y., Lee, I., Oyungerel, S., Jargal, L., Tsedenbal, T. (2019) Cu and S isotopic signatures of the Erdenetiin Ovoo porphyry Cu-Mo deposit, northern Mongolia: Implications for their origin and mineral exploration. *Ore Geology Reviews* 104:656-669. doi: 10.1016/j.oregeorev.2018.11.025.

Klemd, R., Herderich, T., Junge, M., Oberthür, T., Schouwstra, R., Roberts, J. (2016) Platinum-group element concentrations in base-metal sulphides from the Platreef, Mogalakwena Platinum Mine, Bushveld Complex, South Africa. *South African Journal of Geology* 119:623-638. doi: 10.2113/gssajg.119.4.623.

Kobussen, A. F., Griffin, W. L., O'Reilly, S. Y. (2009) Cretaceous thermo-chemical modification of the Kaapvaal cratonic lithosphere, South Africa. *Lithos* 112:886-895. doi: 10.1016/j.lithos.2009.06.031.

Korobeinikov, A. N., Mitrofanof, F. P., Gehör, S., Laajoki, K., Pavlov, V. P., Mamontov, V. P. (1998) Geology and copper sulphide mineralization of the Salmagorskii Ring Igneous Complex, Kola Peninsula, NW Russia. *Journal of Petrology* 39:2033-2041.

Kraus, K. A., Moore, G. E. (1953) Anion exchange studies. V. Adsorption of hydrochloric acid by a strong base anion exchanger. *Journal of American Chemical Society* 75:1457-1460.

Krasnova, N. I., Balaganskaya, E. G., Garcia, D. (2004a) Kovdor - classic phoscorite In: Zaitsev, A., Wall, F. (eds) Phoscorites and Carbonatites from Mantle to Mine: the Key Example of the Kola Alkaline Province. London, pp 95-127.

Krasnova, N. I., Petrov, T. G., Balaganskaya, E. G., Garcia, D., Moutte, J., Zaitsev, A. N., Wall, F. (2004b) Introduction to phoscorites: occurences, composition, nomenclature and petrogenesis In: Zaitsev, A. N., Wall, F. (eds) Phoscorites and Carbonatites from Mantle to Mine: the key Example of the Kola Alkaline Province. London, pp 43-72.

Kruger, F. (1994) The Sr-isotopic stratigraphy of the western Bushveld Complex. *South African Journal of Geology* 97:393-398.

Larner, F., Rehkämper, M., Coles, B. J., Kreissig, K., Weiss, D. J., Sampson, B., Unsworth, C., Strekopytov, S. (2011) A new separation procedure for Cu prior to stable isotope analysis by MC-ICP-MS. *Journal of Analytical Atomic Spectrometry* 26:1627-1632. doi: 10.1039/c1ja10067j.

Larson, P. B., Maher, K., Ramos, F.C., Chang, Z., Gaspar, M., Meinert, L. D. (2003) Copper isotope ratios in magmatic and hydrothermal ore-forming environments. *Chemical Geology* 201:337-350. doi: 10.1016/j.chemgeo.2003.08.006.

Le Bras, L. Y., Bolhar, R., Bybee, G. M., Nex, P. A. M., Guy, B. M., Moyana, T., Lourens, P. (2020) Platinum-Group and trace elements in Cu-sulphides from the Loolekop pipe, Phalaborwa: Implications for ore-forming processes. *Mineralium Deposita*. doi: 10.1007/s00126-020-01005-4.

Lee, C.-T. A., Luffi, P., Chin, E. J., Bouchet, R., Dasgupta, R., Morton, D. M., Le Roux, V., Yin, Q.-Z., Jin, D. (2012) Copper systematics in arc magmas and implications for crust-mantle differentiation. *Science* 336:64-68. doi: 10.1126/science.1217313.

Lesher, C. E., Dannberg, J., Barfod, G. H., Bennett, N. R., Glessner JJG, Lacks DJ, Brenan JM (2020) Iron isotope fractionation at the core–mantle boundary by thermodiffusion. *Nature Geoscience*. doi: 10.1038/s41561-020-0560-y.

Li, K., Brugger, J., Pring, A. (2018) Exsolution of chalcopyrite from bornite-digenite solid solution: an example of a fluid-driven back-replacement reaction. *Mineralium Deposita* 53:903-908. doi: 10.1007/s00126-018-0820-6.

Li, W., Jackson, S. E., Pearson, N. J., Alard, O., Chappell, B. W. (2009) The Cu isotopic signature of granites from the Lachlan Fold Belt, SE Australia. *Chemical Geology* 258:38-49. doi: 10.1016/j.chemgeo.2008.06.047.

Li, J.-X., Qin, K.-Z., Li, G.-M., Evans, N. J., Huang, F., Zhao, J.-X. (2018) Iron isotope fractionation during magmatic-hydrothermal evolution: A case study from the Duolong porphyry Cu-Au deposit, Tibet. *Geochimica et Cosmochimica Acta* 238:1-15. doi: 10.1016/j.gca.2018.07.008.

Li, H., Xu, X.-W., Borg, G., Gilg, H. A., Dong, L.-H., Fan. T.-B., Zhou, G., Liu, R.-L., Hong, T., Ke, Q., Wu, C., Zhang, G., Li, H. (2019) Geology and geochemistry of the giant Huoshaoyun zinc-lead deposit, Karakorum Range, northwestern Tibet. *Ore Geology Reviews* 106:251-272. doi: 10.1016/j.oregeorev.2019.02.002.

Liu, S.-A., Huang, J., Liu, J., Wörner, G., Yang, W., Tang, Y.-J., Chen, Y., Tang, L., Zheng, J., Li, S. (2015) Copper isotopic composition of the silicate Earth. *Earth and Planetary Science Letters* 427:95-103. doi: 10.1016/j.epsl.2015.06.061.

Liu, S.-A., Li, D., Li, S., Teng, F.-Z., Ke, S., He, Y., Lu, Y. (2014) High-precision copper and iron isotope analysis of igneous rock standards by MC-ICP-MS. *Journal of Analytical Atomic Spectrometry* 29:122-133. doi: 10.1039/c3ja50232e.

Liu, B., Li, H., Wu, Q.-H., Kong, H., Xi, X.-S. (2019) Double-vein (ore-bearing vs. ore-free) structures in the Xitian ore field, South China: Implications for fluid evolution and mineral exploration. *Ore Geology Reviews* 115. doi: 10.1016/j.oregeorev.2019.103181.

Logue, A., Bybee, G. M., Tappa, M., Baxter, E., Iaccheri, L., WIG Laboratory (2018) A novel, laser-based micro-sampling technique allowing texturally controlled, spiked, multi-isotope analysis at the crystal and sub-crystal scale in magmatic and mineralized bodies. 2018 AGU Fall Meeting. Washington D.C.

Lombaard, A. F., Ward-Able, N. M., Bruce, R. W. (1964) The exploration and main geological features of the copper deposit in carbonatite Loolekop, Palabora Complex. In: Haughton, S. H. (ed) The geology of some ore deposits in Southern Africa. Geological Society of South Africa, Johannesburg, pp 23.

Lowe, D. R. (1994) Accretionary history of the Archean Barberton greenstone belt (3.55-3.22 Ga), southern Africa. *Geology* 22:1099-1102.

Lowe, D. R., Byerly, G. R. (1999) Stratigraphy of the west-central part of the Barberton greenstone belt, South Africa. *Geological Society of America Special Papers* 329:1-36.

Lowe, D. R., Byerly, G. R. (2007) An overview of the geology of the Barberton greenstone belt and vicinity: implications for early crustal development. In: Van Kranendonk M, J., Smithies RH, Bennett VC (eds) Earth's Oldest Rocks. pp 481-526.

Luck, J., Ben Othman, D., Albarède, F. (2005) Zn and Cu isotopic variations in chondrites and iron meteorites: Early solar nebula reservoirs and parent-body processes. *Geochimica et Cosmochimica Acta* 69:5351-5363. doi: 10.1016/j.gca.2005.06.018.

Luck, J., Ben Othman, D., Barrat, J., Albarède, F. (2003) Coupled 63Cu and 16O excesses in chondrites. *Geochimica et Cosmochimica Acta* 67:143-151.

Lundstrom, C. (2009) Hypothesis for the origin of convergent margin granitoids and Earth's continental crust by thermal migration zone refining. *Geochimica et Cosmochimica Acta* 73:5709-5729. doi: 10.1016/j.gca.2009.06.020.

Lv, Y., Liu, S.-A., Zhu, J.-M., Li, S. (2016) Copper and zinc isotope fractionation during deposition and weathering of highly metalliferous black shales in central China. *Chemical Geology* 445:24-35. doi: 10.1016/j.chemgeo.2016.01.016.

Lyubetskaya, T., Korenaga, J. (2007) Chemical composition of Earth's primitive mantle and its variance: 1. Method and results. *Journal of Geophysical Research* 112. doi: 10.1029/2005JB004223.

Maier, W. D., Andreoli, M. A. G., Groves, D. I., Barnes, S.-J. (2012) Petrogenesis of Cu-Ni sulphide ores from O'okiep and Kliprand, Namaqualand, South Africa: Constraints from chalcophile metal contents. *South African Journal of Geology* 115:499-514. doi: 10.2113/gssajg.115.4.499.

Maier, W. D., Barnes, S.-J. (1996) Unusually high concentrations of magnetite at Caraíba and other Cu-sulfide deposits in the Curaçá valley, Bahia, Brazil. *The Canadian Mineralogist* 34:717-731.

Maier, W. D., Barnes, S.-J. (2004) Pt/Pd and Pd/Ir ratios in mantle-derived magmas: A possible role for mantle metasomatism. *South African Journal of Geology* 107:333-340. doi: 10.2113/107.3.333.

Maréchal, C., Albarède, F. (2002) Ion-exchange fractionation of copper and zinc isotopes. *Geochimica et Cosmochimica Acta* 66:1499-1509. doi: 10.1016/S0016-7037(01)00815-8.

Maréchal, C., Télouk, P., Albarède, F. (1999) Precise analysis of copper and zinc isotopic compositions by plasma source mass spectrometry. *Chemical Geology* 156:251-273. doi: 10.1016/S0009-2541(98)00191-0.

Markl, G., Lahaye, Y., Schwinn, G. (2006a) Copper isotopes as monitors of redox processes in hydrothermal mineralization. *Geochimica et Cosmochimica Acta* 70:4215-4228. doi: 10.1016/j.gca.2006.06.1369.

Markl, G., von Blanckenburg, F., Wagner, T. (2006b) Iron isotope fractionation during hydrothermal ore deposition and alteration. *Geochimica et Cosmochimica Acta* 70:3011-3030. doi: 10.1016/j.gca.2006.02.028.

Marsh, J., Bowen, M., Rogers, N., Bowen, T. (1989) Volcanic rocks of the Witwatersrand Triad, South Africa. II: Petrogenesis of mafic and felsic rocks of the Dominion Group. *Precambrian Research* 44:39-65.

Mason, T. F. D., Weiss, D. J., Chapman, J. B., Wilkinson, J. J., Tessalina, S.G., Spiro, B., Horstwood, M. S. A., Spratt, J., Coles, B. J. (2005) Zn and Cu isotopic variability in the Alexandrinka volcanic-hosted massive sulphide (VHMS) ore deposit, Urals, Russia. *Chemical Geology* 221:170-187. doi: 10.1016/j.chemgeo.2005.04.011.

Mason, T. F. D., Weiss, D. J., Horstwood, M., Parrish, R. R., Russell, S. S., Mullane, E., Coles, B. J. (2004) High-precision Cu and Zn isotope analysis by plasma source mass spectrometry. *Journal of Analytical Atomic Spectrometry* 19. doi: 10.1039/b306953b.

Mathur, R., Dendas, M., Titley, S., Phillips, A. (2010) Patterns in the copper isotope composition of minerals in porphyry copper deposits in southwestern United States. *Economic Geology* 105:1457-1467. doi: 10.2113/econgeo.105.8.1457.

Mathur, R., Fantle, M. S. (2015) Copper isotopic perspectives on supergene processes: implications for the global Cu cycle. *Elements* 11:323-329. doi: 10.2113/gselements.11.5.323.

Mathur, R., Ruiz, J., Casselman, M. J., Megaw, P., van Egmond, R. (2012) Use of Cu isotopes to distinguish primary and secondary Cu mineralization in the Cañariaco Norte porphyry copper deposit, Northern Peru. *Mineralium Deposita* 47:755-762. doi: 10.1007/s00126-012-0439-y.

Mathur, R., Ruiz, J., Titley, S., Liermann, L., Buss, H., Brantley, S. (2005) Cu isotopic fractionation in the supergene environment with and without bacteria. *Geochimica et Cosmochimica Acta* 69:5233-5246. doi: 10.1016/j.gca.2005.06.022.

Mathur, R., Titley, S., Barra, F., Brantley, S., Wilson, M., Phillips, A., Munizaga, F., Maksaev, V., Vervoort, J., Hart, G. (2009) Exploration potential of Cu isotope fractionation in

porphyry copper deposits. *Journal of Geochemical Exploration* 102:1-6. doi: 10.1016/j.gexplo.2008.09.004.

Mauk, J. L., Kelly, C. W., van der Pluijm, B. A., Seasor, R. W. (1992) Relations between deformation and sediment-hosted copper mineralization: Evidence from the White Pine part of the Midcontinent rift system. *Geology* 20:427-430.

Milani, L., Bolhar, R., Cawthorn, R. G., Frei, D. (2017a) In situ LA–ICP-MS and EPMA trace element characterization of Fe–Ti oxides from the phoscorite–carbonatite association at Phalaborwa, South Africa. *Mineralium Deposita* 52:747-768. doi: 10.1007/s00126-016-0696-2.

Milani, L., Bolhar, R., Frei, D., Harlov, D. E., Samuel, V. O. (2017b) Light rare earth element systematics as a tool for investigating the petrogenesis of phoscorite-carbonatite associations, as exemplified by the Phalaborwa Complex, South Africa. *Mineralium Deposita* 52:1105-1125. doi: 10.1007/s00126-016-0708-2.

Millet, M.-A., Baker, J. A., Payne, C. E. (2012) Ultra-precise stable Fe isotope measurements by high resolution multiple-collector inductively coupled plasma mass spectrometry with a 57Fe–58Fe double spike. *Chemical Geology* 304-305:18-25. doi: 10.1016/j.chemgeo.2012.01.021.

Mirnejad, H., Mathur, R., Einali, M., Dendas, M., Alirezaei, S. (2010) A comparative copper isotope study of porphyry copper deposits in Iran. *Geochemistry: Exploration, Environment, Analysis* 10:413-418. doi: 10.1144/1467-7873/09-229.

Moynier, F., Vance, D., Fujii, T., Savage, P. S. (2017) The isotope geochemistry of zinc and copper. In: Teng, F.-Z., Watkins, J. M., Dauphas, N. (eds) Non-Traditional Stable Isotopes. *Reviews in Mineralogy & Geochemistry* 82:543-600.

Mullane, E., Russell, S. S., Gounelle, M. (2005) Nebular and asteroidal modification of the iron isotope composition of chondritic components. *Earth and Planetary Science Letters* 239:203-218. doi: 10.1016/j.epsl.2005.07.026.

Mungall, J. E., Andrews, D. R. A., Cabri, L. J., Sylvester, P. J., Tubrett, M. (2005) Partitioning of Cu, Ni, Au, and platinum-group elements between monosulfide solid solution and sulfide melt under controlled oxygen and sulfur fugacities. *Geochimica et Cosmochimica Acta* 69:4349-4360.

Mungall, J. E., Brenan, J. M., Godel, B., Barnes, S. J., Gaillard, F. (2015) Transport of metals and sulphur in magmas by flotation of sulphide melt on vapour bubbles. *Nature Geoscience* 8:216-219. doi: 10.1038/ngeo2373.

Myers, R., McCarthy, T., Bunyard, M., Cawthorn, R., Falatsa, T., Hewitt, T., Linton, P., Myers, J., Palmer, K., Spencer, R. (1990) Geochemical stratigraphy of the Klipriviersberg Group volcanic rocks. *South African Journal of Geology* 93:224-238.

Naldrett, A. J. (2004) Magmatic Sulfide Deposits. Springer, Germany.

Nebel, O., Sossi, P. A., Bénard, A., Arculus, R. J., Yaxley, G. M., Woodhead, J. D., Rhodri Davies, D., Ruttor, S. (2019) Reconciling petrological and isotopic mixing mechanisms in the Pitcairn mantle plume using stable Fe isotopes. *Earth and Planetary Science Letters* 521:60-67. doi: 10.1016/j.epsl.2019.05.037.

Needham, A., Porcelli, D., Russell, S. (2009) An Fe isotope study of ordinary chondrites. *Geochimica et Cosmochimica Acta* 73:7399-7413. doi: 10.1016/j.gca.2009.08.034.

Nelson, F., Kraus, K. A. (1958). Anion-exchange Studies. XXIII. 1, 2 Activity Coefficients of Some Electrolytes in the Resin Phase. *Journal of the American Chemical Society* 80:4154-4161.O'Brien, W. (2015) Prehistoric Copper Mining in Europe: 5500-500 BC. Oxford University Press.

O'Neil, J. R. (1986) Appendix; Terminology and standards. *Reviews in Mineralogy and Geochemistry* 16:561-570.

Oszczepalski, S. (1999) Origin of the Kupferschiefer polymetallic mineralization in Poland. *Mineralium Deposita* 34:599-613.

Ottonello, G., Zuccolini, M. V. (2009) Ab-initio structure, energy and stable Fe isotope equilibrium fractionation of some geochemically relevant H–O–Fe complexes. *Geochimica et Cosmochimica Acta* 73:6447-6469. doi: 10.1016/j.gca.2009.06.034.

Palabora Mining Company Ltd Staff (1976) The geology and the economic deposits of copper, iron, and vermiculite in the Palabora Igneous Complex: a brief review. *Economic Geology* 71:177-192.

Parman, S., Dann, J., Grove, T., De Wit, M. (1997) Emplacement conditions of komatiite magmas from the 3.49 Ga Komati Formation, Barberton greenstone belt, South Africa. *Earth and Planetary Science Letters* 150:303-323.

Peach, C. L., Mathez, E. A., Keays, R. R. (1990) Sulfide melt-silicate distribution coefficients for noble metals and other chalcophile elements as deduced from MORB: Implications for partial melting. *Geochimica et Cosmochimica Acta* 54:3379-3389.

Pearce, C. I., Pattrick, R. A. D., Vaughan, D. J., Henderson, C. M. B., van der Laan, G. (2006) Copper oxidation state in chalcopyrite: Mixed Cu d9 and d10 characteristics. *Geochimica et Cosmochimica Acta* 70:4635-4642. doi: 10.1016/j.gca.2006.05.017.

Peel, K., Weiss, D., Chapman, J., Arnold, T., Coles, B. (2008) A simple combined sample–standard bracketing and inter-element correction procedure for accurate mass bias correction and precise Zn and Cu isotope ratio measurements. *Journal of Analytical Atomic Spectrometry* 23:103-110. doi: 10.1039/b710977f.

Peters, B. J., Shahar, A., Carlson, R. W., Day, J. M. D., Mock, T. D. (2019) A sulfide perspective on iron isotope fractionation during ocean island basalt petrogenesis. *Geochimica et Cosmochimica Acta* 245:59-78. doi: 10.1016/j.gca.2018.10.015.

Piña, R., Gervilla, F., Barnes, S.-J., Ortega, L., Lunar, R. (2012) Distribution of platinum-group and chalcophile elements in the Aguablanca Ni-Cu sulfide deposit (SW Spain): Evidence from a LA-ICP-MS study. *Chemical Geology* 302-302:61-75. doi: 10.1016/j.chemgeo.2011.02.010.

Pitron, G. (2018) La Guerre des Métaux Rares. Les Liens qui Libèrent.

Poitrasson, F., Delpech, G., Grégoire, M. (2013) On the iron isotope heterogeneity of lithospheric mantle xenoliths: implications for mantle metasomatism, the origin of basalts and the iron isotope composition of the Earth. *Contributions to Mineralogy and Petrology* 165:1243-1258. doi: 10.1007/s00410-013-0856-7.

Poitrasson, F., Freydier, R. (2005) Heavy iron isotope composition of granites determined by high resolution MC-ICP-MS. *Chemical Geology* 222:132-147. doi: 10.1016/j.chemgeo.2005.07.005.

Poitrasson, F., Halliday, A. N., Lee, D.-C., Levasseur, S., Teutsch, N. (2004) Iron isotope differences between Earth, Moon, Mars and Vesta as possible records of contrasted accretion mechanisms. *Earth and Planetary Science Letters* 223:253-266. doi: 10.1016/j.epsl.2004.04.032.

Poitrasson, F., Roskosz, M., Corgne, A. (2009) No iron isotope fractionation between molten alloys and silicate melt to 2000 °C and 7.7 GPa: Experimental evidence and implications for planetary differentiation and accretion. *Earth and Planetary Science Letters* 278:376-385. doi: 10.1016/j.epsl.2008.12.025.

Pretorius, D. A. (1976) The nature of the Witwatersrand gold-uranium deposits. In: Wolf KH (ed) Handbook of Stratabound Stratiform Ore Deposits. Elsevier, pp 29-88.

Ramdohr, P. (1969) The Ore Minerals and their Intergrowths. Akademie-Verlag, Berlin.

Rayleigh, L. (1902) LIX. On the distillation of binary mixtures. *The London, Edinburgh, and Dublin Philosophical Magazine and Journal of Science* 4:521-537.Reischmann, T. (1995) Precise U/Pb age determination with baddeleyite (ZrO_2), a case study from the Phalaborwa Igneous Complex, South Africa. *South African Journal of Geology* 98:1-4.

Richter, F. M. (2004) Timescales determining the degree of kinetic isotope fractionation by evaporation and condensation. *Geochimica et Cosmochimica Acta* 68:4971-4992. doi: 10.1016/j.gca.2004.06.008.

Richter, F. M., Dauphas, N., Teng, F.-Z. (2009a) Non-traditional fractionation of non-traditional isotopes: evaporation, chemical diffusion and Soret diffusion. *Chemical Geology* 258:92-103. doi: 10.1016/j.chemgeo.2008.06.011.

Richter, F. M., Davis, A. M., Ebel, D. S., Hashimoto, A. (2002) Elemental and isotopic fractionation of Type B calcium-, aluminum-rich inclusions: experiments, theoretical considerations, and constraints on their thermal evolution. *Geochimica et Cosmochimica Acta* 66:521-540.

Richter, F. M., Janney, P. E., Mendybaev, R. A., Davis, A. M., Wadhwa, M. (2007) Elemental and isotopic fractionation of Type B CAI-like liquids by evaporation. *Geochimica et Cosmochimica Acta* 71:5544-5564. doi: 10.1016/j.gca.2007.09.005.

Richter, F. M., Watson, E. B., Mendybaev, R., Dauphas, N., Georg, B., Watkins, J., Valley, J. (2009b) Isotopic fractionation of the major elements of molten basalt by chemical and thermal diffusion. *Geochimica et Cosmochimica Acta* 73:4250-4263. doi: 10.1016/j.gca.2009.04.011.

Robb, L. J., Meyer, F. M. (1995) The Witwatersrand Basin, South Africa: Geological framework and mineralization processes. *Ore Geology Reviews* 10:67-94.

Roering, C., van Reenen, D. D., de Wit, M. J., Smit, C. A., de Beer, J. H., van Schalkwyk, J. F. (1992) Structural geological and metamorphic significance of the Kaapvaal Craton-Limpopo Belt contact. *Precambrian Research* 55:69-80.

Rouxel, O., Dobbek, N., Ludden, J., Fouquet, Y. (2003) Iron isotope fractionation during oceanic crust alteration. *Chemical Geology* 202:155-182. doi: 10.1016/j.chemgeo.2003.08.011.

Rouxel, O., Fouquet, Y., Ludden, J. N. (2004) Copper isotope systematics of the Lucky Strike, Rainbow and Logatchev seafloor hydrothermal fields on the Mid Atlantic Ridge. *Economic Geology* 99:585-600. doi: 10.2113/gsecongeo.99.3.585.

Rudashevsky, N. S., Kretser, Y. L., Rudashevsky, V. N., Sukharzhevskaya, E. S. (2004) A review and comparison of PGE, noble-metal and sulphide mineralization in phoscorites and carbonatites from Kovdor and Phalaborwa. In: Zaitsev, A., Wall, F. (eds) Phoscorites and Carbonatites from Mantle to Mine: the Key Example of the Kola Alkaline Province. Mineralogical Society, London, pp 363-392.

Rudnick, R. L., Gao, S. (2003) Composition of the continental crust In: Holland HD, Turekian KK (eds) Treatise on Geochemistry. Elsevier, pp 1-64.

Rusk, B. G., Reed, M. H., Dilles, J. H. (2008) Fluid Inclusion Evidence for Magmatic-Hydrothermal Fluid Evolution in the Porphyry Copper-Molybdenum Deposit at Butte, Montana. *Economic Geology* 103:307-334. doi: 10.2113/gsecongeo.103.2.307.

Russell, H. D., Hiemstra, S. A., Groeneveld, D. (1954) The Mineralogy and Petrology of the Carbonatite at Loolekop, Eastern Transvaal. *Transactions of the Geological Society of South Africa* 57:197-208.

Rustad, J. R., Dixon, D. A. (2009) Prediction of iron-isotope fractionation between hematite (α-Fe2O3) and ferric and ferrous iron in aqueous solution from density functional theory. *The Journal of Physical Chemistry* A 113:12249-12255. doi: 10.1021/jp9065373.

Saintilan, N. J., Selby, D., Creaser, R. A., Dewaele, S. (2018) Sulphide Re-Os geochronology links orogenesis, salt and Cu-Co ores in the Central African Copperbelt. *Scientific Reports 8*. doi: 10.1038/s41598-018-33399-7.

Saunier, G., Pokrovski, G. S., Poitrasson, F. (2011) First experimental determination of iron isotope fractionation between hematite and aqueous solution at hydrothermal conditions. *Geochimica et Cosmochimica Acta* 75:6629-6654. doi: 10.1016/j.gca.2011.08.028.

Savage, P. S., Moynier, F., Chen, H., Shofner, G., Siebert, J., Badro, J., Puchtel, I. S. (2015) Copper isotope evidence for large-scale sulphide fractionation during Earth's differentiation. *Geochemical Perspectives Letters* 1:53-64. doi: 10.7185/geochemlet.1506.

Schauble, E. A. (2004) Applying stable isotope fractionation theory to new systems. *Reviews in Mineralogy & Geochemistry* 55:65-111.

Schauble, E. A., Meheut, M., Hill, P. S. (2009) Combining metal stable isotope fractionation theory with experiments. *Elements* 5:369-374. doi: 10.2113/gselements.5.6.369.

Schoenberg, R., von Blanckenburg, F. (2006) Modes of planetary-scale Fe isotope fractionation. *Earth and Planetary Science Letters* 252:342-359. doi: 10.1016/j.epsl.2006.09.045.

Schuessler, J. A., Schoenberg, R., Behrens, H., von Blanckenburg, F. (2007) The experimental calibration of the iron isotope fractionation factor between pyrrhotite and peralkaline rhyolitic melt. *Geochimica et Cosmochimica Acta* 71:417-433. doi: 10.1016/j.gca.2006.09.012.

Schwartz, G. M. (1927) Intergrowths of chalcopyrite and cubanite: experimental proof of the origin of intergrowths and their bearing on the geologic thermometer. *Economic Geology* 22:44-61.

Schweitzer, J., Hatton, C., De Waal, S. (1995) Regional lithochemical stratigraphy of the Rooiberg Group, upper Transvaal Supergroup: a proposed new subdivision. *South African Journal of Geology* 98:245-255.

Shahar, A., Hillgren, V. J., Horan, M. F., Mesa-Garcia, J., Kaufman, L. A., Mock, T. D. (2015) Sulfur-controlled iron isotope fractionation experiments of core formation in planetary bodies. *Geochimica et Cosmochimica Acta* 150:253-264. doi: 10.1016/j.gca.2014.08.011.

Shahar, A., Young, E. D., Manning, C. E. (2008) Equilibrium high-temperature Fe isotope fractionation between fayalite and magnetite: An experimental calibration. *Earth and Planetary Science Letters* 268:330-338. doi: 10.1016/j.epsl.2008.01.026.

Sherman, D. M. (2013) Equilibrium isotopic fractionation of copper during oxidation/reduction, aqueous complexation and ore-forming processes: Predictions from hybrid density functional theory. *Geochimica et Cosmochimica Acta* 118:85-97. doi: 10.1016/j.gca.2013.04.030.

Sillitoe, R. H., Perelló, J., Creaser, R. A., Wilton, J., Wilson, A. J., Dawborn, T. (2017) Age of the Zambian Copperbelt. *Mineralium Deposita* 52:1245-1268. doi: 10.1007/s00126-017-0726-8.

Skulan, J. L., Beard, B. L., Johnson, C. M. (2002) Kinetic and equilibrium Fe isotope fractionation between aqueous Fe (III) and hematite. *Geochimica et Cosmochimica Acta* 66:2995-3015.

Sossi, P. A., Foden, J. D., Halverson, G. P. (2012) Redox-controlled iron isotope fractionation during magmatic differentiation: an example from the Red Hill intrusion, S. Tasmania. *Contributions to Mineralogy and Petrology* 164:757-772. doi: 10.1007/s00410-012-0769-x.

Sossi, P. A., Halverson, G. P., Nebel, O., Eggins, S. M. (2015) Combined separation of Cu, Fe and Zn from rock matrices and improved analytical protocols for stable isotope determination. *Geostandards and Geoanalytical Research* 39:129-149. doi: 10.1111/j.1751-908X.2014.00298.x.

Sossi, P. A., O'Neill, H. S. C. (2017) The effect of bonding environment on iron isotope fractionation between minerals at high temperature. *Geochimica et Cosmochimica Acta* 196:121-143. doi: 10.1016/j.gca.2016.09.017.

Spötl, C., Mattey, D. (2006) Stable isotope microsampling of speleothems for palaeoenvironmental studies: A comparison of microdrill, micromill and laser ablation techniques. *Chemical Geology* 235:48-58. doi: 10.1016/j.chemgeo.2006.06.003.

Sugaki, A., Shima, H., Kitakaze, A., Harada, H. (1975) Isothermal phase relations in the system Cu-Fe-S under hydrothermal conditions at 350°C and 300°C. *Economic Geology* 70:806-823.

Sun, S., McDonough, W. F. (1989) Chemical and isotopic systematics of oceanic basalts: implications for mantle composition and processes. In: Saunders, A. D., Norry, M. J. (eds) Magmatism in the Ocean Basins. Geological Society Special Publication, pp 313-345.

Telus, M., Dauphas, N., Moynier, F., Tissot, F. L. H., Teng, F.-Z., Nabelek, P. I., Craddock, P. R., Groat, L. A. (2012) Iron, zinc, magnesium and uranium isotopic fractionation during continental crust differentiation: The tale from migmatites, granitoids, and pegmatites. *Geochimica et Cosmochimica Acta* 97:247-265. doi: 10.1016/j.gca.2012.08.024.

Urey, H. C. (1947) The thermodynamic properties of isotopic substances. *Journal of the Chemical Society (Resumed)*:562-581.

van Achterbergh, E., Ryan, C. G., Griffin, W. L. (2000) GLITTER On-line Interactive Data Reduction for LA-ICPMS. Macquarie Research Ltd.

van der Walt, T. N., Strelow, F. W. E., Verheij, R. (1985) The influence of crosslinkage on the distribution coefficients and anion exchange behaviour of some elements in hydrochloric acid. *Solvent Extraction and Ion Exchange* 3:723-740. doi: 10.1080/07366298508918536.

Van der Westhuizen, W. A., De Bruiyn, H., Meintjes, P. G. (1991) The Ventersdorp Supergroup: an overview. *Journal of African Earth Sciences* 13:83-105.

Van Rensburg, W. C. J. (1965) Copper Mineralization in the Carbonate Members and Phoscorite, Phalaborwa, South Africa. University of Wisconsin-Madison, pp 242.

Von Gruenewaldt, G., Sharpe, M. R., Hatton, C. J. (1985) The Bushveld Complex; introduction and review. *Economic Geology* 80:803-812.

Vielreicher, N. M., Groves, D. I., Vielreicher, R. M. (2000) The Phalaborwa (Palabora) deposit and its potential connection to iron-oxide copper-gold deposits of Olympic Dam type In: Porter, T. M. (ed) Hydrothermal Iron Oxide Copper-Gold & Related Deposits: A Global Perspective. PGC Publishing, Adelaide, pp 321-329.

Walraven, F., Armstrong, R., Kruger, F. (1990) A chronostratigraphic framework for the north-central Kaapvaal craton, the Bushveld Complex and the Vredefort structure. *Tectonophysics* 171:23-48.

Walter, B. F., Scharrer, M., Burisch, M., Apukthina, O., Markl, G. (2019) Limited availability of sulfur promotes copper-rich mineralization in hydrothermal Pb-Zn veins: a case study from the Schwarzwald, SW Germany. *Chemical Geology* doi: 10.1016/j.chemgeo.2019.119358.

Wang, P., Dong, G., Santosh, M., Liu, K., Li, X. (2017) Copper isotopes trace the evolution of skarn ores: A case study from the Hongshan-Hongniu Cu deposit, southwest China. *Ore Geology Reviews* 88:822-831. doi: 10.1016/j.oregeorev.2016.11.023.

Wang, Y., Zhu, X.-K., Cheng, Y. (2015) Fe isotope behaviours during sulfide-dominated skarn-type mineralisation. *Journal of Asian Earth Sciences* 103:374-392. doi: 10.1016/j.jseaes.2014.11.005.

Wang, Y., Zhu, X.-K., Mao, J.-W., Li, Z.-H., Cheng, Y.-B. (2011) Iron isotope fractionation during skarn-type metallogeny: A case study of Xinqiao Cu–S–Fe–Au deposit in the Middle–Lower Yangtze valley. *Ore Geology Reviews* 43:194-202. doi: 10.1016/j.oregeorev.2010.12.004.

Wawryk, C. M., Foden, J. D. (2015) Fe-isotope fractionation in magmatic-hydrothermal mineral deposits: A case study from the Renison Sn–W deposit, Tasmania. *Geochimica et Cosmochimica Acta* 150:285-298. doi: 10.1016/j.gca.2014.09.044.

Wawryk, C. M., Foden, J. D. (2017) Iron-isotope systematics from the Batu Hijau Cu-Au deposit, Sumbawa, Indonesia. *Chemical Geology* 466:159-172. doi: 10.1016/j.chemgeo.2017.06.004.

Weis, F. (2013) Oxygen and Iron Isotope Systematics of the Grängensberg Mining District (GMD), Central Sweden. Uppsala universitet, pp 83.

Welch, S. A., Beard, B. L., Johnson, C. M., Braterman, P. S. (2003) Kinetic and equilibrium Fe isotope fractionation between aqueous Fe(II) and Fe(III). *Geochimica et Cosmochimica Acta* 67:4231-4250. doi: 10.1016/s0016-7037(03)00266-7.

Wells, S., Alfe, D., Blanchard, L., Brodholt, J., Calleja, M., Catlow, R., Price, D., Tyler, R., Wright, K. (2005) Ab-initio simulations of magnetic iron sulphides. *Molecular Simulation* 31:379-384. doi: 10.1080/08927020500066361.

Weyer, S., Ionov, D. A. (2007) Partial melting and melt percolation in the mantle: The message from Fe isotopes. *Earth and Planetary Science Letters* 259:119-133. doi: 10.1016/j.epsl.2007.04.033.

Weyer, S., Schwieters, J. B. (2003) High precision Fe isotope measurements with high mass resolution MC-ICPMS. *International Journal of Mass Spectrometry* 226:355-368. doi: 10.1016/s1387-3806(03)00078-2.

Weyer, S., Anbar, A., Brey, G., Munker, C., Mezger, K., Woodland, A. (2005) Iron isotope fractionation during planetary differentiation. *Earth and Planetary Science Letters* 240:251-264. doi: 10.1016/j.epsl.2005.09.023.

Wiesli, R. A., Beard, B. L., Johnson, C. M. (2004) Experimental determination of Fe isotope fractionation between aqueous Fe(II), siderite and "green rust" in abiotic systems. *Chemical Geology* 211:343-362. doi: 10.1016/j.chemgeo.2004.07.002.

Willbold, M., Hibbert, K., Lai, Y.-J., Freymuth, H., Hin, R. C., Coath, C., Vils, F., Elliott, T. (2015) High-precision mass-dependent molybdenum isotope variations in magmatic rocks determined by double-spike MC-ICP-MS. *Geostandards and Geoanalytical Research* 40:389-403. doi: 10.1111/ggr.12109.

Williams, H. M., Bizimis, M. (2014) Iron isotope tracing of mantle heterogeneity within the source regions of oceanic basalts. *Earth and Planetary Science Letters* 404:396-407. doi: 10.1016/j.epsl.2014.07.033.

Williams H, McCammon C, Peslier A, Halliday A, Teutsch N, Levasseur S, Burg J-P (2004) Iron isotope fractionation and the oxygen fugacity of the mantle. *Science* 304:1656-1659. doi: 10.1126/science.1095679.

Williams, H., Peslier, A., McCammon, C., Halliday, A., Levasseur, S., Teutsch, N., Burg, J. (2005) Systematic iron isotope variations in mantle rocks and minerals: The effects of partial melting and oxygen fugacity. *Earth and Planetary Science Letters* 235:435-452. doi: 10.1016/j.epsl.2005.04.020.

Williams, H. M., Prytulak, J., Woodhead, J. D., Kelley, K. A., Brounce, M., Plank, T. (2018) Interplay of crystal fractionation, sulfide saturation and oxygen fugacity on the iron isotope composition of arc lavas: An example from the Marianas. *Geochimica et Cosmochimica Acta* 226:224-243. doi: 10.1016/j.gca.2018.02.008.

Wilson, A. H. (2015) The Earliest Stages of Emplacement of the Eastern Bushveld Complex: Development of the Lower Zone, Marginal Zone and Basal Ultramafic Sequence. *Journal of Petrology* 56:347-388. doi: 10.1093/petrology/egv003.

Winter, H. (1976) A lithostratigraphic classification of the Ventersdorp succession. *South African Journal of Geology* 79:31-46.

Wohlgemuth-Ueberwasser, C. C., Ballhaus, C., Berndt, J., Stotter nee Paliulionyte, V., Meisel, T. (2007) Synthesis of PGE sulfide standards for laser ablation inductively coupled mass spectrometry (LA-ICP-MS). *Contributions to Mineralogy and Petrology* 154:607-617. doi: 10.1007/s00410-007-0212-x.

Wu, L., Beard, B. L., Roden, E. E., Kennedy, C. B., Johnson, C. M. (2010) Stable Fe isotope fractionations produced by aqueous Fe(II)-hematite surface interactions. *Geochimica et Cosmochimica Acta* 74:4249-4265. doi: 10.1016/j.gca.2010.04.060.

Wu, F.-Y., Yang, Y.-H., Li, Q.-L., Mitchell, R. H., Dawson, J. B. (2011) *In situ* determination of U-Pb ages and Sr-Nd-Hf isotopic constraints on the petrogenesis of the Phalaborwa carbonatite Complex, South Africa. *Lithos* 127:309-322. doi: 10.1016/j.lithos.2011.09.005.

Wronkiewicz, D. J., Condie, K. C. (1990) Geochemistry and mineralogy of sediments from the Ventersdorp and Transvaal Supergroups, South Africa: cratonic evolution during the early Proterozoic. *Geochimica et Cosmochimica Acta* 54:343-354.

Yuhara, M., Kohno, M., Kagami, H., Hiroi, Y., Tsuchiya, N. (2003) Geochemistry of syenite of the Phalaborwa Carbonatite Complex, South Africa. *Polar Geoscience* 16:176-195.

Zambardi, T., Lundstrom, C. C., Li, X., McCurry, M. (2014) Fe and Si isotope variations at Cedar Butte volcano; insight into magmatic differentiation. *Earth and Planetary Science Letters* 405:169-179. doi: 10.1016/j.epsl.2014.08.020.

Zeh, A., Ovtcharova, M., Wilson, A. H., Schaltegger, U. (2015) The Bushveld Complex was emplaced and cooled in less than one million years – results of zirconology, and geotectonic implications. *Earth and Planetary Science Letters* 418:103-114. doi: 10.1016/j.epsl.2015.02.035.

Zhao, Y., Xue, C., Liu, S.-A., Mathur, R., Zhao, X., Yang, Y., Dai, J., Man, R., Liu, X. (2019) Redox reactions control Cu and Fe isotope fractionation in a magmatic Ni–Cu mineralization system. *Geochimica et Cosmochimica Acta* 249:42-58. doi: 10.1016/j.gca.2018.12.039.

Zhao, X., Zhang, H., Zhu, X., Tang, S., Tang, Y. (2010) Iron isotope variations in spinel peridotite xenoliths from North China Craton: implications for mantle metasomatism. *Contributions to Mineralogy and Petrology* 160:1-14. doi: 10.1007/s00410-009-0461-y.

Zhao, X., Zhang, H., Zhu, X., Tang, S., Yan, B. (2012) Iron isotope evidence for multistage melt–peridotite interactions in the lithospheric mantle of eastern China. *Chemical Geology* 292-293:127-139. doi: 10.1016/j.chemgeo.2011.11.016.

Zhao, X.-M., Zhang, H.-F., Zhu, X.-K., Zhu, B., Cao, H.-h. (2015) Effects of melt percolation on iron isotopic variation in peridotites from Yangyuan, North China Craton. *Chemical Geology* 401:96-110. doi: 10.1016/j.chemgeo.2015.02.031.

Zhu, X., Guo, Y., Williams, R., O'nions, R., Matthews, A., Belshaw, N., Canters, G., De Waal, E., Weser, U., Burgess, B. (2002) Mass fractionation processes of transition metal isotopes. *Earth and Planetary Science Letters* 200:47-62.

Zhu, X. K., O'Nions, R. K., Guo, Y., Belshaw, N. S., Rickard, D. (2000) Determination of natural Cu-isotope variation by plasma-source mass spectrometry: implications for use as geochemical tracers. *Chemical Geology* 163:139-149. doi: 10.1016/S0009-2541(99)00076-5.

Zhu, B., Zhang, H.-F., Zhao, X.-M., He, Y.-S. (2016) Iron isotope fractionation during skarn-type alteration: Implications for metal source in the Han-Xing iron skarn deposit. *Ore Geology Reviews* 74:139-150. doi: 10.1016/j.oregeorev.2015.11.001.

Appendix A: List of samples used for PGE and trace element investigations (Chapter 3)

Bore holes and their GPS coordinates as well as sample references and characteristics. BC = banded carbonatite, PC = phoscorite, TC = transgressive carbonatite, MP = micaceous clinopyroxenite

Drillcore	Collar GPS coordinates	Sample	Depth	Rock type
SL113	23°59'12'' S; 31°07'33'' E	B61(2)	-410.8	PC
SL139	23°59'21'' S; 31°07'30'' E	B61(2)a	-406.87	TC
		B61(2)b	-410.4	PC/BC
VS-12	23°59'43'' S; 31°08'18'' E	B61(ol)	-398.03	MP
SL139	23°59'21'' S; 31°07'30'' E	B62(2)a	-417.5	PC
		B62(2)b	-415.2	TC
		B62(2)c	-418.2	TC
		B63(2)a	-419.75	TC
		B63(2)b	-423.28	PC
SL113	23°59'12'' S; 31°07'33'' E	B65(2)	-434.56	PC
		B66(2)	-444	PC
		B67(2)	-455.85	BC
SMC1	23°59'24'' S; 31°07'35'' E	B05	-40.6	BC
DC28	23°59'26'' S; 31°08'18'' E	B05(ol)	-18.28	MP
SL140	23°59'24'' S; 31°07'49'' E	B08(2)	-50.7	BC
SL94	23°59'36'' S; 31°07'43'' E	B22	-133.08	BC

Appendix B: Mineral Liberation Analysis data (Chapter 3)

Modal proportions of minerals in polished mounts for each sample. BC = banded carbonatite, PC = phoscorite, TC = transgressive carbonatite, MP = micaceous clinopyroxenite

Borehole-Sample	SL113-B67(2)	SMC1-B05	SL140-B08(2)	SL94-B22	SL139-B61(2)b
Rock type	BC	BC	BC	BC	PC/BC
Quartz (%)	0	0	0	0	0
Plagioclase	0	0	0	0	0
Biotite	0	0	0	0	0
Phlogopite	0.04	0.12	0.57	1.99	1.12
Olivine	0.01	0	3.27	0.07	7.85
Diopside	0	1.13	0	0	0
Chrysotile	0.51	0.24	1.96	1.5	9.63
Baddeleyite	0.03	0.01	0.26	0.02	0.05
Calcite	77.78	90.67	62.87	45.17	11.31
Dolomite	10.1	4.08	2.61	1.68	3.56
Apatite	6.93	2.42	10.6	4.27	9.55
Chalcopyrite	0	0	0.03	0	0
Bornite (Cc)	0.01	0	0.65	1.24	0
Chalcocite	0	0	0	0.08	0
Valleriite	0	0	0	0.02	0.29
Fe-oxide	4.47	1.25	17.12	43.71	56.05
Ilmenite	0.03	0	0	0.08	0.09
Total	99.91	99.92	99.94	99.83	99.5

Borehole-Sample	SL139-B63(2)b	SL113-B66(2)	SL113-B61(2)	SL113-B65(2)	SL139-B63(2)a
Rock type	PC	PC	PC	PC	TC
Quartz (%)	0	0	0	0.02	0
Plagioclase	0	0	0	0	0
Biotite	0	0.16	0.01	0.01	0
Phlogopite	4.8	2.09	0.51	0.82	0.01
Olivine	16.55	0.54	0.86	0.24	0.2
Diopside	0	0	0.01	0.01	0
Chrysotile	8.88	32.03	19.65	45.35	0.74
Baddeleyite	0.01	4.04	0.4	0.28	0
Calcite	7.5	0.04	11.95	0.65	83.3
Dolomite	5.08	3.09	3.24	0.35	14.94
Apatite	27.09	21.12	32.76	43.34	0.44
Chalcopyrite	1.94	0	0	0	0
Bornite (Cc)	0.06	0.07	0.1	0	0.02
Chalcocite	0	0	0.05	0.01	0
Valleriite	0.14	0.01	0.01	0	0.09
Fe-oxide	27.75	34.02	29.29	8.37	0.15
Ilmenite	0	2.37	0.99	0.21	0
Total	99.8	99.58	99.83	99.66	99.89

Borehole-Sample	SL139-B61(2)a	SL139-B62(2)b	SL139-B62(2)c	VS12-B61(ol)	DC28-B05(ol)
Rock type	TC	TC	TC	MP	MP
Quartz (%)	0.01	0	0	0	0
Plagioclase	0	0	0.01	0	0
Biotite	0	0	0	20.96	6.53
Phlogopite	0	0.16	0	11.65	59.43
Olivine	1.01	0.51	0	0	0
Diopside	0.01	0	0	12.2	9.09
Chrysotile	0	2.43	0	0.02	6.88
Baddeleyite	0	0.01	0	0.01	0
Calcite	94.09	49.57	31.68	0.08	0.1
Dolomite	0.6	7.61	49.45	0	0
Apatite	1.39	36.84	2.28	36.52	12.9
Chalcopyrite	0	0	3.31	0.17	0
Bornite (Cc)	0	0	10.42	0.42	0
Chalcocite	0	0	0	0.01	0
Valleriite	0	0	1.55	0.02	0
Fe-oxide	2.86	2.75	0.98	0.37	3.47
Ilmenite	0	0	0	16.48	1.35
Total	99.97	99.88	99.68	98.91	99.75

Borehole-Sample	SL139-B62(2)a
Rock type	TC
Quartz (%)	0
Plagioclase	0
Biotite	0
Phlogopite	0.08
Olivine	0
Diopside	0
Chrysotile	4.55
Baddeleyite	0
Calcite	4.55
Dolomite	22.93
Apatite	9.84
Chalcopyrite	1.29
Bornite (Cc)	39.09
Chalcocite	0
Valleriite	15.97
Fe-oxide	0.48
Ilmenite	0
Total	98.78

Copper deportment. BC = banded carbonatite, PC = phoscorite, TC = transgressive carbonatite, MP = micaceous clinopyroxenite

Borehole-Sample	SL113-B67(2)	SMC1-B05	SL140-B08(2)	SL94-B22	SL139-B61(2)b
Rock type	BC	BC	BC	BC	PC/BC
Chalcopyrite (%)	16.26	73.55	2.21	0.08	0
Bornite (Cc) (%)	78.58	26.45	96.93	91.54	0.02
Chalcocite (%)	2.58	0	0.71	7.69	0.01
Valleriite (%)	2.58	0	0.15	0.69	99.97
Total (%)	100	100	100	100	100

Borehole-Sample	SL139-B63(2)b	SL113-B66(2)	SL113-B61(2)	SL113-B65(2)	SL139-B63(2)a
Rock type	PC	PC	PC	PC	TC
Chalcopyrite (%)	90.45	3.62	0.14	0.14	4.55
Bornite (Cc) (%)	4.93	92.99	60.02	2.55	31.94
Chalcocite (%)	0.02	0.28	38.05	89.28	0
Valleriite (%)	4.6	3.11	1.79	8.04	63.51
Total	100	100	100	100.01	100

Borehole-Sample	SL139-B61(2)a	SL139-B62(2)b	SL139-B62(2)c	VS12-B61(ol)	DC28-B05(ol)
Rock type	TC	TC	TC	MP	MP
Chalcopyrite (%)	4.81	0	14.12	17.12	0
Bornite (Cc) (%)	0	100	81.29	78.7	25.06
Chalcocite (%)	0	0	0.01	2.45	0
Valleriite (%)	95.19	0	4.58	1.73	74.94
Total	100	100	100	100	100

Borehole-Sample	SL139-B62(2)a
Rock type	TC
Chalcopyrite (%)	1.54
Bornite (Cc) (%)	85.28
Chalcocite (%)	0
Valleriite (%)	13.18
Total	100

Unaveraged mineral association statistics

Borehole-sample	SL113-B67(2)				SMC1-B05			
Lithology	Banded carbonatite				Banded carbonatite			
Mineral	Ccp	Bn	Cc	V	Ccp	Bn	Cc	V
Biotite	0	0	0	0	0	0	0	0
Clinochlore	0	0	0	0	0	0	0	0
Phlogopite	0.44	0	0	2.4	0	0	0	0
Titanite	0	0	0	0	0	0	0	0
Olivine	0	0	0	0	0	0	0	0
Diopside	0	0	0	0	0	0	0	0
Chrysotile	0	0	0	2.83	0	0	0	0
Zircon	0	0	0	0	0	0	0	0
Pyrrhotite	0	0	0	0.93	0	0	0	0
Chalcopyrite	0	27.66	5.65	4.17	0	32.53	0	0
Bornite (Cc)	36.14	0	14.2	6.37	16.04	0	0	0
Chalcocite	0.57	1.1	0	3.2	0	0	0	0
Valleriite	2.4	2.8	18.17	0	0	0	0	0
Sphalerite	0	0	0	0	0	0	0	0
Galena	0	0	0	0	0	0	0	0
CoNiFe Sulphide	0	0	0	0	0	0	0	0
Fe-oxide	4.17	11.85	0	8.99	10.67	0	0	0
Ilmenite	0	0	0	0	0	0	0	0
Rutile	0	0	0	0	0	0	0	0
Calcite	28.21	24.56	33.65	29.45	73.28	67.47	0	0
Dolomite	21.79	30.82	25.13	27.06	0	0	0	0
Ankerite	0	0	0	0.71	0	0	0	0
Siderite	0	0	0	0	0	0	0	0
Olekminskite	0	0	0	0	0	0	0	0
Apatite	0.4	0.95	3.21	11.82	0	0	0	0
Barite	0	0	0	0	0	0	0	0
Unknown	0	0.26	0	0	0	0	0	0
Total (%)	94.12	100	100	97.93	99.99	100	0	0

Borehole-sample	SL140-B08(2)				SL94-B22			
Lithology	Banded carbonatite				Banded carbonatite			
Mineral	Ccp	Bn	Cc	V	Ccp	Bn	Cc	V
Biotite	0	0	0	0	0	0.02	0.05	0
Clinochlore	0	0.1	0	0	1.42	0.49	0.14	0.96
Phlogopite	0	0.01	0.75	0.39	6.64	4.32	2.86	4.15
Titanite	0	0	0	0	0	0	0	0
Olivine	3.01	2.15	10.96	4.33	0	0.06	0	0.04
Diopside	0	0	0	0	0	0	0	0
Chrysotile	0	0.92	7.78	1.19	0	0.01	0	0.11
Zircon	0	0	0	0	0	0	0	0
Pyrrhotite	0	0	0	0	0	0	0	0
Chalcopyrite	0	15.16	0.92	8.32	0	0.45	0.34	0.56
Bornite (Cc)	64.34	0	8.06	19.22	30.28	0	10.08	20.13
Chalcocite	0.09	0.19	0	1.91	2.76	1.21	0	2.63
Valleriite	1.91	1.04	4.48	0	8.24	4.33	4.7	0
Sphalerite	0	0	0	0	0	0	0	0.05
Galena	0	0	0	0	0	0	0	0
CoNiFe Sulphide	0	0.01	0	0.17	0	0.2	0.64	0.09
Fe-oxide	4.04	13.69	19.61	27.98	13.11	27.95	28.46	49.72
Ilmenite	0	0	0	0	2.75	0.08	0.08	0.2
Rutile	0	0	0	0	0	0	0	0
Calcite	17.41	42.51	27.83	21.04	29.24	37.16	34.67	13.48
Dolomite	2.92	3.91	1.8	2.2	2.29	8.35	6.22	3.01
Ankerite	0.08	0.1	0	0	0	0.11	0.27	0.48
Siderite	0	0.01	4.89	1.3	0	0.04	0	0.24
Olekminskite	0	0	0	0	0	0	0	0
Apatite	2.6	2.56	0	3.42	1.1	0.24	0.33	0.17
Barite	0	0	0	0	0	0	0	0.02
Unknown	0	2.64	1.07	5.73	0	1.53	2.82	1.44
Total (%)	96.4	85	88.15	97.2	97.83	86.55	91.66	97.48

Borehole-sample	SL139-B61(2)b				SL139-B63(2)b			
Lithology	Phoscorite/banded carbonatite				Phoscorite			
Mineral	Ccp	Bn	Cc	V	Ccp	Bn	Cc	V
Biotite	0	0	0	0	0	0	0	0
Clinochlore	0	0	0	0.94	0	0	0	0.36
Phlogopite	0	0	0	0.29	4.17	3.4	0	7.9
Titanite	0	0	0	0	0	0	0	0
Olivine	0	0	0	0.82	17.04	6	0	24.73
Diopside	0	0	0	0	0	0	0	0
Chrysotile	0	12.52	0	0.43	2.71	0.8	0	3.82
Zircon	0	0	0	0	0	0	0	0
Pyrrhotite	0	0	0	0	0	0	0	0
Chalcopyrite	0	0	0	0	0	24	0	21.73
Bornite (Cc)	0	0	0	0	2.35	0	9.12	0.65
Chalcocite	0	0	0	0	0	0	0	0
Valleriite	0	0	0	0	10.06	3.1	0	0
Sphalerite	0	0	0	0	0.04	0	0	0
Galena	0	0	0	0	0	0.1	0	0
CoNiFe Sulphide	0	0	0	0.01	0.02	0.2	0	0.05
Fe-oxide	0	7.68	49.13	52.55	17.59	14	0	11.98
Ilmenite	0	0	0	0.47	0	0	0	0.02
Rutile	0	0	0	0	0	0	0	0
Calcite	0	0	50.87	14.32	18.18	22	0	5.82
Dolomite	0	53.6	0	20.28	7.82	14	48.13	9.62
Ankerite	0	0	0	0.57	0.07	0	0	0.08
Siderite	0	0	0	0.18	0.03	0	0	0.06
Olekminskite	0	0	0	0	0	0	0	0
Apatite	0	0	0	3.47	7.95	8.4	42.75	8.5
Barite	0	0	0	0	0	0	0	0
Unknown	0	0	0	1.16	1.54	0.1	0	1.87
Total (%)	0	73.8	100	95.49	89.57	97	100	97.19

Borehole-sample	SL113-B66(2)				SL113-B61(2)			
Lithology	Phoscorite				Phoscorite			
Mineral	Ccp	Bn	Cc	V	Ccp	Bn	Cc	V
Biotite	0.33	0.29	0	0.46	0	0	0	0
Clinochlore	0.17	0	0	0	0	0.03	0	0
Phlogopite	0.17	0.14	0	0	0	0.22	0.15	0.09
Titanite	0	0	0	0	0	0	0	0
Olivine	2.49	2.18	0	1.41	0.87	3.5	2.35	5.52
Diopside	0	0	0	0	0	0	0	0
Chrysotile	34.05	40.76	17.18	61.29	11.71	10.54	4.32	11.62
Zircon	0	0	0	0	0	0	0	0
Pyrrhotite	0	0	0	0	0	0	0	0
Chalcopyrite	0	2.64	0	2.41	0	0.12	0.49	0.45
Bornite (Cc)	11.59	0	0	3.24	7.82	0	13.52	7.6
Chalcocite	0	0	0	0.05	10.28	4.49	0	5.68
Valleriite	4.74	1.45	3.53	0	7.96	2.11	4.76	0
Sphalerite	0	0	0	0.23	0	0	0	1.16
Galena	0	0	0	0	0	0	0.05	0
CoNiFe Sulphide	0.39	1.61	0	0.79	0	0.08	0.05	0.29
Fe-oxide	29.06	33.21	67.36	12.29	9.14	18.6	22.32	19.47
Ilmenite	0.29	0	0	0.58	0	0.44	2.29	2.26
Rutile	0	0	0	0	0	0	0	0
Calcite	3.62	4.65	11.93	2.14	26	21.96	15.66	10.55
Dolomite	11.39	5.72	0	8.09	6	13.65	7.65	6.44
Ankerite	0.31	0.87	0	0.94	0	0.41	0.29	0.82
Siderite	0	0.67	0	1.15	0	0.25	0.23	0.27
Olekminskite	0	0	0	0	0	0	0	0
Apatite	0.33	1.3	0	3.92	20.22	19.94	21.21	23.75
Barite	0	0	0	0	0	0	0	0
Unknown	0	0.27	0	0	0	0	0	0
Total (%)	98.93	95.76	100	98.99	100	96.34	95.34	95.97

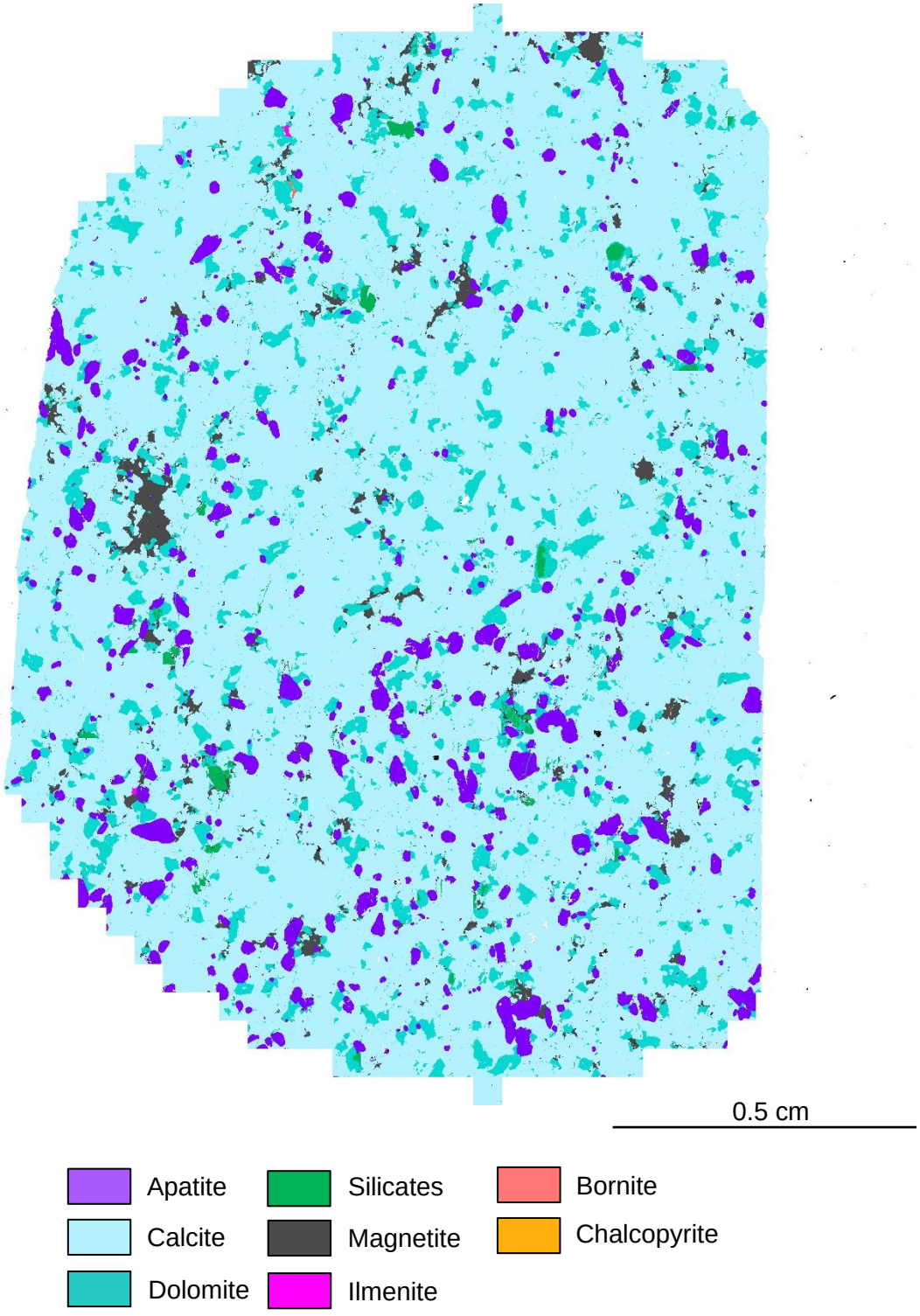
Borehole-sample	SL113-B65(2)				SL139-B63(2)a			
Lithology	Phoscorite				Transgressive carbonatite			
Mineral	Ccp	Bn	Cc	V	Ccp	Bn	Cc	V
Biotite	0	0	0	0	0	0	0	0
Clinochlore	0	0	0	0	0	0	0	0
Phlogopite	17.33	0	0	0	0	0	0	0
Titanite	0	0	0	0	0	0	0	0
Olivine	0	0	0	0	0	0	0	0
Diopside	0	0	0	0	0	0	0	0
Chrysotile	0	0	0	77.26	0	0	0	0.16
Zircon	0	0	0	0	0	0	0	0
Pyrrhotite	0	0	0	0	0.53	0	0	0
Chalcopyrite	0	0	0.57	0	0	3.33	0	0.96
Bornite (Cc)	0	0	1.48	0	3.17	0	0	0.4
Chalcocite	20.71	10.7	0	4.61	0	0	0	0
Valleriite	0	0	3.89	0	8.17	3.59	0	0
Sphalerite	0	0	0	0	0	0.83	0	0.05
Galena	0	0	0	0	0	0	0	0
CoNiFe Sulphide	0	9.47	13.32	0	0	0	0	0.31
Fe-oxide	61.96	33.58	27.26	3.17	1.47	0.39	0	0.05
Ilmenite	0	0	0	0	0	0	0	0
Rutile	0	0	0	0	0	0	0	0
Calcite	0	34.85	27.33	5.12	79.32	59.15	0	57.12
Dolomite	0	11.41	6.45	2.57	4.75	1.16	0	17.43
Ankerite	0	0	3.85	0.99	0	0	0	0.7
Siderite	0	0	0	0	0	0	0	0
Olekminskite	0	0	0	0	0	9.78	0	4.04
Apatite	0	0	15.84	3.67	0	0	0	1.1
Barite	0	0	0	0	0	2.51	0	3.05
Unknown	0	0	0	0	0	0	0	2.75
Total (%)	100	100	99.99	97.39	97.41	80.74	0	88.12

Borehole-sample	SL139-B61(2)a				SL139-B62(2)b			
Lithology	Transgressive carbonatite				Transgressive carbonatite			
Mineral	Ccp	Bn	Cc	V	Ccp	Bn	Cc	V
Biotite	0	0	0	0	0	0	0	0
Clinochlore	0	0	0	0	0	0	0	0
Phlogopite	0	0	0	0	0	0	0	0
Titanite	0	0	0	0	0	0	0	0
Olivine	0	0	0	0	0	0	0	0
Diopside	0	0	0	0	0	0	0	0
Chrysotile	0	0	0	0	0	0	0	0
Zircon	0	0	0	0	0	0	0	0
Pyrrhotite	0	0	0	0	0	0	0	0
Chalcopyrite	0	0	0	0	0	0	0	0
Bornite (Cc)	0	0	0	0	0	0	0	0
Chalcocite	0	0	0	0	0	0	0	0
Valleriite	0	0	0	0	0	0	0	0
Sphalerite	0	0	0	0	0	0	0	0
Galena	0	0	0	0	0	0	0	0
CoNiFe Sulphide	0	0	0	0	0	0	0	0
Fe-oxide	0	0	0	50.57	0	0	0	0
Ilmenite	0	0	0	0	0	0	0	0
Rutile	0	0	0	0	0	0	0	0
Calcite	100	0	0	4.44	0	0	0	0
Dolomite	0	0	0	0	0	0	0	0
Ankerite	0	0	0	0	0	0	0	0
Siderite	0	0	0	10.91	0	0	0	0
Olekminskite	0	0	0	0	0	0	0	0
Apatite	0	0	0	0	0	0	0	0
Barite	0	0	0	0	0	0	0	0
Unknown	0	0	0	34.07	0	0	0	0
Total (%)	100	0	0	99.99	0	0	0	0

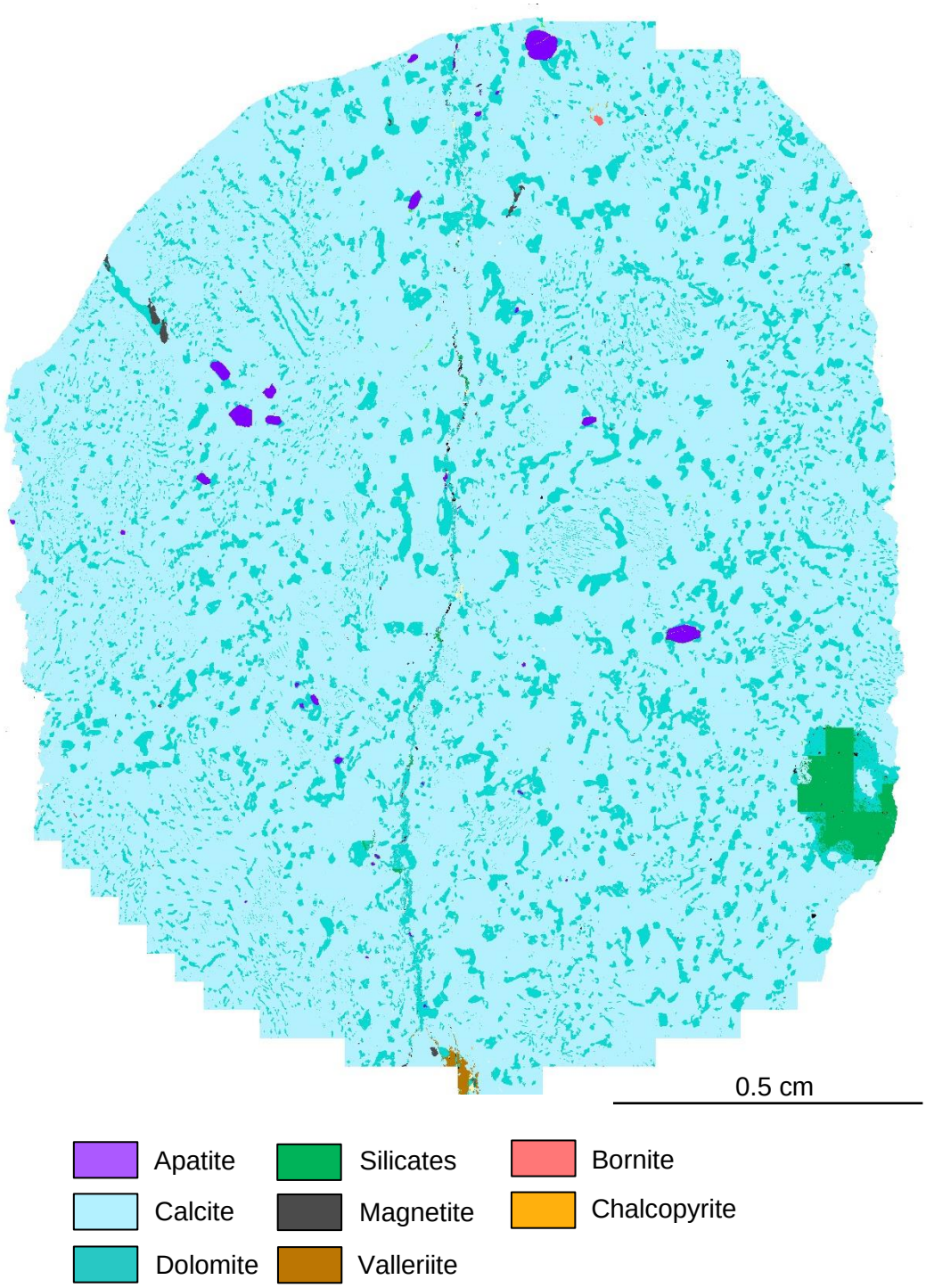
Borehole-sample	SL139-B62(2)c				VS12-B61(ol)			
Lithology	Transgressive carbonatite				Micaceous clinopyroxenite			
Mineral	Ccp	Bn	Cc	V	Ccp	Bn	Cc	V
Biotite	0	0	0	0	22.3	21.93	34.18	33.82
Clinochlore	0.3	0.65	0	0.85	0	0	0	0
Phlogopite	0	0	0	0	8.35	12.42	9.62	19.44
Titanite	0	0	0	0	0.77	0.21	0.59	0.53
Olivine	0	0	0	0	0	0	0	0
Diopside	0	0	0	0	8.62	6.54	4.98	12.28
Chrysotile	0	0.01	0	0.01	1.07	2.53	0	0.42
Zircon	0	0	0	0	0.24	0.64	3.92	0.16
Pyrrhotite	0	0	0	0	0	0	0	0
Chalcopyrite	0	17.94	13.93	5.85	0	14.88	0	5.77
Bornite (Cc)	49.25	0	28.52	31.76	11.98	0	31.21	1.89
Chalcocite	0.02	0.02	0	0.01	0	0.53	0	0
Valleriite	12.18	24.09	7.2	0	2.59	1.05	0	0
Sphalerite	0.01	0	0	0	0	0	0	0
Galena	0.04	0.03	4.64	0	0.18	0.15	0	0.03
CoNiFe Sulphide	0.03	0.1	0	0.13	0	0	0	0
Fe-oxide	0.11	0.57	0.85	9.96	5.82	0.11	0	3.62
Ilmenite	0	0	0	0	5.84	7.46	6.07	1.38
Rutile	0	0	0	0	0.1	0.32	1.09	0.04
Calcite	14.73	21.08	15.98	18.5	1	0.88	0	0.32
Dolomite	10.99	18.87	23.23	26.12	0	0	0	0
Ankerite	0.05	0.08	0	0.27	0.01	0	0	0
Siderite	0	0	0	0.01	0	0	0	0
Olekminskite	0	0.02	0	0.14	0	0	0	0
Apatite	0.29	1.35	0	0.68	26.09	21.84	2.74	17.31
Barite	0	0.04	0	0.01	0	0	0	0
Unknown	0.37	1.88	0.58	0.68	0.81	1.32	0	0.13
Total (%)	88.37	86.73	94.93	94.98	95.77	92.81	94.4	97.14

Borehole-sample	DC28-B05(ol)				SL139-B62(2)a			
Lithology	Micaceous clinopyroxenite				Transgressive carbonatite			
Mineral	Ccp	Bn	Cc	V	Ccp	Bn	Cc	V
Biotite	0	0	0	20.21	0	0	0	0
Clinochlore	0	0	0	0	0	0	0	0
Phlogopite	0	100	0	31.88	0.01	0.09	0	0.07
Titanite	0	0	0	0	0	0	0	0
Olivine	0	0	0	0	0	0	0	0.03
Diopside	0	0	0	0	0	0	0	0
Chrysotile	0	0	0	46.98	0.42	0.86	0	10.42
Zircon	0	0	0	0	0	0	0	0
Pyrrhotite	0	0	0	0	0	0	0	0
Chalcopyrite	0	0	0	0	0	6.23	0	7.96
Bornite (Cc)	0	0	0	0	30.75	0	36.28	43.99
Chalcocite	0	0	0	0	0	0	0	0
Valleriite	0	0	0	0	53.76	60.19	31.1	0
Sphalerite	0	0	0	0	0	0	0	0
Galena	0	0	0	0	0.02	0.08	4.36	0.04
CoNiFe Sulphide	0	0	0	0	0.02	0.03	0	0.03
Fe-oxide	0	0	0	0	0.02	0.13	0	0.77
Ilmenite	0	0	0	0	0	0	0	0
Rutile	0	0	0	0	0	0.01	0	0
Calcite	0	0	0	0	1.67	3.86	0	2.33
Dolomite	0	0	0	0	5.46	7.9	23.82	13.37
Ankerite	0	0	0	0	0.58	0.71	0	2.18
Siderite	0	0	0	0	0	0	0	0
Olekminskite	0	0	0	0	0.51	1.17	0	1.17
Apatite	0	0	0	0	3.59	3.51	0	10.08
Barite	0	0	0	0	0.06	0.2	0	0.14
Unknown	0	0	0	0	0.01	0.03	0	0.02
Total (%)	0	100	0	99.07	96.88	85	95.56	92.6

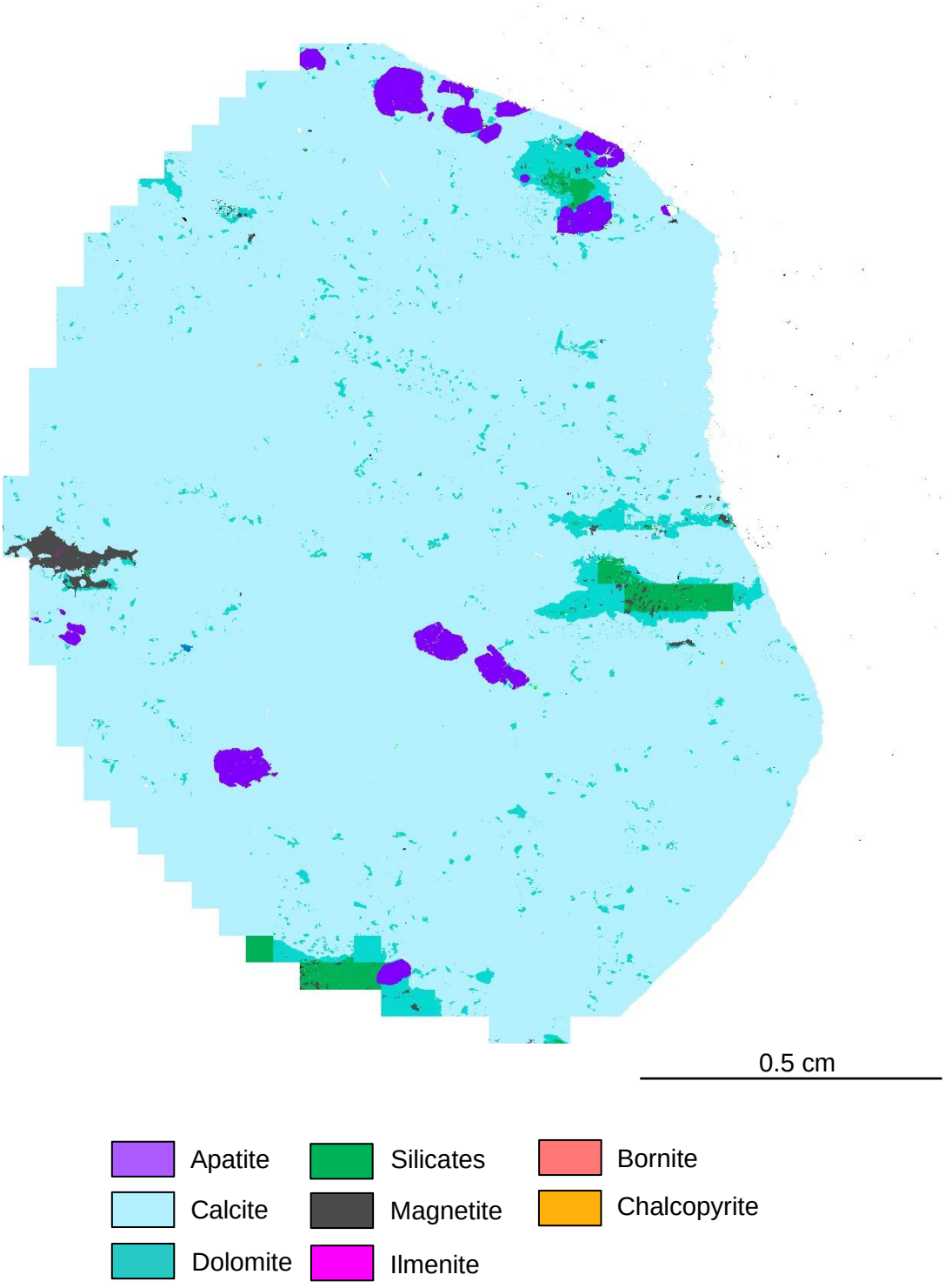
Mineral maps
Borehole – Sample: SL113 – B67(2)



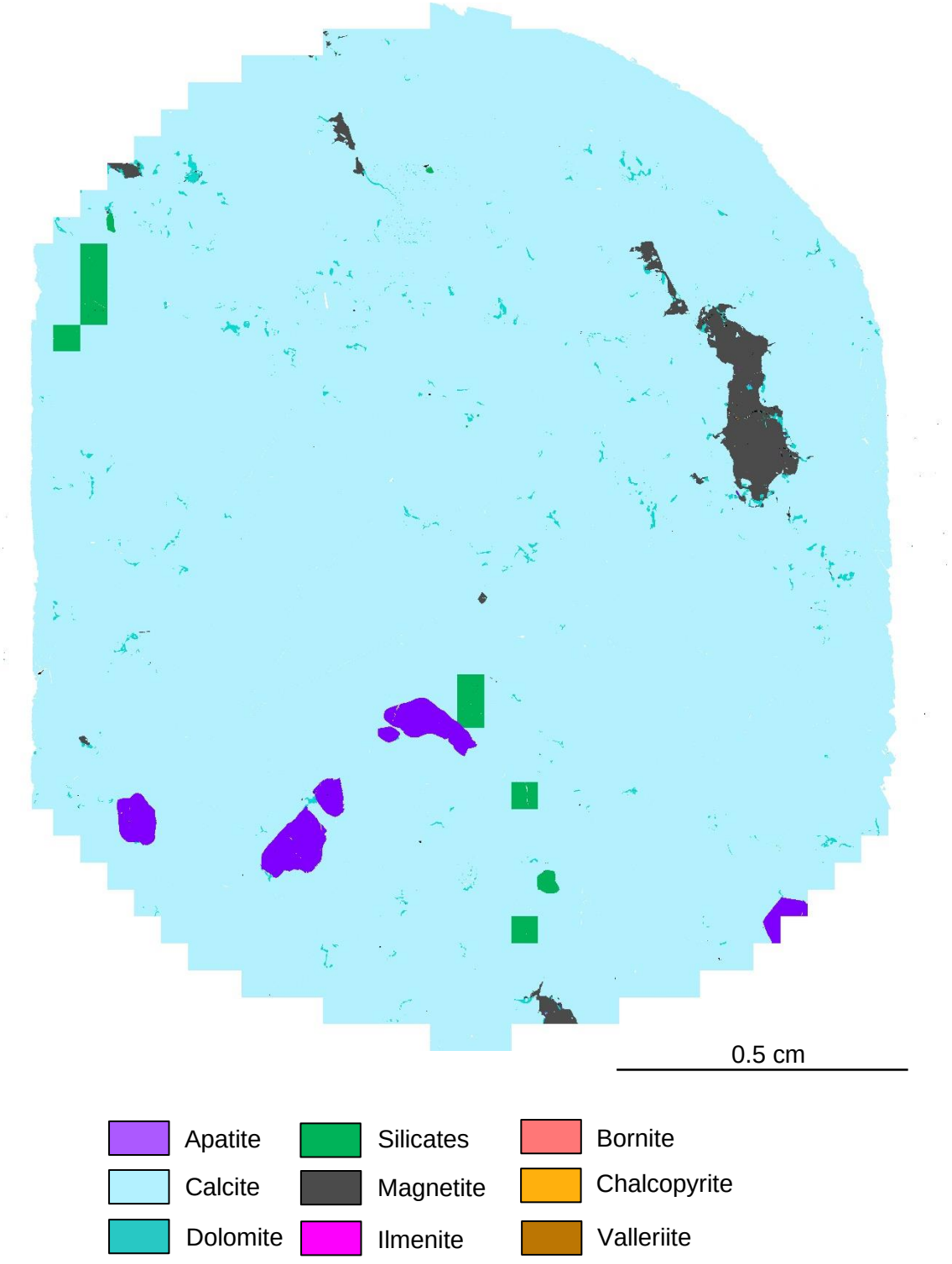
Borehole – Sample: SL139 – B63(2)a



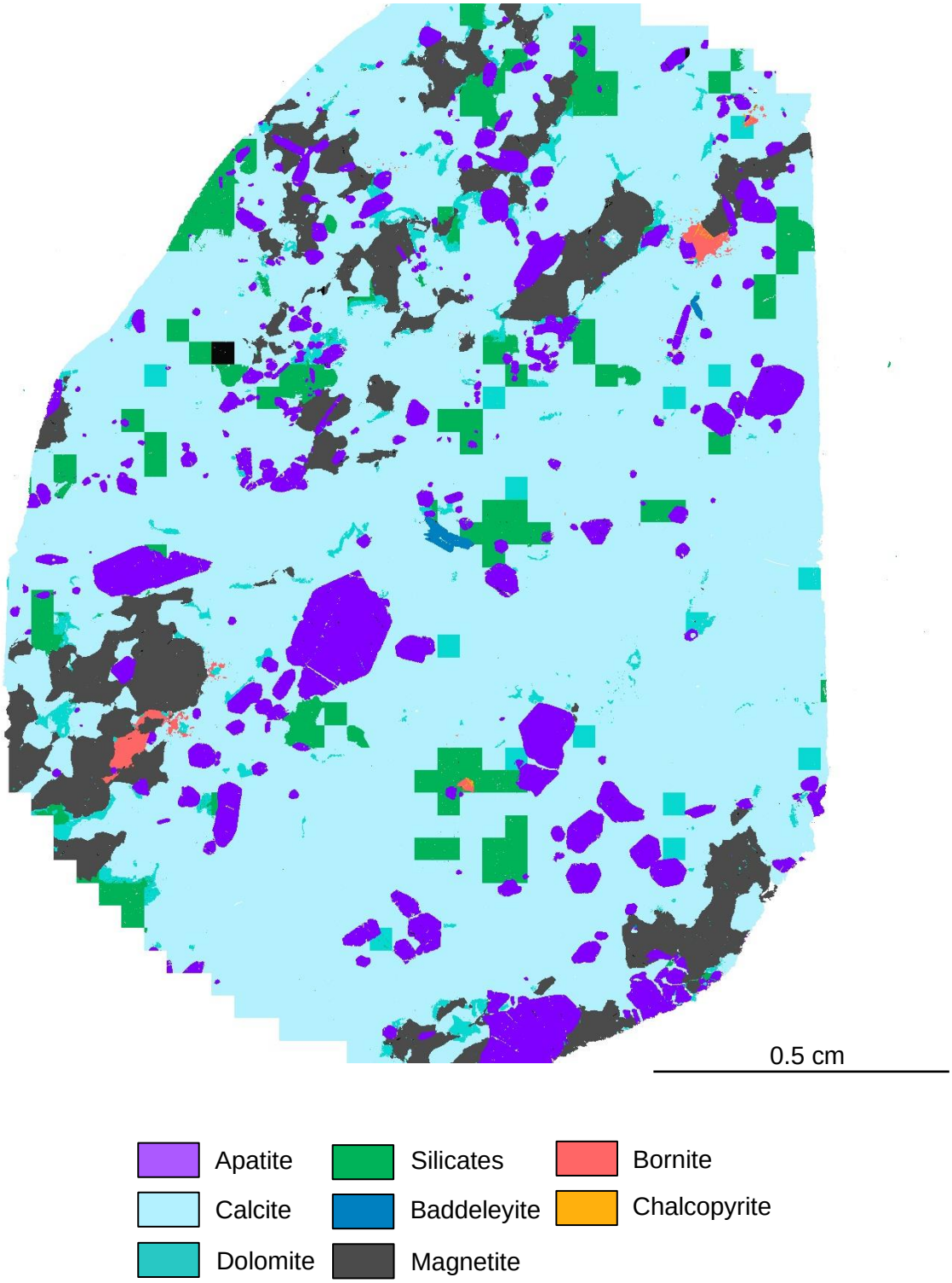
Borehole – Sample: SMC1 – B05



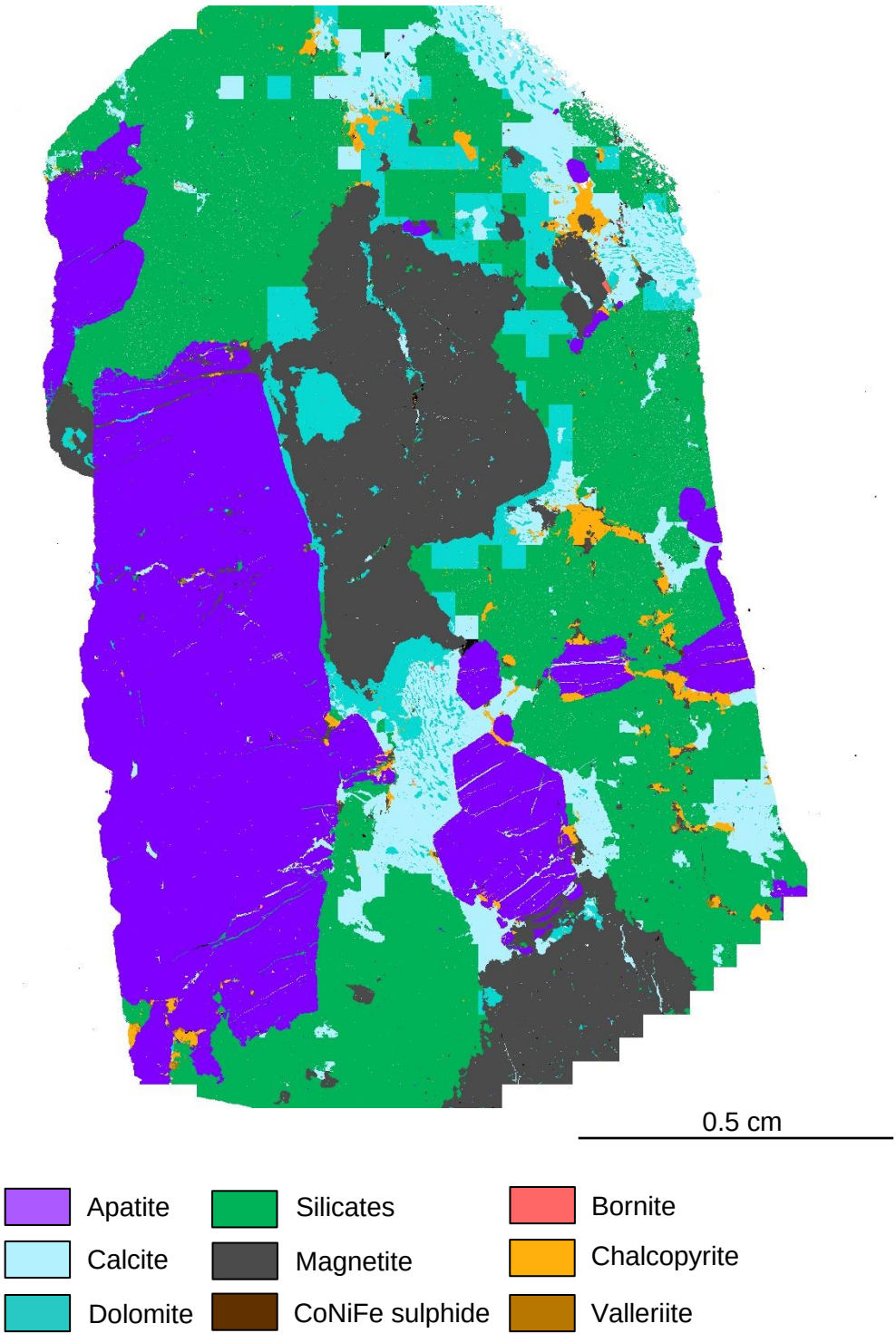
Borehole – Sample: SL139 – B61(2)a



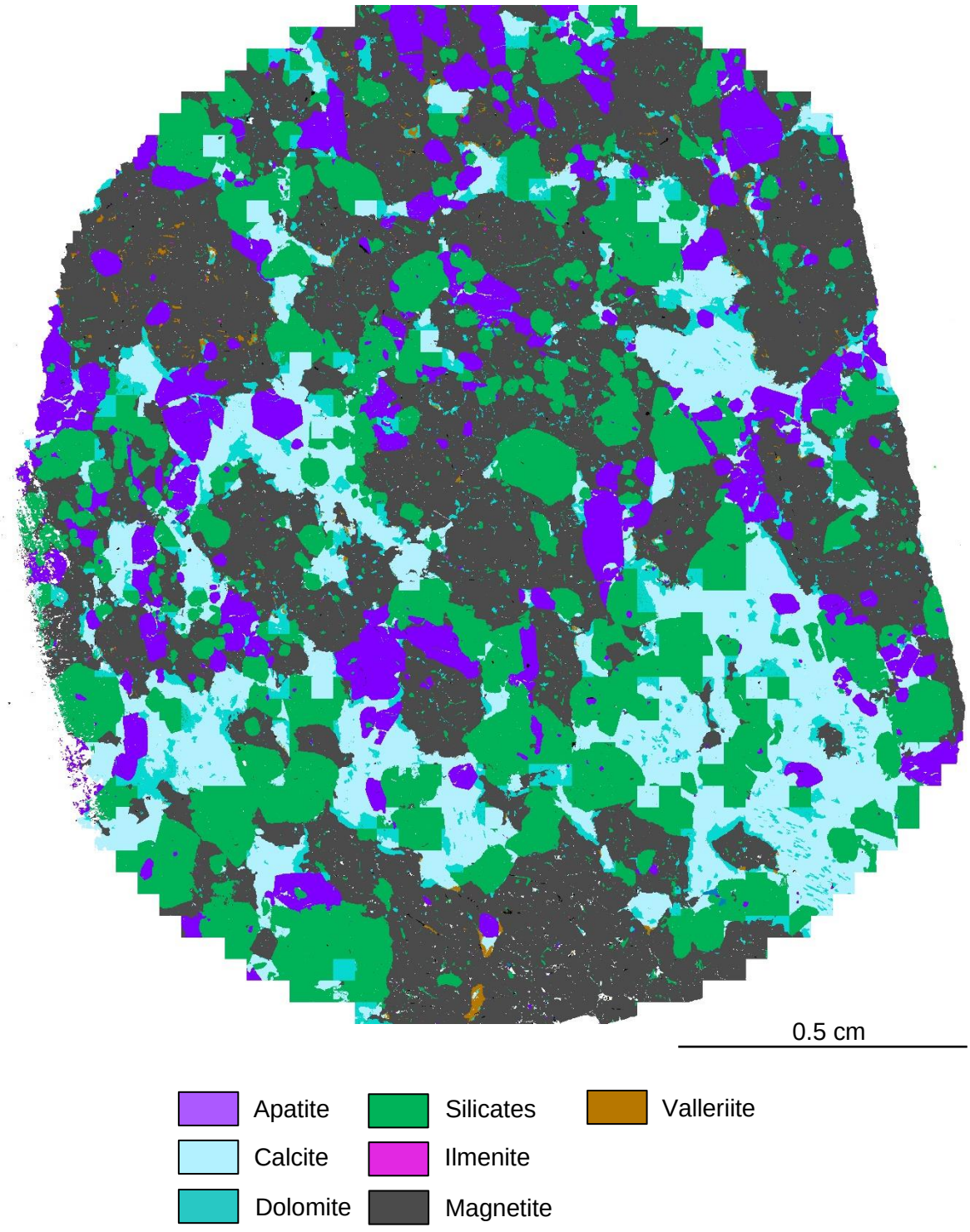
Borehole – Sample: SL140 – B08(2)



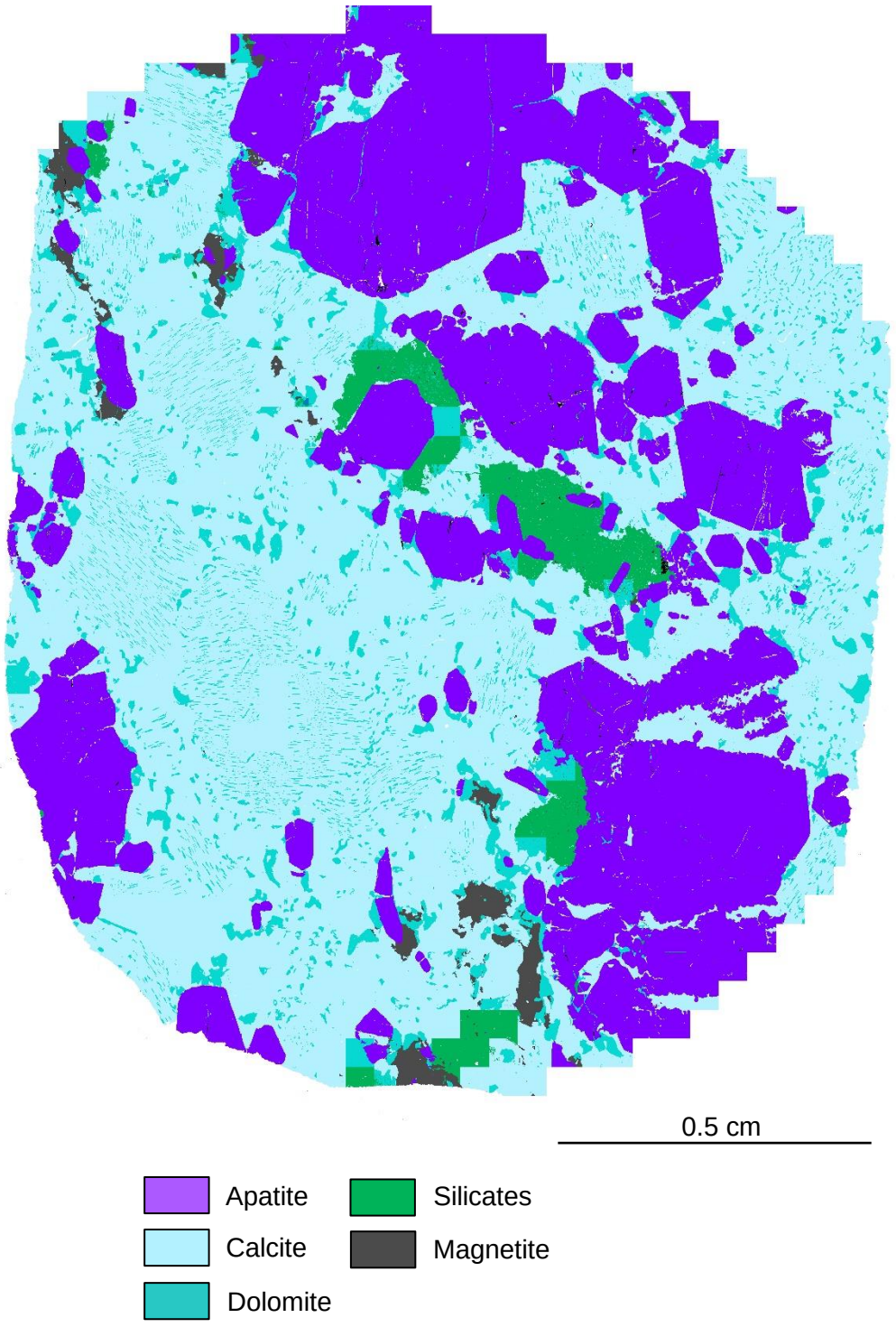
Borehole – Sample: SL139 – B63(2)b



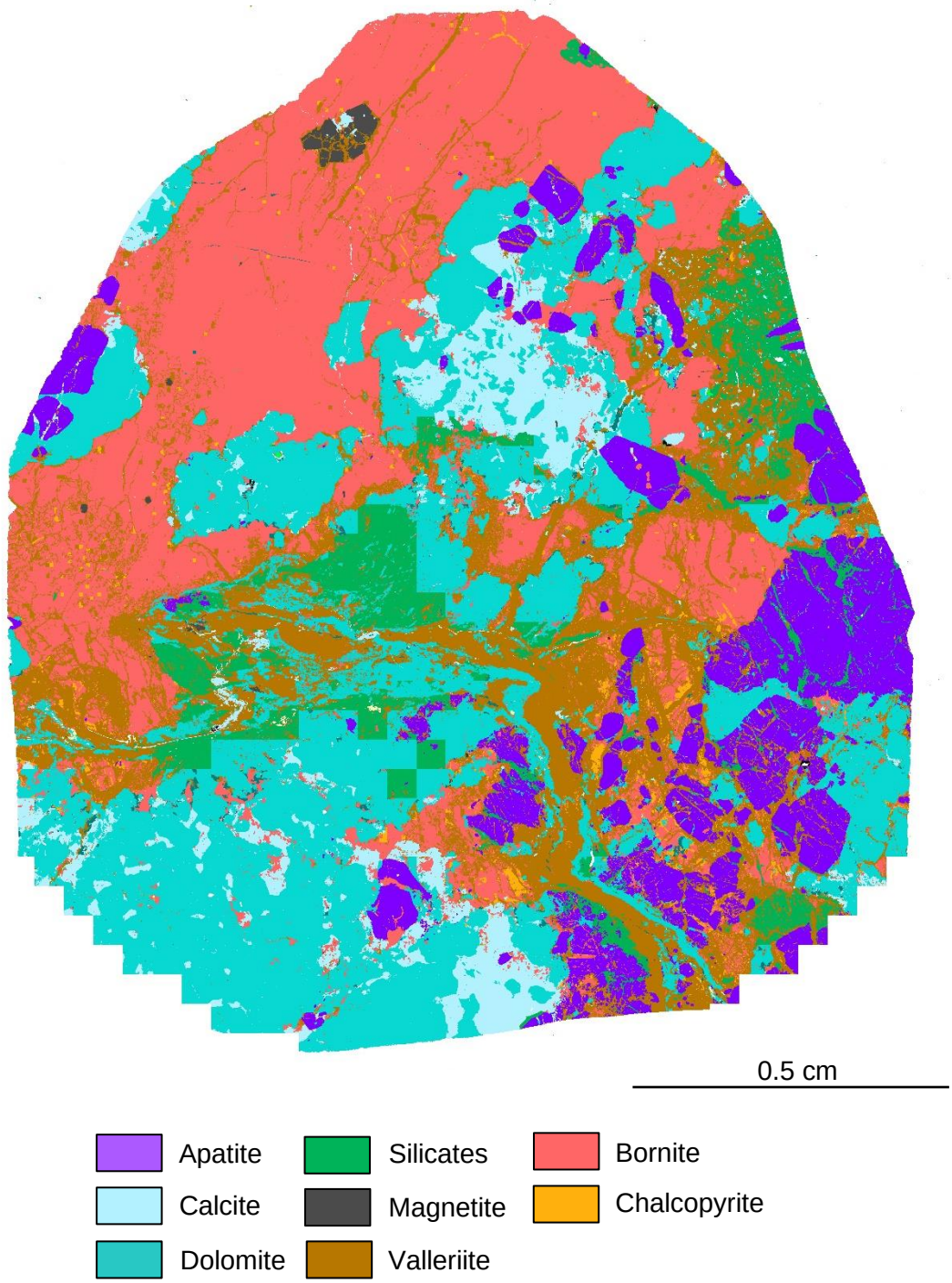
Borehole – Sample: SL139 – B61(2)b



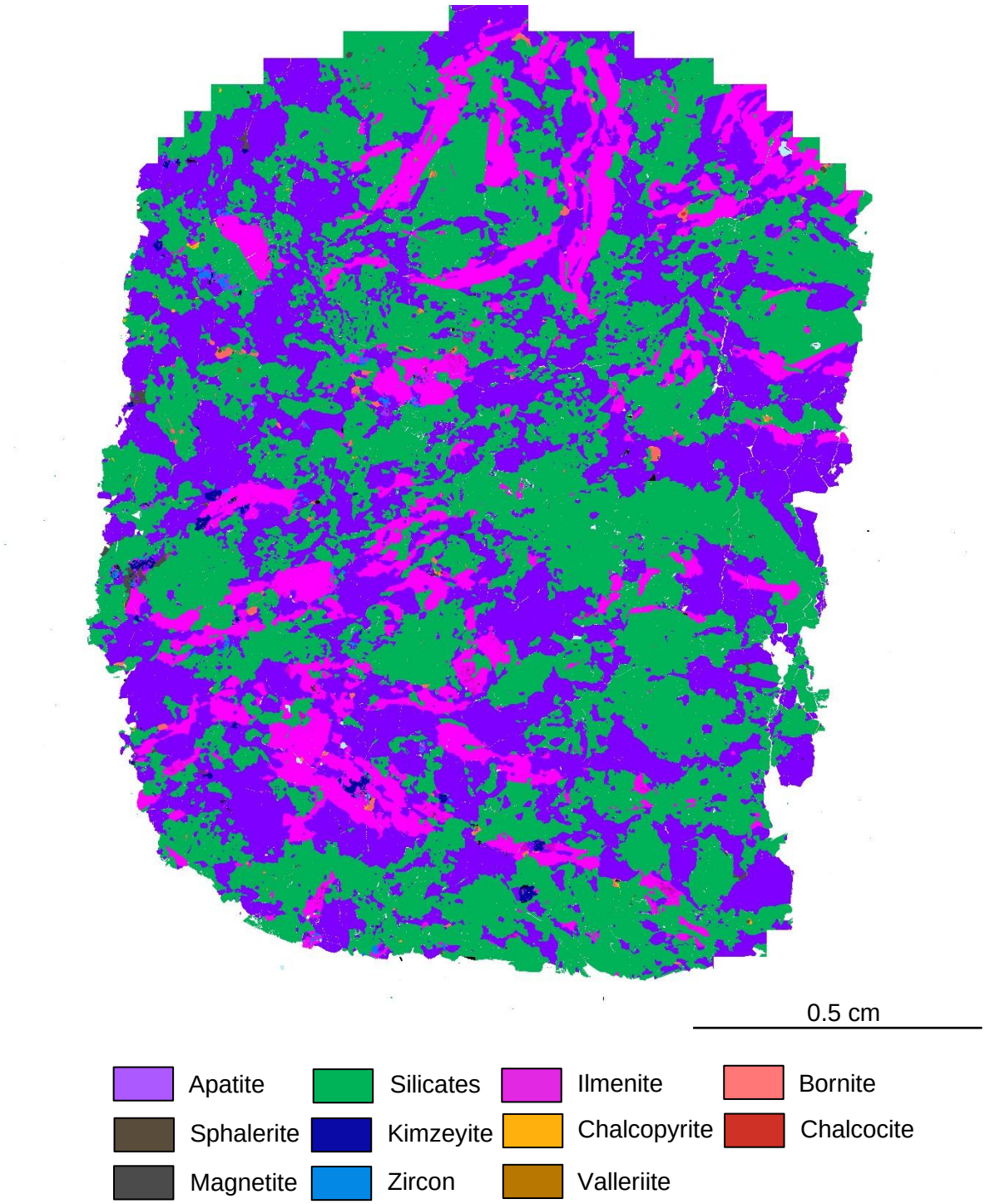
Borehole – Sample: SL139 – B62(2)b



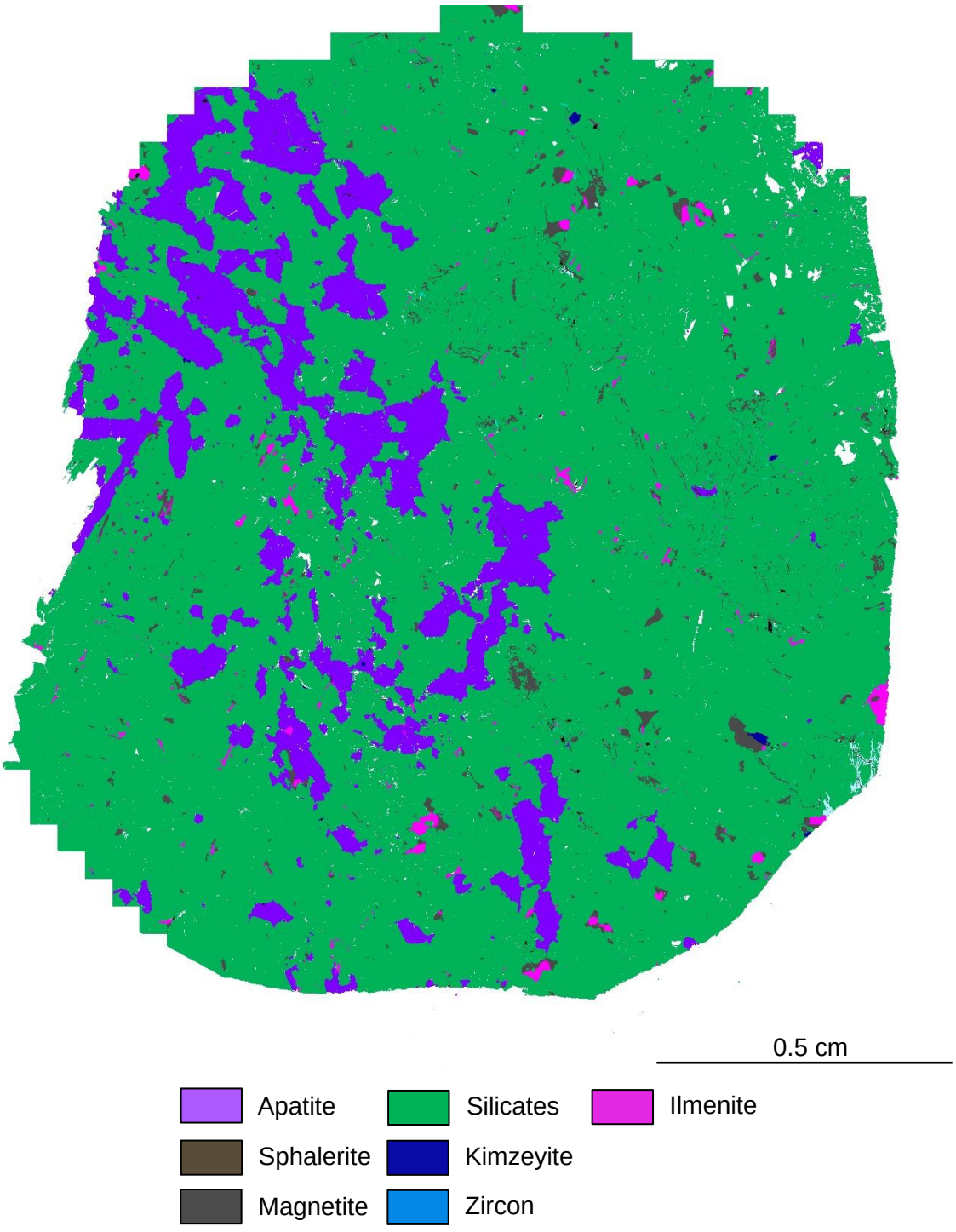
Borehole – Sample: SL139 – B62(2)a



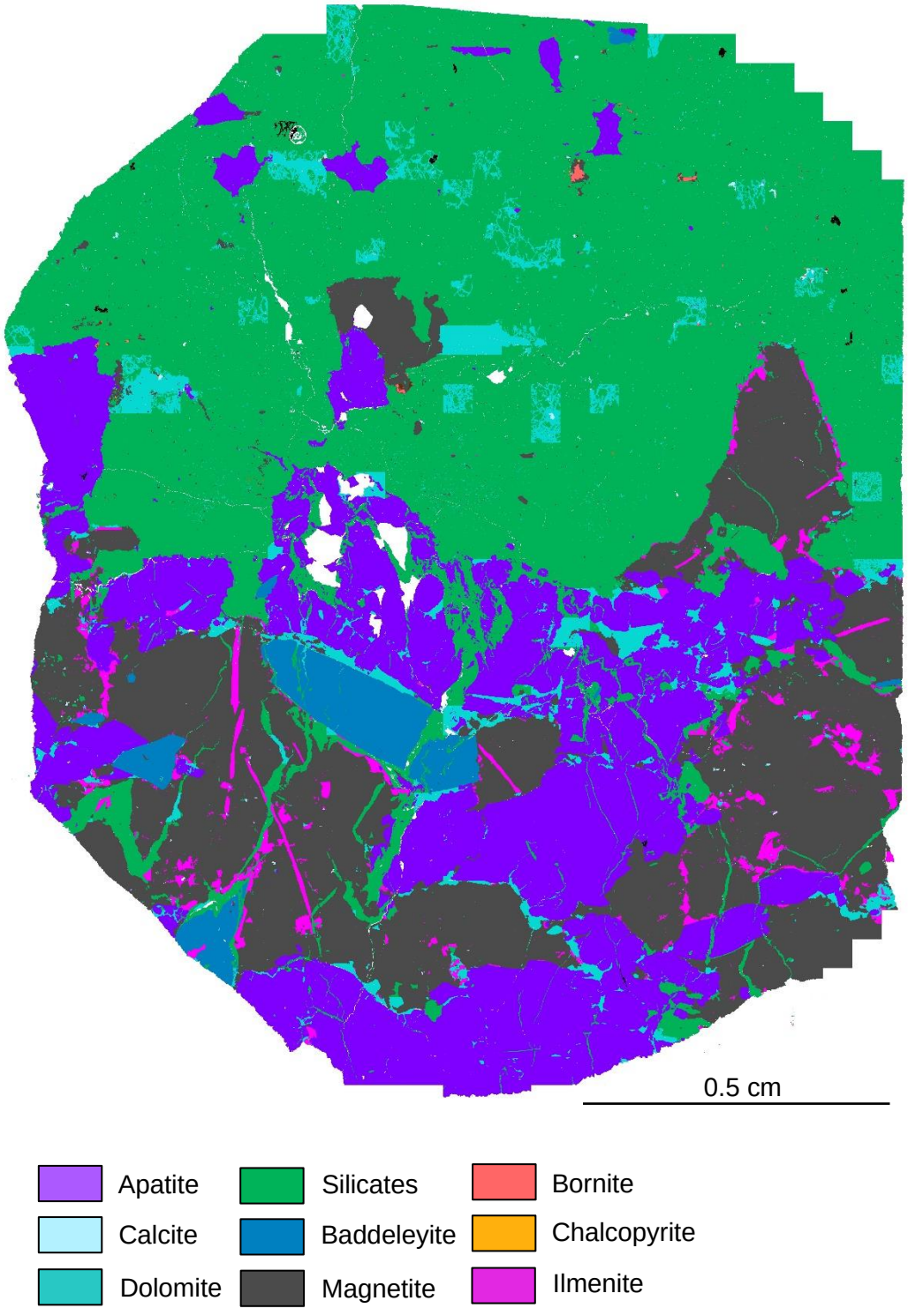
Borehole – Sample: VS12 – B61(ol)



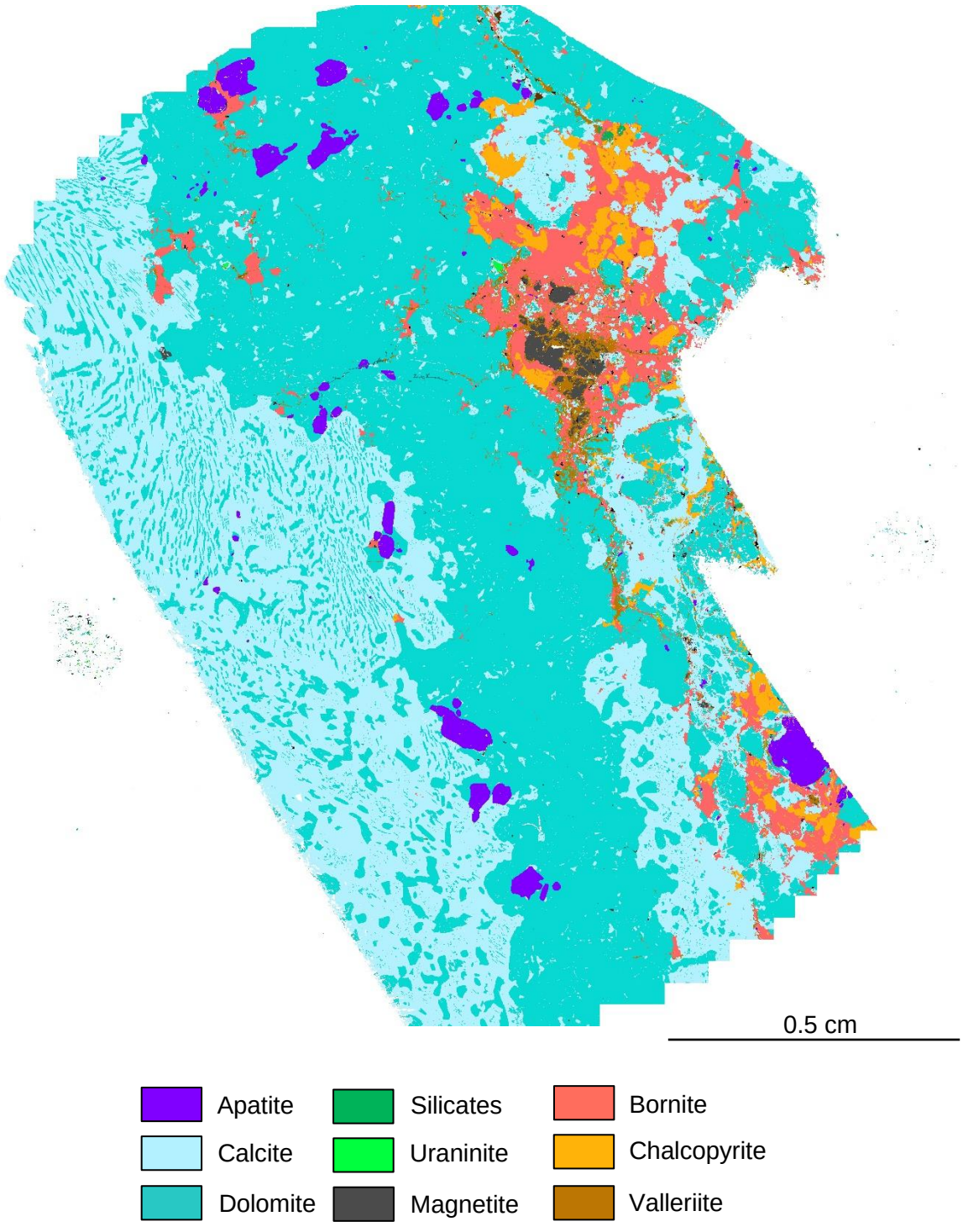
Borehole – Sample: DC28 – B05(ol)



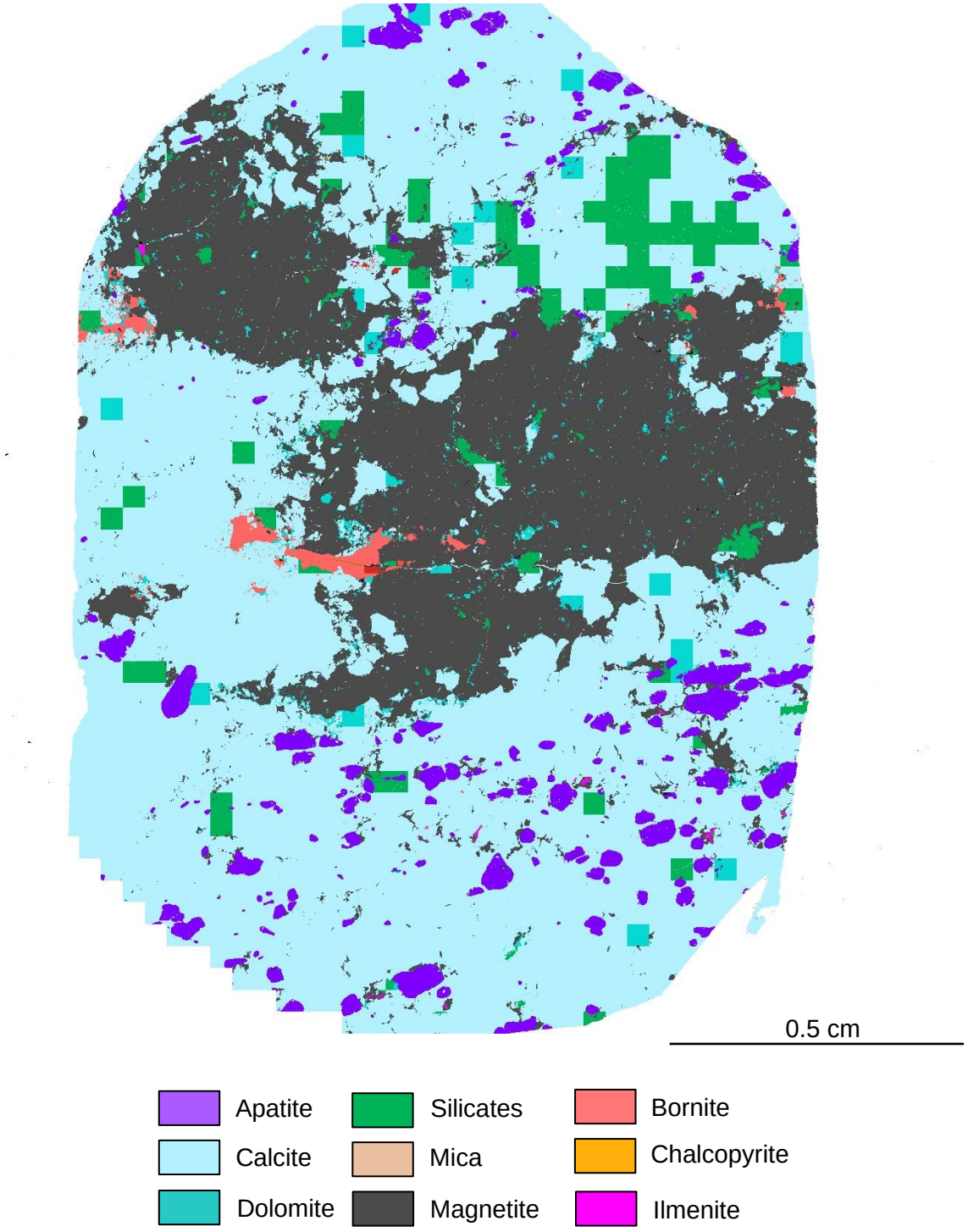
Borehole – Sample: SL113 – B66(2)



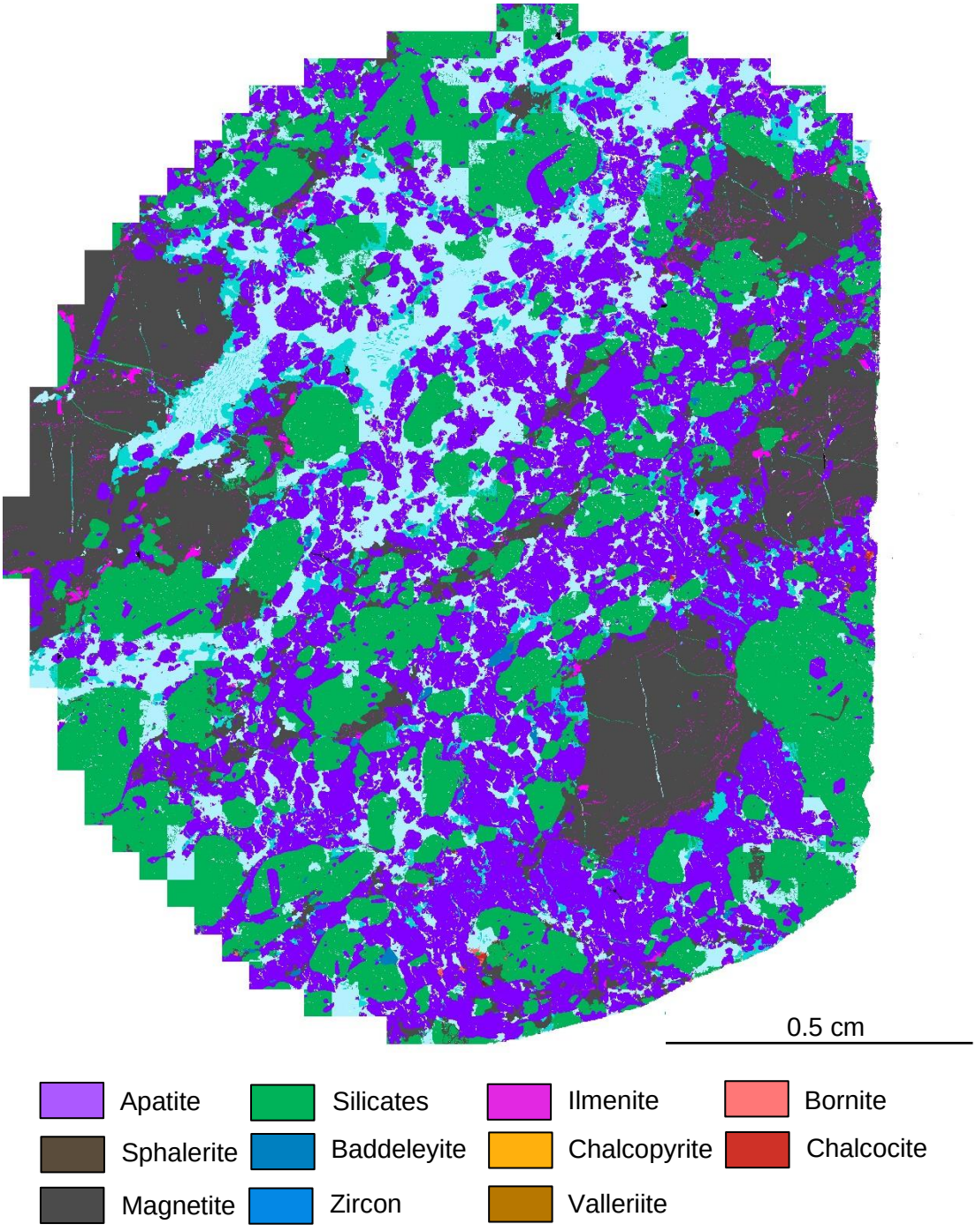
Borehole – Sample: SL113 – B62(2)c



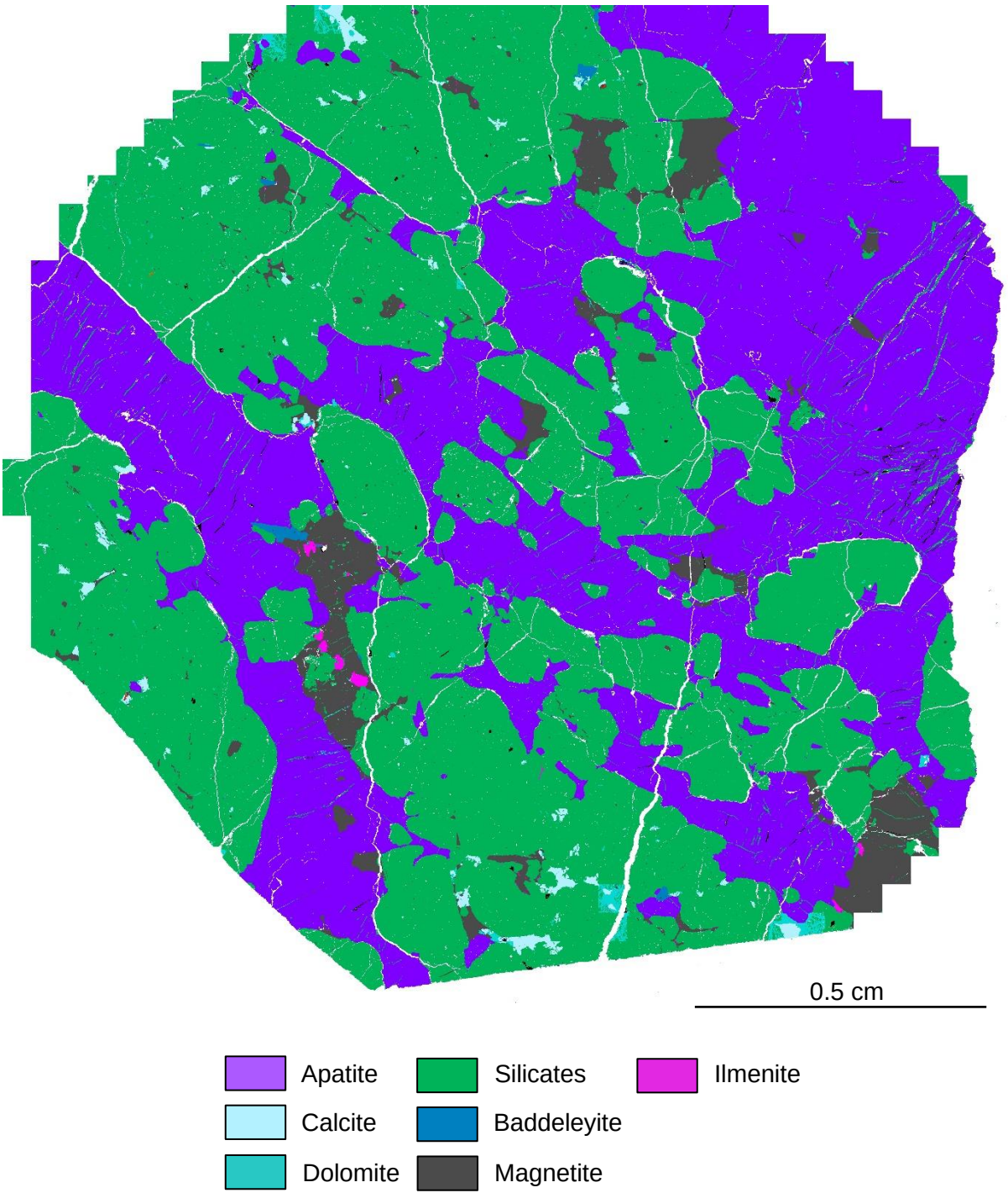
Borehole – Sample: SL94 – B22



Borehole – Sample: SL113 – B61(2)



Borehole – Sample: SL113 – B65(2)



Appendix C: Whole-rock major element compositions (Chapter 3)

Borehole-Sample	SL113-B67(2)	SMC1-B05	SL140-B08(2)	SL94-B22	SL139-B61(2)b
Rock type	BC	BC	BC	BC	PC/BC
SiO_2 (Wt %)	1.83	1.19	1.07	1.40	4.52
Al_2O_3	0.07	0.09	0.10	0.10	0.74
Fe_2O_3	4.35	5.00	5.52	4.42	45.26
MnO	0.11	0.06	0.10	0.07	0.17
MgO	4.85	2.85	3.68	3.48	7.86
CaO	46.68	49.13	47.52	47.92	20.44
Na_2O	0.01	0.00	0.00	0.00	0.00
K_2O	0.01	0.03	0.00	0.02	0.06
TiO_2	0.09	0.09	0.06	0.12	0.45
P_2O_5	3.79	7.45	3.04	1.79	4.79
Cr_2O_3	0.02	0.02	0.02	0.02	0.03
NiO	0.00	0.00	0.00	0.00	0.03
LOI	35.42	31.77	35.44	38.59	11.97
Total	97.22	97.68	96.52	97.91	96.24

Borehole-Sample	SL139-B63(2)b	SL113-B66(2)	SL113-B61(2)	SL113-B65(2)	SL139-B63(2)a
Rock type	PC	PC	PC	PC	TC
SiO_2 (Wt %)	3.27	21.99	13.58	16.04	0.44
Al_2O_3	0.28	0.16	0.17	0.26	0.05
Fe_2O_3	36.34	11.98	16.45	17.28	1.29
MnO	0.10	0.20	0.18	0.17	0.13
MgO	4.47	25.77	16.87	18.84	5.65
CaO	28.01	19.34	27.17	22.69	47.22
Na_2O	0.00	0.05	0.01	0.00	0.00
K_2O	0.09	0.18	0.09	0.17	0.00
TiO_2	0.11	0.30	0.74	1.01	0.02
P_2O_5	15.71	13.37	16.02	15.8	0.16
Cr_2O_3	0.02	0.02	0.02	0.02	0.02
NiO	0.02	0.02	0.02	0.03	0.00
LOI	1.21	5.23	6.41	6.53	42.92
Total	89.5	98.6	97.73	98.82	97.87

Borehole-Sample	SL139-B61(2)a	SL139-B62(2)b	SL139-B62(2)c	VS12-B61(ol)	DC28-B05(ol)
Rock type	TC	TC	TC	MP	MP
SiO_2 (Wt %)	1.35	1.59	0.32	19.64	34.49
Al_2O_3	0.12	0.12	0.12	2.01	3.25
Fe_2O_3	4.24	5.03	7.10	8.49	5.78
MnO	0.09	0.12	0.11	0.11	0.07
MgO	3.66	5.21	8.4	8.92	15.50
CaO	49.02	46.14	26.14	31.16	24.07
Na_2O	0.00	0.00	0.00	0.06	0.10
K_2O	0.00	0.00	0.00	2.36	3.32
TiO_2	0.04	0.03	0.02	5.12	0.80
P_2O_5	1.79	3.39	0.54	19.12	10.68
Cr_2O_3	0.02	0.02	0.01	0.02	0.04
NiO	0.00	0.00	0.12	0.00	0.01
LOI	37.92	36.19	27.38	0.16	0.88
Total	98.21	97.84	70.03	97.18	98.97

Standard	NIM-P	NIM-D	W2	NIM-S	GSP2
SiO_2 (Wt %)	51.19	39.02	53.04	64.01	67.14
Al_2O_3	4.28	0.33	15.54	17.36	15.11
Fe_2O_3	1.28	1.71	1.1	0.14	0.49
MnO	10.34	13.87	8.89	1.12	4
MgO	0.23	0.22	0.16	0.01	0.04
CaO	25.4	43.81	6.48	0.46	0.98
Na_2O	2.62	0.3	10.94	0.68	2.12
K_2O	0.35	0.05	2.22	0.38	2.82
TiO_2	0.09	0	0.63	15.44	5.45
P_2O_5	0.2	0.03	1.09	0.05	0.68
Cr_2O_3	0.03	0.02	0.13	0.12	0.3
NiO	3.56	0.4	0.03	0.01	0.02
LOI	0.08	0.27	0.01	0	0
Total	99.63	100.01	100.26	99.76	99.15

Standard	BCR2	NIM-N	NIM-G	PCC1	BHVO2
SiO_2 (Wt %)	54.88	53.27	76.66	43.9	50.16
Al_2O_3	13.73	16.78	12.27	0.73	13.77
Fe_2O_3	1.4	0.91	0.19	0.86	1.25
MnO	11.35	7.35	1.58	6.97	10.13
MgO	0.2	0.18	0.02	0.12	0.17
CaO	3.66	7.61	0.03	45.84	7.34
Na_2O	7.19	11.55	0.8	0.59	11.43
K_2O	3.2	2.46	3.35	0.06	2.22
TiO_2	1.8	0.25	5.08	0	0.52
P_2O_5	2.3	0.2	0.1	0.02	2.78
Cr_2O_3	0.36	0.02	0.01	0.01	0.27
NiO	0.02	0.02	0.01	0.4	0.06
LOI	0	0.01	0	0.33	0.02
Total	100.09	100.61	100.11	99.84	100.12

Standard	AGV2	G2	DTS1	AGV2
SiO_2 (Wt %)	60.34	69.71	40.88	60.59
Al_2O_3	17.29	15.48	0.25	17.29
Fe_2O_3	0.68	0.27	0.87	0.68
MnO	5.54	2.16	7.07	5.53
MgO	0.1	0.03	0.12	0.1
CaO	1.82	0.77	50.15	1.82
Na_2O	5.3	1.95	0.16	5.27
K_2O	4.27	4.09	0.06	4.27
TiO_2	2.95	4.55	0	2.95
P_2O_5	1.06	0.5	0.02	1.06
Cr_2O_3	0.48	0.15	0.01	0.48
NiO	0.01	0.01	0.57	0.02
LOI	0	0	0.32	0
Total	99.84	99.66	100.47	100.07

Appendix D: Whole-rock trace element compositions (Chapter 3)

Borehole	SL113	SL139	SMC1	SL139	SL140
Sample n°	B67(2)	B63(2)a	B05	B61(2)a	B08(2)
Rock type	BC	TC	BC	TC	BC
Li (ppm)	3.45	1.357	0.858	0.736	0.517
P	16314.80	561.68	33193.69	8098.96	13358.21
Sc	6.08	4.638	5.85	4.95	6.06
Ti	426.07	19.121	620.47	98.78	220.93
V	32.35	2.739	30.20	17.53	28.84
Cr	0.15	-0.185	0.224	0.256	-0.054
Co	15.47	5.538	13.83	13.80	16.22
Ni	39.18	27.373	38.06	45.07	47.00
Cu	328.10	155.397	22.81	259.79	559.61
Zn	25.86	15.186	47.48	25.27	29.48
Ga	10.07	8.884	10.09	7.65	7.76
Rb	3.06	2.334	2.59	1.20	0.889
Sr	4490.62	4565.573	3178.76	4514.24	4546.01
Y	84.69	62.033	88.09	56.99	57.51
Zr	102.10	116.617	652.56	137.16	78.07
Nb	1.18	0.681	1.74	1.25	0.900
Ba	1002.21	490.956	371.38	808.14	282.39
Sn	1.44	0.246	1.98	1.01	1.44
Cs	0.235	0.164	0.051	0.034	0.020
La	303.96	324.463	249.02	233.82	218.56
Ce	615.18	621.03	590.67	478.99	458.71
Pr	89.88	84.681	90.38	67.73	66.31
Nd	428.93	390.137	424.45	316.32	320.86
Sm	76.81	60.234	76.97	51.33	54.33
Eu	18.87	10.091	17.52	12.21	12.58
Gd	69.81	52.748	69.58	45.27	48.33
Tb	6.83	5.008	7.01	4.33	4.70
Dy	25.84	18.991	27.54	17.07	18.21
Ho	3.44	2.467	3.62	2.23	2.35
Er	6.63	5.006	6.97	4.40	4.46
Tm	0.669	0.471	0.679	0.444	0.431
Yb	3.69	2.612	3.65	2.37	2.36
Lu	0.437	0.301	0.419	0.273	0.276
Hf	2.12	1.077	9.34	2.17	1.69
Ta	0.04	0.016	0.060	0.024	0.021
W	0.081	0.273	0.054	0.071	0.05
Pb	6.16	2.592	7.54	3.13	2.33
Th	10.28	18.414	26.66	3.57	4.54
U	1.29	5.369	5.73	0.618	0.531

Borehole	SL139	SL139	SL139	SL139	VS-12
Sample n°	B63(2)b	B61(2)b	B62(2)b	B62(2)a	B61(ol)
Rock type	PC	PC/BC	TC	PC	MP
Li (ppm)	2.31	1.59	0.711	0.737	3.85
P	70547.02	20837.38	15036.04	19636.09	61686.50
Sc	6.08	22.51	9.36	1.25	25.68
Ti	518.85	2481.77	102.12	30.35	7058.37
V	147.79	294.61	22.71	3.69	41.86
Cr	0.361	-0.301	0.47	-0.102	32.27
Co	67.61	121.59	19.89	113.73	35.37
Ni	125.23	202.57	45.66	242.88	37.18
Cu	21753.02	688.74	32.26	-	1678.85
Zn	51.27	73.84	47.87	72.47	100.28
Ga	17.90	17.36	9.13	3.85	19.19
Rb	6.76	2.62	1.36	0.413	103.36
Sr	2434.96	1692.73	5613.36	1046.82	1621.53
Y	64.17	29.39	69.56	18.57	128.16
Zr	134.06	1144.21	10.39	231.49	934.17
Nb	3.41	14.88	1.37	1.68	9.26
Ba	268.57	223.55	734.76	205.59	430.07
Sn	3.94	13.10	1.77	5.63	1.14
Cs	0.122	0.038	0.043	0.023	0.982
La	407.16	143.21	291.21	139.51	340.36
Ce	916.21	343.33	574.19	304.80	812.26
Pr	132.27	46.74	83.59	42.55	133.26
Nd	615.03	216.90	386.66	191.25	658.44
Sm	97.88	36.03	63.46	30.42	136.00
Eu	19.75	7.96	14.11	6.14	28.74
Gd	79.57	30.44	53.86	24.51	113.51
Tb	7.22	2.86	5.38	2.20	12.34
Dy	25.42	10.67	21.84	7.98	50.28
Ho	2.98	1.33	2.83	0.910	6.54
Er	5.95	2.59	5.52	1.92	11.41
Tm	0.458	0.231	0.542	0.151	1.14
Yb	2.39	1.22	2.87	0.806	5.73
Lu	0.251	0.136	0.328	0.086	0.609
Hf	2.66	23.17	0.441	4.21	16.38
Ta	0.184	0.274	0.026	0.024	0.263
W	0.204	0.280	0.052	0.088	0.072
Pb	14.63	4.39	4.12	95.41	54.25
Th	26.62	23.45	4.59	16.81	336.57
U	5.99	9.85	0.609	3.98	127.09

Borehole	DC28	SL113	SL139	SL94	SL113	SL113
Sample n°	B05(ol)	B66(2)	B62(2)c	B22	B61(2)	B65(2)
Rock type	MP	PC	TC	BC	PC	PC
Li (ppm)	1.69	4.53	1.43	0.874	5.92	1.70
P	44418.75	62265.91	3276.18	8878.34	72780.74	68495.36
Sc	26.97	10.43	8.07	7.37	14.18	12.66
Ti	1939.26	1621.52	95.19	624.77	4261.44	4804.57
V	21.77	42.13	20.72	47.32	132.71	140.70
Cr	156.64	1.21	0.299	0.433	2.77	1.73
Co	36.83	95.45	1216.47	15.42	77.01	88.35
Ni	67.72	177.05	888.26	46.35	134.14	180.40
Cu	20.84	588.81	49315.98	2403.25	963.25	48.12
Zn	49.39	71.09	3042.21	17.44	101.59	98.55
Ga	13.53	10.18	5.88	6.67	15.49	11.31
Rb	119.97	8.97	1.84	3.58	4.99	7.46
Sr	899.41	2035.72	5827.86	4514.89	3005.98	1786.08
Y	72.20	62.63	38.42	80.39	91.64	61.64
Zr	377.69	1500.50	125.66	340.29	2883.57	537.04
Nb	0.913	3.55	1.94	1.47	6.67	2.58
Ba	418.86	136.19	1486.29	451.88	337.85	197.44
Sn	0.375	1.51	8.49	1.86	4.69	4.91
Cs	1.16	0.098	0.122	0.022	0.039	0.057
La	271.73	353.90	200.74	224.37	503.59	302.06
Ce	603.32	732.98	437.69	473.45	1097.89	680.12
Pr	95.22	108.57	60.38	69.45	157.36	105.96
Nd	455.69	494.63	271.12	332.53	690.53	505.78
Sm	84.18	81.50	45.90	56.75	116.41	85.64
Eu	16.81	16.65	8.98	12.77	23.78	17.29
Gd	72.05	67.69	36.35	50.53	98.21	70.80
Tb	7.15	6.42	3.38	5.50	9.21	6.64
Dy	27.19	24.19	12.82	23.55	34.12	24.75
Ho	3.33	2.89	1.62	3.28	4.12	2.93
Er	6.12	5.51	3.36	6.21	8.10	5.62
Tm	0.531	0.465	0.316	0.664	0.69	0.448
Yb	2.83	2.41	1.76	3.53	3.72	2.39
Lu	0.314	0.258	0.205	0.398	0.398	0.252
Hf	6.33	31.41	2.01	5.35	64.40	11.14
Ta	0.024	0.072	0.039	0.053	0.205	0.074
W	0.201	0.242	0.327	0.092	0.117	0.142
Pb	12.79	24.54	40.09	3.12	9.36	8.96
Th	83.88	175.57	121.91	4.06	54.21	63.25
U	8.78	30.50	38.45	1.63	8.93	7.14

	BCR2-1	BHVO2-1	BCR2-2	BHVO2-2
Li (ppm)	9.353	5.311	11.049	4.529
P	1556.392	1189.161	1556.216	1189.298
Sc	32.058	30.944	39.688	25.969
Ti	12907.123	15740.362	12991.893	15636.775
V	420.133	324.267	425.275	320.502
Cr	17.016	285	17.324	285
Co	36.732	45.837	37.298	45.185
Ni	15.426	112	15.861	112
Cu	25.876	113.576	25.912	113.481
Zn	137.913	114.547	138.153	114.321
Ga	22.024	21.665	22.823	20.888
Rb	49	11.325	49	7.584
Sr	325.804	376.449	385.997	326.946
Y	31.996	22.306	36.15	20.132
Zr	186.696	166.514	187.957	165.315
Nb	11.91	17.724	12.042	17.502
Ba	628.678	131.273	658.993	125.279
Sn	2.711	2.332	2.739	2.314
Cs	0.764	0.235	0.914	0.153
La	25.275	15.136	27.926	13.895
Ce	51.078	36.586	53.796	34.864
Pr	6.384	4.935	7.002	4.545
Nd	27.78	23.345	30.359	21.609
Sm	6.496	5.63	7.103	5.211
Eu	2.027	1.891	2.252	1.736
Gd	6.541	5.864	7.269	5.335
Tb	0.973	0.84	1.07	0.774
Dy	6.075	4.84	6.685	4.445
Ho	1.228	0.89	1.35	0.819
Er	3.376	2.249	3.772	2.044
Tm	0.478	0.289	0.537	0.263
Yb	3.351	1.933	3.8	1.745
Lu	0.483	0.253	0.541	0.23
Hf	4.867	4.215	4.956	4.137
Ta	0.64	1.203	0.642	1.198
W	0.457	0.26	0.458	0.26
Pb	8.35	2.016	8.412	1.988
Th	5.667	1.146	6.581	1.014
U	1.761	0.432	1.806	0.422

Appendix E: Whole-rock PGE compositions (Chapter 3)

Element (ppb)	LOD (ppb)	SL140-B08(2)	SL94-B22	SL139-B61(2)b
		BC	BC	BC/PC
Ru	1	<LOD	<LOD	1
Rh	1	<LOD	<LOD	<LOD
Pd	1	<LOD	5	2
Os	1	<LOD	<LOD	<LOD
Ir	1	<LOD	<LOD	<LOD
Pt	1	<LOD	2	1
Au	2	21	42	23

Element (ppb)	LOD (ppb)	SL139-B63(2)b	SL139-B62(2)a	SL139-B62(2)c	VS-12-B61(ol)
		PC	PC	TC	MP
Ru	1	2	4	<LOD	1
Rh	1	<LOD	<LOD	<LOD	<LOD
Pd	1	2	8	2	8
Os	1	<LOD	<LOD	<LOD	<LOD
Ir	1	<LOD	<LOD	<LOD	<LOD
Pt	1	1	2	<LOD	9
Au	2	41	34	14	22

Element (ppb)	AMIS0499 Average, n = 2	AMIS0499 recommended values	Difference (%)
Ru	125	120	4
Rh	127	120	5.51
Pd	2400	2420	0.83
Os	17	-	-
Ir	33.5	34	1.49
Pt	2045.5	216	5.6
Au	266	310	16.54

Appendix F: Trace element compositions of sulphide assemblages and location of the spots in the polished mounts (Chapter 3)

Averaged PGE concentrations in sulphides

Sample	Rock	Mineral	n	Pd (ppb)	n (>LOD)	Os (ppb)	n (>LOD)	Ir (ppb)	n (>LOD)
SL94-B22	BC								
		Bn	14	71	14	11	3	4	4
		Cc	6	104	4	8	2	4	1
		V	3	310	3	22	2	<LOD	0
SL140-B08(2)	BC								
		Bn	6	53	5	<LOD	0	3	2
		Ccp	3	64	1	<LOD	0	<LOD	0
SL139-B62(2)a	PC								
		Bn	14	83	14	11	4	1	2
		Ccp	8	61	4	9	1	2	1
		V	4	42	4	4	1	<LOD	0
SL139-B63(2)b	PC								
		Ccp	13	-	0	15	3	3	2
SL139-B61(2)B	PC/BC								
		V	8	-	0	49	2	<LOD	0
SL139-B62(2)c	TC								
		Bn	4	86	4	8	1	<LOD	0
		Ccp	5	35	3	<LOD	0	<LOD	0
		Cc	3	68	2	<LOD	0	4	1
		V	3	204	3	<LOD	0	4	1

Sample	Rock	Mineral	n	Pt (ppb)	n (>LOD)	Au (ppb)	n (>LOD)
SL94-B22	BC						
		Bn	14	5	5	4	7
		Cc	6	4	2	10	5
		V	3	16	1	21	1
SL140-B08(2)	BC						
		Bn	6	3	1	4	2
		Ccp	3	<LOD	0	15	1
SL139-B62(2)a	PC						
		Bn	14	5	4	6	2
		Ccp	8	9	1	<LOD	0
		V	4	2	1	6	2
SL139-B63(2)b	PC						
		Ccp	13	16	2	50	8
SL139-B61(2)B	PC/BC						
		V	8	32	1	24	2
SL139-B62(2)c	TC						
		Bn	4	<LOD	0	<LOD	0
		Ccp	5	31	1	14	1
		Cc	3	<LOD	0	18	1
		V	3	19	1	8	1

Averaged trace element concentrations of sulphides

Sample	Rock	Mineral	n	Co (ppm)	n (>LOD)	Ni (ppm)	n (>LOD)	Zn (ppm)	n (>LOD)
SL94-B22	BC								
		Bn	14	0.15	14	0.38	8	1.1	13
		Cc	6	0.46	5	6.3	5	2.8	5
		V	3	0.59	3	12.6	3	10.6	3
SL140-B08(2)	BC								
		Bn	6	0.09	6	0.18	5	0.6	4
		Ccp	3	8.77	3	3815.2	3	4	3
SL139-B62(2)a	PC								
		Bn	14	0.17	14	4.9	6	0.67	8
		Ccp	8	39.9	8	5018.6	8	3.1	8
		V	4	3.7	4	235.9	4	0.98	4
SL139-B63(2)b	PC								
		Ccp	13	0.81	13	1516.7	13	4.4	13
SL139-B61(2)B	PC/BC								
		V	8	386.1	8	2456.1	8	9.5	6
SL139-B62(2)c	TC								
		Bn	4	0.25	4	86.4	1	2.5	3
		Ccp	5	42.5	5	2133.1	5	4.2	5
		Cc	3	27.9	3	1432	3	9.9	3
		V	3	4.8	3	108.6	3	4.7	3

Sample	Rock	Mineral	n	As (ppm)	n (>LOD)	Se (ppm)	n (>LOD)	Cd (ppm)	n (>LOD)
SL94-B22	BC								
		Bn	14	0.16	2	13.8	14	3.1	14
		Cc	6	0.13	2	12.5	6	1.5	6
		V	3	0.98	3	8.7	3	13.2	3
SL140-B08(2)	BC								
		Bn	6	0.11	1	10.1	6	0.95	5
		Ccp	3	<LOD	0	16.3	3	0.83	1
SL139-B62(2)a	PC								
		Bn	14	0.12	4	6.9	14	2.7	14
		Ccp	8	0.28	1	6.9	8	1.4	4
		V	4	0.12	2	7.2	4	2.1	4
SL139-B63(2)b	PC								
		Ccp	13	0.13	1	8.8	13	0.6	7
SL139-B61(2)B	PC/BC								
		V	8	0.92	2	4.7	7	<LOD	0
SL139-B62(2)c	TC								
		Bn	4	<LOD	0	11.2	4	3.1	4
		Ccp	5	0.13	1	3.6	5	0.71	5
		Cc	3	<LOD	0	2.3	3	3.4	2
		V	3	0.91	3	9.1	3	5.2	3

Sample	Rock	Mineral	n	Pb (ppm)	n (>LOD)	Bi (ppm)	n (>LOD)
SL94-B22	BC						
		Bn	14	44.4	14	0.24	4
		Cc	6	378.8	6	<LOD	0
		V	3	450.3	3	<LOD	0
SL140-B08(2)	BC						
		Bn	6	3.8	6	0.14	6
		Ccp	3	104.1	3	4.8	3
SL139-B62(2)a	PC						
		Bn	14	16.3	14	1	14
		Ccp	8	67.6	8	0.94	7
		V	4	101.1	4	171.9	4
SL139-B63(2)b	PC						
		Ccp	13	1.3	13	0.45	13
SL139-B61(2)B	PC/BC						
		V	8	6.1	8	0.12	6
SL139-B62(2)c	TC						
		Bn	4	103.3	4	17.3	4
		Ccp	5	102.4	5	8.7	4
		Cc	3	210	3	64.9	3
		V	3	837.4	3	22.5	3

Unprocessed PGE and trace element concentrations in sulphides

Spot Size	35µm			35µm		
Sample-spot	14-1			14-2		
Mineral	Bornite			Bornite		
	Conc. (ppm)	1 sigma	LOD	Conc. (ppm)	1 sigma	LOD
^{108}Pd	0.171	0.03	0.02	0.09	0.02	0.02
^{108}Pd corr.	0.14			0.06		
^{189}Os	<0.03	<0.00	0.03	<0.02	<0.00	0.02
^{193}Ir	0.005	0.003	<0.00	<0.0045	0.001	0.005
^{195}Pt	<0.021	0.01	0.02	0.01	0.005	<0.00
^{197}Au	<0.011	0.004	0.01	0.002	0.002	<0.00
^{59}Co	0.13	0.02	0.02	0.10	0.02	0.012
^{60}Ni	0.20	0.09	0.16	<0.15	<0.00	0.15
^{67}Zn	1.09	0.43	0.82	<0.70	0.35	0.70
^{75}As	<0.17	0.08	0.17	<0.17	<0.00	0.17
^{77}Se	14.03	1.55	1.36	13.78	1.44	0.91
^{82}Se	11.34	2.27	4.48	14.64	2.16	3.84
^{106}Cd	3.69	0.71	0.37	3.37	0.65	0.34
^{208}Pb	86.01	6.65	0.03	20.20	1.57	0.03
^{209}Bi	<0.012	0.005	0.01	0.01	0.004	0.01

Spot Size	35µm			35µm		
Sample-spot	14-3			14-4		
Mineral	Bornite			Bornite		
	Conc. (ppm)	1 sigma	LOD	Conc. (ppm)	1 sigma	LOD
^{108}Pd	0.08	0.018	0.01	0.09	0.02	0.02
^{108}Pd corr.	0.05			0.06		
^{189}Os	0.01	0.01	<0.00	<0.00	<0.00	<0.00
^{193}Ir	<0.01	0.003	0.01	<0.005	0.003	0.01
^{195}Pt	<0.01	0.003	0.01	0.004	0.004	<0.00
^{197}Au	0.002	0.002	<0.00	<0.01	0.003	0.01
^{59}Co	0.08	0.02	0.02	0.08	0.02	0.02
^{60}Ni	0.20	0.07	0.10	<0.13	0.07	0.13
^{67}Zn	1.01	0.33	0.59	0.66	0.32	0.59
^{75}As	<0.14	0.06	0.14	<0.11	0.06	0.11
^{77}Se	12.84	1.34	0.72	13.70	1.43	0.76
^{82}Se	13.80	2.04	3.60	15.03	2.02	3.12
^{106}Cd	2.56	0.54	<0.00	2.89	0.62	0.39
^{208}Pb	39.92	3.09	0.02	24.56	1.91	0.02
^{209}Bi	<0.01	0.005	0.01	<0.01	0.004	0.01

Spot Size	35µm			35µm		
Sample-spot	14-5			14-6		
Mineral	Bornite			Bornite		
	Conc. (ppm)	1 sigma	LOD	Conc. (ppm)	1 sigma	LOD
^{108}Pd	0.10	0.02	0.01	0.11	0.02	<0.00
^{108}Pd corr.	0.06			0.08		
^{189}Os	<0.02	0.01	0.02	<0.02	0.01	0.02
^{193}Ir	0.004	0.003	<0.00	0.004	0.003	<0.00
^{195}Pt	<0.02	0.01	0.02	<0.02	0.01	0.02
^{197}Au	<0.01	0.002	0.01	0.01	0.004	<0.00
^{59}Co	0.17	0.02	0.01	0.21	0.03	0.02
^{60}Ni	0.53	0.10	0.13	0.20	0.10	0.17
^{67}Zn	2.09	0.42	0.59	0.85	0.41	0.73
^{75}As	0.11	0.06	0.11	<0.17	0.09	0.17
^{77}Se	17.26	1.70	0.79	13.68	1.52	0.75
^{82}Se	11.90	1.97	3.50	14.75	2.23	3.58
^{106}Cd	3.46	0.69	0.46	3.00	0.67	<0.00
^{208}Pb	92.60	7.17	0.02	64.12	4.97	0.02
^{209}Bi	<0.01	0.004	0.01	<0.01	0.005	0.01

Spot Size	35µm			35µm		
Sample-spot	14-7			14-8		
Mineral	Bornite			Bornite		
	Conc. (ppm)	1 sigma	LOD	Conc. (ppm)	1 sigma	LOD
^{108}Pd	0.09	0.02	0.02	0.07	0.02	0.02
^{108}Pd corr.	0.05			0.04		
^{189}Os	<0.02	0.01	0.02	<0.02	0.01	0.02
^{193}Ir	<0.004	0.002	0.004	<0.004	0.002	0.004
^{195}Pt	<0.01	0.005	0.01	<0.01	0.01	0.01
^{197}Au	0.002	0.002	<0.00	<0.01	0.005	0.01
^{59}Co	0.14	0.02	0.020	0.15	0.02	0.02
^{60}Ni	<0.15	0.07	0.15	<0.15	0.07	0.15
^{67}Zn	0.92	0.35	0.64	0.89	0.33	0.58
^{75}As	<0.14	0.07	0.14	<0.13	0.06	0.13
^{77}Se	14.28	1.46	0.77	12.56	1.33	0.79
^{82}Se	14.04	2.00	3.36	12.95	1.97	3.45
^{106}Cd	3.52	0.66	0.31	2.89	0.61	0.44
^{208}Pb	20.72	1.62	0.02	21.92	1.71	0.02
^{209}Bi	0.01	0.005	0.01	0.01	0.005	0.01

Spot Size	35µm			35µm		
Sample-spot	14-9			14-10		
Mineral	Bornite			Bornite		
	Conc. (ppm)	1 sigma	LOD	Conc. (ppm)	1 sigma	LOD
^{108}Pd	0.12	0.02	0.01	0.13	0.03	0.02
^{108}Pd corr.	0.09			0.10		
^{189}Os	0.01	0.01	<0.00	<0.00	<0.00	<0.00
^{193}Ir	<0.01	0.003	0.01	<0.00	<0.00	<0.00
^{195}Pt	0.004	0.004	<0.00	<0.00	<0.00	<0.00
^{197}Au	0.01	0.004	<0.00	<0.01	0.003	0.01
^{59}Co	0.27	0.03	0.02	0.19	0.03	0.01
^{60}Ni	0.98	0.25	0.13	0.19	0.07	0.09
^{67}Zn	0.64	0.33	0.49	2.25	0.47	0.55
^{75}As	0.22	0.09	0.16	<0.14	0.07	0.15
^{77}Se	13.18	1.44	0.84	13.59	1.52	0.66
^{82}Se	11.31	2.01	3.62	16.58	2.21	3.03
^{106}Cd	3.45	0.69	0.33	3.74	0.76	<0.00
^{208}Pb	98.90	7.70	0.02	37.42	2.92	0.02
^{209}Bi	0.93	0.07	0.01	<0.01	0.004	0.01

Spot Size	35µm			35µm		
Sample-spot	14-11			14-12		
Mineral	Bornite			Bornite		
	Conc. (ppm)	1 sigma	LOD	Conc. (ppm)	1 sigma	LOD
^{108}Pd	0.12	0.02	<0.00	0.04	0.02	0.02
^{108}Pd corr.	0.09			0.02		
^{189}Os	0.02	0.01	<0.00	<0.01	0.01	0.01
^{193}Ir	<0.00	<0.00	<0.00	0.003	0.002	<0.00
^{195}Pt	0.003	0.003	<0.00	0.01	0.005	<0.00
^{197}Au	<0.01	0.005	0.01	<0.004	0.002	0.004
^{59}Co	0.14	0.02	0.01	0.14	0.02	0.01
^{60}Ni	0.59	0.11	0.14	<0.10	0.05	0.10
^{67}Zn	2.27	0.41	0.53	0.63	0.29	0.47
^{75}As	<0.14	0.07	0.14	<0.07	0.03	0.07
^{77}Se	14.11	1.43	0.56	12.63	1.31	0.47
^{82}Se	16.04	1.96	2.81	12.38	1.58	2.01
^{106}Cd	3.02	0.62	0.39	2.46	0.53	0.19
^{208}Pb	57.00	4.40	0.02	16.30	1.20	0.01
^{209}Bi	<0.01	0.004	0.01	<0.004	0.003	0.005

Spot Size	35µm			35µm		
Sample-spot	14-13			14-14		
Mineral	Bornite			Bornite		
	Conc. (ppm)	1 sigma	LOD	Conc. (ppm)	1 sigma	LOD
^{108}Pd	0.12	0.02	0.01	0.07	0.02	0.01
^{108}Pd corr.	0.10			0.04		
^{189}Os	<0.00	<0.00	<0.00	<0.02	0.01	0.02
^{193}Ir	<0.004	0.002	0.004	<0.003	0.001	0.003
^{195}Pt	<0.007	0.01	0.01	<0.01	0.005	0.01
^{197}Au	0.004	0.003	<0.00	0.002	0.002	<0.00
^{59}Co	0.22	0.02	0.01	0.15	0.02	0.02
^{60}Ni	0.15	0.06	0.09	<0.11	0.05	0.11
^{67}Zn	0.49	0.24	0.42	0.96	0.29	0.50
^{75}As	<0.10	0.05	0.11	<0.10	0.05	0.10
^{77}Se	12.97	1.30	0.59	13.96	1.36	0.53
^{82}Se	13.68	1.67	2.36	12.58	1.68	2.69
^{106}Cd	2.05	0.47	0.32	4.01	0.66	0.36
^{208}Pb	21.63	1.70	0.01	19.68	1.55	0.01
^{209}Bi	<0.01	0.003	0.01	<0.01	0.004	0.01

Spot Size	35µm			35µm		
Sample-spot	14-15			14-16		
Mineral	Chalcocite			Chalcocite		
	Conc. (ppm)	1 sigma	LOD	Conc. (ppm)	1 sigma	LOD
^{108}Pd	0.002	0.003	<0.00	0.13	0.02	0.01
^{108}Pd corr.	0.00			0.11		
^{189}Os	0.003	0.003	<0.00	<0.01	0.004	0.01
^{193}Ir	0.004	0.002	0.003	<0.01	0.002	0.01
^{195}Pt	<0.01	0.003	0.01	0.003	0.003	<0.00
^{197}Au	<0.003	0.002	0.003	0.01	0.004	<0.00
^{59}Co	<0.01	0.005	0.01	1.20	0.08	0.01
^{60}Ni	<0.06	0.03	0.06	9.89	0.70	0.12
^{67}Zn	<0.35	0.18	0.35	6.43	0.63	0.49
^{75}As	<0.07	0.04	0.07	0.11	0.06	0.09
^{77}Se	11.52	1.10	0.35	13.93	1.38	0.48
^{82}Se	11.26	1.27	1.56	13.92	1.68	2.29
^{106}Cd	0.35	0.17	0.15	1.93	0.45	0.22
^{208}Pb	3.58	0.29	0.01	1127.50	88.57	0.01
^{209}Bi	<0.004	0.002	0.004	<0.01	0.003	0.01

Spot Size	35µm			35µm		
Sample-spot	14-17			14-18		
Mineral	Chalcocite			Chalcocite		
	Conc. (ppm)	1 sigma	LOD	Conc. (ppm)	1 sigma	LOD
^{108}Pd	0.09	0.02	<0.00	0.14	0.03	0.01
^{108}Pd corr.	0.08			0.12		
^{189}Os	0.01	0.01	<0.00	<0.02	0.01	0.02
^{193}Ir	<0.003	0.001	0.003	<0.00	<0.00	<0.00
^{195}Pt	<0.01	0.01	0.01	<0.01	0.01	0.01
^{197}Au	0.01	0.01	0.01	0.01	0.01	<0.00
^{59}Co	0.84	0.06	0.02	0.18	0.02	0.01
^{60}Ni	7.05	0.51	0.12	11.36	0.81	0.12
^{67}Zn	4.72	0.51	0.52	1.92	0.37	0.41
^{75}As	<0.10	0.05	0.10	0.16	0.06	0.08
^{77}Se	13.38	1.29	0.47	11.55	1.27	0.58
^{82}Se	12.25	1.60	2.56	10.89	1.57	2.21
^{106}Cd	0.70	0.30	0.42	2.90	0.59	<0.00
^{208}Pb	834.02	65.66	0.02	208.00	16.00	0.01
^{209}Bi	<0.01	0.004	0.01	<0.005	0.003	0.005

Spot Size	35µm			35µm		
Sample-spot	14-19			14-20		
Mineral	Chalcocite			Chalcocite		
	Conc. (ppm)	1 sigma	LOD	Conc. (ppm)	1 sigma	LOD
^{108}Pd	<0.01	0.01	0.01	0.13	0.03	0.01
^{108}Pd corr.				0.11		
^{189}Os	<0.01	0.01	0.01	<0.02	0.01	0.02
^{193}Ir	<0.002	0.001	0.002	<0.01	0.003	0.01
^{195}Pt	<0.01	0.004	0.01	0.004	0.004	<0.00
^{197}Au	0.01	0.005	<0.00	0.01	0.005	<0.00
^{59}Co	0.04	0.01	0.01	0.03	0.01	0.02
^{60}Ni	2.61	0.25	0.07	0.41	0.10	0.12
^{67}Zn	0.44	0.22	0.30	0.68	0.32	0.50
^{75}As	<0.06	0.04	0.06	<0.10	0.05	0.11
^{77}Se	13.50	1.40	0.32	11.22	1.30	0.49
^{82}Se	11.72	1.49	1.58	12.55	1.80	2.49
^{106}Cd	0.78	0.32	0.21	2.43	0.61	0.36
^{208}Pb	15.88	1.27	0.01	83.7	6.65	0.01
^{209}Bi	<0.004	0.002	0.004	<0.007	0.005	0.01

Spot Size	25µm			25µm		
Sample-spot	14-21			14-22		
Mineral	Valleriite			Valleriite		
	Conc. (ppm)	1 sigma	LOD	Conc. (ppm)	1 sigma	LOD
^{108}Pd	0.99	0.11	0.03	0.24	0.05	<0.00
^{108}Pd corr.	0.71			0.19		
^{189}Os	0.04	0.02	<0.00	<0.03	0.02	0.03
^{193}Ir	<0.01	0.003	0.01	<0.01	0.003	0.01
^{195}Pt	0.02	0.01	<0.00	<0.01	0.004	0.01
^{197}Au	0.02	0.01	0.01	<0.01	<0.00	0.01
^{59}Co	0.90	0.09	0.04	0.59	0.07	0.02
^{60}Ni	25.45	1.83	0.28	9.79	0.82	0.20
^{67}Zn	17.54	1.64	1.05	11.19	1.25	0.66
^{75}As	1.66	0.27	0.29	1.12	0.22	0.22
^{77}Se	9.82	1.63	1.63	5.92	1.28	1.30
^{82}Se	13.59	3.21	5.95	6.62	2.41	4.07
^{106}Cd	31.65	3.45	<0.00	5.50	1.24	0.40
^{208}Pb	967.48	76.94	0.03	157.78	12.60	0.02
^{209}Bi	<0.02	0.01	0.02	<0.01	<0.00	0.01

Spot Size	25µm			35µm		
Sample-spot	14-23			9-01		
Mineral	Valleriite			Bornite		
	Conc. (ppm)	1 sigma	LOD	Conc. (ppm)	1 sigma	LOD
^{108}Pd	0.05	0.02	0.01	0.13	0.03	0.01
^{108}Pd corr.	0.03			0.10		
^{189}Os	0.01	0.01	<0.00	<0.02	0.01	0.02
^{193}Ir	<0.07	0.004	0.01	<0.003	0.002	0.003
^{195}Pt	<0.02	0.01	0.02	<0.00	<0.00	<0.00
^{197}Au	<0.01	0.01	0.01	<0.01	0.004	0.01
^{59}Co	0.27	0.04	0.02	0.17	0.02	0.01
^{60}Ni	2.57	0.28	0.17	<0.02	0.06	0.10
^{67}Zn	3.16	0.57	0.64	0.80	0.27	0.34
^{75}As	0.16	0.09	0.15	<0.11	0.05	0.11
^{77}Se	10.47	1.35	0.83	8.50	1.05	0.40
^{82}Se	9.93	2.05	3.50	5.25	1.29	2.08
^{106}Cd	2.35	0.64	0.34	3.66	0.70	<0.00
^{208}Pb	225.68	18.05	0.02	14.46	1.17	0.01
^{209}Bi	<0.01	0.01	0.01	0.48	0.04	0.01

Spot Size	35µm			35µm		
Sample-spot	9-02			9-03		
Mineral	Bornite			Bornite		
	Conc. (ppm)	1 sigma	LOD	Conc. (ppm)	1 sigma	LOD
^{108}Pd	0.11	0.02	<0.00	0.1	0.02	<0.00
^{108}Pd corr.	0.08			0.08		
^{189}Os	<0.01	0.003	0.01	<0.01	0.01	0.01
^{193}Ir	0.001	0.001	<0.00	0.001	0.001	<0.00
^{195}Pt	0.004	0.004	<0.00	<0.01	0.01	0.01
^{197}Au	<0.06	0.003	0.01	0.002	0.002	<0.00
^{59}Co	0.16	0.02	0.01	0.14	0.02	0.01
^{60}Ni	<0.11	0.06	0.11	<0.12	0.06	0.13
^{67}Zn	<0.35	0.21	0.35	0.40	0.21	0.37
^{75}As	<0.09	0.04	0.09	<0.10	0.05	0.10
^{77}Se	5.86	0.80	0.36	6.12	0.76	0.44
^{82}Se	5.96	1.22	1.88	5.10	1.12	2.04
^{106}Cd	2.85	0.60	0.19	2.36	0.48	0.29
^{208}Pb	14.8	1.20	0.01	10.50	0.85	0.01
^{209}Bi	0.72	0.06	0.01	0.59	0.04	0.01

Spot Size	35µm			35µm		
Sample-spot	9-04			9-05		
Mineral	Bornite			Bornite		
	Conc. (ppm)	1 sigma	LOD	Conc. (ppm)	1 sigma	LOD
^{108}Pd	0.12	0.02	0.01	0.09	0.02	0.01
^{108}Pd corr.	0.10			0.075		
^{189}Os	<0.01	0.003	0.01	<0.01	0.01	0.01
^{193}Ir	<0.003	0.002	0.003	<0.005	0.002	0.01
^{195}Pt	<0.01	0.004	0.01	<0.01	0.01	0.01
^{197}Au	0.01	0.005	<0.00	<0.01	0.003	0.01
^{59}Co	0.17	0.02	0.01	0.12	0.02	0.01
^{60}Ni	<0.11	0.06	0.11	0.16	0.06	0.08
^{67}Zn	0.55	0.23	0.34	0.60	0.23	0.35
^{75}As	<0.11	0.05	0.11	0.10	0.05	0.07
^{77}Se	7.40	0.91	0.30	9.58	1.06	0.39
^{82}Se	6.11	1.19	1.83	8.98	1.34	1.93
^{106}Cd	2.30	0.50	<0.00	1.99	0.47	0.27
^{208}Pb	27.57	2.24	0.01	8.65	0.72	0.01
^{209}Bi	0.63	0.05	0.003	0.41	0.03	0.003

Spot Size	25µm			25µm		
Sample-spot	9-06			9-07		
Mineral	Chalcopyrite			Chalcopyrite		
	Conc. (ppm)	1 sigma	LOD	Conc. (ppm)	1 sigma	LOD
^{108}Pd	0.05	0.03	0.02	0.15	0.07	0.05
^{108}Pd corr.				0.14		
^{189}Os	<0.04	0.03	0.04	<0.05	0.02	0.05
^{193}Ir	<0.01	0.003	0.01	<0.00	<0.00	<0.00
^{195}Pt	<0.03	0.01	0.03	<0.03	0.01	0.03
^{197}Au	<0.00	<0.00	<0.00	<0.03	0.02	0.03
^{59}Co	50.79	3.07	0.03	18.46	1.20	0.03
^{60}Ni	5265.00	347.14	0.34	3023.11	200.39	0.29
^{67}Zn	2.61	0.92	1.13	3.35	1.14	0.95
^{75}As	<0.28	0.14	0.28	<0.27	0.16	0.27
^{77}Se	8.43	1.88	1.67	6.87	1.89	0.96
^{82}Se	12.23	3.68	5.80	11.87	4.35	5.79
^{106}Cd	<0.61	0.19	0.61	0.62	0.62	<0.00
^{208}Pb	25.4	2.10	0.03	82.97	6.84	0.02
^{209}Bi	4.04	0.32	0.01	1.96	0.16	0.01

Spot Size	25µm			35µm		
Sample-spot	9-08			9-09		
Mineral	Chalcopyrite			Chalcopyrite		
	Conc. (ppm)	1 sigma	LOD	Conc. (ppm)	1 sigma	LOD
^{108}Pd	0.05	0.04	0.02	0.05	0.02	0.02
^{108}Pd corr.	0.03			0.04		
^{189}Os	<0.04	0.01	0.04	<0.02	0.01	0.02
^{193}Ir	<0.01	0.01	0.01	0.002	0.002	<0.00
^{195}Pt	<0.03	0.02	0.03	0.01	0.01	<0.00
^{197}Au	<0.01	0.00	0.01	<0.01	0.01	0.01
^{59}Co	1.70	0.17	0.02	62.30	3.74	0.01
^{60}Ni	2546.23	169.36	0.34	3796.67	252.76	0.18
^{67}Zn	3.56	1.11	1.02	2.32	0.47	0.58
^{75}As	<0.26	0.15	0.26	<0.11	0.07	0.11
^{77}Se	4.52	1.47	1.03	7.22	1.00	0.45
^{82}Se	<5.76	3.60	5.76	10.13	1.89	3.19
^{106}Cd	2.69	1.34	0.93	1.39	0.47	0.33
^{208}Pb	8.18	0.72	0.04	88.11	7.26	0.02
^{209}Bi	0.06	0.02	0.01	0.19	0.02	0.01

Spot Size	35µm			35µm		
Sample-spot	9-10			9-11		
Mineral	Chalcopyrite			Chalcopyrite		
	Conc. (ppm)	1 sigma	LOD	Conc. (ppm)	1 sigma	LOD
^{108}Pd	0.03	0.02	0.02	<0.02	0.01	0.02
^{108}Pd corr.						
^{189}Os	<0.02	0.01	0.02	<0.02	0.01	0.02
^{193}Ir	<0.01	0.004	0.01	<0.01	0.003	0.01
^{195}Pt	<0.02	0.005	0.02	<0.02	0.01	0.02
^{197}Au	<0.01	0.01	0.01	<0.01	0.005	0.01
^{59}Co	57.88	3.49	0.02	51.56	3.12	0.01
^{60}Ni	7417.81	495.55	0.18	5956.88	399.47	0.15
^{67}Zn	3.36	0.55	0.62	2.64	0.55	0.76
^{75}As	<0.150	0.08	0.15	0.28	0.08	0.10
^{77}Se	9.13	1.19	0.64	6.75	1.01	0.71
^{82}Se	7.92	1.95	3.66	6.86	1.87	3.50
^{106}Cd	<0.61	0.27	0.61	<0.49	0.25	0.49
^{208}Pb	120.69	9.97	0.02	122.58	10.17	0.01
^{209}Bi	0.05	0.01	0.01	0.05	0.01	0.01

Spot Size	35µm			35µm		
Sample-spot	9-12			9-13		
Mineral	Chalcopyrite			Bornite		
	Conc. (ppm)	1 sigma	LOD	Conc. (ppm)	1 sigma	LOD
^{108}Pd	<0.02	0.01	0.02	0.13	0.02	<0.00
^{108}Pd corr.				0.09		
^{189}Os	0.01	0.01	<0.00	<0.01	0.01	0.01
^{193}Ir	<0.005	0.004	0.005	<0.004	0.002	0.004
^{195}Pt	<0.01	0.01	0.01	0.003	0.003	<0.00
^{197}Au	<0.01	0.004	0.01	0.01	0.003	<0.00
^{59}Co	59.60	3.62	0.01	0.13	0.02	0.01
^{60}Ni	9758.24	656.88	0.21	<0.12	0.07	0.12
^{67}Zn	2.56	0.57	0.68	<0.45	0.22	0.45
^{75}As	<0.18	0.09	0.18	<0.09	0.05	0.09
^{77}Se	5.34	0.95	0.66	3.55	0.59	0.42
^{82}Se	6.98	1.93	3.34	3.90	1.09	1.94
^{106}Cd	<0.59	0.31	0.60	3.57	0.63	<0.00
^{208}Pb	27.18	2.28	0.02	9.92	0.89	0.01
^{209}Bi	<0.01	0.01	0.01	7.18	0.48	0.005

Spot Size	35µm			35µm		
Sample-spot	9-14			9-15		
Mineral	Bornite			Chalcopyrite		
	Conc. (ppm)	1 sigma	LOD	Conc. (ppm)	1 sigma	LOD
^{108}Pd	0.15	0.02	0.006	0.04	0.02	0.01
^{108}Pd corr.	0.13			0.04		
^{189}Os	0.01	0.01	<0.00	<0.01	0.005	0.01
^{193}Ir	<0.005	0.002	0.005	<0.005	0.005	0.01
^{195}Pt	0.003	0.003	<0.00	<0.01	0.004	0.01
^{197}Au	<0.003	0.002	0.003	<0.009	0.003	0.01
^{59}Co	0.13	0.02	0.01	17.01	1.07	0.02
^{60}Ni	<0.07	0.05	0.08	2385.03	162.57	0.17
^{67}Zn	<0.30	0.16	0.30	4.21	0.68	0.60
^{75}As	<0.08	0.03	0.08	<0.15	0.08	0.15
^{77}Se	5.06	0.70	0.45	7.30	1.15	0.65
^{82}Se	5.44	1.01	1.55	<2.91	1.64	2.91
^{106}Cd	1.82	0.43	0.23	0.80	0.46	0.50
^{208}Pb	9.98	0.84	0.005	65.70	5.50	0.01
^{209}Bi	0.67	0.05	0.004	0.21	0.02	0.01

Spot Size	35µm			35µm		
Sample-spot	9-16			9-17		
Mineral	Bornite			Bornite		
	Conc. (ppm)	1 sigma	LOD	Conc. (ppm)	1 sigma	LOD
^{108}Pd	0.11	0.02	0.01	0.14	0.03	<0.00
^{108}Pd corr.	0.08			0.11		
^{189}Os	<0.009	0.01	0.01	0.02	0.01	<0.00
^{193}Ir	<0.002	0.002	0.002	<0.003	0.002	0.003
^{195}Pt	<0.009	0.003	0.01	<0.007	0.002	0.01
^{197}Au	<0.007	0.003	0.01	<0.009	0.004	0.01
^{59}Co	0.16	0.02	0.01	0.16	0.02	0.01
^{60}Ni	0.43	0.09	0.10	0.16	0.06	0.09
^{67}Zn	0.47	0.24	0.38	<0.33	0.20	0.33
^{75}As	<0.08	0.04	0.08	0.14	0.05	0.07
^{77}Se	5.93	0.78	0.30	4.45	0.67	0.37
^{82}Se	4.42	1.04	1.71	4.79	1.11	1.81
^{106}Cd	3.04	0.60	0.31	3.35	0.63	0.19
^{208}Pb	9.68	0.83	0.01	12.75	1.09	0.01
^{209}Bi	0.42	0.03	0.004	0.44	0.04	0.004

Spot Size	35µm			35µm		
Sample-spot	9-18			9-19		
Mineral	Bornite			Valleriite		
	Conc. (ppm)	1 sigma	LOD	Conc. (ppm)	1 sigma	LOD
^{108}Pd	0.09	0.02	0.01	0.03	0.01	0.02
^{108}Pd corr.	0.07			0.002		
^{189}Os	<0.02	0.01	0.02	0.004	0.004	<0.00
^{193}Ir	<0.00	<0.00	<0.00	<0.003	0.001	0.003
^{195}Pt	<0.01	0.003	0.01	<0.01	0.005	0.01
^{197}Au	<0.005	0.002	0.01	<0.01	0.004	0.01
^{59}Co	0.51	0.05	0.01	3.59	0.24	0.01
^{60}Ni	23.78	1.74	0.11	187.51	13.05	0.12
^{67}Zn	<0.37	0.26	0.37	0.68	0.23	0.35
^{75}As	<0.08	0.05	0.08	0.14	0.05	0.08
^{77}Se	9.71	1.22	0.29	8.02	0.94	0.44
^{82}Se	8.56	1.43	1.70	6.68	1.23	2.05
^{106}Cd	2.27	0.60	0.30	2.81	0.54	0.21
^{208}Pb	27.66	2.37	0.01	70.30	6.02	0.01
^{209}Bi	0.41	0.04	0.004	14.10	0.97	0.01

Spot Size	35µm			35µm		
Sample-spot	9-20			9-21		
Mineral	Valleriite			Valleriite		
	Conc. (ppm)	1 sigma	LOD	Conc. (ppm)	1 sigma	LOD
^{108}Pd	0.08	0.02	0.02	0.06	0.02	0.01
^{108}Pd corr.	0.05			0.05		
^{189}Os	<0.02	0.01	0.02	<0.02	0.01	0.02
^{193}Ir	<0.003	0.002	0.003	<0.005	0.002	0.01
^{195}Pt	0.002	0.002	<0.00	<0.01	0.01	0.01
^{197}Au	0.01	0.003	<0.00	0.005	0.004	0.005
^{59}Co	3.70	0.24	0.01	3.17	0.21	0.01
^{60}Ni	242.02	16.88	0.15	296.17	20.75	0.11
^{67}Zn	1.26	0.29	0.52	0.87	0.23	0.35
^{75}As	<0.11	0.04	0.11	<0.10	0.04	0.10
^{77}Se	6.85	0.82	0.71	6.68	0.84	0.65
^{82}Se	8.32	1.30	2.38	8.52	1.35	2.26
^{106}Cd	2.67	0.49	0.44	1.98	0.46	0.44
^{208}Pb	116.82	10.04	0.01	103.81	8.96	0.01
^{209}Bi	186.80	12.62	0.01	461.14	31.26	0.01

Spot Size	35µm			35µm		
Sample-spot	9-22			9-23		
Mineral	Valleriite			Bornite		
	Conc. (ppm)	1 sigma	LOD	Conc. (ppm)	1 sigma	LOD
^{108}Pd	0.07	0.02	<0.00	0.10	0.02	0.01
^{108}Pd corr.	0.06			0.08		
^{189}Os	<0.01	0.01	0.01	<0.03	0.01	0.03
^{193}Ir	<0.003	0.002	0.003	<0.003	0.001	0.003
^{195}Pt	<0.01	0.004	0.01	0.01	0.01	<0.00
^{197}Au	<0.01	0.003	0.01	<0.005	0.004	0.01
^{59}Co	4.21	0.28	0.02	0.11	0.02	0.02
^{60}Ni	217.83	15.35	0.13	<0.13	0.07	0.13
^{67}Zn	1.12	0.26	0.33	0.82	0.33	0.51
^{75}As	0.10	0.05	0.08	<0.11	0.06	0.11
^{77}Se	7.22	0.90	0.58	5.79	0.87	0.49
^{82}Se	4.99	1.25	2.41	5.46	1.40	2.36
^{106}Cd	1.15	0.39	0.50	2.21	0.54	<0.00
^{208}Pb	113.31	9.83	0.01	15.27	1.34	0.01
^{209}Bi	25.45	1.74	0.01	0.34	0.03	0.01

Spot Size	35µm			35µm		
Sample-spot	9-24			9-25		
Mineral	Bornite			Bornite		
	Conc. (ppm)	1 sigma	LOD	Conc. (ppm)	1 sigma	LOD
^{108}Pd	0.07	0.02	0.01	0.08	0.02	0.02
^{108}Pd corr.	0.04			0.05		
^{189}Os	<0.01	0.004	0.01	0.005	0.005	<0.00
^{193}Ir	<0.004	0.002	0.004	<0.006	0.003	0.01
^{195}Pt	<0.01	0.003	0.01	<0.02	0.01	0.02
^{197}Au	<0.01	0.003	0.01	<0.01	0.004	0.01
^{59}Co	0.22	0.03	0.01	0.10	0.02	0.02
^{60}Ni	4.53	0.41	0.11	<0.18	0.09	0.19
^{67}Zn	0.56	0.27	0.38	1.14	0.37	0.70
^{75}As	0.09	0.06	0.08	<0.13	0.06	0.13
^{77}Se	4.90	0.77	0.19	10.41	1.20	0.74
^{82}Se	4.91	1.25	1.90	8.99	1.68	3.19
^{106}Cd	2.83	0.64	<0.00	3.01	0.61	0.47
^{208}Pb	17.74	1.56	0.01	20.35	1.80	0.01
^{209}Bi	0.74	0.06	0.005	0.66	0.05	0.01

Spot Size	35µm			35µm		
Sample-spot	9-26			5-01		
Mineral	Bornite			Bornite		
	Conc. (ppm)	1 sigma	LOD	Conc. (ppm)	1 sigma	LOD
^{108}Pd	0.10	0.02	0.01	0.06	0.02	0.01
^{108}Pd corr.	0.07			0.04		
^{189}Os	0.01	0.01	<0.00	<0.01	0.005	0.01
^{193}Ir	<0.005	0.002	0.005	0.001	0.001	<0.00
^{195}Pt	<0.01	0.01	0.01	<0.01	0.004	0.01
^{197}Au	<0.01	0.004	0.01	<0.00	<0.00	<0.00
^{59}Co	0.12	0.02	0.02	0.12	0.02	0.01
^{60}Ni	0.20	0.10	0.19	0.13	0.06	0.09
^{67}Zn	<0.80	0.36	0.80	0.46	0.20	0.32
^{75}As	0.13	0.07	0.13	<0.07	0.04	0.07
^{77}Se	9.78	1.21	0.61	9.93	1.10	0.22
^{82}Se	12.90	2.02	3.36	9.09	1.26	1.60
^{106}Cd	3.27	0.67	<0.00	1.80	0.43	0.23
^{208}Pb	29.56	2.62	0.01	3.61	0.33	0.01
^{209}Bi	0.79	0.06	0.01	0.19	0.02	0.005

Spot Size	35µm			35µm		
Sample-spot	5-02			5-03		
Mineral	Bornite			Bornite		
	Conc. (ppm)	1 sigma	LOD	Conc. (ppm)	1 sigma	LOD
^{108}Pd	0.07	0.02	0.01	0.09	0.02	<0.00
^{108}Pd corr.	0.06			0.08		
^{189}Os	<0.01	0.002	0.01	<0.01	0.005	0.01
^{193}Ir	0.005	0.002	<0.00	<0.002	0.001	0.002
^{195}Pt	0.003	0.003	<0.00	<0.01	0.005	0.01
^{197}Au	<0.01	0.003	0.01	<0.005	0.003	0.01
^{59}Co	0.11	0.02	0.01	0.20	0.02	0.01
^{60}Ni	0.17	0.06	0.08	0.34	0.08	0.09
^{67}Zn	0.61	0.18	0.19	0.89	0.23	0.24
^{75}As	<0.06	0.03	0.06	<0.07	0.04	0.07
^{77}Se	10.32	1.15	0.27	10.15	1.15	0.27
^{82}Se	11.84	1.38	1.22	12.41	1.46	1.31
^{106}Cd	0.56	0.26	0.24	1.01	0.35	0.32
^{208}Pb	4.33	0.39	0.01	6.36	0.58	0.01
^{209}Bi	0.23	0.02	0.002	0.29	0.03	0.004

Spot Size	25µm			20µm		
Sample-spot	5-04			5-05		
Mineral	Chalcopyrite			Chalcopyrite		
	Conc. (ppm)	1 sigma	LOD	Conc. (ppm)	1 sigma	LOD
^{108}Pd	0.07	0.04	0.03	<0.20	0.08	0.20
^{108}Pd corr.	0.06					
^{189}Os	<0.059	0.05	0.06	<0.00	<0.00	<0.00
^{193}Ir	<0.00	<0.00	<0.00	<0.03	0.01	0.03
^{195}Pt	<0.0227	0.01	0.02	<0.08	0.06	0.08
^{197}Au	<0.014	0.01	0.01	0.02	0.02	<0.00
^{59}Co	5.00	0.40	0.04	3.03	0.29	0.12
^{60}Ni	3169.54	231.28	0.38	3705.00	271.81	1.72
^{67}Zn	4.84	1.18	1.18	4.92	1.94	3.46
^{75}As	<0.25	0.16	0.25	<1.18	0.45	1.18
^{77}Se	16.09	2.77	1.00	16.38	4.45	7.38
^{82}Se	15.32	4.20	5.94	<21.46	9.80	21.46
^{106}Cd	0.83	0.76	0.66	<4.11	1.76	4.11
^{208}Pb	51.99	4.72	0.04	224.30	20.33	0.10
^{209}Bi	3.45	0.27	0.01	7.41	0.57	0.08

Spot Size	20µm			35µm		
Sample-spot	5-06			5-07		
Mineral	Chalcopyrite			Bornite		
	Conc. (ppm)	1 sigma	LOD	Conc. (ppm)	1 sigma	LOD
^{108}Pd	0.06	0.05	0.04	0.03	0.01	0.01
^{108}Pd corr.				0.02		
^{189}Os	<0.115	0.06	0.12	<0.01	0.002	0.01
^{193}Ir	<0.021	0.02	0.02	<0.004	0.002	0.004
^{195}Pt	<0.038	0.01	0.04	<0.01	0.004	0.01
^{197}Au	<0.033	0.01	0.03	0.01	0.003	<0.00
^{59}Co	18.29	1.34	0.05	0.02	0.01	0.01
^{60}Ni	4571.21	337.14	0.63	<0.09	0.05	0.09
^{67}Zn	2.33	1.66	2.24	<0.29	0.17	0.29
^{75}As	<0.45	0.32	0.45	<0.06	0.03	0.06
^{77}Se	16.56	3.75	1.99	9.32	1.09	0.33
^{82}Se	21.78	7.22	10.25	10.33	1.36	1.51
^{106}Cd	<1.11	1.02	1.11	0.79	0.27	<0.00
^{208}Pb	36.00	3.35	0.05	2.85	0.27	0.01
^{209}Bi	3.56	0.31	0.02	0.03	0.01	0.001

Spot Size	35µm			35µm		
Sample-spot	5-08			5-09		
Mineral	Bornite			Bornite		
	Conc. (ppm)	1 sigma	LOD	Conc. (ppm)	1 sigma	LOD
^{108}Pd	0.07	0.02	0.01	0.04	0.02	0.01
^{108}Pd corr.	0.06					
^{189}Os	<0.01	0.003	0.01	<0.01	0.003	0.01
^{193}Ir	<0.004	0.001	0.004	<0.002	0.001	0.002
^{195}Pt	<0.01	0.003	0.01	<0.01	0.004	0.01
^{197}Au	0.002	0.002	<0.00	<0.004	0.001	0.004
^{59}Co	0.04	0.01	0.01	0.05	0.01	0.01
^{60}Ni	0.15	0.07	0.10	0.11	0.06	0.09
^{67}Zn	0.46	0.22	0.35	<0.33	0.19	0.33
^{75}As	0.11	0.05	0.07	<0.07	0.04	0.07
^{77}Se	10.91	1.26	0.43	10.01	1.18	0.18
^{82}Se	12.75	1.61	1.74	10.63	1.47	1.74
^{106}Cd	0.61	0.27	0.19	<0.45	0.30	0.45
^{208}Pb	3.51	0.33	0.01	2.20	0.21	0.01
^{209}Bi	0.04	0.01	0.004	0.04	0.01	0.005

Spot Size	35µm			35µm		
Sample-spot	7-01			7-02		
Mineral	Valleriite			Valleriite		
	Conc. (ppm)	1 sigma	LOD	Conc. (ppm)	1 sigma	LOD
^{108}Pd	<0.03	0.02	0.03	<0.03	0.01	0.03
^{108}Pd corr.						
^{189}Os	<0.04	0.02	0.05	<0.05	0.02	0.05
^{193}Ir	<0.01	0.005	0.01	<0.01	0.01	0.01
^{195}Pt	<0.02	0.01	0.02	<0.03	0.02	0.03
^{197}Au	<0.01	0.01	0.02	<0.02	0.02	0.02
^{59}Co	373.16	25.03	0.04	331.31	22.34	0.03
^{60}Ni	2126.96	159.79	0.35	2169.92	163.86	0.35
^{67}Zn	2.78	0.78	0.92	3.12	0.87	1.03
^{75}As	<0.21	0.14	0.21	<0.25	0.15	0.25
^{77}Se	4.80	1.26	1.27	3.71	1.13	1.12
^{82}Se	<4.15	2.33	4.15	5.02	2.60	4.48
^{106}Cd	<0.87	0.50	0.87	<0.74	<0.00	0.74
^{208}Pb	0.33	0.05	0.02	4.37	0.43	0.03
^{209}Bi	<0.01	0.004	0.01	0.04	0.01	0.01

Spot Size	35µm			35µm		
Sample-spot	7-03			7-04		
Mineral	Valleriite			Valleriite		
	Conc. (ppm)	1 sigma	LOD	Conc. (ppm)	1 sigma	LOD
^{108}Pd	<0.05	0.02	0.05	0.04	0.03	0.02
^{108}Pd corr.						
^{189}Os	<0.04	0.01	0.05	0.06	0.04	0.04
^{193}Ir	<0.01	0.01	0.01	<0.01	0.003	0.01
^{195}Pt	<0.04	0.03	0.04	0.03	0.03	0.02
^{197}Au	<0.04	0.03	0.05	0.01	0.01	0.01
^{59}Co	416.41	28.30	0.04	293.38	20.00	0.04
^{60}Ni	2582.12	196.41	0.41	2239.53	170.91	0.33
^{67}Zn	25.29	3.31	1.24	<1.06	0.75	1.06
^{75}As	<0.28	0.24	0.28	<0.19	0.14	0.20
^{77}Se	6.05	2.11	1.39	3.52	1.21	1.06
^{82}Se	<5.63	3.88	5.63	6.11	2.67	3.87
^{106}Cd	<1.38	0.43	1.38	<0.78	0.62	0.78
^{208}Pb	14.19	1.39	0.03	0.38	0.06	0.02
^{209}Bi	<0.01	0.01	0.02	<0.01	0.01	0.01

Spot Size	35µm			35µm		
Sample-spot	7-05			7-06		
Mineral	Valleriite			Valleriite		
	Conc. (ppm)	1 sigma	LOD	Conc. (ppm)	1 sigma	LOD
^{108}Pd	<0.05	0.02	0.06	0.03	0.03	<0.00
^{108}Pd corr.						
^{189}Os	0.04	0.03	0.03	<0.05	0.05	0.05
^{193}Ir	<0.01	0.01	0.01	<0.02	0.01	0.02
^{195}Pt	<0.04	0.01	0.04	<0.05	0.02	0.05
^{197}Au	0.03	0.02	0.02	<0.02	0.02	0.02
^{59}Co	321.70	22.04	0.04	263.00	18.00	0.06
^{60}Ni	2739.63	210.11	0.52	2924.25	225.66	0.56
^{67}Zn	<1.19	0.79	1.19	4.66	1.40	1.13
^{75}As	<0.26	0.17	0.26	1.54	0.40	0.27
^{77}Se	5.72	1.68	1.67	<1.69	1.24	1.69
^{82}Se	<5.23	2.88	5.23	<5.31	3.84	5.31
^{106}Cd	<1.30	0.73	1.30	<1.02	1.01	1.02
^{208}Pb	4.24	0.43	0.02	14.22	1.40	0.02
^{209}Bi	0.04	0.01	0.01	0.39	0.06	0.01

Spot Size	35µm			35µm		
Sample-spot	7-07			7-08		
Mineral	Valleriite			Valleriite		
	Conc. (ppm)	1 sigma	LOD	Conc. (ppm)	1 sigma	LOD
^{108}Pd	<0.02	0.01	0.02	<0.02	0.02	0.02
^{108}Pd corr.						
^{189}Os	<0.03	0.03	0.03	<0.02	0.01	0.02
^{193}Ir	<0.01	0.003	0.01	<0.01	0.004	0.01
^{195}Pt	<0.02	0.01	0.02	<0.02	0.01	0.02
^{197}Au	<0.01	0.01	0.01	<0.00	<0.00	<0.00
^{59}Co	668.89	46.21	0.03	420.72	29.19	0.02
^{60}Ni	2402.02	186.14	0.24	2464.10	191.71	0.21
^{67}Zn	10.76	1.61	0.98	10.43	1.12	0.64
^{75}As	<0.18	0.12	0.18	0.30	0.11	0.15
^{77}Se	5.17	1.35	0.66	4.20	0.88	0.61
^{82}Se	<3.90	2.51	3.90	4.27	1.88	3.42
^{106}Cd	<0.61	0.19	0.61	<0.64	0.39	0.64
^{208}Pb	5.72	0.58	0.02	5.34	0.53	0.01
^{209}Bi	0.13	0.02	0.01	0.01	0.01	0.01

Spot Size	35µm			35µm		
Sample-spot	6-01			6-02		
Mineral	Chalcopyrite			Chalcopyrite		
	Conc. (ppm)	1 sigma	LOD	Conc. (ppm)	1 sigma	LOD
^{108}Pd	<0.02	0.01	0.02	<0.03	0.01	0.03
^{108}Pd corr.						
^{189}Os	<0.03	0.02	0.03	0.01	0.01	<0.00
^{193}Ir	<0.01	0.004	0.01	<0.01	0.003	0.01
^{195}Pt	<0.02	0.01	0.02	0.02	0.01	0.01
^{197}Au	<0.02	0.01	0.02	<0.01	0.01	0.01
^{59}Co	0.75	0.07	0.02	0.63	0.06	0.02
^{60}Ni	1460.78	114.24	0.22	1539.14	120.99	0.19
^{67}Zn	3.64	0.60	0.76	4.86	0.68	0.74
^{75}As	<0.11	0.06	0.11	<0.17	0.07	0.17
^{77}Se	8.28	1.18	0.74	8.78	1.24	0.80
^{82}Se	7.26	1.85	3.52	10.66	1.99	3.32
^{106}Cd	0.69	0.35	0.39	0.67	0.31	<0.00
^{208}Pb	1.13	0.12	0.01	1.83	0.19	0.02
^{209}Bi	0.89	0.07	0.01	0.05	0.01	0.01

Spot Size	35µm			35µm		
Sample-spot	6-03			6-04		
Mineral	Chalcopyrite			Chalcopyrite		
	Conc. (ppm)	1 sigma	LOD	Conc. (ppm)	1 sigma	LOD
^{108}Pd	<0.03	0.01	0.03	<0.01	0.01	0.01
^{108}Pd corr.						
^{189}Os	<0.02	0.01	0.02	<0.03	0.01	0.03
^{193}Ir	<0.01	0.003	0.01	<0.005	0.002	0.005
^{195}Pt	<0.02	0.01	0.02	<0.01	0.01	0.01
^{197}Au	0.04	0.01	0.01	<0.01	0.01	0.01
^{59}Co	0.47	0.05	0.02	0.717	0.07	0.03
^{60}Ni	1577.03	124.62	0.17	1524.74	121.13	0.18
^{67}Zn	3.41	0.59	0.81	3.38	0.57	0.72
^{75}As	<0.14	0.07	0.14	0.132	0.07	0.12
^{77}Se	5.81	0.96	0.87	8.99	1.23	0.60
^{82}Se	6.04	1.83	3.70	11.06	1.93	3.06
^{106}Cd	0.39	0.23	<0.00	<0.52	0.21	0.52
^{208}Pb	1.11	0.12	0.02	1.44	0.15	0.02
^{209}Bi	0.04	0.01	0.01	0.05	0.01	0.005

Spot Size	35µm			35µm		
Sample-spot	6-05			6-06		
Mineral	Chalcopyrite			Chalcopyrite		
	Conc. (ppm)	1 sigma	LOD	Conc. (ppm)	1 sigma	LOD
^{108}Pd	<0.04	0.02	0.04	<0.03	0.01	0.03
^{108}Pd corr.						
^{189}Os	<0.05	0.02	0.05	<0.03	0.01	0.03
^{193}Ir	0.003	0.002	<0.00	<0.01	0.004	0.01
^{195}Pt	<0.03	0.01	0.03	<0.01	0.004	0.01
^{197}Au	0.05	0.01	0.01	0.06	0.02	0.02
^{59}Co	0.79	0.07	0.03	0.98	0.09	0.03
^{60}Ni	1442.74	115.21	0.25	1511.06	121.31	0.28
^{67}Zn	4.94	0.64	0.79	6.15	0.71	0.61
^{75}As	<0.21	0.08	0.21	<0.19	0.08	0.19
^{77}Se	7.28	1.07	1.07	11.54	1.45	0.63
^{82}Se	7.62	1.93	4.07	12.31	2.05	3.33
^{106}Cd	<0.46	0.23	0.46	0.49	0.30	0.38
^{208}Pb	0.87	0.09	0.02	0.63	0.07	0.01
^{209}Bi	0.14	0.02	0.01	0.19	0.03	0.01

Spot Size	35µm			35µm		
Sample-spot	6-07			6-08		
Mineral	Chalcopyrite			Chalcopyrite		
	Conc. (ppm)	1 sigma	LOD	Conc. (ppm)	1 sigma	LOD
^{108}Pd	<0.01	0.01	0.02	<0.02	0.01	0.03
^{108}Pd corr.						
^{189}Os	<0.02	0.01	0.02	<0.03	0.02	0.03
^{193}Ir	<0.005	0.002	0.01	<0.01	0.003	0.01
^{195}Pt	0.01	0.01	<0.00	<0.02	0.01	0.02
^{197}Au	0.14	0.02	0.01	0.06	0.01	0.01
^{59}Co	1.10	0.09	0.02	1.08	0.09	0.03
^{60}Ni	1575.48	127.14	0.19	1655.43	134.32	0.24
^{67}Zn	4.68	0.61	0.73	4.85	0.69	0.89
^{75}As	<0.18	0.07	0.18	<0.14	0.06	0.14
^{77}Se	9.35	1.21	0.66	7.45	1.12	0.92
^{82}Se	8.20	1.80	3.55	7.97	1.96	3.93
^{106}Cd	<0.57	0.25	0.57	<1.11	0.49	1.11
^{208}Pb	1.36	0.14	0.02	0.78	0.09	0.02
^{209}Bi	0.29	0.03	0.01	0.16	0.02	0.01

Spot Size	35µm			35µm		
Sample-spot	6-09			6-10		
Mineral	Chalcopyrite			Chalcopyrite		
	Conc. (ppm)	1 sigma	LOD	Conc. (ppm)	1 sigma	LOD
^{108}Pd	<0.03	0.02	0.03	<0.02	0.01	0.02
^{108}Pd corr.						
^{189}Os	<0.03	0.01	0.03	<0.04	0.01	0.04
^{193}Ir	<0.01	0.003	0.01	<0.01	0.003	0.01
^{195}Pt	<0.02	0.01	0.02	<0.02	0.01	0.02
^{197}Au	0.03	0.01	<0.00	0.01	0.01	0.01
^{59}Co	0.81	0.07	0.02	0.73	0.07	0.02
^{60}Ni	1507.04	122.93	0.24	1399.83	114.82	0.18
^{67}Zn	3.62	0.54	0.70	4.36	0.62	0.53
^{75}As	<0.18	0.07	0.18	<0.14	0.06	0.14
^{77}Se	6.80	1.03	0.97	8.91	1.29	0.76
^{82}Se	4.30	1.79	3.97	13.25	2.16	3.06
^{106}Cd	0.67	0.28	<0.00	1.00	0.39	<0.00
^{208}Pb	2.99	0.31	0.02	0.62	0.07	0.01
^{209}Bi	0.13	0.02	0.01	0.07	0.01	0.004

Spot Size	35µm			35µm		
Sample-spot	6-11			6-12		
Mineral	Chalcopyrite			Chalcopyrite		
	Conc. (ppm)	1 sigma	LOD	Conc. (ppm)	1 sigma	LOD
^{108}Pd	<0.03	0.02	0.03	<0.03	0.01	0.03
^{108}Pd corr.						
^{189}Os	0.01	0.01	<0.00	0.03	0.02	0.02
^{193}Ir	0.003	0.002	<0.00	<0.01	0.003	0.01
^{195}Pt	<0.03	0.01	0.03	<0.03	0.01	0.03
^{197}Au	<0.01	0.01	0.01	0.01	0.01	0.01
^{59}Co	0.71	0.07	0.02	0.89	0.08	0.03
^{60}Ni	1468.48	121.08	0.24	1476.94	122.45	0.22
^{67}Zn	3.92	0.54	0.50	4.06	0.62	0.65
^{75}As	<0.15	0.06	0.16	<0.17	0.07	0.17
^{77}Se	7.79	1.15	0.91	10.89	1.51	0.93
^{82}Se	9.80	1.91	3.36	8.10	2.04	3.83
^{106}Cd	<0.37	0.12	0.37	<0.72	0.26	0.72
^{208}Pb	1.05	0.11	0.01	2.43	0.26	0.01
^{209}Bi	0.06	0.01	0.01	3.71	0.30	0.01

Spot Size	35µm			35µm		
Sample-spot	6-13			13-01		
Mineral	Chalcopyrite			Chalcopyrite		
	Conc. (ppm)	1 sigma	LOD	Conc. (ppm)	1 sigma	LOD
^{108}Pd	<0.02	0.01	0.02	<0.01	0.01	0.01
^{108}Pd corr.						
^{189}Os	<0.04	0.02	0.04	<0.02	0.01	0.02
^{193}Ir	<0.09	0.003	0.01	<0.004	0.003	0.004
^{195}Pt	<0.02	0.01	0.02	<0.02	0.005	0.02
^{197}Au	<0.01	0.002	0.01	<0.01	0.003	0.01
^{59}Co	0.83	0.08	0.02	39.79	2.99	0.01
^{60}Ni	1578.11	131.54	0.20	2426.24	203.28	0.17
^{67}Zn	5.70	0.73	0.65	5.12	0.66	0.32
^{75}As	<0.14	0.07	0.14	<0.10	0.06	0.10
^{77}Se	11.97	1.63	1.06	3.39	0.74	0.64
^{82}Se	11.84	2.11	3.27	<2.91	1.49	2.91
^{106}Cd	0.28	0.20	<0.00	1.01	0.46	0.45
^{208}Pb	1.11	0.12	0.01	29.93	3.10	0.01
^{209}Bi	0.09	0.01	0.01	0.09	0.01	0.01

Spot Size	35µm			35µm		
Sample-spot	13-02			13-03		
Mineral	Chalcopyrite			Chalcopyrite		
	Conc. (ppm)	1 sigma	LOD	Conc. (ppm)	1 sigma	LOD
^{108}Pd	<0.03	0.01	0.03	0.04	0.02	0.02
^{108}Pd corr.				0.03		
^{189}Os	<0.02	0.01	0.02	<0.02	0.01	0.02
^{193}Ir	<0.005	0.003	0.005	<0.004	0.001	0.004
^{195}Pt	<0.01	0.004	0.01	<0.02	0.01	0.02
^{197}Au	0.01	0.01	0.01	<0.01	0.00	0.01
^{59}Co	30.74	2.32	0.01	50.77	3.84	0.01
^{60}Ni	1472.87	124.09	0.22	2693.69	228.12	0.20
^{67}Zn	2.87	0.48	0.53	6.38	0.76	0.60
^{75}As	<0.14	0.06	0.14	<0.09	0.05	0.09
^{77}Se	4.19	0.80	0.78	4.96	0.89	0.72
^{82}Se	4.61	1.64	3.26	3.43	1.50	2.92
^{106}Cd	0.66	0.37	0.49	0.77	0.42	0.56
^{208}Pb	122.68	12.73	0.01	128.50	13.40	0.02
^{209}Bi	6.53	0.53	0.01	0.04	0.01	0.005

Spot Size	35µm			20µm		
Sample-spot	13-04			13-05		
Mineral	Chalcopyrite			Chalcocite		
	Conc. (ppm)	1 sigma	LOD	Conc. (ppm)	1 sigma	LOD
^{108}Pd	0.03	0.01	<0.00	0.16	0.06	0.03
^{108}Pd corr.	0.03			0.12		
^{189}Os	<0.04	0.02	0.04	<0.03	0.01	0.03
^{193}Ir	<0.005	0.003	0.005	<0.01	0.004	0.01
^{195}Pt	<0.02	0.01	0.02	<0.02	0.02	0.02
^{197}Au	<0.01	0.004	0.01	0.02	0.02	0.01
^{59}Co	42.32	3.22	0.02	22.00	1.74	0.01
^{60}Ni	1718.68	146.36	0.21	1313.83	112.81	0.27
^{67}Zn	2.72	0.50	0.66	17.00	2.17	0.55
^{75}As	0.13	0.06	0.09	<0.21	0.15	0.21
^{77}Se	2.28	0.59	0.73	2.87	1.20	0.95
^{82}Se	3.25	1.56	3.25	4.36	2.97	4.19
^{106}Cd	0.51	0.30	0.36	5.12	1.75	0.81
^{208}Pb	20.76	2.18	0.01	337.35	35.59	0.02
^{209}Bi	<0.01	0.005	0.01	177.31	14.48	0.01

Spot Size	20µm			35µm		
Sample-spot	13-06			13-07		
Mineral	Chalcocite			Chalcocite		
	Conc. (ppm)	1 sigma	LOD	Conc. (ppm)	1 sigma	LOD
^{108}Pd	<0.04	0.01	0.04	0.04	0.02	0.02
^{108}Pd corr.				0.02		
^{189}Os	<0.00	<0.00	<0.00	<0.02	0.01	0.02
^{193}Ir	<0.006	0.002	0.01	0.004	0.003	0.003
^{195}Pt	<0.01	0.02	0.01	<0.01	0.003	0.01
^{197}Au	<0.01	0.003	0.01	<0.01	0.002	0.01
^{59}Co	30.14	2.37	0.03	31.52	2.44	0.01
^{60}Ni	1452.19	125.34	0.21	1530.00	138.94	0.13
^{67}Zn	1.60	0.82	0.82	11.26	1.01	0.36
^{75}As	<0.15	0.12	0.15	<0.09	0.04	0.09
^{77}Se	2.42	1.02	0.56	1.48	0.43	0.44
^{82}Se	4.11	2.84	3.79	<2.04	1.04	2.04
^{106}Cd	<0.93	0.29	0.93	1.68	0.48	0.22
^{208}Pb	3.40	0.39	0.02	289.19	30.79	0.01
^{209}Bi	0.03	0.01	0.01	17.36	1.43	0.004

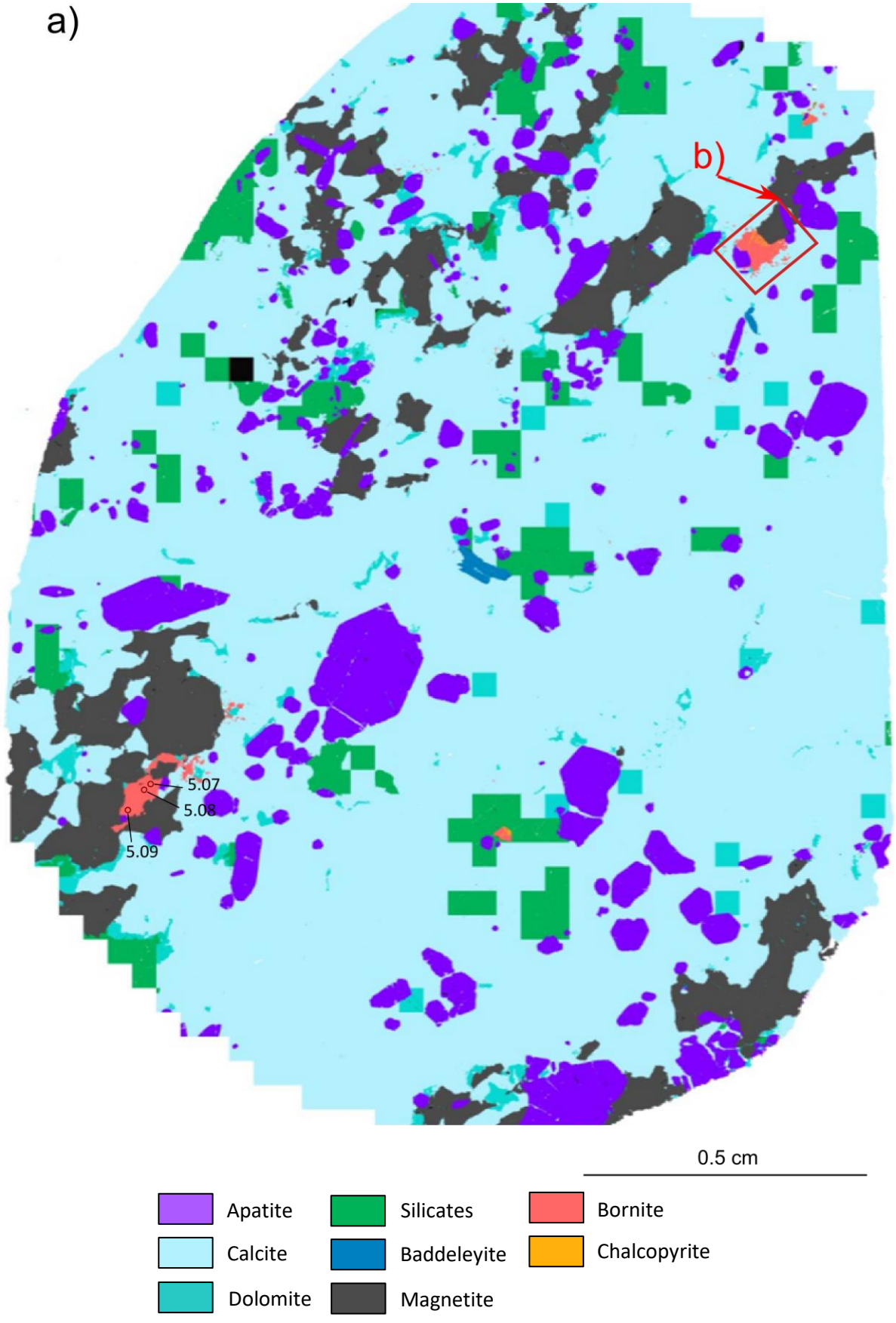
Spot Size	35µm			35µm		
Sample-spot	13-08			13-09		
Mineral	Bornite			Bornite		
	Conc. (ppm)	1 sigma	LOD	Conc. (ppm)	1 sigma	LOD
^{108}Pd	0.13	0.02	0.01	0.13	0.02	0.01
^{108}Pd corr.	0.10			0.09		
^{189}Os	<0.01	0.01	0.01	0.01	0.01	<0.00
^{193}Ir	<0.003	0.002	0.003	<0.003	0.001	0.003
^{195}Pt	<0.01	0.01	0.01	<0.004	0.001	0.005
^{197}Au	<0.004	0.00	0.00	<0.005	0.002	0.005
^{59}Co	0.14	0.02	0.01	0.13	0.02	0.01
^{60}Ni	<0.09	0.05	0.09	<0.08	0.05	0.08
^{67}Zn	0.68	0.19	0.23	<0.26	0.15	0.26
^{75}As	<0.04	0.03	0.05	<0.04	0.02	0.04
^{77}Se	13.95	1.63	0.33	9.55	1.19	0.30
^{82}Se	16.76	1.99	1.32	9.28	1.27	1.11
^{106}Cd	3.16	0.60	0.32	3.54	0.64	0.31
^{208}Pb	117.26	12.55	0.01	60.33	6.50	0.004
^{209}Bi	24.60	2.04	0.001	32.17	2.68	0.002

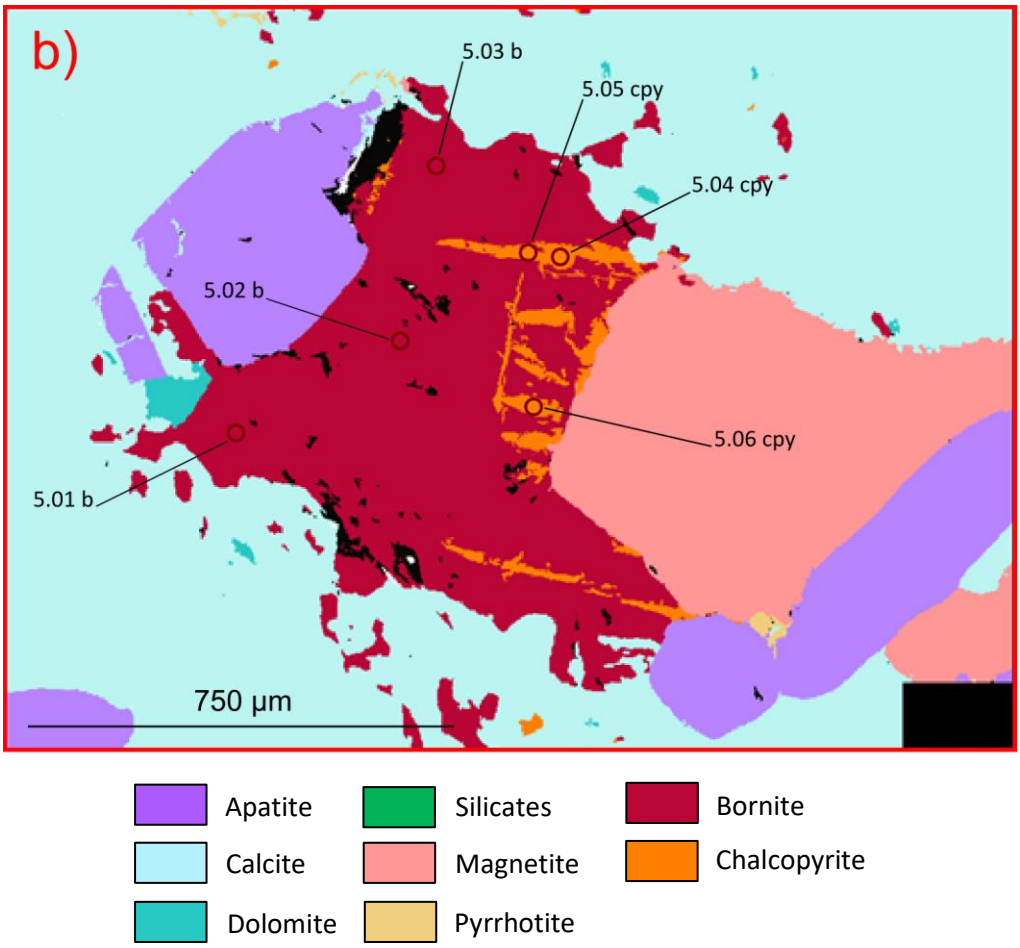
Spot Size	35µm			35µm		
Sample-spot	13-10			13-11		
Mineral	Bornite			Valleriite		
	Conc. (ppm)	1 sigma	LOD	Conc. (ppm)	1 sigma	LOD
^{108}Pd	0.10	0.02	0.01	0.53	0.07	0.01
^{108}Pd corr.	0.07			0.44		
^{189}Os	<0.01	0.004	0.01	<0.00	<0.00	<0.00
^{193}Ir	<0.003	0.002	0.003	0.004	0.003	<0.00
^{195}Pt	<0.005	0.001	0.005	<0.01	0.003	0.01
^{197}Au	<0.005	0.002	0.005	<0.00	<0.00	<0.00
^{59}Co	0.17	0.02	0.005	5.45	0.45	0.01
^{60}Ni	<0.08	0.05	0.08	113.75	10.14	0.10
^{67}Zn	0.44	0.18	0.23	4.02	0.58	0.36
^{75}As	<0.05	0.02	0.05	0.59	0.12	0.11
^{77}Se	10.30	1.28	0.25	9.59	1.37	0.32
^{82}Se	10.45	1.42	1.25	8.08	1.53	1.88
^{106}Cd	3.41	0.63	0.22	9.66	1.50	0.48
^{208}Pb	86.47	9.36	0.01	1253.14	136.25	0.01
^{209}Bi	9.72	0.82	0.002	52.61	4.42	0.003

Spot Size	35µm			35µm		
Sample-spot	13-12			13-13		
Mineral	Valleriite			Valleriite		
	Conc. (ppm)	1 sigma	LOD	Conc. (ppm)	1 sigma	LOD
^{108}Pd	0.12	0.02	0.01	0.11	0.03	0.01
^{108}Pd corr.	0.09			0.09		
^{189}Os	<0.03	0.01	0.03	<0.022	0.01	0.02
^{193}Ir	<0.00	<0.00	<0.00	<0.0042	0.001	0.004
^{195}Pt	0.02	0.01	<0.00	<0.0062	0.002	0.01
^{197}Au	0.01	0.004	<0.00	<0.0083	0.004	0.01
^{59}Co	7.47	0.60	0.02	1.55	0.14	0.01
^{60}Ni	156.18	13.94	0.15	55.98	5.08	0.12
^{67}Zn	4.20	0.52	0.50	6.03	0.68	0.23
^{75}As	1.38	0.18	0.11	0.77	0.13	0.07
^{77}Se	9.43	1.26	0.81	8.44	1.21	0.31
^{82}Se	8.12	1.53	2.56	9.21	1.49	1.51
^{106}Cd	3.26	0.62	<0.00	2.77	0.66	0.25
^{208}Pb	1121.04	122.52	0.01	137.90	15.16	0.01
^{209}Bi	11.14	0.94	0.01	3.81	0.33	0.003

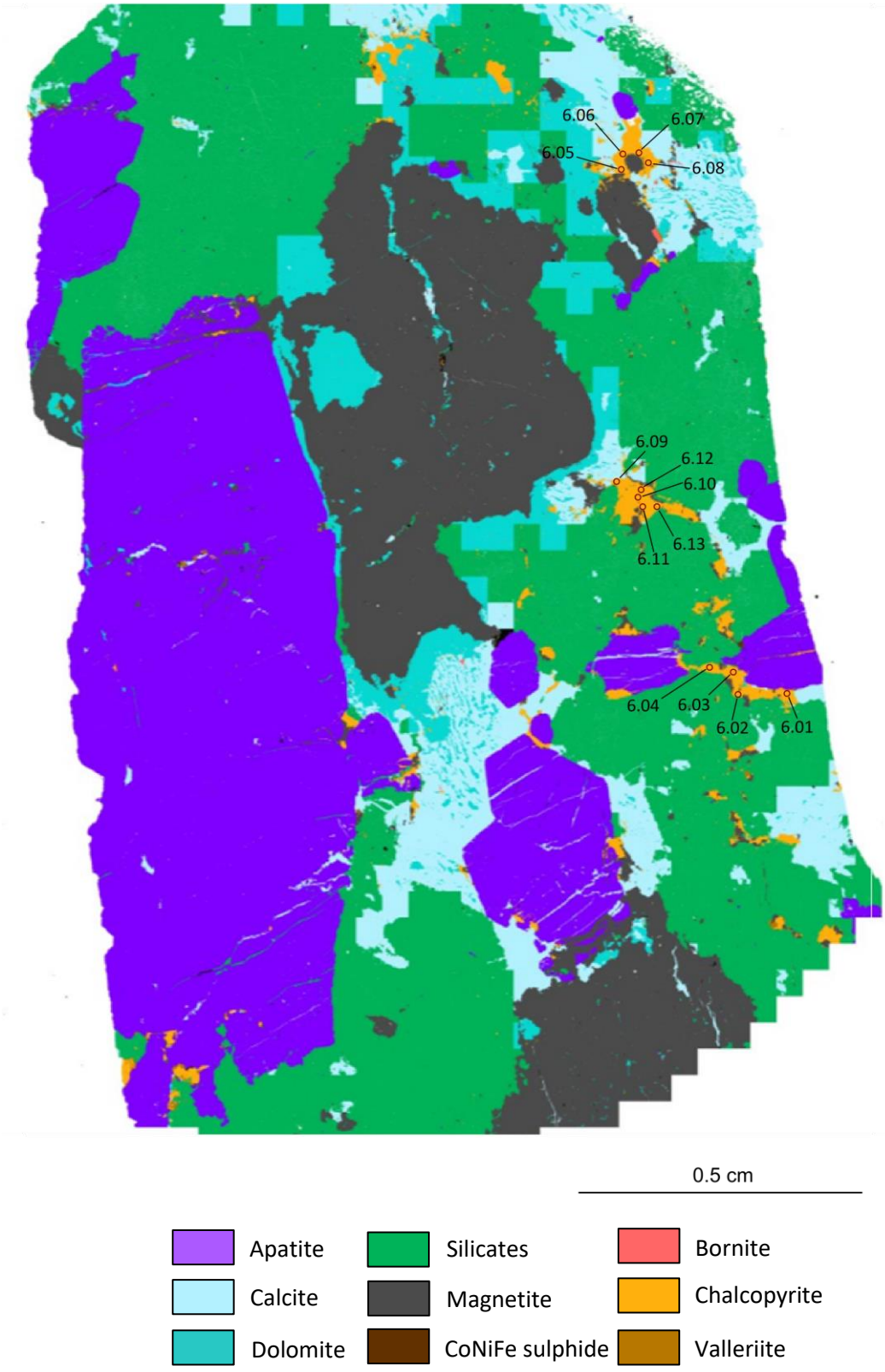
Spot Size	35µm			35µm		
Sample-spot	13-14			13-15		
Mineral	Chalcopyrite			Bornite		
	Conc. (ppm)	1 sigma	LOD	Conc. (ppm)	1 sigma	LOD
^{108}Pd	0.05	0.02	0.01	0.10	0.02	0.01
^{108}Pd corr.	0.04			0.07		
^{189}Os	<0.02	0.01	0.02	<0.02	0.01	0.02
^{193}Ir	<0.01	0.003	0.01	<0.004	0.002	0.005
^{195}Pt	0.03	0.01	<0.00	<0.01	0.01	0.01
^{197}Au	<0.01	0.004	0.01	<0.004	0.003	0.004
^{59}Co	48.90	3.92	0.02	0.57	0.06	0.01
^{60}Ni	2353.99	211.64	0.22	86.42	7.88	0.11
^{67}Zn	4.05	0.63	0.62	6.51	0.73	0.37
^{75}As	<0.12	0.06	0.12	<0.07	0.04	0.07
^{77}Se	2.97	0.72	0.78	11.03	1.50	0.40
^{82}Se	<3.19	1.55	3.19	8.58	1.52	1.78
^{106}Cd	0.62	0.35	0.36	2.31	0.59	0.19
^{208}Pb	210.12	23.22	0.01	149.15	16.57	0.01
^{209}Bi	28.33	2.42	0.01	2.71	0.24	0.004

Sample 5

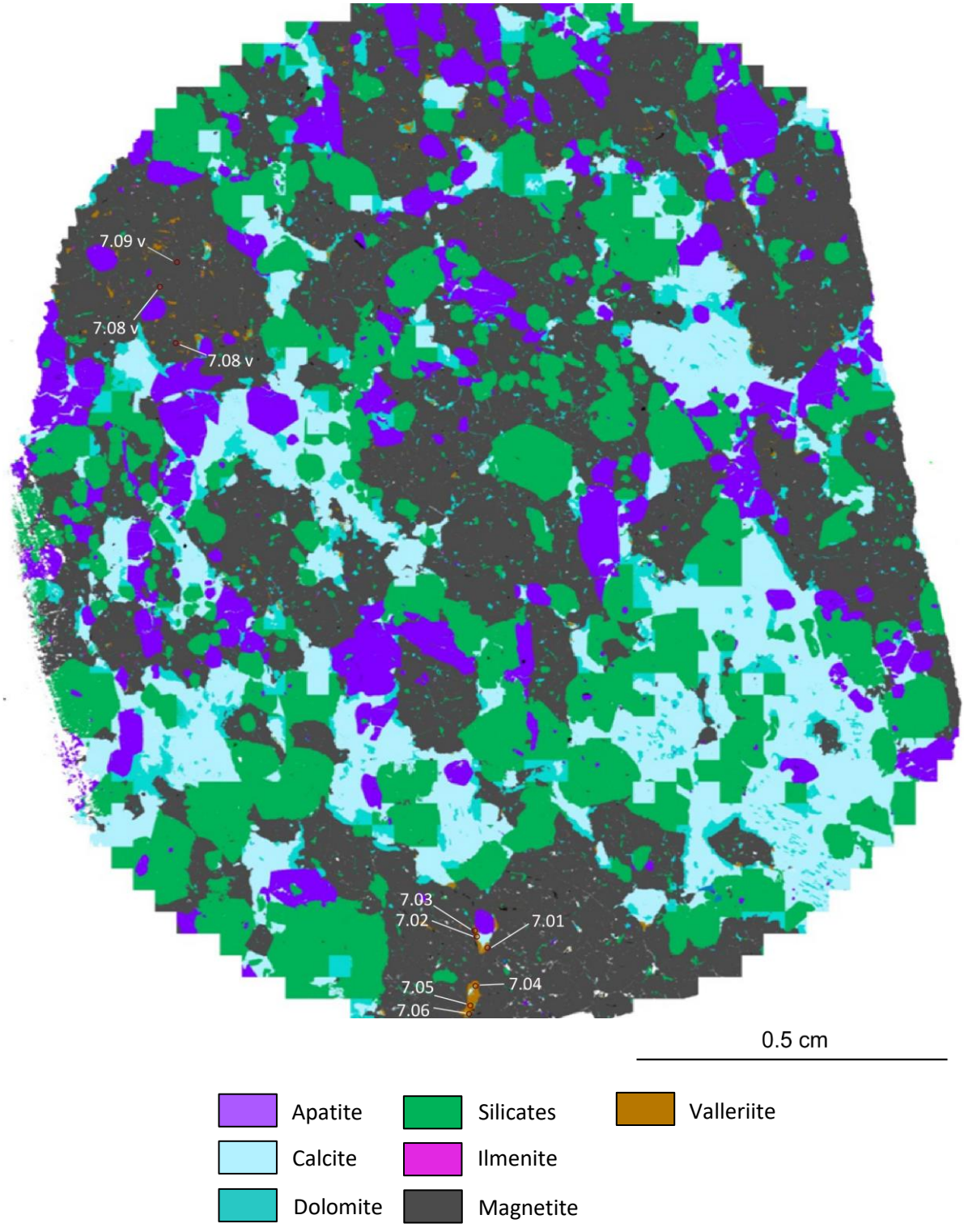

a)
b)
5.07
5.08
5.09
0.5 cm
Apatite
Calcite
Dolomite
Silicates
Baddeleyite
Magnetite
Bornite
Chalcopyrite


b)
5.03 b
5.05 cpy
5.04 cpy
5.02 b
5.06 cpy
5.01 b
750 µm
Apatite
Calcite
Dolomite
Silicates
Magnetite
Pyrrhotite
Bornite
Chalcopyrite

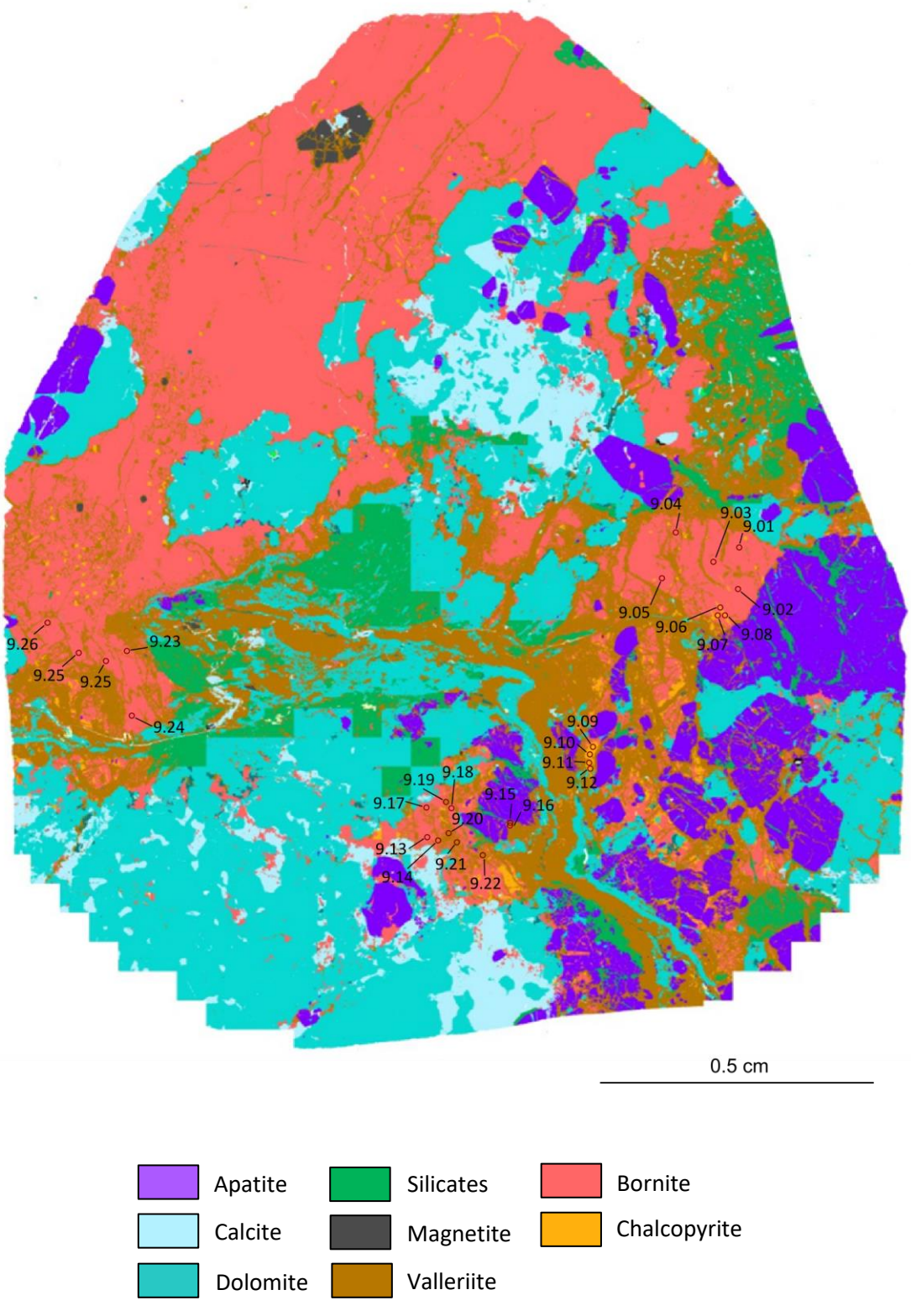
Sample 6


6.06
6.07
6.05
6.08
6.09
6.12
6.10
6.13
6.11
6.04
6.03
6.02
6.01
0.5 cm
Apatite
Silicates
Bornite
Calcite
Magnetite
Chalcopyrite
Dolomite
CoNiFe sulphide
Valleriite

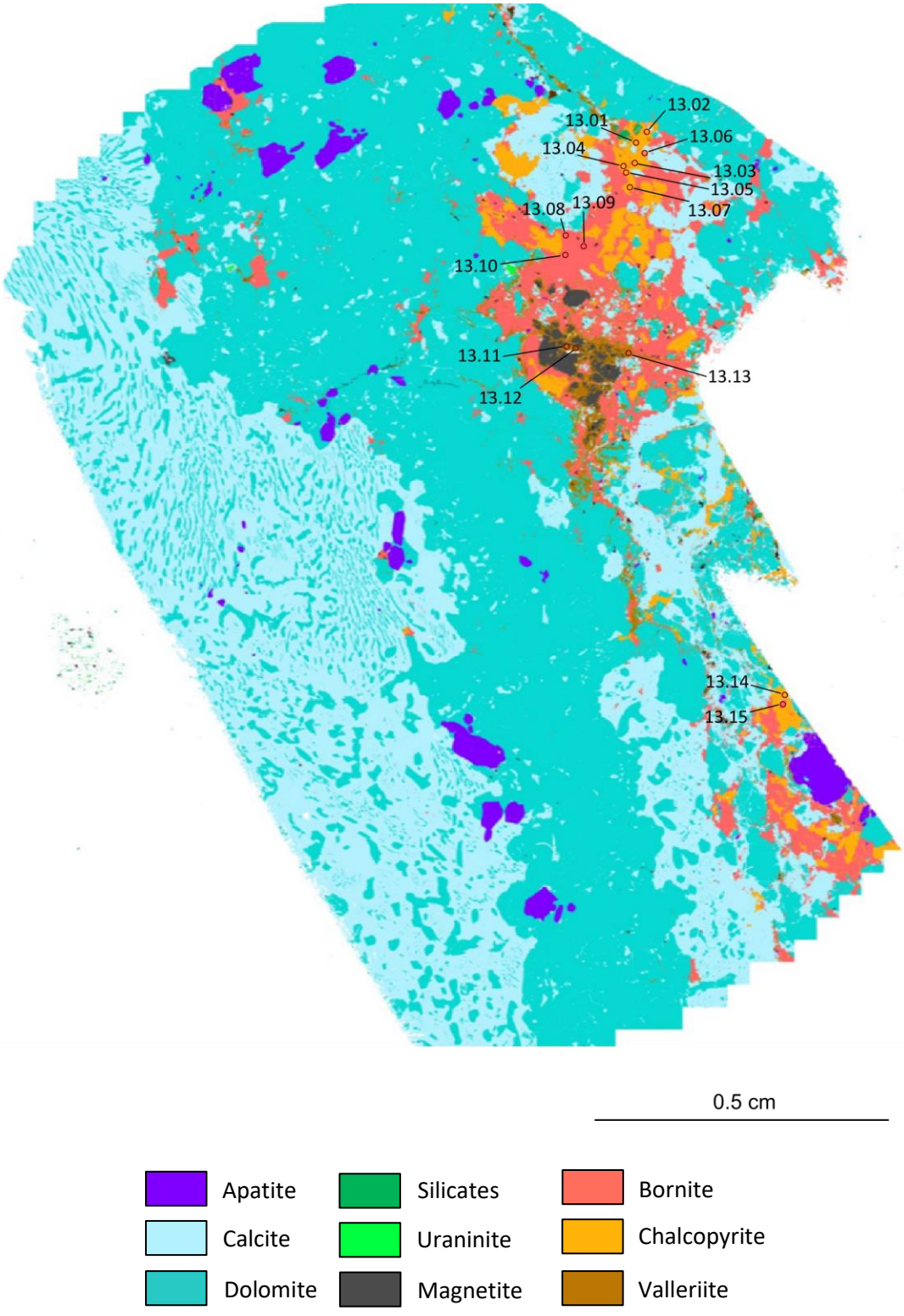
Sample 7


7.09 v
7.08 v
7.08 v
7.03
7.02
7.01
7.05
7.04
7.06
0.5 cm
Apatite
Silicates
Valleriite
Calcite
Ilmenite
Dolomite
Magnetite

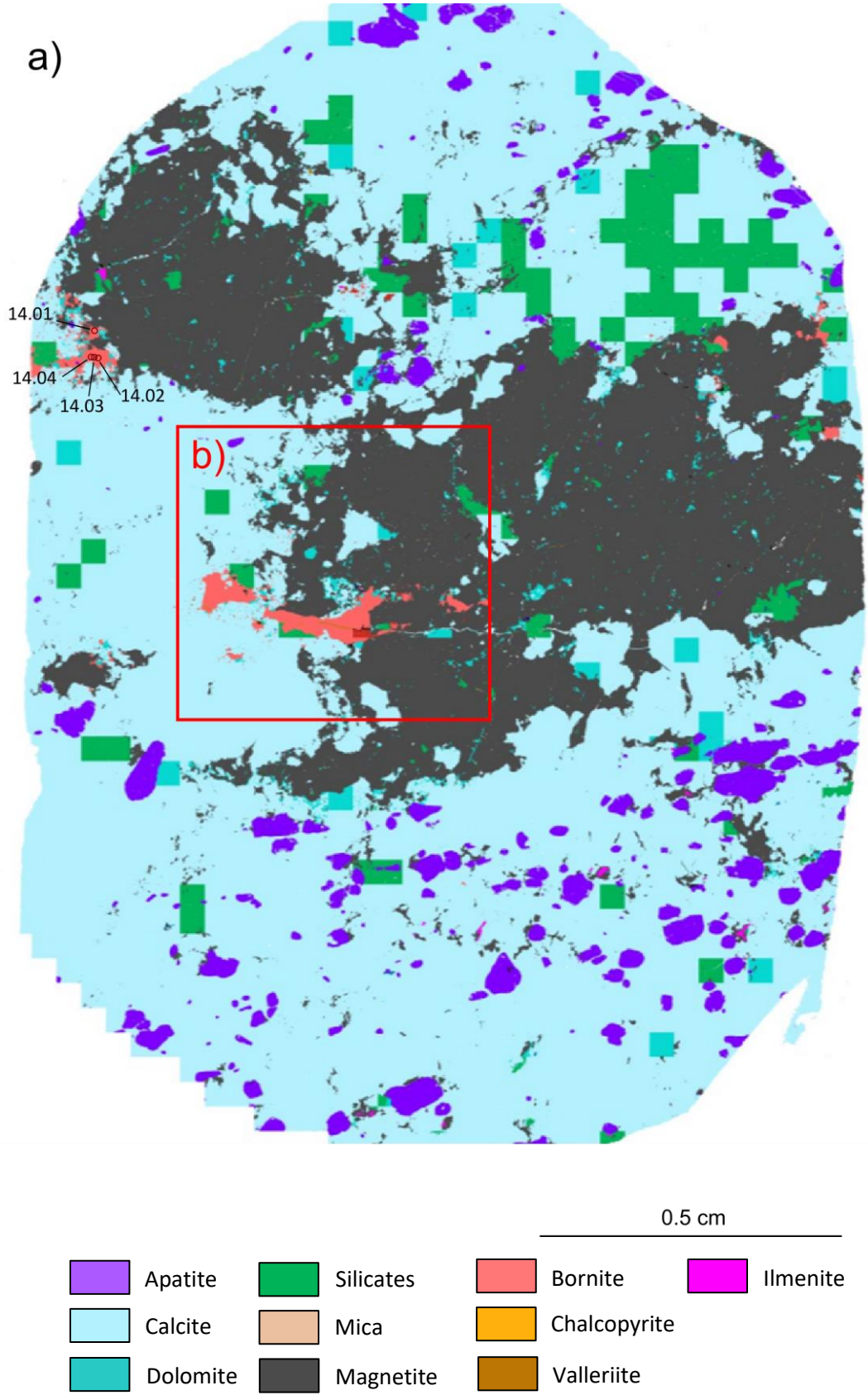
Sample 9

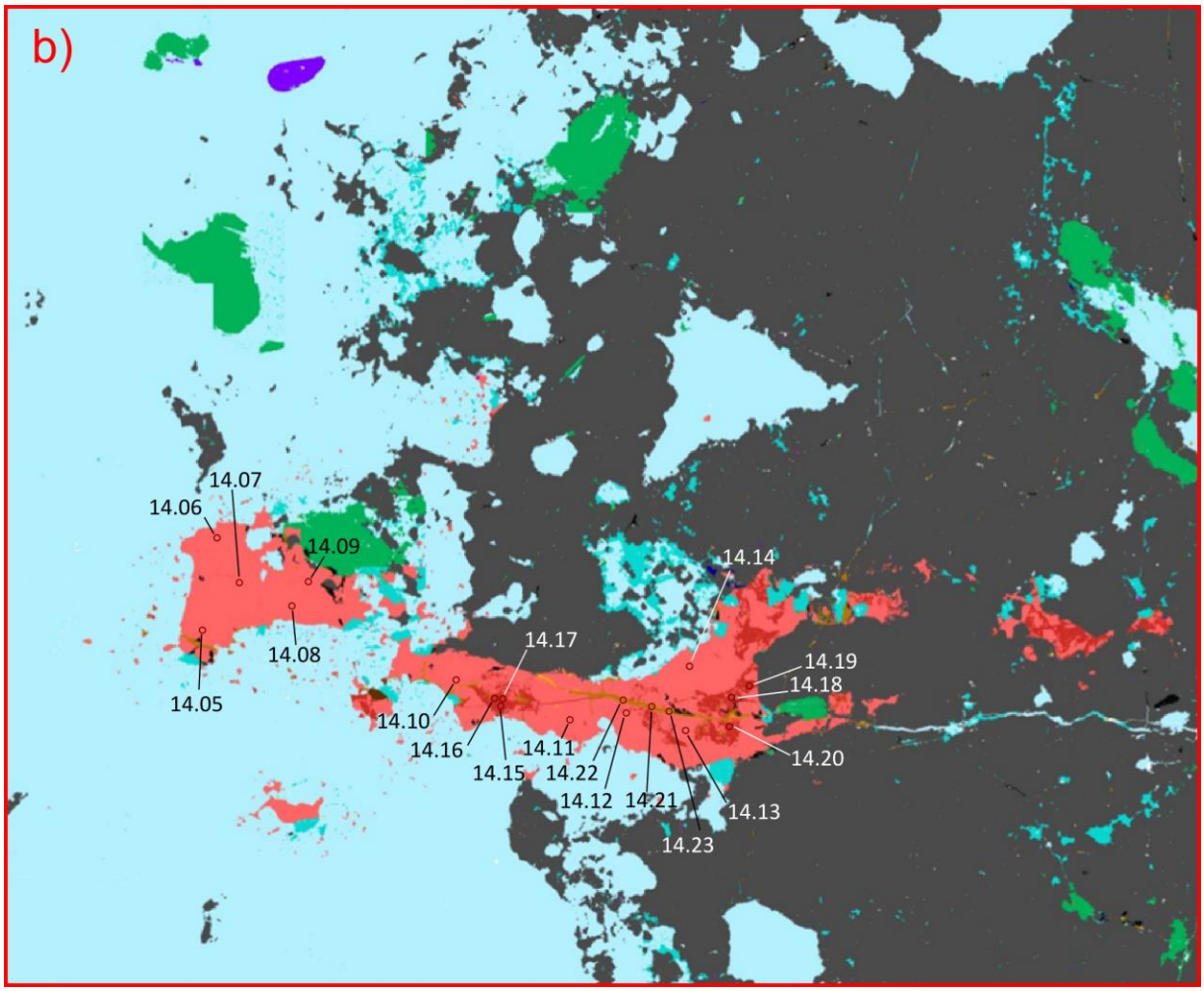

9.04
9.03
9.01
9.05
9.02
9.06
9.08
9.07
9.26
9.23
9.25
9.25
9.24
9.09
9.10
9.11
9.12
9.19
9.18
9.17
9.15
9.16
9.20
9.13
9.21
9.14
9.22
0.5 cm
Apatite
Silicates
Bornite
Calcite
Magnetite
Chalcopyrite
Dolomite
Valleriite

Sample 13

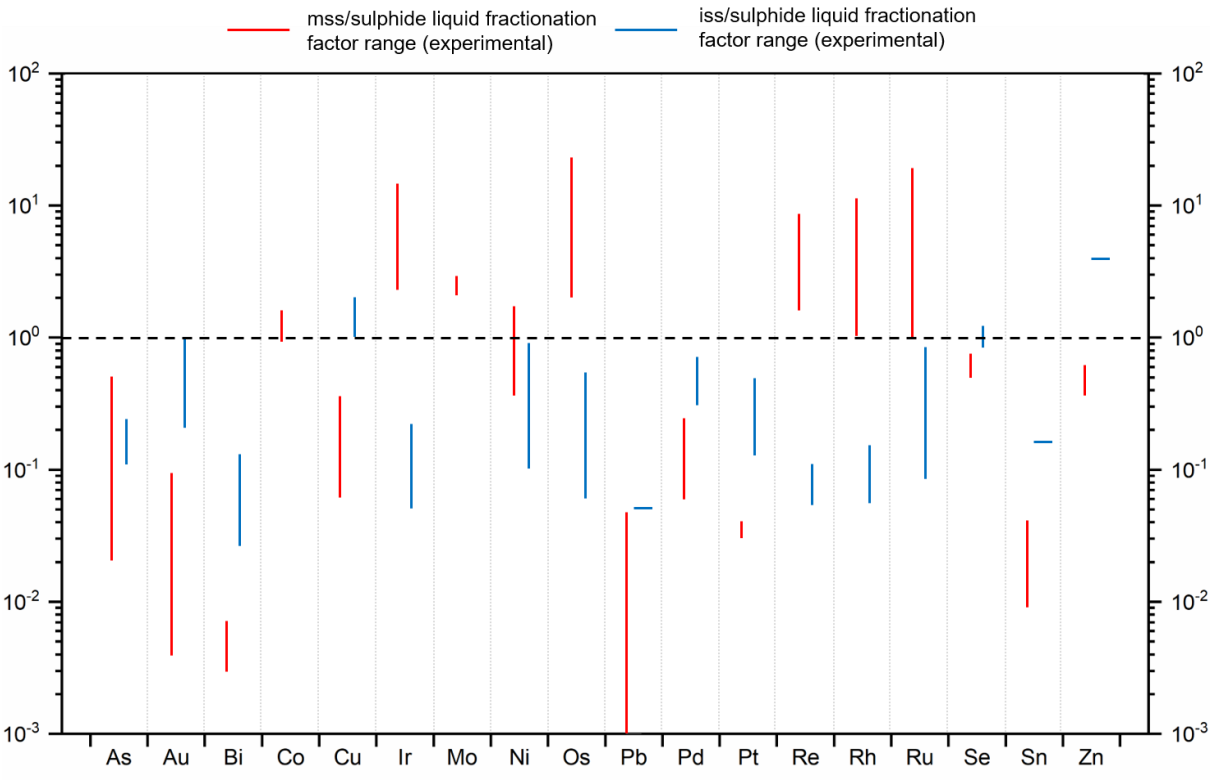

13.02
13.01
13.06
13.04
13.03
13.05
13.08
13.09
13.07
13.10
13.11
13.13
13.12
13.14
13.15
0.5 cm
Apatite
Silicates
Bornite
Calcite
Uraninite
Chalcopyrite
Dolomite
Magnetite
Valleriite

Sample 14


a)
14.01
14.04
14.03
14.02
b)
0.5 cm
Apatite
Silicates
Bornite
Ilmenite
Calcite
Mica
Chalcopyrite
Dolomite
Magnetite
Valleriite


b)
14.07
14.06
14.09
14.14
14.08
14.17
14.19
14.18
14.05
14.10
14.16
14.11
14.20
14.15
14.22
14.12
14.21
14.13
14.23
Apatite
Silicates
Bornite
Calcite
Magnetite
Chalcopyrite
Dolomite
Valleriite
Chalcocite

Appendix G: Summary of PGE and trace element mss/sulphide liquid and iss/sulphide liquid fractionation coefficients (Chapter 3)



Appendix H: List of samples used for microCT investigations (Chapter 4)

Borehole	Collar GPS coordinates	Sample ID	Depth (m)	Lithology
HD027	31° 7’ 55’’ S; 23° 59’ 33’’ E	17	-1251.9	BC
		18	-1255.3	BC
		21	-1267.8	BC/PC
		22	-1271.6	BC
		24	-1273.6	BC
		31	-1313.5	TC/PC
		33	-1315.4	TC
HD049	31° 7’ 55’’ S; 23° 59’ 34’’ E	51	-1201	BC
		53	-1196.8	BC
		56	-1193.9	BC
		57	-1193.6	BC
		58	-1193.2	BC

Appendix I: MicroCT results (Chapter 4)

See separate file.

Appendix J: Iron and Cu isotope analyses (Chapter 6)

Rock sample ref	Rock type	Ore mineral	Sample type
21	BC/PC	Cpy	Concentrate
21	BC/PC	Cpy	Concentrate
25	BC	Cpy	Concentrate
25	BC	Bn	Concentrate
27	BC	Cpy	Concentrate
27	BC	Cpy	Concentrate
36	BC	Cpy	Concentrate
36	BC	Bn	Concentrate
41	BC	Cpy	Concentrate
18	BC	Cpy	Drilled
21	BC/PC	Cpy	Drilled
25	BC	Cpy	Drilled
27	BC	Cpy	Drilled
27	BC	Cpy	Drilled
33	BC	Cpy	Drilled
51	TC	Cpy	Drilled
42	BC	Cpy	Concentrate
51	TC	Cpy	Concentrate
58	TC	Cpy	Concentrate
9	PC	Cpy	Concentrate
13	TC	Cpy	Concentrate
33	BC	Cpy	Concentrate
41	BC	Cpy	Concentrate
42	BC	Cpy	Concentrate
43	TC	Bn	Concentrate
58	TC	Cpy	Concentrate
9	PC	Cpy	Concentrate
0	PC	Bn	Concentrate
33	BC	Cpy	Concentrate
41	BC	Cpy	Concentrate
43	TC	Cpy	Concentrate
51	TC	Cpy	Concentrate
58	TC	Cpy	Concentrate
58	TC	Cpy	Concentrate
6	PC	Cpy	Drilled
13	TC	V	Drilled
13	TC	Cpy	Drilled
13	TC	Bn	Drilled
9	PC	V	Drilled
9	PC	Bn	Drilled
9	PC	Cpy	Drilled
29	BC	Mag	Concentrate
35	TC	Mag	Concentrate
37	BC/PC	Mag	Concentrate
1	BC	Mag	Concentrate
4	TC	Mag	Concentrate
10	MP	Mag	Concentrate
15	PC	Mag	Concentrate
	Standard		Powder
	Standard		Powder
	Standard		Powder

Sample ref	$\delta^{56}Fe$ (‰)						Rock sample ref	Rock type
	Analysis 1 (‰)	2(‰)	3 (‰)	Mean (‰)	Stdev	n		
Cu_1	0.15	0.12		0.14	0.02	2	21	BC/PC
Cu_2	0.13	0.21	0.16	0.17	0.04	3	21	BC/PC
Cu_3	-0.03	-0.03		-0.03	0.00	2	25	BC
Cu_4	0.07	0.07		0.07	0.00	2	25	BC
Cu_5	0.19	0.25		0.22	0.04	2	27	BC
Cu_6	0.19	0.19		0.19	0.00	2	27	BC
Cu_7	0.24	0.23		0.23	0.01	2	36	BC
Cu_8	-0.07	-0.07		-0.07	0.00	2	36	BC
Cu_9	0.18	0.14		0.16	0.03	2	41	BC
Cu01	-0.02	0.01		-0.01	0.02	2	18	BC
Cu02	0.03	-0.01		0.01	0.02	2	21	BC/PC
Cu03	-0.01	0.04		0.02	0.03	2	25	BC
Cu04	0.19	0.24		0.21	0.04	2	27	BC
Cu05	0.23	0.23		0.23	0.01	2	27	BC
Cu06	0.21	0.24		0.23	0.03	2	33	BC
Cu07	-0.38	-0.37		-0.37	0.01	2	51	TC
Cu10	-0.22	-0.21		-0.22	0.00	2	42	BC
Cu12	-0.29	-0.27		-0.28	0.01	2	51	TC
Cu15	-0.58	-0.55		-0.57	0.02	2	58	TC
Cu21	0.08	0.11		0.09	0.02	2	9	PC
Cu22	-0.26	-0.26		-0.26	0.00	2	13	TC
Cu23	0.37	0.39		0.38	0.02	2	33	BC
Cu24	-0.01	-0.03		-0.02	0.02	2	41	BC
Cu25	-0.38	-0.37		-0.37	0.01	2	42	BC
Cu26	-0.54	-0.56		-0.55	0.01	2	43	TC
Cu27	-0.66	-0.67		-0.66	0.00	2	58	TC
Cu31	-0.05	-0.05		-0.05	0.00	2	9	PC
Cu32	-0.47	-0.53		-0.50	0.04	2	0	PC
Cu33	0.14	0.15		0.15	0.01	2	33	BC
Cu34	0.07	-0.01	0.01	0.02	0.04	3	41	BC
Cu35	0.21	0.21		0.21	0.01	2	43	TC
Cu36	-0.34	-0.36		-0.35	0.01	2	51	TC
Cu37	-0.46	-0.50		-0.48	0.03	2	58	TC
Cu38	-0.44	-0.41		-0.42	0.02	2	58	TC
Cu41	-0.14	-0.17		-0.15	0.02	2	6	PC
Cu42	-0.26	-0.19	-0.17	-0.21	0.05	3	13	TC
Cu43	-0.48	-0.46		-0.47	0.01	2	13	TC
Cu44	-0.55	-0.54		-0.54	0.01	2	13	TC
Cu45	0.11	0.09		0.10	0.02	2	9	PC
Cu46	-0.45	-0.44		-0.44	0.01	2	9	PC
Cu47	-0.37	-0.37		-0.37	0.00	2	9	PC
Mgt 1	0.19	0.22		0.20	0.03	2	29	BC
Mgt 2	0.12	0.16		0.14	0.03	2	35	TC
Mgt 3	0.31	0.27		0.29	0.02	2	37	BC/PC
Wr1	0.04	0.04		0.04	0.00	2	1	BC
Wr2	-0.28	-0.27		-0.27	0.01	2	4	TC
Wr3	0.15	0.14		0.14	0.01	2	10	MP
Wr4	0.08	0.13		0.10	0.03	2	15	PC
BHVO-2	0.11	0.15		0.13	0.03	2		Standard
BIR-1	0.05	0.06		0.05	0.01	2		Standard
W-2a	0.03	0.05		0.04	0.02	2		Standard

Sample ref	δ^{57}Fe (‰)						Rock sample ref	Rock type
	Analysis 1 (‰)	2(‰)	3 (‰)	Mean (‰)	Stdev	n		
Cu_1	0.21	0.20		0.20	0.01	2	21	BC/PC
Cu_2	0.16	0.26	0.24	0.22	0.05	3	21	BC/PC
Cu_3	-0.05	-0.07		-0.06	0.01	2	25	BC
Cu_4	0.09	0.14		0.11	0.04	2	25	BC
Cu_5	0.28	0.38		0.33	0.07	2	27	BC
Cu_6	0.35	0.30		0.32	0.04	2	27	BC
Cu_7	0.37	0.40		0.39	0.02	2	36	BC
Cu_8	-0.05	-0.08		-0.06	0.02	2	36	BC
Cu_9	0.24	0.21		0.23	0.02	2	41	BC
Cu01	0.02	-0.03		0.00	0.04	2	18	BC
Cu02	0.03	0.02		0.03	0.00	2	21	BC/PC
Cu03	0.07	0.02		0.04	0.04	2	25	BC
Cu04	0.31	0.30		0.30	0.01	2	27	BC
Cu05	0.30	0.35		0.33	0.03	2	27	BC
Cu06	0.31	0.41		0.36	0.07	2	33	BC
Cu07	-0.55	-0.56		-0.56	0.00	2	51	TC
Cu10	-0.40	-0.36		-0.38	0.03	2	42	BC
Cu12	-0.48	-0.44		-0.46	0.03	2	51	TC
Cu15	-0.86	-0.85		-0.86	0.01	2	58	TC
Cu21	0.12	0.11		0.11	0.01	2	9	PC
Cu22	-0.36	-0.43		-0.40	0.05	2	13	TC
Cu23	0.53	0.61		0.57	0.05	2	33	BC
Cu24	0.00	0.01		0.00	0.01	2	41	BC
Cu25	-0.54	-0.44		-0.49	0.07	2	42	BC
Cu26	-0.82	-0.89		-0.85	0.05	2	43	TC
Cu27	-1.03	-0.99		-1.01	0.03	2	58	TC
Cu31	-0.01	-0.12		-0.07	0.08	2	9	PC
Cu32	-0.67	-0.82		-0.74	0.11	2	0	PC
Cu33	0.19	0.21		0.20	0.01	2	33	BC
Cu34	0.14	0.04	0.00	0.06	0.07	3	41	BC
Cu35	0.39	0.29		0.34	0.07	2	43	TC
Cu36	-0.49	-0.49		-0.49	0.00	2	51	TC
Cu37	-0.67	-0.71		-0.69	0.02	2	58	TC
Cu38	-0.63	-0.63		-0.63	0.00	2	58	TC
Cu41	-0.21	-0.21		-0.21	0.00	2	6	PC
Cu42	-0.39	-0.24	-0.30	-0.31	0.08	3	13	TC
Cu43	-0.73	-0.65		-0.69	0.06	2	13	TC
Cu44	-0.73	-0.76		-0.74	0.02	2	13	TC
Cu45	0.17	0.10		0.14	0.05	2	9	PC
Cu46	-0.62	-0.56		-0.59	0.04	2	9	PC
Cu47	-0.51	-0.44		-0.48	0.05	2	9	PC
Mgt 1	0.30	0.34		0.32	0.03	2	29	BC
Mgt 2	0.21	0.19		0.20	0.01	2	35	TC
Mgt 3	0.47	0.40		0.43	0.05	2	37	BC/PC
Wr1	0.05	0.04		0.04	0.01	2	1	BC
Wr2	-0.50	-0.44		-0.47	0.04	2	4	TC
Wr3	0.22	0.19		0.20	0.02	2	10	MP
Wr4	0.15	0.10		0.12	0.04	2	15	PC
BHVO-2	0.20	0.24		0.22	0.03	2		Standard
BIR-1	-0.04	0.06		0.01	0.07	2		Standard
W-2a	0.05	0.01		0.03	0.02	2		Standard

Sample ref	Rock sample ref	Rock type	Ore mineral	Sampling type
Cu_1	21	BC/PC	Cpy	Concentrate
Cu_2	21	BC/PC	Cpy	Concentrate
Cu_3	25	BC	Cpy	Concentrate
Cu_4	25	BC	Bn	Concentrate
Cu_5	27	BC	Cpy	Concentrate
Cu_6	27	BC	Cpy	Concentrate
Cu_7	36	BC	Cpy	Concentrate
Cu_8	36	BC	Bn	Concentrate
Cu_9	41	BC	Cpy	Concentrate
Cu01	18	BC	Cpy	Drilled
Cu02	21	BC/PC	Cpy	Drilled
Cu03	25	BC	Cpy	Drilled
Cu04	27	BC	Cpy	Drilled
Cu05	27	BC	Cpy	Drilled
Cu06	33	BC	Cpy	Drilled
Cu07	51	TC	Cpy	Drilled
Cu10	42	BC	Cpy	Concentrate
Cu12	51	TC	Cpy	Concentrate
Cu15	58	TC	Cpy	Concentrate
Cu21	9	PC	Cpy	Concentrate
Cu22	13	TC	Cpy	Concentrate
Cu23	33	BC	Cpy	Concentrate
Cu24	41	BC	Cpy	Concentrate
Cu25	42	BC	Cpy	Concentrate
Cu26	43	TC	Bn	Concentrate
Cu27	58	TC	Cpy	Concentrate
Cu31	9	PC	Cpy	Concentrate
Cu32	0	PC	Bn	Concentrate
Cu33	33	BC	Cpy	Concentrate
Cu34	41	BC	Cpy	Concentrate
Cu35	43	TC	Cpy	Concentrate
Cu36	51	TC	Cpy	Concentrate
Cu37	58	TC	Cpy	Concentrate
Cu38	58	TC	Cpy	Concentrate
Cu41	6	PC	Cpy	Drilled
Cu42	13	TC	V	Drilled
Cu43	13	TC	Cpy	Drilled
Cu44	13	TC	Bn	Drilled
Cu45	9	PC	V	Drilled
Cu46	9	PC	Bn	Drilled
Cu47	9	PC	Cpy	Drilled
Mgt 1	29	Standard		Powder
Mgt 2	35	Standard		Powder
Mgt 3	21	BC/PC	Cpy	Concentrate
Wr1	21	BC/PC	Cpy	Concentrate
Wr2	25	BC	Cpy	Concentrate
Wr3	25	BC	Bn	Concentrate
Wr4	27	BC	Cpy	Concentrate
BHVO-2	27	BC	Cpy	Concentrate
BIR-1	36	BC	Cpy	Concentrate
W-2a	36	BC	Bn	Concentrate

Sample ref	δ^{65}Cu (‰)							
	Analysis 1 (‰)	2(‰)	3 (‰)	4 (‰)	5 (‰)	Mean (‰)	Stdev	n
Cu_1	-0.08	-0.08	-0.08			-0.08	0.00	3
Cu_2	-0.11	-0.06	-0.22			-0.13	0.08	3
Cu_3	-0.67	-0.68	-0.58			-0.64	0.05	3
Cu_4	-0.59	-0.60	-0.58			-0.59	0.01	3
Cu_5	0.21	0.23	0.22			0.22	0.01	3
Cu_6	0.52	0.20	0.12	0.24		0.27	0.17	4
Cu_7	-0.51	-0.41				-0.46	0.07	2
Cu_8	-0.41	-0.34				-0.38	0.05	2
Cu_9	-0.42	-0.36				-0.39	0.04	2
Cu01	0.30	0.43	0.03	0.08	-0.19	0.13	0.24	5
Cu02	-0.04	-0.08	-0.21			-0.11	0.09	3
Cu03	-0.68	-0.77	-0.83			-0.76	0.07	3
Cu04	-0.98	-1.06	-1.36			-1.13	0.20	3
Cu05	0.00	0.10	-0.20			-0.03	0.16	3
Cu06	-0.45	-0.45	-0.53	-0.50		-0.48	0.04	4
Cu07	-0.59	-0.73	-0.73			-0.68	0.08	3
Cu10	-0.49	-0.48				-0.49	0.01	2
Cu12	-0.53	-0.46				-0.49	0.05	2
Cu15	-0.43	-0.38				-0.40	0.04	2
Cu21	0.34	0.33	0.28			0.31	0.03	3
Cu22	0.48	0.31	0.29	0.30		0.34	0.09	4
Cu23	-0.28	-0.30	-0.34			-0.31	0.03	3
Cu24	-0.51	-0.47	-0.46			-0.48	0.03	3
Cu25	0.13	-0.05	0.03	-0.16		-0.01	0.12	4
Cu26	-0.07	-0.20	-0.16	-0.22		-0.16	0.07	4
Cu27	-0.41	-0.47	-0.51			-0.46	0.05	3
Cu31	0.44	0.39	0.35	0.37		0.39	0.04	4
Cu32	0.03	0.02	0.09			0.05	0.04	3
Cu33	-0.17	-0.06	-0.11	-0.10		-0.11	0.04	4
Cu34	-0.32	-0.17	-0.39	-0.33		-0.30	0.09	4
Cu35	-0.11	-0.08	-0.06			-0.08	0.02	3
Cu36	-0.48	-0.49	-0.42			-0.46	0.04	3
Cu37	-0.29	-0.32	-0.29			-0.30	0.02	3
Cu38	-0.39	-0.38	-0.41			-0.39	0.01	3
Cu41	0.77	0.77	0.76			0.77	0.01	3
Cu42	0.33	0.38	0.37			0.36	0.03	3
Cu43	0.45	0.41	0.41			0.42	0.02	3
Cu44	0.54	0.56	0.53			0.54	0.01	3
Cu45	0.32	0.31	0.30			0.31	0.01	3
Cu46	0.2	0.19	0.19			0.19	0.01	3
Cu47	0.3	0.30	0.33			0.31	0.02	3
BHVO-2	0.14					0.14		1
BIR-1a	0.03					0.03		1
Cu_1	-0.08	-0.08	-0.08			-0.08	0.00	3
Cu_2	-0.11	-0.06	-0.22			-0.13	0.08	3
Cu_3	-0.67	-0.68	-0.58			-0.64	0.05	3
Cu_4	-0.59	-0.60	-0.58			-0.59	0.01	3
Cu_5	0.21	0.23	0.22			0.22	0.01	3
Cu_6	0.52	0.20	0.12	0.24		0.27	0.17	4
Cu_7	-0.51	-0.41				-0.46	0.07	2
Cu_8	-0.41	-0.34				-0.38	0.05	2